

Distribution Agreement

In presenting this thesis or dissertation as a partial fulfillment of the requirements for an advanced degree from Emory University, I hereby grant to Emory University and its agents the non-exclusive license to archive, make accessible, and display my thesis or dissertation in whole or in part in all forms of media, now or hereafter known, including display on the world wide web. I understand that I may select some access restrictions as part of the online submission of this thesis or dissertation. I retain all ownership rights to the copyright of the thesis or dissertation. I also retain the right to use in future works (such as articles or books) all or part of this thesis or dissertation.

Signature:

Stephanie Prince

Date

Neural codes underlying memory and flexible navigation in health and Alzheimer's disease

By

Stephanie Prince
Doctor of Philosophy

Graduate Division of Biological and Biomedical Science
Neuroscience

Annabelle C. Singer, Ph.D.
Advisor

Jocelyne Bachevalier, Ph.D.
Committee Member

Joseph R. Manns, Ph.D.
Committee Member

Samuel J. Sober, Ph.D.
Committee Member

Garrett B. Stanley, Ph.D.
Committee Member

Accepted:

Kimberly Jacob Arriola, Ph.D, MPH
Dean of the James T. Laney School of Graduate Studies

Date

Neural codes underlying memory and flexible navigation in health and Alzheimer's disease

By

Stephanie Prince
B.S., University of Notre Dame, 2016

Advisor: Annabelle C. Singer, Ph.D.

An abstract of a dissertation submitted to the Faculty of the James T. Laney School of Graduate
Studies of Emory University in partial fulfillment of the requirements for the degree of Doctor of
Philosophy in Neuroscience
2023

Neural codes underlying memory and flexible navigation in health and Alzheimer's disease

By

Stephanie Prince

In our day-to-day lives, we seamlessly integrate our past experiences, present circumstances, and future plans in our thoughts. Our brains constantly switch between memories and incoming information in order to decide between potential options and make plans. But how do we flexibly adapt those plans when pursuing our goals? And what underlies the degradation of these processes in neurodegenerative diseases such as Alzheimer's?

In the first part of this dissertation, we asked how neural representations of future goals influence our ability to flexibly adapt plans with new information. We designed a novel decision-making task in which we precisely controlled the introduction of new, pivotal information using virtual reality, and recorded neural activity from hippocampus and prefrontal cortex as animals had to adapt their behavior in response to new information. We found that prospective codes are rapidly modulated by new information from dynamic stimuli, specifically when the new information indicates animals must update their previous choices to obtain a reward. We also found that failure to switch from old to new choice representations in prefrontal cortex occurred when animals were unable to adapt to new information. These results show how prospective codes for future locations or choices play a role in the ability to rapidly adapt behavior in response to new information.

In the second part of this dissertation, we asked how neural representations important for memory were disrupted during navigation in Alzheimer's disease. We recorded neural activity from the *5XFAD* mouse model of Alzheimer's disease during spatial navigation and found deficits in interneuron connection strength onto pyramidal cells in hippocampus. These deficits occurred in awake, behaving mice and were most pronounced during sharp-wave ripple oscillations that are important for memory and require inhibition. In addition to these synaptic deficits *in vivo*, we also found the mouse model of Alzheimer's disease had fewer and shorter sharp-wave ripple oscillations and impaired reactivation of neuronal firing during sharp-wave ripples. These results show that inhibitory synaptic dysfunction occurs during spatial navigation in *5XFAD* mice and suggest a potential mechanism underlying deficits in network activity that is critical for memory and cognitive function.

The results of this work demonstrate how prospective codes in hippocampus and prefrontal cortex adapt for flexible behavior in our dynamic world and show how neural codes for memory in the hippocampus might be disrupted by Alzheimer's pathology via synaptic dysfunction.

Neural codes underlying memory and flexible navigation in health and Alzheimer's disease

By

Stephanie Prince
B.S., University of Notre Dame, 2016

Advisor: Annabelle C. Singer, Ph.D.

A dissertation submitted to the Faculty of the James T. Laney School of Graduate Studies of
Emory University in partial fulfillment of the requirements for the degree of Doctor of Philosophy
in Neuroscience
2023

Acknowledgements

My favorite part of dissertations and defenses is always the acknowledgements section, where you get a glimpse behind the scenes of all the people who contributed to the research and PhD process in both scientific and personal ways. Here are some of the people I would like to thank for their contributions to this work.

Thanks first and foremost to my advisor Annabelle for being a wonderful and supportive mentor over the years. I came to the lab knowing not that much about neuroscience and even less about experimental design, electrophysiology, data analysis, presentations, or all the other skills that might be important to our research. But you have been a great mentor and patient teacher and have given me all the resources and encouragement to learn, improve these skills, and grow as a scientist. I'm especially thankful for the freedom you gave me to pursue my own scientific and academic interests, while showing me how to prioritize and clarify my goals so I could both explore and make progress on my research.

Thanks to my committee, Joe Manns, Jocelyne Bachevalier, Sam Sober, and Garrett Stanley for your support over the years. You have intervened at several moments along this project's development with great advice, important critical feedback, and helpful perspectives that have made this work better. I really appreciate all the time you have invested in my training.

Thanks to all the Singer lab members, Abby Paulson, Nuri Jeong, Lou Blanpain, Kristie Garza, Sina Dabiri, Xiao Zheng, Lu Zhang, Tina Franklin, Ashley Prichard, Matty Attokaren, and Matthew Goodson. It has been so fun to watch the lab grow with all of your efforts, and you have made the lab a very positive and encouraging environment. Thanks for listening to all the many practice talks and lab meeting presentations and always being helpful, supportive colleagues. Thanks also to Navya Katragadda, Teema Yassine, and Tyler Roberts, for your critical role in collecting this data with me.

Thanks to all the neuro and neuro-adjacent researchers at Georgia Tech. You have been a welcoming research community, an endless resource for experimental advice, and an overall

excellent group of people to work alongside. I'm especially thankful to Abby, Joseph, Gio, and Andy for all the extended lunches, strange breakroom conversations, potentially excessive coffee walks, and post-work adventures - the past six and a half years would have been much less fun without you.

Thanks to my fellow graduate students, Kate, Erin, Zeena, and Miao, for being my first friends in Atlanta. Even while we shared struggles together, we always encouraged each other to push towards the finish line over the years. To the Gables crew, Ben, Mary, Mahir, Megan, Kate, and Brian, I'm so lucky to have had you all as my little neighborhood community and am grateful for all the pool days, tailgates, and festivities that made life outside of lab better. To my friends Katie C, Anna, Erin, Ryanne, Katie H., thanks for being the best support system from the very beginning stages of grad school applications to today.

Thanks to my sisters Mar, Anna, Cat, and Tess, and my brothers, Matt, Charlie, and Michael for sending funny life updates that brightened long experiment days. To my mom, for your constant support and encouragement of all my goals and dreams. To my dad, for sharing your enthusiasm for science and engineering with me from when I was little to today. To my grandparents, for welcoming us at our home away from home every Thanksgiving and always sending me back to Atlanta with more items than I could fit in my suitcase.

Finally, thanks to Andy, who has been by my side with me these past six years. You have given me unending support – letting me bounce ideas off you, listening to my practice talks, and most of all, picking me back up on the worst days and celebrating with me on the best days.

Thank you all.

Table of Contents

CHAPTER 1 - INTRODUCTION	1
1.1 Integrating past, present, and future experiences in navigation and decision making. 2	
1.1.1 The role of hippocampus in memory and navigation	2
1.1.2 The role of prefrontal cortex in decision making and navigation.....	4
1.2 Hippocampal-prefrontal interactions and neural codes for memory and decision making.....	5
1.2.1 Theoretical frameworks for hippocampal-prefrontal interactions	5
1.2.2 Anatomical features and connections between hippocampus and prefrontal cortex	6
1.2.3 Neural codes during theta in the hippocampus	10
1.2.4 Neural codes during sharp-wave ripples in the hippocampus	12
1.2.5 Hippocampal-prefrontal interactions during theta and sharp-wave ripples.....	14
1.3 Network-level approaches to understanding Alzheimer’s disease	16
1.3.1 Cognitive deficits to memory and planning processes in Alzheimer’s disease	16
1.3.2 Network dysfunction in Alzheimer’s disease	17
1.4 Dissertation objectives	20
1.4.1 How do hippocampal and prefrontal cortex prospective codes contribute to flexible decision making when new information is presented?	20
1.4.2 Are hippocampal neural codes of memory and in vivo synaptic activity altered in a mouse model of Alzheimer’s disease?	21
CHAPTER 2 – NEW INFORMATION TRIGGERS PROSPECTIVE CODES FOR FLEXIBLE ADAPTATION OF ONGOING CHOICES	23
2.1 Abstract.....	24
2.2 Introduction	25
2.3 Results	28
2.3.1 Animals rapidly update their choices in response to new information in a spatial memory task	28
2.3.2 Enhanced non-local codes of both goal locations in hippocampus in response to new pivotal information	31
2.3.3 Rapid switch from old to new choice estimates in prefrontal cortex when new information is presented.....	38
2.3.4 Goal codes predict ability to accurately update decisions in response to new information	42
2.3.5 Increased goal representations are correlated with choice commitment.....	47

2.4. Discussion	51
2.5. Methods	54
2.5.1 Animals.....	54
2.5.2 Surgical procedures	55
2.5.3 Behavioral task and training.....	55
2.5.4 Electrophysiology recordings.....	57
2.5.5 Local field potential and single unit preprocessing.....	58
2.5.6 Behavioral analysis	59
2.5.7 Choice modelling.....	60
2.5.8 Decoding analyses.....	60
2.5.9 Theta cycles and phase	62
2.5.10 Prediction of behavioral choice.....	63
2.5.11 Statistical analyses.....	64
2.6 Supplementary Figures and Tables	65
CHAPTER 3 - ALZHEIMER'S PATHOLOGY CAUSES IMPAIRED INHIBITORY CONNECTIONS AND REACTIVATION OF SPATIAL CODES DURING SPATIAL NAVIGATION	88
3.1 Abstract	90
3.2 Introduction	91
3.2.1. Synaptic dysfunction in Alzheimer's disease.....	91
3.2.2. Deficits in neural activity across multiple models of Alzheimer's disease	91
3.3. Results	94
3.3.1. 5XFAD mice and wild-type littermates lick for reward in a virtual reality spatial task....	94
3.3.2. Interneuron-to-pyramidal monosynaptic connections are weaker in 5XFAD mice	96
3.3.3. 5XFAD mice have shorter and fewer sharp-wave ripples compared to WT mice	103
3.3.4. Place cells of 5XFAD mice have decreased reactivation during sharp-wave ripples..	105
3.4. Discussion	109
3.4.1. Linking synaptic dysfunction and interneuron deficit hypotheses in Alzheimer's disease	109
3.4.2. Synaptic changes and sharp-wave ripple deficits could underlie memory impairment	111
3.5. Methods	114
3.5.1. Animals.....	114
3.5.2. Surgical procedures	114

3.5.3. Behavioral training and analysis	115
3.5.4. Electrophysiology recordings	116
3.5.5. Local Field Potential Analyses	117
3.5.6. Classification of cell types.....	118
3.5.7. Identification of monosynaptic connections.....	120
3.5.8. Quantification of connection strength	121
3.5.9. Place cell identification.....	123
3.5.10. Reactivation during sharp-wave ripples.....	124
3.5.11. Quantification and statistical analysis.....	126
3.6. Supplementary Figures and Tables	128
CHAPTER 4 - DISCUSSION.....	146
4.1 Results summary.....	147
4.2 Caveats and limitations	149
4.2.1 Ethological validity of virtual reality experiments	149
4.2.2 Clinical relevance of mouse models of Alzheimer’s disease	150
4.3 Future directions	150
4.3.1 Causally manipulating prospective codes to impact behavior	150
4.3.2 Integrating environmental changes and neural activity.....	152
4.3.3 Rescuing neural activity deficits and memory in Alzheimer’s disease.....	153
4.3.4 Leveraging unique virtual reality tasks to test cognitive function	153
4.4 Conclusions	155
CHAPTER 5 – APPENDIX: A SPATIAL NAVIGATION PARADIGM TO TEST FLEXIBLE DECISION MAKING IN MICE USING VIRTUAL REALITY.....	156
5.1 Introduction.....	156
5.2 Behavioral task development and validation	157
5.2.1 A virtual reality paradigm to test flexible decision making in response to new information	157
5.2.2 Virtual reality environments across stages of behavior training.....	159
5.2.3 Behavioral training procedure	162
5.2.4 Behavioral interventions for successful task acquisition and performance	165
5.3 Software and analysis features.....	168

5.3.1 Automation approaches to task software use and behavioral training	168
5.3.2 Synchronization to other acquisition systems	169
5.4 Discussion.....	170
REFERENCES	172

List of Figures

Figure 1.1 Schematic of anatomical pathways in prefrontal-hippocampal circuit.....	9
Figure 1.2 Schematic of hippocampal activity during theta and sharp-wave ripple oscillations .	13
Figure 1.3 Gap in understanding how prospective codes in hippocampus and prefrontal cortex underlie deliberation and adaptation of plans with new information.....	21
Figure 1.4. Gap in understanding between synaptic dysfunction due to Alzheimer’s pathology and cognitive memory impairments.....	22
Figure 2.1. Mice rapidly and selectively update their choices in response to new information...	30
Figure 2.2. Non-local representations for both initial and new goals increase in hippocampus in response to new information	34
Figure 2.3. Non-local codes occur on distinct theta phases from local position codes and increase with new information	37
Figure 2.4. Prefrontal cortex rapidly switches from representing the old choice to the new choice in response to new information.....	42
Figure 2.5 Prefrontal cortex decoding of choice predicts correct response while hippocampal goal coding remains elevated regardless of trial outcome.....	46
Figure 2.6. Hippocampal codes for new goal locations increase more strongly when animals are more committed to the initial goal.....	49
Figure 2.7. Additional update task behavioral metrics and task details.....	71
Figure 2.8 Recording location details and Bayesian decoding validation for hippocampal position	74
Figure 2.9. Individual session and animal breakdown of hippocampal position codes around the update cue	75
Figure 2.10. Bayesian decoding validation of position representation for prefrontal cortex	78
Figure 2.11 Theta phase modulation of position representations for stay and delay only trials .	79
Figure 2.12 Bayesian decoding validation of choice representation and additional controls.....	80
Figure 2.13 Individual session and animal breakdown of prefrontal cortex choice codes around the update cue	82
Figure 2.14. Bayesian decoding of choice representation in hippocampus.	85
Figure 2.15. Choice commitment breakdown of decoding outputs across trial types	86
Figure 3.1 Cover image illustration of findings on neural activity in Alzheimer’s disease	89
Figure 3.2 5XFAD mice and wild-type littermates lick for reward in a virtual reality spatial task.	95
Figure 3.3 Interneuron-to-pyramidal monosynaptic connections are weaker in 5XFAD mice. ...	99
Figure 3.4 Pyramidal-to-interneuron monosynaptic connections in 5XFAD mice.	101
Figure 3.5 5XFAD mice have shorter and fewer sharp-wave ripples compared to WT mice. ..	104
Figure 3.6 Place cells of 5XFAD mice have lower probability of activation and coactivation during sharp-wave ripples.....	107
Figure 3.7 Experimental timeline and behavioral metrics for individual animals.....	129
Figure 3.8 Recording locations and classification of putative pyramidal cells and interneurons.	130
Figure 3.9 Interneuron-to-pyramidal cell connection strength for individual animals and percent connections.....	133
Figure 3.10 Pyramidal-to-interneuron connection strength for individual animals and percent connections.....	136
Figure 3.11 Distribution of monosynaptically connected cell pairs across the electrode.....	137
Figure 3.12 Ripple abundance, duration, and power per recording and resampled distributions.	140
Figure 3.13 Place cell properties and place cell pair reactivation during sharp-wave ripples for individual sessions.....	141

Figure 5.1. A novel behavioral task to test flexible responses to new information during spatial navigation.....	158
Figure 5.2. Animals progress across training phases and learn to successfully perform task across all trial types.	161
Figure 5.3. Implementing behavioral interventions can produce quicker and better training outcomes.....	168
Figure 5.4. Software and automation pipeline to facilitate efficient and consistent training practices.....	170

List of Tables

Table 2.1 Experimental metadata for all recording sessions.	65
Table 2.2 Statistical analysis details.....	70
Table 3.1 Genotypes, recording sessions, single units, sharp-wave ripples, and putative monosynaptic connections per animal.	145
Table 5.1 Advancement criteria and goals of each training phase for update task paradigm. .	164

CHAPTER 1 - INTRODUCTION

In our day-to-day lives, we seamlessly integrate our past experiences, present circumstances, and future plans in our thoughts. Over the course of seconds, we can remember an errand we had to run, consider whether we have time to make a detour, and then pinpoint a later time when we can go. This thread of recollection, perception, and planning is often interwoven with a set of decisions as the environment and consequences of our ongoing choices unfold. The errand we chose to postpone suddenly becomes urgent when we get a call with new information, and we must choose how to adapt our plans accordingly. The store we planned to go to will close by the time we arrive, and we must choose a new destination. The route to our errand destination that we know so well is under construction today, and we must choose a new road. How do our brains flip through potential scenarios and perform integrations of past, present, and future in order to make decisions and flexibly adapt plans with such rapidity?

1.1 Integrating past, present, and future experiences in navigation and decision making

1.1.1 The role of hippocampus in memory and navigation

One of the first brain structures to examine for insights into cognitive processes involving past, present, and future experiences is the hippocampus. The earliest sign that the hippocampus was a critical region in the brain for memory and planning was the groundbreaking case of the patient H.M. H.M. underwent surgical resection of his hippocampus and medial temporal lobes in an experimental surgery to treat his epilepsy, but after the surgery he suffered from severe amnesia even while other cognitive faculties remained more intact (Scoville & Milner, 1957). His ability to form and use new memories for experiences after his surgery was profoundly impaired. This pivotal work led to the theory of the hippocampus as a locus for encoding and retrieval of memories.

Further research led to the idea that the hippocampus not only forms memory representations of past experiences, but also builds models connecting these experiences and knowledge of our

world. Tolman was the first to propose that animals connected their experiences to form internal models of their environment. Tolman observed that animals in a maze could identify novel shortcuts in environments even when those shortcuts had not been previously experienced, suggesting that these animals were building a 'cognitive map' more than just using simple motor responses as a navigational strategy (Tolman, 1948). When single neuron recording techniques began to be developed in rodents, O'Keefe and Nadel observed that neurons in hippocampus fired in specific locations of an environment (O'Keefe & Dostrovsky, 1971). They theorized that these neurons, known as 'place cells', might be a neural substrate of these cognitive maps by encoding representations of different environmental locations (O'Keefe & Nadel, 1978). The idea of a 'cognitive map' continues to be often studied in the context of navigation. Researchers build various environments and experimental paradigms to test how animals form spatial representations and employ them for memory and navigation. Cognitive maps for task rules and other non-spatial features have also been proposed to exist in the hippocampus and other regions such as prefrontal cortex and orbitofrontal cortex (Behrens et al., 2018).

One of the ways these maps are used is in memory tasks where animals must seek out a goal location. When navigating towards a goal destination, a cognitive map of the environment can be used to plan routes from our current position to our future destination, and to flexibly adapt those plans as needed. To arrive at our destination during goal-directed behavior, we must maintain representations of our goal destinations in our mind while also accessing representations of our current location (Nyberg et al., 2022). It has thus been proposed that with this cognitive map, the hippocampus can do more than represent current state, but also plan and imagine future or novel states (Buckner, 2010; Comrie et al., 2022; Pezzulo et al., 2019). Non-local neural codes for novel or future locations have been observed in the hippocampus across a variety of memory and navigation tasks. In addition to spatial navigation and decision making, recent work has also found that neural correlates of internal model-based planning exist

in hippocampus in rats during non-spatial tasks, and hippocampal inactivation leads to planning impairments (K. J. Miller et al., 2017). Later work looking back at the cognitive deficits exhibited by H.M. and other hippocampal damage patients also found that future planning and experiential imagination abilities were disrupted (Hassabis et al., 2007; Klein et al., 2002, unpublished personal communications from S. Corkin and S. Steinvorth, cited in Buckner, 2010; de Vito & della Sala, 2011). This research suggests that memory and planning in the hippocampus might have a shared mechanism in which internal models are used to integrate past, present, and future across spatial and nonspatial experiences (Mullally & Maguire, 2014).

1.1.2 The role of prefrontal cortex in decision making and navigation

Prefrontal cortex is known to be an important brain region for flexible decision making and goal-directed behavior. Early studies recording neurophysiological activity in awake, behaving monkeys for the first time found that prefrontal cortex neurons in monkeys were active over delay intervals and suggested they could maintain task-relevant information (Fuster & Alexander, 1971; Kubota & Niki, 1971). Further work in humans and non-human primates identified the role of prefrontal cortex in higher-order cognitive processes such as attention, working memory, and general executive function (Fuster, 2015; Goldman-Rakic, 1995). Later reviews proposed that prefrontal cortex maintains patterns of activity that represent goals and how to select the appropriate actions to achieve those goals (E. K. Miller & Cohen, 2001). Prefrontal cortex is thought to be capable specifically of highly flexible switching between tasks or moving from one goal to another. Damage to prefrontal cortex often leads to perseveration (not updating with new information) and distractibility (updating at inappropriate times) in primates (Chao & Knight, 1997; Mishkin, 1964). Prefrontal cortex has also been proposed to encode non-spatial cognitive maps, linking together more abstract task rules or general environmental features (Behrens et al., 2018).

Much of the general functions attributed to prefrontal cortex are also required in more complex navigation tasks (Patai & Spiers, 2021). Not all navigation tasks are thought to engage the prefrontal cortex, but specifically more complex tasks that require selection between multiple goals or considerations of alternatives. Patients with damage to prefrontal cortex exhibit difficulties in spatial navigation, but in contrast to patients with hippocampal damage, the patients with prefrontal damage can successfully navigate if they are repeatedly reminded of their goal location during navigation (Ciaramelli, 2008; Spiers, 2008). This research suggests that prefrontal cortex might be important for keeping goal locations in mind when determining upcoming movements and action plans. 'Backtracking' to switch from one navigational plan to another has also been associated with prefrontal cortex activity in humans (Javadi et al., 2019). While spatial representations are traditionally observed in hippocampus, recent work has found that prefrontal cortex also has spatial and goal related activity in rodents as well (Hok et al., 2005). However, there is still debate as to the circumstances in which goal-representations are maintained over delay periods in prefrontal cortex of rodents during spatial memory tasks (Bohm & Lee, 2020).

It is important to note that integrating and interpreting prefrontal cortex results across species can be incredibly challenging due to neuroanatomical and nomenclature differences across species. There has been a long-standing debate as to how to relate rodent prefrontal cortex studies to those conducted in monkeys and humans (Laubach et al., 2018; Preuss, 1995). In this dissertation we will focus predominantly on rodent studies and functions attributed specifically to rodent subregions.

1.2 Hippocampal-prefrontal interactions and neural codes for memory and decision making

1.2.1 Theoretical frameworks for hippocampal-prefrontal interactions

Hippocampus and prefrontal cortex are thought to have important roles in navigation, memory, and decision-making both individually and in coordination. It is theorized that hippocampal-prefrontal interactions are important for memory-guided spatial navigation, as the hippocampal spatial map and model can interact with an action-planning system during goal-directed behavior (Ito, 2018; Shin & Jadhav, 2016). These theories suggest that in a scenario where the environment is constantly changing as events and their outcomes unfold, the hippocampus provides current contextual information about the environment to prefrontal cortex, and prefrontal cortex selects appropriate action plans. In this section, we will discuss the existing evidence for how these regions interact during memory and decision-making, and the implications for their potential role in service of flexible navigation.

1.2.2 Anatomical features and connections between hippocampus and prefrontal cortex

To begin to study hippocampal and prefrontal cortex neural codes during flexible decision making and navigation, we will first discuss the neuroanatomical structures and connections between these brain regions. The hippocampal formation has several subregions, and each is thought to have a unique functional role in navigation and memory (van Strien et al., 2009). Together, these regions are defined as dentate gyrus, hippocampus proper (CA3, CA2, CA1), and subiculum. In what is known as the trisynaptic pathway, inputs from medial and lateral entorhinal cortex are sent to dentate gyrus to CA3, and then to CA1. Parallel to this pathway, entorhinal cortex sends direct projections to CA3, CA1, and subiculum. CA3 also has recurrent projections onto itself, and CA1 then projects to entorhinal cortex as well (**Figure 1.1A**). Hippocampal CA1 it is thought to be an integrator of incoming sensory information from medial entorhinal cortex inputs and recall information from hippocampal CA3 inputs through the hippocampal trisynaptic pathway (J. E. Lisman & Grace, 2005). This neuroanatomical structure has led to a theory that CA1 performs comparisons between incoming sensory information with stored memory information to detect relevant differences between the two (Duncan et al., 2012). Given the focus of this dissertation

on flexibly responding to new, incoming information while performing memory-based, goal-directed behavior, the studies of this dissertation will focus on hippocampal CA1. CA1 is also the major output region of the hippocampus and sends projections to many brain regions, including prefrontal cortex, which we will focus on next as a brain region also critical for flexible decision-making (van Groen & Wyss, 1990).

In rodents, medial prefrontal cortex is largely thought to include three main regions, prelimbic cortex, infralimbic cortex, and dorsal anterior cingulate areas (**Figure 1.1B**). The term anterior cingulate cortex can also be used to refer to those three medial frontal areas as a whole (Vogt & Gabriel, 1993). The prefrontal subregions are overall strongly interconnected, and several studies on spatial navigation in prefrontal cortex often group these regions together (Vertes, 2004). It can thus be challenging to identify the unique functional roles for each of these subregions. Recent work looking across all medial prefrontal subregions in rodents during a complex decision-making task suggests a combination of 'everything is everywhere' functionality in medial prefrontal cortex with more distinct functional gradients along the dorso-ventral axis, in line with some neuro-anatomical predictions (Diehl & Redish, 2022; Heidbreder & Groenewegen, 2003). In this work, the researchers suggest that individual cell spiking characteristics and task-feature coding is similar across medial prefrontal cortex, but there is a gradient of function along the dorso-ventral axis. Active decision-making codes relating to neural activity at critical decision-making times are more dorsally located, and codes for slower task variables such as motivation are more ventrally located. Outside of this work, anterior cingulate cortex has been linked to the evaluation of potential actions and outcomes, prelimbic cortex has been linked to goal-directed responses, task structure representations, and working memory, and infralimbic cortex has been linked to the development and execution of habitual actions (Coutureau & Killcross, 2003; Hyman et al., 2013; Mashhoori et al., 2018; Ragozzino et al., 1998; Seamans et al., 1995; Smith et al., 2012; Tran-Tu-Yen et al., 2009).

Hippocampus and medial prefrontal cortex in rodents interact through several pathways both direct and indirect (**Figure 1.1C-D**). As mentioned previously, hippocampal CA1 is a major output center of the hippocampus. Ventral hippocampal CA1 and proximal subiculum both have direct monosynaptic projections to medial prefrontal cortex, most densely contacting the infralimbic and prelimbic areas (Cenquizca & Swanson, 2007; Hoover & Vertes, 2007; Jay & Witter, 1991). These ventral projections are thought to play a role in sending contextual information to prefrontal cortex (Spellman et al., 2015). Recent work has also identified direct dorsal hippocampal projections to the prelimbic area of medial prefrontal cortex thought to mediate fear memory retrieval (Ye et al., 2017). Further work identified direct projections from dorsal anterior cingulate to hippocampal CA1 and CA3 neurons (Rajasethupathy et al., 2015), though only one major study has found this connection and its definitive presence is still debated (Andrianova et al., 2022). Finally long-range inhibitory projections have been found from the prelimbic area to inhibitory neurons in dorsal CA1 (Malik et al., 2022). In addition to these direct pathways, there are several indirect pathways between these regions. One pathway passes from prelimbic and infralimbic areas through the perirhinal and entorhinal cortices to CA1 and CA3 of the hippocampus (Agster & Burwell, 2009; Burwell & Amaral, 1998). The other pathway is bidirectional and passes through the thalamic subregion, nucleus reuniens, from prelimbic and infralimbic areas to and from the hippocampal formation (Vertes, 2006; Vertes et al., 2007).

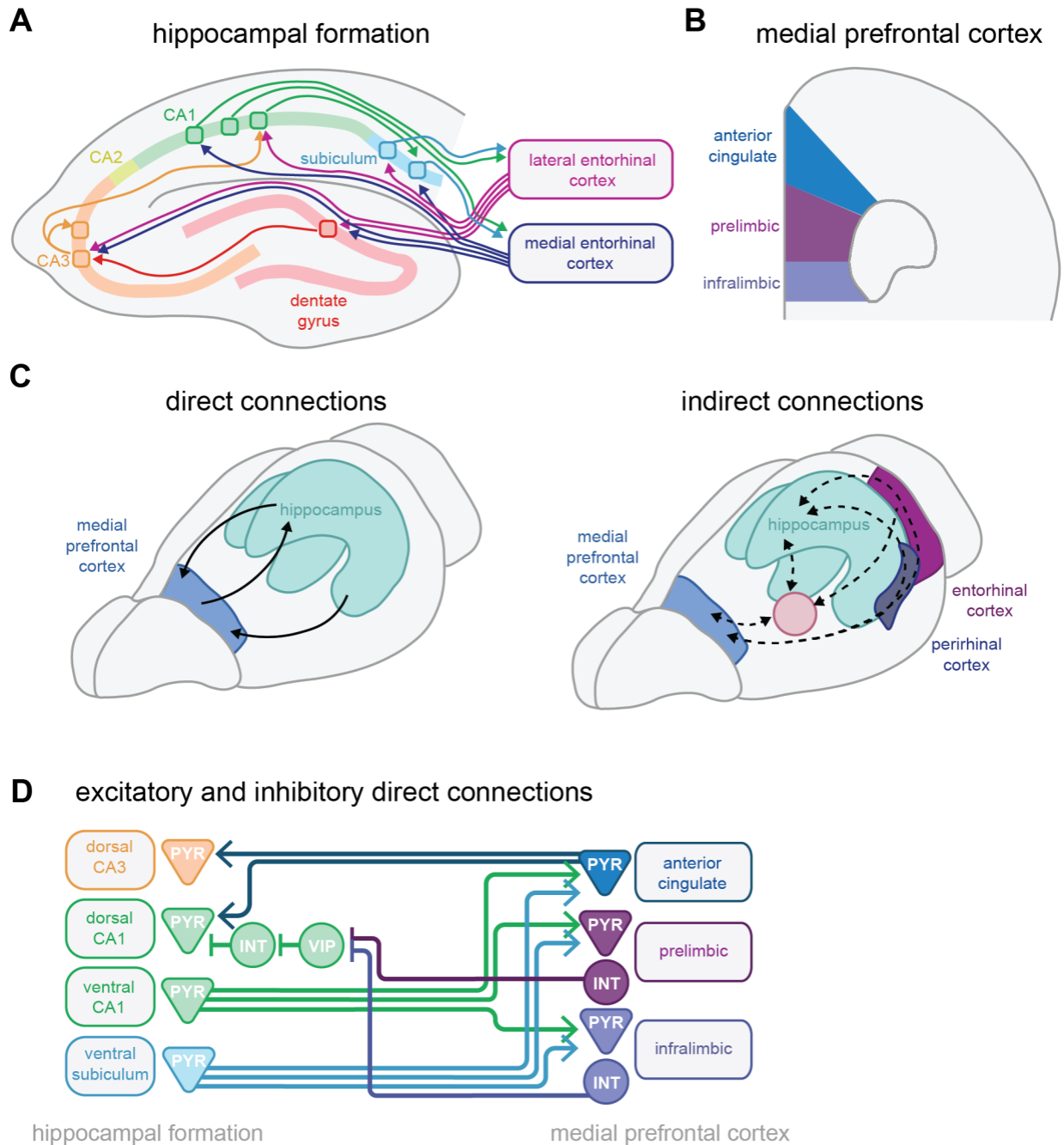


Figure 1.1 Schematic of anatomical pathways in prefrontal-hippocampal circuit

- Hippocampal formation circuitry and subregion connections, presubiculum and parasubiculum regions are not shown. Based on figure from Hartley et al., 2014
- Medial prefrontal cortex structure is agranular and highly interconnected in rodents.
- Direct and indirect connections between hippocampus and prefrontal cortex. Based on figure from Robinson & Brandon, 2021.
- Excitatory and inhibitory details for direct connections between hippocampus and prefrontal cortex (excitatory indicated with arrow, inhibitory indicated with flat line). PYR

indicates pyramidal cells, INT indicates interneurons (multiple subtypes), VIP indicates vasointestinal peptide expressing interneurons.

1.2.3 Neural codes during theta in the hippocampus

To understand hippocampal-prefrontal interactions for navigation and decision-making, we first must understand some of the key neural activity features that are thought to coordinate communication between hippocampus and other brain regions. Theta (4-12 Hz) and sharp-wave ripples (150-250 Hz) are two oscillatory events that occur in hippocampus and are associated with functionally distinct behavioral or neural processes (**Figure 1.2A**). Theta rhythms in hippocampus are generated by medial septum and are known to occur in rodents during engaged behaviors such as movement, exploration, and sniffing (Vertes & Kocsis, 1997; Winson, 1974). These theta rhythms provide a temporal coding scheme by which spatial coding in the hippocampus is organized. During theta oscillations, place cells in the hippocampus participate in a phenomenon known as 'theta phase precession' (O'Keefe & Recce, 1993; Skaggs et al., 1996). As animals run through an environment, place cells will shift their preferred theta phase firing location from late to early as animals pass through their place fields. Place cells that have fields in front of the animal will fire more on the later phase of the theta oscillation, while place cells with fields behind the animal will fire on the earlier half (**Figure 1.2B**). This theta phase specific coding demonstrates a hippocampal coding schema for past, present, and future experiences. 'Theta sequences' are a related but distinct phenomenon in the hippocampus, in which place cells spanning a subset of an environment will fire sequentially, representing a trajectory through the environment (**Figure 1.2D**). Sequences were originally theorized to be generated as a by-product of phase precession, but recent work has identified them as unique phenomena with distinct mechanisms. These sequences will emerge with experience in an environment, and it is theorized that these theta sequences play an important role in the binding of successive locations in the environment to form memories (Feng et al., 2015).

Recent work has revealed that neural codes during theta oscillations may have a particularly important role for prospective coding and planning. During tasks in which rodents must choose between two arms to obtain a reward, theta sequences can occur at the choice point that represent possible paths (e.g., to the left or right) that are available to the animal (Johnson & Redish, 2007). These sequences often occur during behavioral signatures of deliberation in rodents and have been observed to represent upcoming goals (Wikenheiser & Redish, 2015). Other work has shown that representations of future paths that are both taken or not taken occur on alternating theta cycles as animals approach a choice point (**Figure 1.2C**). This research suggests that the representations on later theta phases are not only future paths but also represent hypothetical paths available to rodents (Kay et al., 2020). Similar theta-paced flickering between distinct representations has also been observed for entire environments when rodents are rapidly switched between multiple experienced environments (Jezek et al., 2011). This work has led to the theory that during theta, neural codes for non-local spaces may be a neural correlate of planning and deliberation (Comrie et al., 2022; J. Lisman & Redish, 2009; Pezzulo et al., 2019; Redish, 2016; Robinson & Brandon, 2021). These ideas are not incompatible with other frameworks that suggest the theta-phase organization of information facilitates communication between subregions of hippocampus. In these experiments and models, it is proposed that different phases of theta oscillations are important for either encoding of information via input from entorhinal cortex to CA1 and CA3 at the trough of the theta rhythm, or retrieval of information via input from CA3 to CA1 at the peak of the theta oscillation (Hasselmo et al., 2002; Manns et al., 2007; Siegle & Wilson, 2014). These theories might be complementary to the ideas for actual and hypothetical segregation of experience during theta oscillations; non-local information for hypothetical future scenarios recalled from past experience would occur during the later phase of theta, in which CA3 inputs to CA1 are more prominent and promote memory retrieval.

1.2.4 Neural codes during sharp-wave ripples in the hippocampus

Another key oscillation thought to be important for memory and planning in the hippocampus is sharp-wave ripple activity (Buzsáki, 2015). Sharp-wave ripples are high frequency oscillations that occur during sleep or during pauses in awake behavior such as immobility, eating, drinking, and grooming. They originate from bursts of synchronized activity in CA3, a strongly recurrent and excitatory hippocampal subregion, which then generate sharp waves in the local field potential of downstream CA1 (Buzsáki, 1986; Csicsvari et al., 2000). The CA3 coordinated activity then recruits excitatory and inhibitory activity in CA1, leading to a transient ripple oscillation (~100ms, 150-250Hz) (Ylinen, Soltész, et al., 1995). These transient events recruit large assemblies of neurons to have bursts of synchronized spiking activity occurring in both CA3 and CA1. These large and fast bursts of population spiking activity can encode spatial trajectories that occur during navigation and exploration, a phenomenon known as ‘replay’ (**Figure 1.2E**, Foster & Wilson, 2006; Skaggs & McNaughton, 1996; Wilson & McNaughton, 1994). These ‘replay’ reactivation events are theorized to be a mechanism of memory consolidation in which previous experiences are selectively strengthened during coordinated activity that occurs offline from active navigation (Carr et al., 2011). Sharp-wave ripples and accompanying reactivation sequences are thought to be important to memory; disrupting sharp-wave ripples in rodents impacts learning and memory and prolonging them can improve memory performance (Ego-Stengel & Wilson, 2007; Fernández-Ruiz et al., 2019; Girardeau et al., 2009; Jadhav et al., 2012).

Reactivation sequences are also theorized to support deliberation and planning. Some studies have shown that the trajectories represented during sharp-wave ripple sequences might preferentially represent future paths to goal locations and play a role in memory-guided decision making (Singer et al., 2013). While replay can reflect upcoming paths, the content of sharp-

wave ripple activity does not always predict upcoming choices in rodents (Gillespie et al., 2021). Replay trajectories also suggest more imaginative thoughts of environments, in that they do not always reflect actual experience but can occur over locations not experienced by the animal (Gupta et al., 2010; Stella et al., 2019). Interestingly, reactivation of sequences of activity similar to hippocampal replay has also been observed in other brain regions such as prefrontal cortex. During sleep, sequences from recently performed tasks are replayed in prefrontal cortex in rats, suggesting a possible role for memory consolidation across regions (Euston et al., 2007). The reactivation of sequences of task-related patterns have also been observed in prefrontal cortex of rodents in coordination with hippocampal sharp-wave ripples, but also independently from them (Kaefer et al., 2020; Peyrache et al., 2009; Shin et al., 2019).

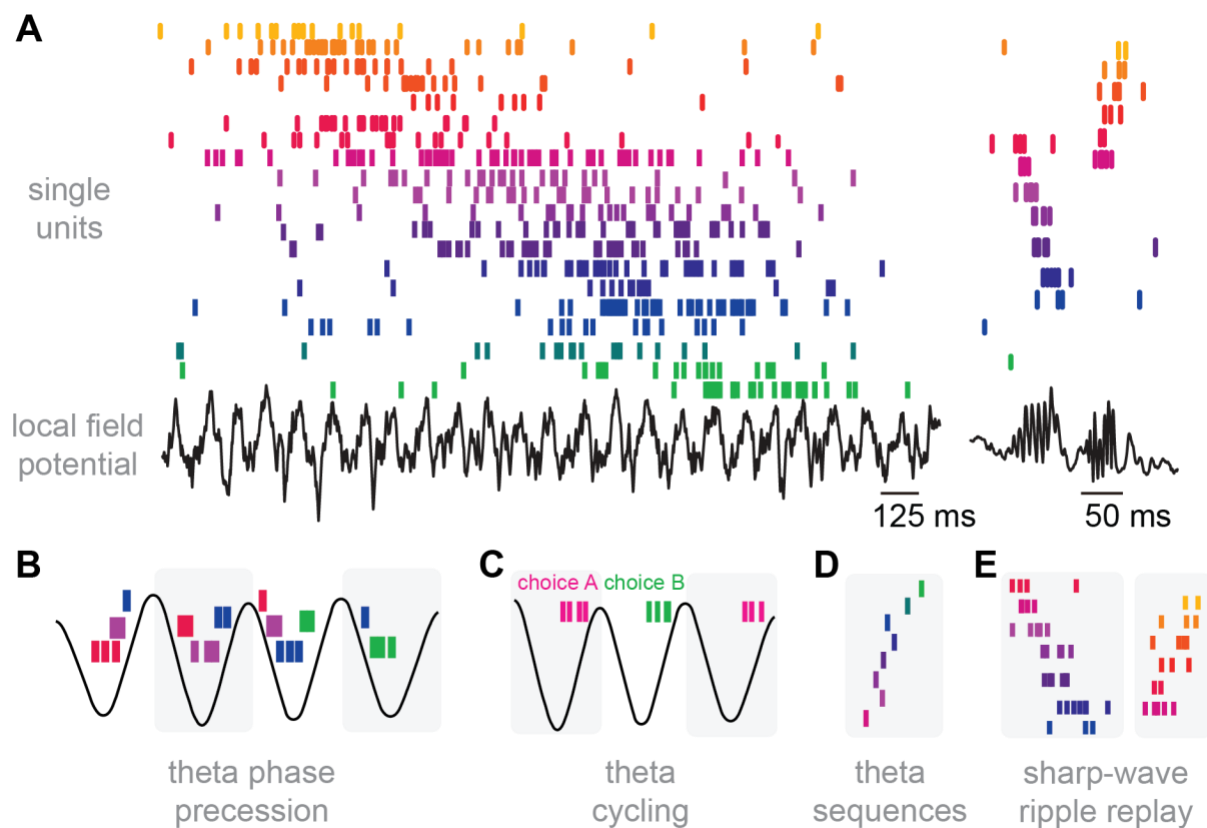


Figure 1.2 Schematic of hippocampal activity during theta and sharp-wave ripple oscillations

- A. Illustration of spiking activity and local field potential in the hippocampus, units sorted by place field location. *Left*, during theta oscillations when an animal is moving, single neurons will fire sequentially with spatial selectivity in an environment. *Right*, these same sequences of 'place cell' activity will be reactivated on a compressed timescale during sharp-wave ripple oscillations and the accompanying bursts in population activity.
- B. Place cells will fire at different phases of individual theta cycles and will shift from later to earlier phases as animals run through them.
- C. In environments with multiple choices, potential paths will fire on the latter half of theta cycles and alternate across cycles.
- D. During theta, sequences of place cells will fire for different trajectories in the environment.
- E. During sharp-wave ripples, place cells will fire sequentially for various trajectories, experienced or not.

1.2.5 Hippocampal-prefrontal interactions during theta and sharp-wave ripples

Prefrontal-hippocampal coordination is thought to play an important role during navigation and decision-making. There is a large body of literature focusing on hippocampal-prefrontal interactions during sleep as a form of potential memory consolidation, but for the scope of this dissertation we will focus on interactions between these regions during the awake state. While theta oscillations are very prominent in the local field potential of hippocampus, theta-modulated or related activity can be observed in other brain regions as well. Prefrontal cortex neurons can be phase-locked to hippocampal theta oscillations (i.e., preferentially fire more at a specific phase of the theta oscillation), and prefrontal cell activity shifts during task acquisition to be more aligned to hippocampal theta troughs (Benchenane et al., 2010; Siapas et al., 2005). This theta coordination seems to be important to spatial memory and decision making in rodents (Fujisawa & Buzsáki, 2011; M. W. Jones & Wilson, 2005; Siapas et al., 2005; Zielinski et al., 2019). Furthermore, disruption to hippocampal-prefrontal coordination impairs mice's behavior in spatial working memory tasks (Spellman et al., 2015). Recent work on neural codes in hippocampus and prefrontal cortex suggests a potential coordinated role in memory, navigation, and flexible decision-making. Spatial position coding is coherent between hippocampus and prefrontal cortex during theta oscillations, and coordination between theta sequences in prefrontal cortex and hippocampus is stronger for an rat's upcoming choice versus alternative

paths (W. Tang et al., 2021). Disrupting the medial prefrontal cortex of rodents during deliberation and decision-making alters hippocampal theta sequences (Schmidt et al., 2019). In humans, there is also increased hippocampal-prefrontal coherence during imagination of future navigation scenarios (Kaplan et al., 2017). Hippocampal-prefrontal coordination is also important for behavioral flexibility; increased hippocampal-prefrontal synchrony in rats leads to less interference from previous learned rules in a spatial task requiring rule switching (Guise & Shapiro, 2017). Evidence points to the role of hippocampus sending contextual information, and then prefrontal cortex driving hippocampal activity when goal representations need to be retrieved in a context-dependent manner from the hippocampus (Place et al., 2016). Prefrontal cortex activity has also been observed to predict non-local hippocampal spiking or representations of goal locations in rats (Hasz & Redish, 2020; Yu & Frank, 2021).

Hippocampal-prefrontal coordination has also been observed during hippocampal sharp-wave ripple events in both awake and sleep states. Prefrontal cortex neurons alter their spiking, co-firing, or reactivation during sharp-wave ripples, and their responses to sharp-wave ripples are modulated differently during learning (Jadhav et al., 2016; Peyrache et al., 2011; W. Tang et al., 2017; D. v. Wang & Ikemoto, 2016; Wierzynski et al., 2009). Recent work has found increased hippocampal-prefrontal coordination in rats for actual versus alternative choices during sharp wave ripples as well as increased reactivation strength in hippocampus and prefrontal cortex that can predict correct versus incorrect performance (Shin et al., 2019). Interestingly, additional work has found that prefrontal neurons in rats are selective specifically to non-local hippocampal activity during hippocampal replay (Berners-Lee et al., 2021). Awake hippocampal-prefrontal coordination during replay has been proposed to be suited for memory storage related to current experiences in addition to retrieval and planning for ongoing behaviors.

What are the different roles of hippocampal-prefrontal coordination for planning, navigation, and decision-making during theta versus during sharp-wave ripples? Overall, it has been suggested that non-local sharp-wave ripple replay and non-local codes during theta sequences might be part of the same general mechanism for planning, but the distinction is that they are employed at different timescales (Pezzulo et al., 2017). Theta oscillations occur during active behavior with constant incoming sensory information streams. Thus, it has been suggested that these sequences are important for online, short-timescale predictions, outcome assessment, decision-making, and facilitating short-timescale spike-timing dependent plasticity (J. Lisman & Redish, 2009; Skaggs et al., 1996). These short-timescale predictions and outcome assessment are thought to be especially important for rapidly adapting behavior in response to new sensory information. However, much of the research supporting these theories is built on self-driven deliberation and path modification in animals, thus it is unclear how these codes might be altered when flexible adaptation is driven by sensory cues from the environment. In contrast to theta oscillations, sharp-wave ripples occur predominantly when the animal is paused or during sleep. These offline events have been proposed to play a role in memory consolidation, retrieval, or planning (Buzsáki, 2015; Carr et al., 2011). In a specific spatial navigation planning scenario, sharp-wave ripples may be used to generate a rough plan preceding movement initiation. Once the animal initiates movement, theta sequences may be used to continually assess the environment and maintain or adapt plans as needed. Prefrontal coordination with hippocampus in these cases may reflect different processes. For example, during sharp-wave ripples this coordination may reflect more systems consolidation and during theta this coordination may reflect information flow of action and motor plans.

1.3 Network-level approaches to understanding Alzheimer's disease

1.3.1 Cognitive deficits to memory and planning processes in Alzheimer's disease

Alzheimer's disease is a devastating neurodegenerative disorder and the most common form of dementia. The hippocampus is one of the first regions impacted in Alzheimer's disease, and hippocampal-associated functions are some of the first cognitive processes to be affected (Braak & Braak, 1991). The ability to form and retrieve memories is one of the key symptoms of disease onset and is also a major criterion for a typical Alzheimer's diagnosis (Dubois et al., 2014). Patients also experience challenges in navigation; getting lost while navigating in familiar routes and places is one of the earliest cognitive functions to be affected in Alzheimer's disease (Allison et al., 2016; delpolyi et al., 2007). Furthermore, the ability to plan sequences of actions is also impaired in patients with Alzheimer's disease (Satler et al., 2017). Decades of research has attempted to find treatments to effectively prevent, slow, or reverse the effects of Alzheimer's disease. Recently, drugs targeting amyloid plaque accumulation show promise for slowing disease progression and have been approved by the US Food and Drug Administration (Salloway et al., 2022; Sevigny et al., 2016; van Dyck et al., 2023). However, how the molecular and pathological changes of Alzheimer's such as amyloid beta aggregation lead to cognitive deficits is still unclear. Recently, there has been a push to approach this question by looking at the level of neural activity and network-level dysfunction.

1.3.2 Network dysfunction in Alzheimer's disease

An improved network-level understanding of Alzheimer's disease is motivated by several factors. First, changes to neural activity at a circuit level might be a potential biomarker or predictor of cognitive deficits in Alzheimer's disease and could be used for measuring susceptibility or diagnosing pre-symptomatic Alzheimer's (Goutagny & Krantic, 2013; Palop et al., 2006). Second, neural activity could be a potential therapeutic target to improve cognitive function. Patients with Alzheimer's disease experience fluctuations in cognitive capabilities depending on time of day and other factors, suggesting brain activity dysfunction at a shorter timescale than neuronal degeneration progression may contribute to cognitive deficits

(Bradshaw et al., 2004; Palop et al., 2006). Manipulating neural circuits using sensory stimulation, transcranial magnetic stimulation, transcranial direct current stimulation, or other non-invasive measures might also be potential avenues of treatment (Holczer et al., 2020; Iaccarino et al., 2016; Martorell et al., 2019). Finally, identifying network level deficits would bridge our gap in understanding between the molecular pathology and cognitive deficits. Alzheimer's disease is characterized by the accumulation of extracellular plaques made of amyloid beta peptides and neurofibrillary tangles from aggregated tau protein. Although plaques and tangles are widely acknowledged as pathological hallmarks of Alzheimer's, it is unclear if plaques and tangles on their own are enough to result in Alzheimer's disease without other biochemical and molecular changes as well. With a network level approach, we might better understand what parts of the neural circuit are particularly susceptible or underlie the degradation of memory and planning processes in the hippocampus. Thus, we can more precisely target those pathological changes and aspects of the disease.

Some of the original signs of network level dysfunction potentially underlying cognitive deficits in Alzheimer's disease came from studies showing epileptic seizures occur early in the course of disease (Palop et al., 2006; Vossel et al., 2013). Epileptiform activity was also observed in certain mouse models of Alzheimer's and was proposed to be due to altered excitatory and inhibitory activity at a circuit level (Palop & Mucke, 2016; Verret et al., 2012). Further work has looked more specifically at how the hippocampus is affected at a network level, given its role in memory processing and early susceptibility to neurodegeneration and plaque accumulation. Work in rodents has found that neural correlates of memory are impaired in rodent models of Alzheimer's disease. Sharp-wave ripple activity has been shown to be disrupted in Alzheimer's disease across multiple mouse models; many models have decreased abundance of sharp-wave ripples (Gillespie et al., 2016; Iaccarino et al., 2016; Jura et al., 2019; Nicole et al., 2016; Witton et al., 2016). Interestingly, work in the apoE4 knock-in model of Alzheimer's shows that

sharp-wave ripple deficits early in the disease progression can predict later learning and memory impairments (E. A. Jones et al., 2019). However, the mechanism of altered sharp-wave ripples in Alzheimer's is still unclear. Some work with other network level approaches has led to the theory that inhibitory GABAergic activity might play a specific role, given the importance of inhibition to oscillation generation. Reduced Nav1.1 sodium channel levels has been observed in both humans and animal models of Alzheimer's disease, and implanting inhibitory interneurons that overexpress Nav1.1 rescues gamma oscillations and cognition in this mouse model (Martinez-Losa et al., 2018; Verret et al., 2012). Removal of apoE4 specifically from GABAergic neurons also rescues gamma oscillations during sharp-wave ripples, though not abundance (Gillespie et al., 2016). Other lines of work have examined how synaptic transmission might underlie network deficits in Alzheimer's disease. Synapse loss is one of the strongest correlates for cognitive deficits in Alzheimer's disease, and amyloid beta oligomers have been shown to alter synaptic activity (Abramov et al., 2009; Bero et al., 2011; Chapman et al., 1999; DeKosky & Scheff, 1990; Freir et al., 2017; Hsia et al., 1999; Puzzo et al., 2008; Selkoe, 2002; Stéphan et al., 2001; Terry, 2000; Terry et al., 1991; Walsh et al., 2002). However, many studies examining synaptic deficits have been conducted in vitro or under anesthesia, so it is still unclear how these deficits might manifest or relate to oscillation disruption in vivo.

Outside of sharp-wave ripple alterations in Alzheimer's, other work has looked at the impact of Alzheimer's on theta oscillations. Theta-gamma coupling (modulation of gamma frequency activity in the hippocampus by theta oscillations) is thought to be a potential mechanism of communication across hippocampal subregions during encoding and retrieval processes. Theta-gamma coupling is impaired in mice that over-express human tau (Booth et al., 2016). Hippocampal-prefrontal interactions are also impaired in Alzheimer's disease; theta coherence between hippocampus and anterior cingulate cortex is hypersynchronous in a hyperglycemia

risk-factor model of Alzheimer's that results in increased phosphorylated tau in the hippocampus (Wirt et al., 2021).

1.4 Dissertation objectives

1.4.1 How do hippocampal and prefrontal cortex prospective codes contribute to flexible decision making when new information is presented?

Hippocampus and prefrontal cortex are known to be important for navigation, memory, and flexible decision making. Non-local hippocampal codes during theta sequences and sharp-wave ripples have been proposed to be a neural correlate of deliberation and planning. Additional work has suggested that prefrontal cortex is selective to non-local hippocampal activity and might support the selection and maintenance of decisions. This interplay of deliberation and decision-making in goal-directed behavior has been proposed to facilitate flexible adaptation of plans with new information. However, previous work has largely occurred in static environments where animals are not required to flexibly adapt plans with new information, thus this hypothesized role has not been explicitly tested. In *Chapter 2*, we addressed this question by designing a novel virtual reality task to test how animals adapt their plans to new information, and how neural codes in hippocampus and prefrontal cortex facilitate this behavior. We hypothesized that prospective, non-local codes in hippocampus and goal-selective codes in prefrontal cortex contribute to the ability to perform flexible decision making in dynamic environments.

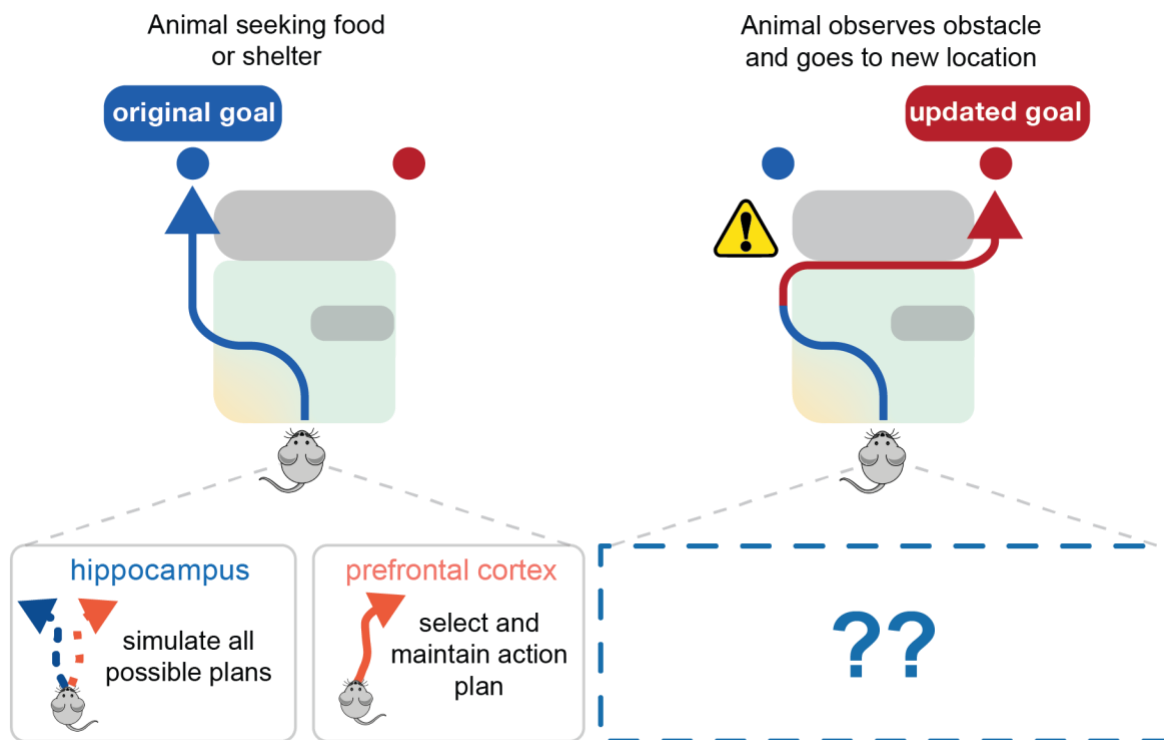


Figure 1.3 Gap in understanding how prospective codes in hippocampus and prefrontal cortex underlie deliberation and adaptation of plans with new information.

Schematic shows a proposed role for hippocampus in simulating all possible outcomes and spatial paths in an environment and for prefrontal cortex in representing upcoming choices in coordination with hippocampus during navigation.

1.4.2 Are hippocampal neural codes of memory and in vivo synaptic activity altered in a mouse model of Alzheimer's disease?

Within the hippocampus, we rely on healthy neural activity from synapses to circuits to oscillations in order to support intact memory and navigation processing. In Alzheimer's disease, this neural activity is disrupted across multiple levels. Much is known about the molecular pathology and cognitive deficits in Alzheimer's disease, but it is less understood how deficits at neural microcircuit, coding, and network levels might underlie memory loss and navigation impairments in Alzheimer's disease. Some evidence suggests that synaptic activity is disrupted by amyloid beta plaques in Alzheimer's disease and these deficits might cause network level dysfunction. However much of the previous research has been conducted in vitro

or under anesthesia, which can drastically influence synaptic activity dynamics (Haider et al., 2013). Thus, it is still unclear how excitatory and inhibitory synaptic activity is altered *in vivo* in a mouse model of Alzheimer's. Sharp-wave ripple activity, a neural correlate of memory, has also been shown to be disrupted in mouse models of Alzheimer's disease. However, whether the reactivation patterns that occur during sharp-wave ripples are impaired and what neuronal changes might underlie these oscillation deficits is not clear. In *Chapter 3*, we addressed these gaps by recording neural activity *in vivo* from hippocampus of a mouse model of Alzheimer's disease. We hypothesized that *in vivo* synaptic dysfunction underlies neural coding deficits in hippocampus in Alzheimer's disease.

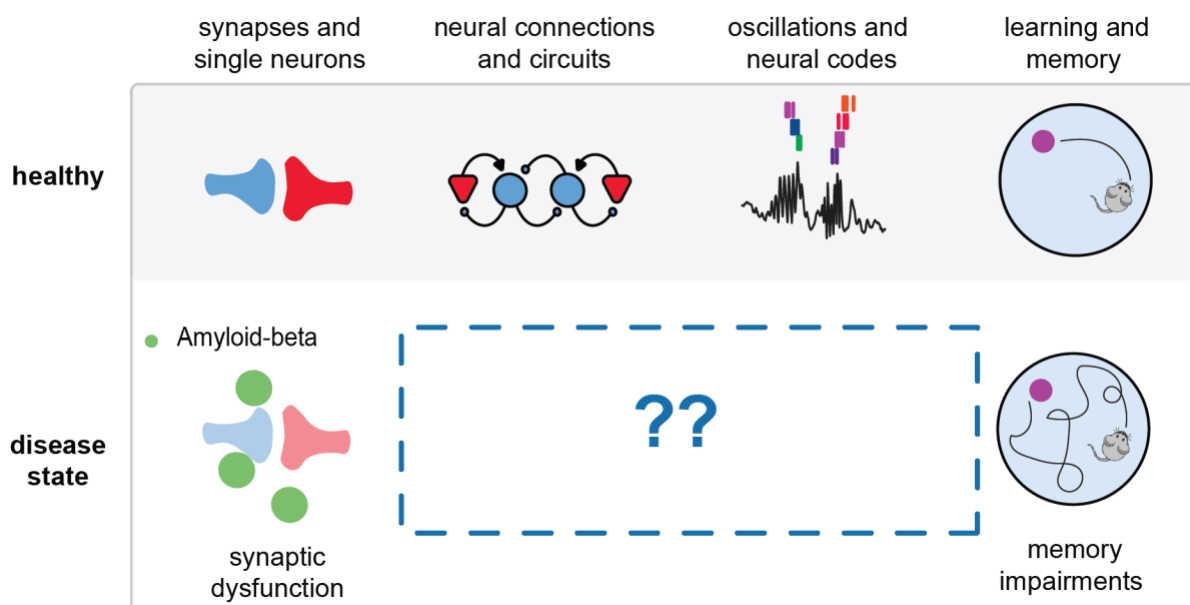


Figure 1.4. Gap in understanding between synaptic dysfunction due to Alzheimer's pathology and cognitive memory impairments.

Schematic shows gaps in understanding how synaptic deficits lead to cognitive impairment at scales of neural circuits, codes, and oscillations in memory circuits *in vivo*.

CHAPTER 2 – NEW INFORMATION TRIGGERS PROSPECTIVE CODES FOR FLEXIBLE ADAPTATION OF ONGOING CHOICES

This chapter is currently a manuscript in preparation for submission:

Prince SM, Katragadda N, Yassine, TA, Roberts TC, Singer AC. (2023) *New information triggers prospective codes for flexible adaptation of ongoing choices.*

Abstracts presented from this work:

Prince SM, Katragadda N, Roberts TC, Yassine, TA, Paulson AL, Singer AC. (2022) *New information triggers simulation of possible choices and rapid decision updating in hippocampus and prefrontal cortex. Society for Neuroscience Annual Meeting. Poster Presentation.*

Prince SM, Katragadda N, Roberts TC, Yassine, TA, Paulson AL, Singer AC. (2022) *Hippocampal and prefrontal activity during rapid updating of spatial trajectories in response to new information. Collaborative Research in Computational Neuroscience (CRCNS) PI Meeting. Poster Presentation.*

Prince SM, Katragadda N, Roberts TC, Yassine, TA, Paulson AL, Singer AC. (2022) *Hippocampal and prefrontal activity during rapid updating of spatial trajectories in response to new information. Simons-Emory International Consortium Meeting. Poster Presentation.*

Prince SM, Katragadda N, Roberts TC, Yassine, TA, Paulson AL, Singer AC. (2022) *Hippocampal and prefrontal activity during rapid updating of spatial trajectories in response to new information. Gordon Research Conference: Neurobiology of Cognition. Poster Presentation.*

Prince SM. (2022) *Thinking on your feet: rapid updating of spatial trajectories in response to new information. Emory University Graduate Division of Biological and Biomedical Sciences Student Research Symposium. Talk.*

2.1 Abstract

The ability to rapidly update our choices by integrating past experiences with new information is essential to navigating our world. In hippocampus and prefrontal cortex, regions that play key roles in memory and decision-making, neural activity that represents future goal locations and choices is theorized to support planning. However, a key aspect of planning in navigation has not been addressed: how representations of goals update in the face of new, crucial information to support flexible navigation. To address this question, we designed a novel decision-making navigation task in which we precisely controlled the introduction of new, pivotal information using virtual reality, and recorded neural activity from hippocampus and prefrontal cortex as animals had to flexibly adapt their planned destinations in response to this new information. We found that prospective codes of upcoming locations and goals are rapidly modulated by new information. In hippocampus, new information triggers increased goal representations of both possible locations while in prefrontal cortex, new information causes goal representations of choices to rapidly shift from the old to the new choice. The prefrontal choice codes failed to switch when animals did not flexibly shift behavior, despite elevated goal representations in hippocampus. Interestingly, these elevated goal representations are dependent on the animals' level of commitment to the initial choice and the degree of adaptation needed. This work shows that prospective codes are triggered in response to new, pivotal information in the environment to flexibly integrate new information to adapt navigational plans.

2.2 Introduction

The ability to rapidly update our choices in response to new information is essential to navigating our dynamic world. During navigation, animals often hold an internal representation of their world via a cognitive map (Behrens et al., 2018; O'Keefe & Nadel, 1978; Tolman, 1948). When navigation is goal-directed, this internal model is employed to represent not only current state information, but also upcoming choices or possible actions. Current theories propose that these prospective representations of future choices are a neural correlate of planning or deliberation, to simulate consequences of potential actions before they occur (Buckner, 2010; Comrie et al., 2022; Hunt et al., 2021; J. Lisman & Redish, 2009; Mullally & Maguire, 2014; Pezzulo et al., 2019; Redish, 2016). Such theories imply that these prospective codes facilitate flexible navigation in which animals continuously adapt between potential actions as events unfold. However, many of the studies testing prospective codes occur in static environments where animals do not need to adapt their behavior after their initial choices have been made. In dynamic environments, animals must continuously assess new sensory information to inform their decisions and update choices as needed. Thus, it is unclear how prospective codes contribute to flexible navigation in which navigating to rewarding outcomes requires continuous assessment of and responses to new information.

Hippocampus, which is essential for spatial navigation, is classically known to encode an animal's current position in an environment, but research has also found non-local representations occur during active navigation. Sweeps of coordinated place cell activity that tile space behind and in front of an animal have been observed during behavioral hallmarks of deliberation (Hasz & Redish, 2018; Johnson & Redish, 2007; Wikenheiser & Redish, 2015). During theta oscillations, place cells in rodents fire on different phases of theta depending on whether the place field is in front of (future), at the current location (present), or behind (past) the animal (Foster & Wilson, 2007; Gupta et al., 2012; Skaggs et al., 1996; Y. Wang et al., 2014; Wikenheiser & Redish, 2012).

This phenomenon does not seem to be spatially restricted; place cells with fields far removed from the animals' current position have also been observed to fire more on the latter phase of the theta oscillation (Kapl et al., 2022; Kay et al., 2020; Yu & Frank, 2021). In addition to intra-cycle theta codes, studies have shown that different locations in the environment, or sometimes between environments, are alternatively represented across multiple theta cycles (Jezek et al., 2011; Kay et al., 2020; M. Wang et al., 2020). One theory is that these sequences and sweeps reflect upcoming choices or might steer behavior towards a specific goal, but the degree to which choices can be predicted from this activity is inconsistent across studies (Wikenheiser & Redish, 2014). Another theory is that these non-local position codes are not just representations of the animal's upcoming choice but are presentations of all possible hypothetical paths and thus allow animals to quickly decide between potential options. This type of constant path simulation might be especially valuable in dynamic environments, however studies of these non-local codes during navigation have predominantly been performed in static environments.

During goal-directed navigation, animals must not only encode spatial trajectories through their environment, but they must also select and maintain choice information as their trajectories unfold. Prefrontal cortex is thought to represent upcoming choice information and is required for flexible decision making. Several studies have found evidence that prefrontal-hippocampal coordination during theta might facilitate decision-making and planning for upcoming choices. Prefrontal neurons can be modulated by hippocampal theta, and prefrontal-hippocampal coherence across the theta band increases around the decision point in memory tasks (Benchenane et al., 2010; Hyman et al., 2005; M. W. Jones & Wilson, 2005; P.-K. O'Neill et al., 2013; Siapas et al., 2005; Tamura et al., 2017). Prefrontal cortex neural activity in rodents has also been observed to co-occur specifically when hippocampal activity encodes non-local spatial representations, suggesting prefrontal cortex may play a role in navigation by evaluating these non-local codes as potential choices (Berners-Lee et al., 2021; Yu & Frank, 2021). Indeed,

hippocampal-prefrontal spatial representations in rodents are more coordinated when both regions are representing upcoming choices (W. Tang et al., 2021). However, the question remains, what is the role of hippocampus and prefrontal cortex together in a *dynamic* environment that requires flexible decision making and re-consideration of potential choices? Previous navigation research has been predominantly performed in static memory-based tasks; thus, it has not been explicitly tested if these hippocampal non-local codes and prefrontal cortex choice representations are important to flexible navigation in an environment with dynamic stimuli. For similar reasons, it is unclear how these prospective codes might relate to the ability to *accurately* update decisions when plans need to be changed. Finally, why non-local representations have been observed to sometimes predict upcoming behavior and at other times reflect both options equally has not been explained. By precisely controlling the timing of new, pivotal information, we evaluated how prospective codes change in response to new information that initiates flexible navigation. We hypothesized that new, pivotal information would cause (1) fluctuations in prospective code content or magnitude and (2) differences in prospective code content or magnitude when animals successfully versus unsuccessfully adapt.

We recorded many units from hippocampus and prefrontal cortex and tested how prospective codes responded to new information to support navigation in a memory-based decision-making task. In hippocampus we found new, pivotal information causes non-local representations of both possible goals to rapidly increase and increase specifically when new information requires updating current choices. In prefrontal cortex we found new, pivotal information causes choice codes to rapidly switch in response to new information, and this activity precedes behavioral changes. We then found prospective codes were different when animals failed to adapt; prefrontal choice codes did not flip despite increased goal representations in hippocampus. Neural activity predicted this failure to adapt before the new information was presented, suggesting that the animal's behavioral state at the time of new information impacted the ability to respond. We then

assessed the neural responses as a function of how strongly an animal was committed to one arm or the other before new information was presented. We found that both hippocampal and prefrontal cortex prospective codes depended on the animals' level of commitment to the initial choice and the degree of adaptation needed. These findings show that prospective codes change specifically when new, pivotal information is presented that requires animals to consider alternative action plans, revealing how these codes contribute to flexible planning and decision making in dynamic environments.

2.3 Results

2.3.1 Animals rapidly update their choices in response to new information in a spatial memory task

To investigate how animals update plans when presented with new pivotal information, we designed a virtual reality spatial navigation task (**Figure 2.1A**). Mice ($n = 7$ animals) were trained to navigate a y-maze using visual cues displayed on the wall (see **Methods** for training paradigm). The first original cue, presented on the walls in the central arm of the track, indicated which arm of the track (left or right) was the rewarded location. On most trials (65%), the original cue then disappeared and was replaced with uninformative grey checkered walls for the remainder of the trial (delay only trials). The mice had to maintain the memory of the correct goal arm during the delay period (10.53 ± 0.07 seconds, $n = 7313$ trials, **Figure 2.7**). On a subset of trials, a second visual cue appeared after a shortened delay period (1.39 ± 0.03 seconds, $n = 1886$ trials). During the second cue, the visual patterns appear on the opposite wall from the original cue indicating that the reward location switched from the initial arm, and animals must switch from their initial decision maintained in memory to the opposite choice (switch trials, 25%). The second visual cue was then followed by another delay period before the reward location (6.01 ± 0.08 seconds). An additional subset of trials had the same structure as the switch trials, but the second visual cue was on the same side of the track as initially shown, thus only providing additional evidence for

the initial reward location (stay trials, 10%). After several phases of behavioral training, animals learned to remember and follow the cues across all trial types and performed above 50% accuracy (delay only: $68 \pm 0.00\%$, stay: $92 \pm 0.01\%$, switch: $78 \pm 0.01\%$, $p < 0.0001$ delay only vs. 50% correct, $p < 0.0001$ switch vs. 50% correct, $p < 0.0001$ stay vs. 50% correct, **Figure 2.1B**, **Figure 2.7B**). Performance was slightly worse overall on delay only trials, likely due to the longer delay duration between the original cue and reward compared to update trials. Indeed, behavioral performance varied as a function of delay duration during brief warm-up periods at the start of each session (**Figure 2.7C**). Overall, these results show animals successfully perform both flexible and memory-guided decision-making in this spatial navigation task.

Given our central question about how prospective codes respond to flexible navigation demands, we were specifically interested in the behavior around the update cue on the switch and stay trials, when animals had to update their behavioral trajectories in response to new information. The animal's heading direction (view angle) slowly diverged on average as animals approached the ends of the track (**Figure 2.1C**). We found that on switch trials around the update cue onset, the animals heading direction shifted from one direction to the opposite in response to the reward location change (**Figure 2.1D**, see **Figure 2.7D** for other behavioral metrics). These behavioral data show that animals rapidly switch decisions in response to new information.

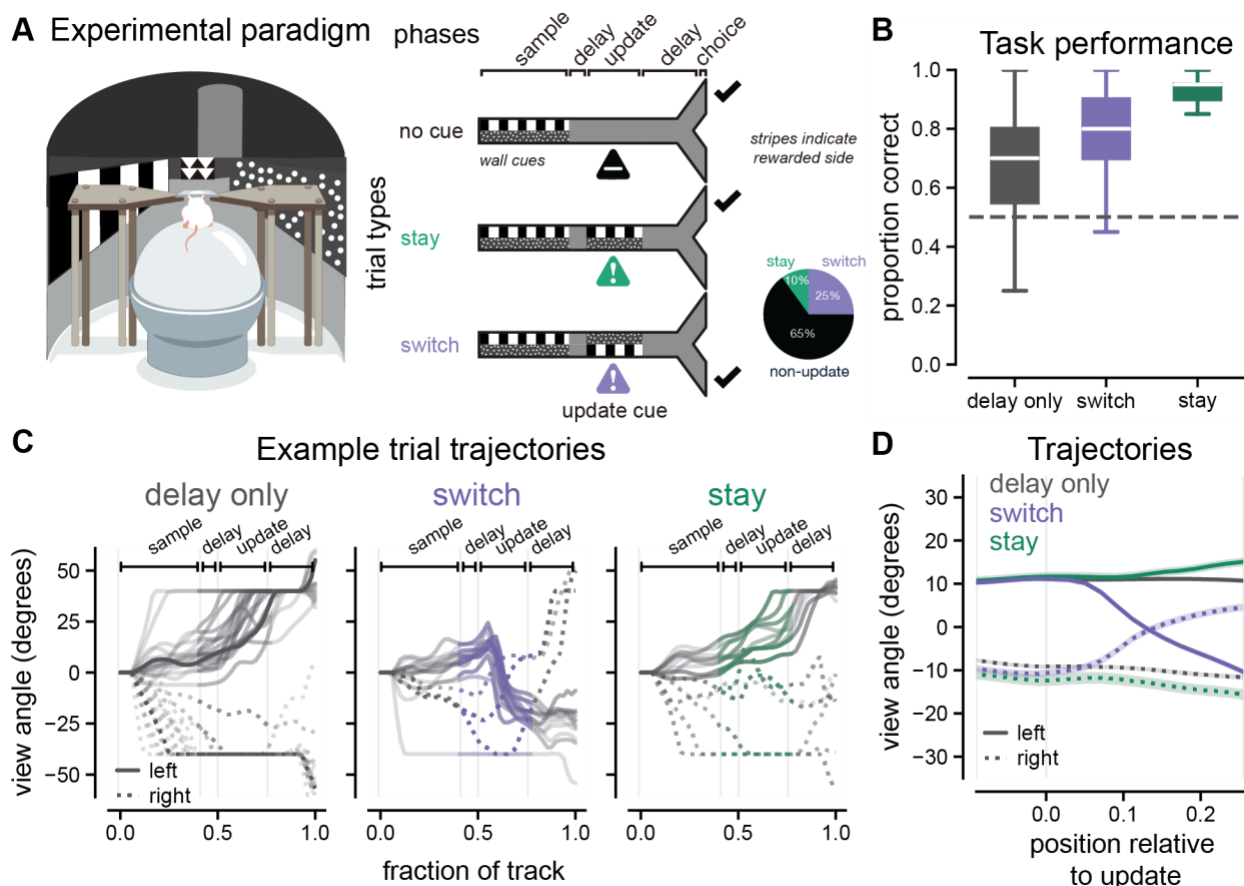


Figure 2.1. Mice rapidly and selectively update their choices in response to new information.

- A.** *Left, A.* Left, schematic of the virtual reality system. *Right,* Update task paradigm with cues displayed along the walls of the track. Delay only trials (black, top) consisted of an original cue period followed by a delay period during which no cue information was visible. Stay trials (green, middle) consisted of an original cue period, a brief delay period, and then a second cue period during which the wall cues appeared in the same orientation as the original cue. Switch trials (purple, bottom) were similar to stay trials except that the second wall cues appeared on the opposite side as the original cues. Check marks indicate correct, rewarded side. Pie chart indicates proportion of each trial type during a behavioral session.
- B.** Proportion correct on delay only trials (black), switch trials (purple), and stay trials (green) for all animals ($n = 7$ animals). Box plots indicate median and quartiles of distribution of 40-trial bins. (Delay only: 0.68 ± 0.00 , $n = 6379$ trial windows, percentiles = 0.13, 0.53, 0.67, 0.87, 1.00, stay: 0.92 ± 0.01 , $n = 128$ trial windows, percentiles = 0.47, 0.87, 0.93, 1.00, 1.00, switch: 0.78 ± 0.01 , $n = 1034$ trial windows, percentiles = 0.27, 0.67, 0.80, 0.93, 1.00). All stats reported as mean \pm SEM with minimum, 25%, 50%, 75%, and maximum percentiles
- C.** Example behavioral trajectories for individual trials of each trial type. View angle (heading direction) across locations in the track for example correct left (solid lines) and right (dashed lines) trials. Task phases indicated with brackets and light grey lines. Heading direction is set at 0 at trial onset. The delay period preceding the update location and the update cue location are highlighted with color.

- D.** Average view angle trajectories across all trials. Dashed lines indicate initial right trials, solid lines indicate initial left trials, mean + SEM.

2.3.2 Enhanced non-local codes of both goal locations in hippocampus in response to new pivotal information

To determine whether prospective codes change with new information in a dynamic environment, we recorded single unit and local field potential activity in dorsal hippocampal CA1 and medial prefrontal cortex during behavior (n = 3276 units in hippocampus, n = 2188 units in medial prefrontal cortex, **Figure 2.8A, 2B, Table 2.1**). We found that neurons in both hippocampus and prefrontal cortex had spatial tuning curves that tiled the environment (**Figure 2.8C, Figure 2.10A**). To obtain a population level representation estimate, we analyzed hippocampal and prefrontal activity from all cells using a memoryless Bayesian decoding algorithm (see **Methods**). As expected from prior work, we found that hippocampal and prefrontal activity could reliably decode the animals' current location in the environment; decoded positions from neural activity represented the animals true position across locations in the environment (**Figure 2.8D, Figure 2.10B**).

We then wanted to understand how neural representations change when animals receive new information that directs them away from a previous goal destination to a new goal. To do so, we focused specifically on neural activity around the update cue onset. We expected that neural activity in hippocampus would predominantly represent the animal's current position, but there would be some remote prospective position coding (Jezek et al., 2011; Kapl et al., 2022; Kay et al., 2020; Yu & Frank, 2021). We hypothesized the amount of non-local representation would remain constant, and both goal locations would be represented equally in hippocampus even when new information was presented, and animals switched from a previous goal destination to a new one. We were surprised to observe that when the update cue was presented on switch trials, the decoding output rapidly jumped from predominantly representing the animal's current

location, to representing the goal arm locations (**Figure 2.2A, 2B, Figure 2.9**). We quantified this elevated non-local representation and found that the overall probability of the goal location being decoded, the posterior probability integrated over each goal arm, was elevated on switch trials compared to stay and non-update trials ($p < 0.0001$, initial, switch vs. initial, delay only, $p < 0.0001$, initial, switch vs. initial stay, $p < 0.0001$, new, switch vs. new, delay only, $p = 0.0139$ new, switch vs. new, stay, **Figure 2.2C, 2D, Figure 2.8E-F**). Interestingly, both the new correct goal location and the initial correct goal location increased similar amounts on average. When we compared differences between the amount of initial goal location and new goal location representations on a trial-by-trial basis, the differences were not significantly different from zero and were not significantly different between switch, stay, and delay only trials ($p = 0.3014$, stay vs. delay only, $p = 1.00$ switch vs. delay only, $p = 0.3178$, switch vs. stay, **Figure 2.2D**, see **Table 2.2** for additional statistical details). To confirm this elevation of non-local coding was not due to a complete loss of accurate decoding, we compared the representation of the goal arms to a uniform decoding output, that is the theoretical posterior probability value if all locations in the track were equally represented. We found that the elevated probability in hippocampus was 15% and 20% greater than uniform decoding for initial and new goal locations. Furthermore, this increased non-local activity was not due to overall poor decoding of that part of the environment. On delay only trials, the neural activity continued to predominantly represent the animals' current location in the central arm of the track over the same time interval (84% greater than uniform decoding on delay only trials, **Figure 2.8E**). We trained our encoding model with delay only trials, so that the spatial tuning curves were not influenced by the neural activity that occurred on the update trials and we could accurately assess how neural activity varied on update trials compared to delay only. However, we wondered if these results showing increased non-local decoding after the update and suppressed local representation were due to the fact that our model was trained on delay only trials. To control for this possibility, we also ran the analysis using all trials in the encoding model and found that while there was more accurate representation of the animals' current

location during the update cue, the non-local coding results remained similar. Because the update trials are interleaved with the delay only trials, it is unlikely that these differences are due to spatial remapping, single unit instability, or behavioral disengagement. Overall, these results show that when new, crucial information is presented that requires animals to update their goal destinations, hippocampus suppresses local position coding and increases non-local coding of *both* potential goal locations.

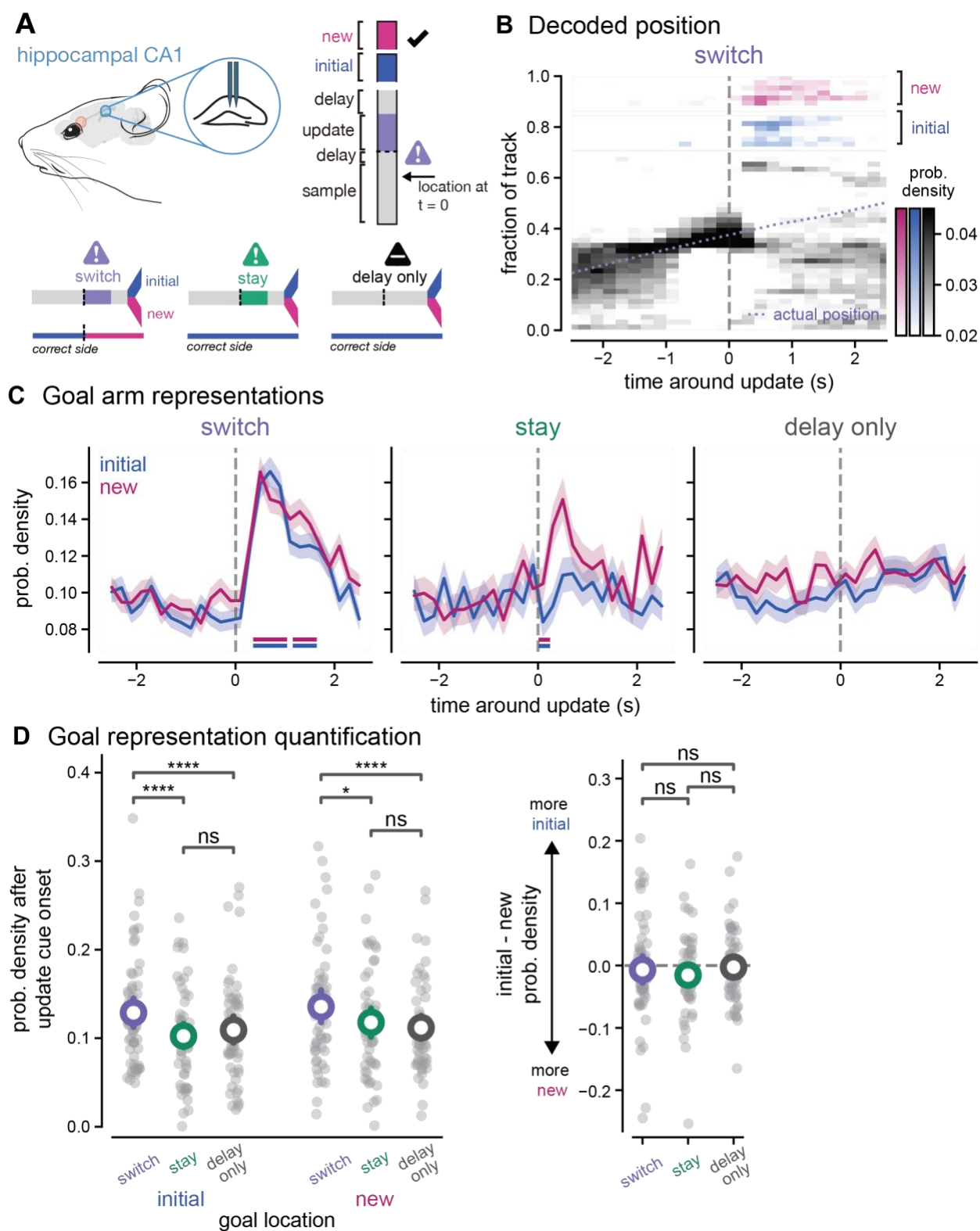


Figure 2.2. Non-local representations for both initial and new goals increase in hippocampus in response to new information

- A. *Left*, schematic of hippocampal CA1 recording locations. *Right*, schematic of phases of the task as shown on y-axis of panel B. *Bottom*, schematic of trial types illustrating goal locations and the update cue onset.
- B. Decoding output (posterior probability density) before and after the update cue is presented, average across all recording sessions. Heatmap indicates stronger likelihood of those position being decoded by the spiking activity of all hippocampal neurons. Animals actual position (purple dashed line) shown over the same time window. Data from both left and right trial types were combined so initial and new arms of the track matched. Two-dimensional position in the virtual track was converted to a 1D position (see **Methods**) to disambiguate the new and initial arms of the environment.
- C. Top, integrated probability densities of the new (pink) and initial (blue) goal arms around the update cue on switch, stay, and delay only trials. Dark pink and blue lines indicate bins significantly different from baseline. Mean \pm SEM across all trials shown. (initial, delay only: 0.11 ± 0.00 , $n = 945$ trials, percentiles = 0.00, 0.02, 0.07, 0.16, 0.88; initial, stay: 0.10 ± 0.00 , $n = 572$ trials, percentiles = 0.00, 0.02, 0.08, 0.16, 0.58; initial, switch: 0.13 ± 0.00 , $n = 1337$ trials, percentiles = 0.00, 0.03, 0.10, 0.19, 0.87; new, delay only: 0.11 ± 0.00 , $n = 945$ trials, percentiles = 0.00, 0.02, 0.08, 0.16, 1.00; new, stay: 0.12 ± 0.00 , $n = 572$ trials, percentiles = 0.00, 0.03, 0.09, 0.18, 0.67; new, switch: 0.14 ± 0.00 , $n = 1337$ trials, percentiles = 0.00, 0.04, 0.10, 0.21, 0.97).
- D. Left, quantification of average probability density decoding output in the first 1.5 seconds after the update cue onset. Each gray data point reflects the average for a single recording session. Larger colored point and line indicate mean \pm 95% CI computed with $n = 1000$ bootstrap samples (purple: switch, green: stay, black: delay only). Right, quantification of difference between initial and new probability densities after the update cue. (delay only: -0.01 ± 0.01 , $n = 945$ trials, percentiles = -0.99, -0.08, -0.00, 0.07, 0.88; stay: -0.02 ± 0.01 , $n = 572$ trials, percentiles = -0.66, -0.10, -0.01, 0.07, 0.51; switch: -0.01 ± 0.01 , $n = 1337$ trials, percentiles = -0.95, -0.11, -0.00, 0.10, 0.87).

In prefrontal cortex, we expected that decoding position from neural activity would also reveal representation of primarily the animal's current position with some weaker representation of the remote goal arms. We hypothesized that in the update task, prospective codes for goal locations in prefrontal cortex would switch from the initial goal location to a new one when the animal switched its behavioral trajectory. We found that the overall decoding output was much less spatially specific in medial prefrontal cortex than hippocampus. Furthermore, neural activity represented the animal's current position more than distal locations (**Figure 2.10A-D**). Non-local representations in medial prefrontal cortex were not significantly different across trial types and both goal locations were equally represented until the animal approached the goal arm (**Figure 2.10E-F**). In summary, these results show that when new information is presented that requires an update in goal destination, prefrontal cortex spatial representations continue to predominantly

represent the animal's current position, and do not seem to diverge in representing one goal location over the other at this timescale until the animal approaches the choice point.

Given the suppression of local coding and increase of non-local coding we found in hippocampus, we wondered if current and future location coding was segregated by theta phase, as in static environments without updates (Feng et al., 2015; O'Keefe & Recce, 1993; Skaggs et al., 1996; Wikenheiser & Redish, 2015). We hypothesized that intra-cycle codes for prospective locations would increase when animals were presented with new information that required them to reconsider potential choices. Using our population level metrics, we identified the theta phase of each decoded time bin and the corresponding location in the environment (initial goal arm, new goal arm, or central arm). We found that prospective goal locations were more often represented on the opposite theta phase as current location representations ($p = 0.048$, initial first half vs. central first half, $p = 0.0103$, new first half vs. central first half, $p < 0.0001$, initial second half vs. central second half, $p < 0.0001$, new second half vs. central second half **Figure 2.3A-C**). We found that when comparing before and after the update cue was shown, there was an overall increase in the amount of goal location decoding at a theta-timescale, but the goal location phase preferences were still maintained ($p < 0.0001$, pre, initial vs. post initial, $p < 0.0001$ pre, new vs. post new, **Figure 2.3D**). There was also a significant decrease in the amount of local coding by theta phase on switch trials when new information was presented ($p < 0.0001$, pre, home vs. post home). Non-local codes were also significantly larger on switch trials compared to stay and delay only trials ($p < 0.0001$ switch vs. stay, $p < 0.0001$ switch vs. delay only, **Figure 2.11**). Overall, these results show that even with large increases in non-local coding and decreased local coding at longer timescales, non-local goal representations remain segregated from local codes during theta oscillations.

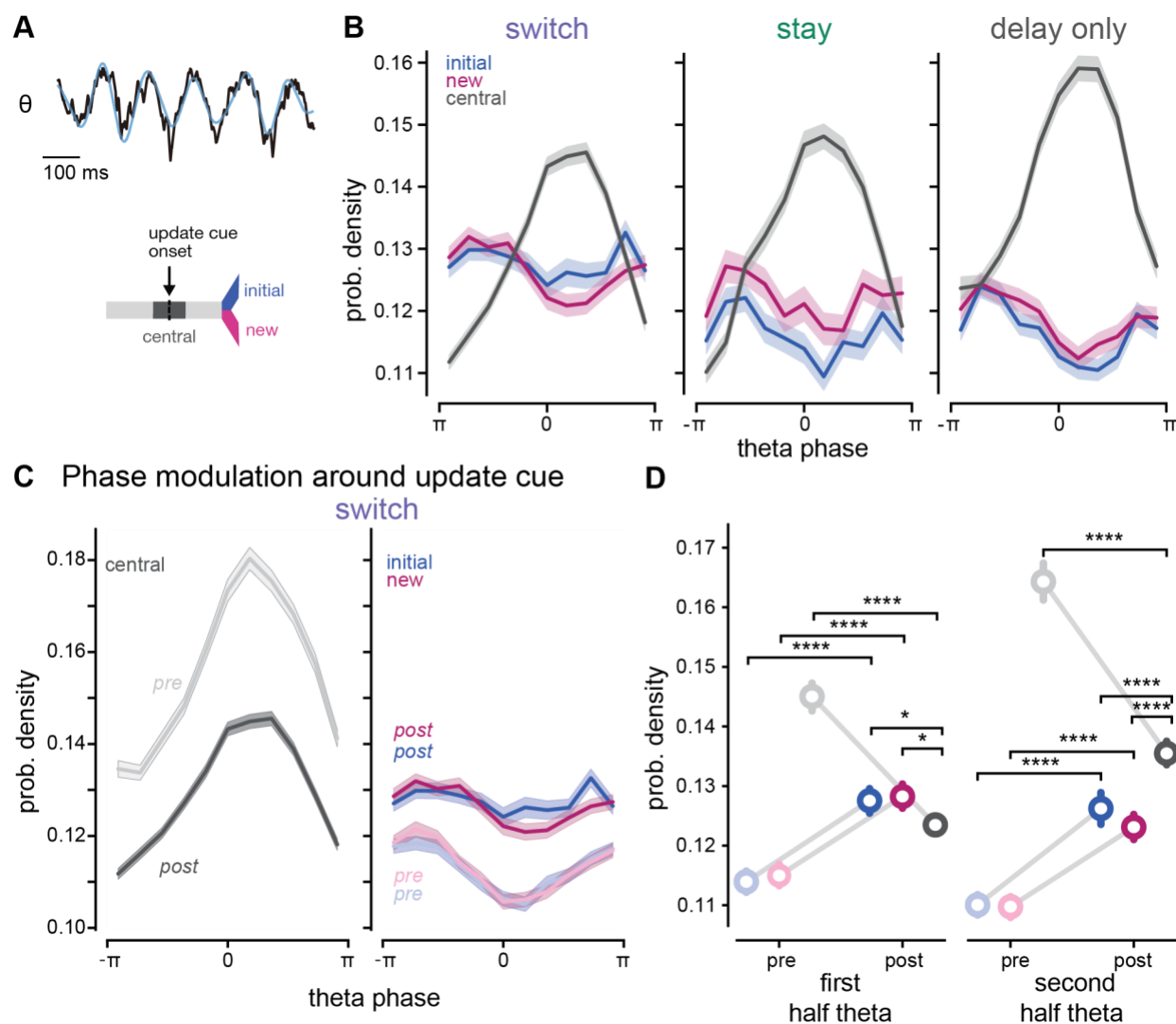


Figure 2.3. Non-local codes occur on distinct theta phases from local position codes and increase with new information

- Top, example theta oscillation detected in hippocampal CA1 from the local field potential. Low pass filtered signal in black, theta band amplitude in blue. Bottom, schematic of initial goal, new goal, and central arm bins used to quantify local and non-local representations by theta phase.
- Average decoded goal arms (pink: new, blue: initial) and central arm (black) posterior probability densities by theta phase. Data shown from 1.5 second time period after the update cue onset, time window based on previous longer timescale elevation in non-local hippocampal codes from **Figure 2.2**. From left to right, switch, stay, and delay only trials. Mean \pm SEM across all trials shown.
- As in **B** for pre (-1.5 to 0 seconds) and post (0 to 1.5 seconds) the update cue onset for switch trials. *Left*, update trial quantification of central arm representation by theta phase. Pre-cue shown in lighter shades, post cue shown in darker shades. *Right*, as in left for initial and new arms.
- Quantification of pre (-1.5 to 0 seconds, on left) and post (0 to 1.5 seconds, on right) probability density around the update cue onset. *Left*, first half of theta cycle. *Right*, second half of theta cycle. Switch trials, first half, pre: home: 0.15 ± 0.00 , $n = 1337$ trials,

percentiles = 0.03, 0.12, 0.13, 0.17, 0.37, initial: 0.11 ± 0.00 , $n = 1337$ trials, percentiles = 0.01, 0.09, 0.11, 0.13, 0.31, new: 0.11 ± 0.00 , $n = 1337$ trials, percentiles = 0.01, 0.09, 0.11, 0.13, 0.30. Switch trials, first half, post: home: 0.12 ± 0.00 , $n = 1337$ trials, percentiles = 0.01, 0.11, 0.12, 0.14, 0.30, initial: 0.13 ± 0.00 , $n = 1337$ trials, percentiles = 0.02, 0.10, 0.12, 0.14, 0.34, new: 0.13 ± 0.00 , $n = 1337$ trials, percentiles = 0.02, 0.11, 0.12, 0.15, 0.38. Switch trials, second half, pre: home: 0.16 ± 0.00 , $n = 1337$ trials, percentiles = 0.01, 0.13, 0.15, 0.18, 0.50, initial: 0.11 ± 0.00 , $n = 1337$ trials, percentiles = 0.00, 0.09, 0.11, 0.13, 0.31, new: 0.11 ± 0.00 , $n = 1337$ trials, percentiles = 0.01, 0.09, 0.11, 0.13, 0.24, switch trials, second half, post: home: 0.14 ± 0.00 , $n = 1337$ trials, percentiles = 0.02, 0.12, 0.13, 0.15, 0.45, initial: 0.13 ± 0.00 , $n = 1337$ trials, percentiles = 0.02, 0.10, 0.12, 0.14, 0.45, new: 0.12 ± 0.00 , $n = 1337$ trials, percentiles = 0.01, 0.10, 0.12, 0.14, 0.43.

2.3.3 Rapid switch from old to new choice estimates in prefrontal cortex when new information is presented

While we were surprised that activity in prefrontal cortex did not represent the future goal location more than the alternative goal, this may be explained by the overall minimal non-local coding we observed in prefrontal cortex around the update. Because medial prefrontal cortex is known to encode neural correlates of choice in decision-making tasks, we wanted to explicitly test how choice codes in prefrontal cortex were altered around the update cue. We hypothesized that in medial prefrontal cortex the choice representation would be stronger for the initial choice preceding the update cue and would then shift from the initial choice to the new choice after the new information was presented. To test this hypothesis, we took advantage of the continuous evolution of choice that occurs as animals run down the virtual reality environment and is reflected in the animal's changing velocity and heading direction over the course of the track (Tseng et al., 2022). To obtain a continuous estimate of relative choice commitment throughout the trial, we trained a long short-term memory (LSTM) neural network to predict the mouse's ultimate choice from the velocity, heading direction, and forward position trajectories throughout the trial (**Figure 2.4A**). At each timepoint in the trial, all previous trial time points were used to estimate the animals' final choice. The output choice estimate varied throughout the course of a trial, starting at chance-level accuracy at the start of the trial on average, and ending with a highly accurate, or -0.17 ± 0.02 log likelihood on average, prediction of the animals' final choice, where

0 is perfect and 1 is a chance level prediction accuracy (**Figure 2.4B**). We then used this choice measure to obtain a population level estimate of the animals' choice commitment from medial prefrontal cortex using a Bayesian decoder, similar to our previous decoding of position representation (**Figure 2.12A-B**). Indeed, we observed that the choice estimates for strong commitment to the initial and new choice began to diverge preceding the update and then rapidly flipped after the reward location changed ($p < 0.0001$ initial switch vs. initial, delay only, $p < 0.0001$ new, switch vs. new, delay only **Figure 2.4C-D, Figure 2.13**). Interestingly, on update trials the neural activity rapidly switched from high commitment to the initial choice to high commitment to the new choice with minimal time spent showing no strong choice commitment. In contrast on stay trials, we observed the initial choice commitment remained relatively constant and was significantly lower than on delay trials. Meanwhile, new choice coding on stay trials was at similar levels to delay only trials ($p = 0.0015$, initial, stay vs. initial, delay only, $p = 0.6968$, initial, stay vs. initial, delay only **Figure 2.4C-D**). Overall, the difference between initial and new choice decoding was significantly different between trial types ($p < 0.0001$ initial – new for switch vs. delay only, $p < 0.0001$ initial – new for switch vs. stay, $p = 0.0018$ initial – new for stay vs. delay only **Figure 2.4E, 3F**). On switch trials, after the update cue the new choice decoding was larger than initial choice decoding on average. Meanwhile on stay and delay only trials, the initial choice decoding was larger than the new choice after the update cue or during the delay where no new information was presented (**Figure 2.12**). We compared the choice representations to a uniform decoding output, that is the theoretical posterior probability value if all choice values were equally represented. We found that the elevated probability in prefrontal cortex was 18% greater than uniform decoding for new choices after the update, while at uniform representation levels for initial choice codes after the update. On average, the change in neural activity choice decoding preceded the movement change showing that these effects are not likely due to motor response execution (**Figure 2.4F**). Overall, these results show that when animals were presented with new information that required a switch from one choice to another, the new choice is quickly

represented more than the initial choice, compared to trials in which new information was presented that confirmed the previous choice or when no new information is presented.

While the hippocampus is traditionally associated with position more than choice representations, prior work has shown that choice can be decoded from hippocampal activity during decision-making tasks. We wondered how the decoded choice estimate representation in hippocampus around update cues would change compared to choice codes in prefrontal cortex (**Figure 2.14A-B**). Given our previous results on equal hippocampal position representations, we hypothesized that both choices would be represented equally in hippocampus around the update or would diverge between choices very slightly. We found that initial choice representations in hippocampus were higher than the alternative choice preceding the update, and then switched after the update cue was presented and the new choice representation increased (**Figure 2.14C-E**). However, while the decoded activity followed a similar pattern of switching from the initial to the new choice, this change evolved over a longer time period in hippocampus. There was an extended period in which both choices were equally represented in hippocampus, but the choice information had already flipped in medial prefrontal cortex. Overall, these findings show that new crucial information that requires animals to update their choices results in a switch from old to new choice commitment in both hippocampus and prefrontal cortex. However, representation of both choices converges to similar levels in hippocampus for an extended period of time while stronger commitment to one choice or another occurs more rapidly in prefrontal cortex.

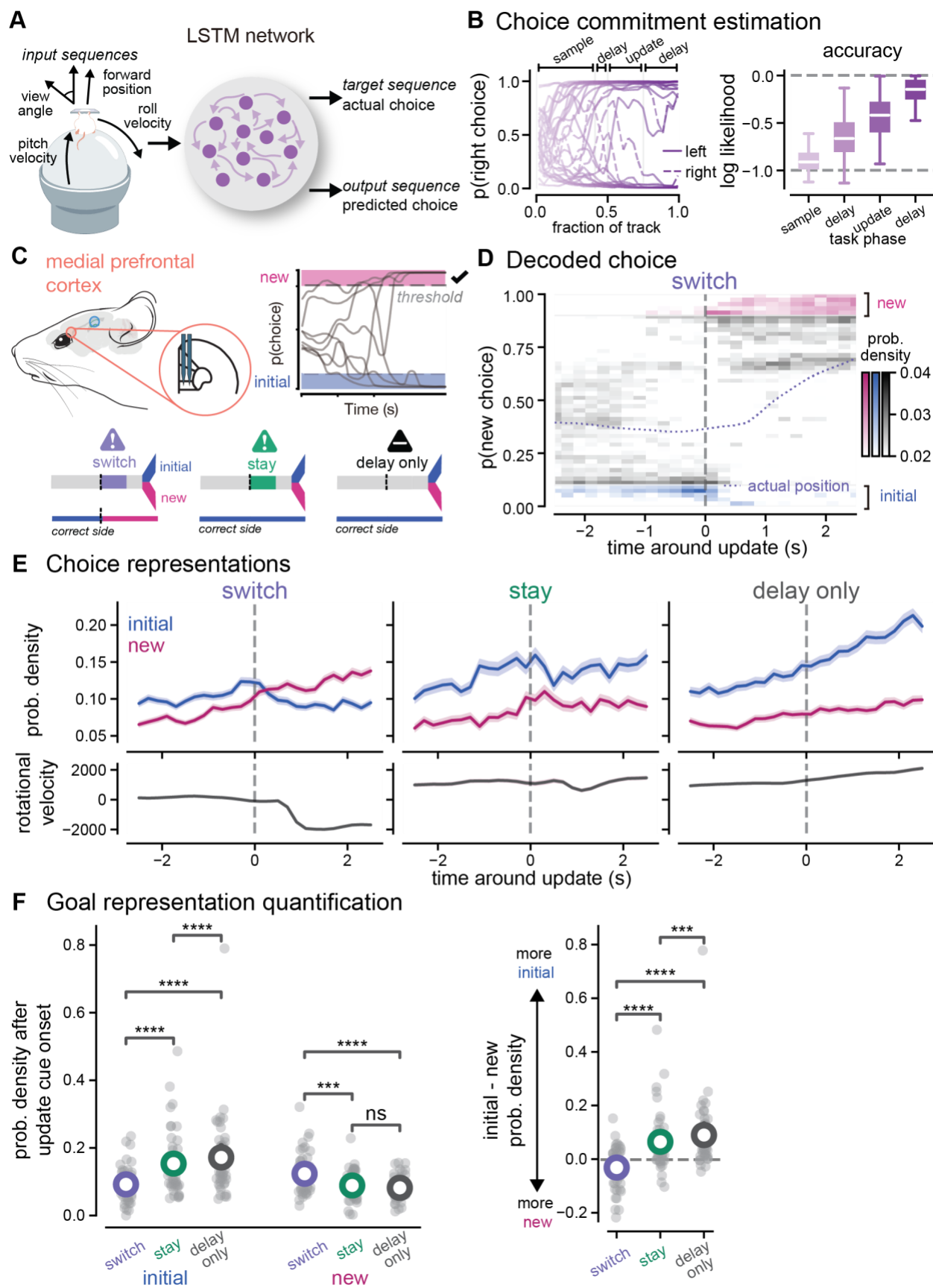


Figure 2.4. Prefrontal cortex rapidly switches from representing the old choice to the new choice in response to new information.

- A. Schematic of long short-term memory (LSTM) neural network for predicting the animals' choice from the behavioral trajectories.
- B. Left, example trials of the LSTM output for trials with left (solid) and right (dashed) reported choices. Right, session-averaged overall accuracy of the LSTM choice output throughout the virtual environment. (initial cue: -0.98 ± 0.05 , $n = 67$ session averages, percentiles = -2.62, -0.97, -0.91, -0.83, -0.60; delay cue: -0.63 ± 0.03 , $n = 67$ session averages, percentiles = -1.13, -0.79, -0.66, -0.51, -0.07; update cue: -0.43 ± 0.03 , $n = 67$ session averages, percentiles = -1.07, -0.58, -0.42, -0.29, -0.01; delay2 cue: -0.17 ± 0.02 , $n = 67$ session averages, percentiles = -0.72, -0.24, -0.15, -0.06, -0.00)
- C. *Left*, schematic of medial prefrontal cortex recordings. *Right*, schematic of choice commitment as shown on y-axis of right section. Data from both left and right trial types were combined so initial and new choices of the track matched. *Bottom*, schematic of trial types and correct and incorrect choices around the update cue onset.
- D. Decoding output (posterior probability density) before and after the update cue is presented, averaged across all recording sessions. Heatmap indicates stronger likelihood of that choice being decoded by the spiking activity of all prefrontal neurons. Animal's actual averaged choice commitment (purple dashed line) shown over the same time window.
- E. Integrated probability densities of the new (pink) and initial (blue) choice estimates around the update cue on switch, stay, and delay only trials. Mean \pm SEM shown. Integrations were performed for a subset of "high commitment" decoding outputs, i.e. the highest 10% of all choice commitment values for either choice.
- F. *Left*, quantification of probability density values after the update cue. Each gray data point reflects the average for a single recording session. Larger colored point indicates mean. 95% CI computed with $n = 1000$ bootstrap samples but not visible due to size (purple: switch, green: stay, black: delay only). (initial, delay only: 0.16 ± 0.01 , $n = 817$ trials, percentiles = 0.00, 0.05, 0.11, 0.23, 0.97; initial, stay: 0.14 ± 0.01 , $n = 504$ trials, percentiles = 0.00, 0.04, 0.10, 0.19, 0.70; initial, switch: 0.10 ± 0.00 , $n = 1151$ trials, percentiles = 0.00, 0.03, 0.07, 0.13, 0.85; new, delay only: 0.08 ± 0.00 , $n = 817$ trials, percentiles = 0.00, 0.02, 0.06, 0.12, 0.71; new, stay: 0.10 ± 0.00 , $n = 504$ trials, percentiles = 0.00, 0.02, 0.07, 0.12, 0.66; new, switch: 0.12 ± 0.00 , $n = 1151$ trials, percentiles = 0.00, 0.04, 0.08, 0.16, 0.69). *Right*, quantification of difference between initial and new probability densities after the update cue. (delay only: 0.08 ± 0.01 , $n = 817$ trials, percentiles = -0.71, -0.02, 0.04, 0.16, 0.97; stay: 0.05 ± 0.01 , $n = 504$ trials, percentiles = -0.66, -0.05, 0.03, 0.13, 0.70; switch: -0.02 ± 0.00 , $n = 1151$ trials, percentiles = -0.66, -0.09, -0.01, 0.05, 0.83).

2.3.4 Goal codes predict ability to accurately update decisions in response to new information

After finding that new pivotal information in the update task caused elevated non-local coding for both goal locations in hippocampus and a rapid switch from old to new choice codes in the prefrontal cortex, we then asked how these codes contribute to the ability to accurately update decisions. We hypothesized that if increases in non-local goal codes in hippocampus contribute to responding to new information, then failure to switch goals in response to new information

would co-occur with a failure to increase both non-local goal representations after the update cue is presented. To test this, we compared our population estimates of position in hippocampus and choice in prefrontal cortex on correct versus incorrect switch trials. We found that indeed on incorrect trials in hippocampus, the new goal arm coding was not as elevated as correct trials ($p = 0.0002$, new correct vs. incorrect, $p = 0.5475$ initial correct vs. incorrect, **Figure 2.5A, C**). However, the difference in new goal arm coding on correct versus incorrect trials was small. Furthermore, there was no significant difference in the initial goal arm coding or the relative difference in initial versus new goal arm representation between correct and incorrect trials ($p = 0.3831$, initial – new correct vs. incorrect **Figure 2.5C**). Interestingly, preceding the update there was a more noticeable increase in initial goal arm representation ($p < 0.0001$, initial correct vs. incorrect). These results show that when animals failed to switch goals, new goal arm codes did not increase as much in response to the update cue, though overall both goals were represented similarly, and initial goal arm codes were elevated *before* the update cue compared to correct trials.

In prefrontal cortex, we had earlier observed that there was a significantly larger initial choice representation *preceding* the update cue on correct switch trials compared to stay and delay only trials ($p < 0.0001$, initial, switch vs. stay, $p = 0.0094$, switch vs. delay only, **Figure 2.4E**). We hypothesized that these differences might be occurring because animals with a stronger commitment to the initial choice would be less likely to flexibly and correctly respond to new information, and so correct switch trials had distinct neural signatures preceding the update cue. Indeed, when we compared correct vs. incorrect trials, we observed that there was a striking difference in the amount of initial choice representation preceding the update cue onset ($p < 0.001$ initial, correct vs. incorrect, **Figure 2.5B**). We also expected that when animals failed to correctly respond to new information, the new and initial choice representations would fail to flip from the initial choice being more strongly represented to the new choice being more

represented. Indeed, we observed that on incorrect switch trials in prefrontal cortex the new correct choice representation was smaller and the initial choice representation was larger than correct trials after new information was presented ($p < 0.0001$, new correct vs. incorrect, $p < 0.0001$ initial correct vs. incorrect, **Figure 2.5B, D**). These differences held across single trials, the new choice was more strongly represented than the initial choice on correct trials and this was significantly different from incorrect trials, during which the old choice was more strongly represented than the new choice, even after new information was presented ($p < 0.0001$, initial – new for correct vs. incorrect **Figure 2.5D**). These results show that similar to hippocampus, when animals failed to switch destinations in response to new information, there was significantly larger representation of the initial choice in prefrontal cortex both preceding and after the update cue onset.

To test whether these observed codes were important to the animals' behavioral performance, we then used the population measures of goal coding to predict behavioral outcomes on a trial-by-trial basis. We found that in both hippocampus and prefrontal cortex, the population representation of the initial and new goals after the update cue was presented could predict whether the animal would choose the correct or incorrect side ($p < 0.0001$, permutation test, **Figure 2.5E**). However, the prediction accuracy was overall low using hippocampal position decoding (53.03% accuracy) and slightly higher with prefrontal choice decoding (61.36% accuracy). As described above in both regions, there was an overall higher initial choice representation *preceding* the new update cue on incorrect trials, which may reflect a neural signature of stronger choice commitment or perseveration that results in increased difficulty responding to new information. We thus asked whether the neural representations of the initial and new choices *preceding* the new information, when the opposite choice to the animals' final decision was more likely to be strongly represented, predict behavior on a trial-by-trial basis. We found that these representations before the update cue predicted the animal's final choice better

than the shuffled controls ($p < 0.0001$, permutation test, **Figure 2.5E**). Overall, we found hippocampal and prefrontal goal representations, both preceding and after the update cue onset, predicted whether animals flexibly and accurately adapt plans on a trial-by-trial basis as would be expected if these codes were important to the animals' behavioral performance.

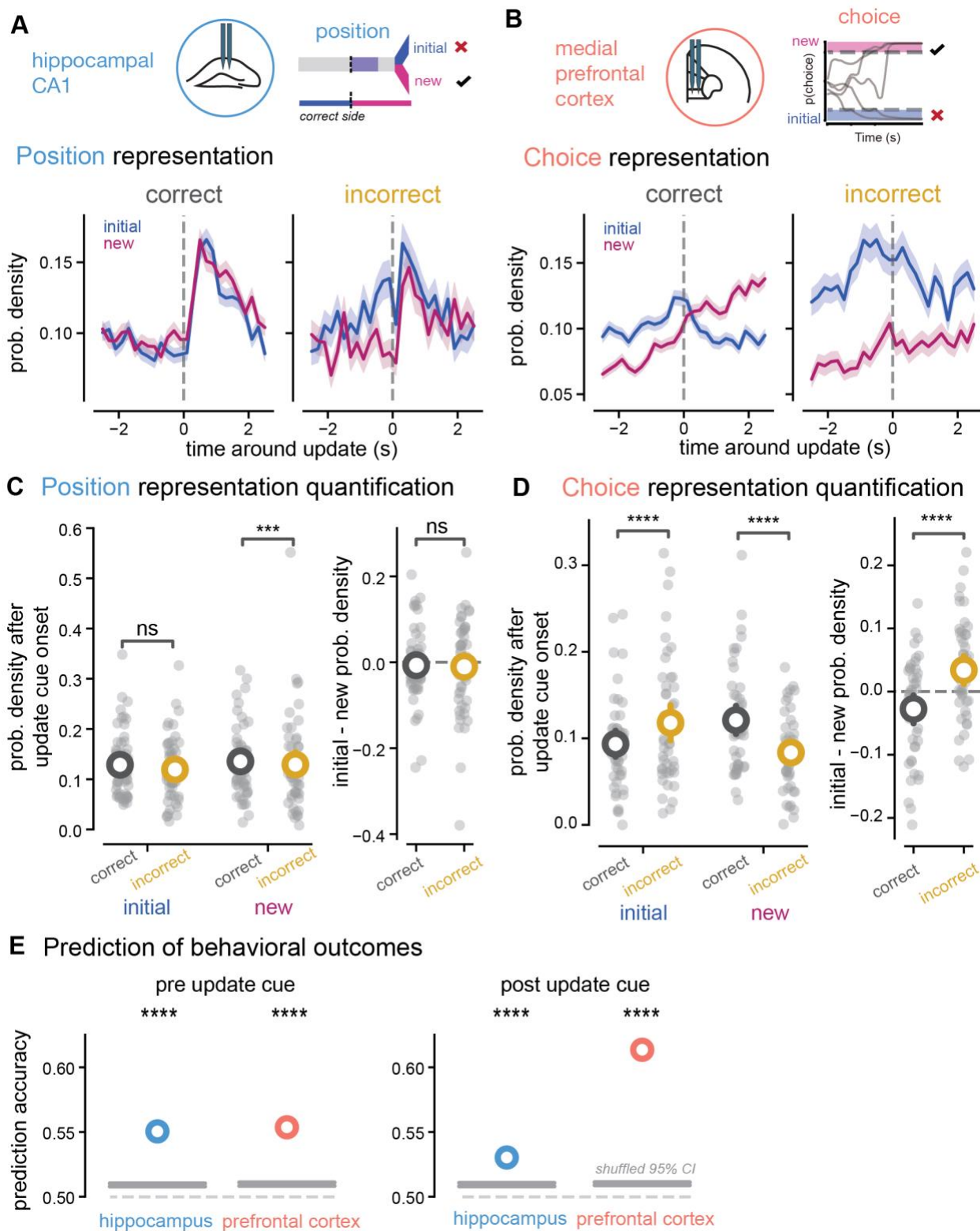


Figure 2.5 Prefrontal cortex decoding of choice predicts correct response while hippocampal goal coding remains elevated regardless of trial outcome.

- A.** Integrated decoding output (probability densities) from hippocampus of the new (pink) and initial (blue) position representations around the presentation of the update cue on correct versus incorrect switch trials.
- B.** As in **A** for choice representations in prefrontal cortex
- C.** Quantification of probability density differences after the update cue of hippocampal position codes on correct versus incorrect trials (black: correct, yellow: incorrect). Each gray data point reflects the average for a single recording session. Larger colored points and line indicate mean \pm 95% CI computed with $n = 1000$ bootstrap samples. *Left*: quantification of probability density differences after the update cue of hippocampal position codes on correct versus incorrect trials (initial, correct: 0.10 ± 0.00 , $n = 1151$ trials, percentiles = 0.00, 0.03, 0.07, 0.13, 0.85; initial, incorrect: 0.14 ± 0.01 , $n = 363$ trials, percentiles = 0.00, 0.05, 0.11, 0.19, 0.73; new, correct: 0.12 ± 0.00 , $n = 1151$ trials, percentiles = 0.00, 0.04, 0.08, 0.16, 0.69; new, incorrect: 0.09 ± 0.01 , $n = 363$ trials, percentiles = 0.00, 0.02, 0.06, 0.12, 0.83), *Right*, quantification of difference between initial and new probability densities after the update cue (correct: -0.02 ± 0.00 , $n = 1151$ trials, percentiles = -0.66, -0.09, -0.01, 0.05, 0.83; incorrect: 0.05 ± 0.01 , $n = 363$ trials, percentiles = -0.80, -0.03, 0.03, 0.13, 0.70)
- D.** As in **C**, for prefrontal choice codes. *Left*: quantification of probability density differences after the update cue of prefrontal choice codes on correct versus incorrect trials (initial, correct: 0.13 ± 0.00 , $n = 1337$ trials, percentiles = 0.00, 0.03, 0.10, 0.19, 0.87; initial, incorrect: 0.13 ± 0.01 , $n = 411$ trials, percentiles = 0.00, 0.04, 0.11, 0.18, 0.65; new, correct: 0.14 ± 0.00 , $n = 1337$ trials, percentiles = 0.00, 0.04, 0.10, 0.21, 0.97; new, incorrect: 0.12 ± 0.01 , $n = 411$ trials, percentiles = 0.00, 0.03, 0.09, 0.17, 0.83). *Right*, quantification of difference between initial and new probability densities after the update cue (correct: -0.01 ± 0.01 , $n = 1337$ trials, percentiles = -0.95, -0.11, -0.00, 0.10, 0.87; incorrect: 0.01 ± 0.01 , $n = 411$ trials, percentiles = -0.82, -0.07, 0.01, 0.10, 0.64).
- E.** Prediction of behavioral outcome (correct vs. incorrect final choice) using decoded choice estimates in prefrontal cortex and decoded position in hippocampus. Dashed lines indicate 50% prediction accuracy, grey lines indicated 95% CI for shuffled predictions. *Left*, prediction from data preceding the update cue onset (55.05% accuracy for hippocampus, 55.37% accuracy for prefrontal cortex), *Right*, prediction from data after the update cue onset (53.03% accuracy for hippocampus and 61.36% accuracy for prefrontal cortex).

2.3.5 Increased goal representations are correlated with choice commitment

Given that choice representations preceding the introduction of new information were predictors of the animal's final choice, we asked if the degree of choice commitment was related to the neural representations of goal coding in response to new information. We hypothesized that commitment to the initial decision at the time of the update cue onset would influence the degree of modulation of the initial and new goals representations. In other words, if the animal was less committed to its initial choice, the need to consider the alternative goal would be lower compared to trials where it was more committed and more behavioral adaptation would be needed. To test this, we leveraged a behavioral readout of evolving choice in the virtual reality environment and separated

out trials by view angle at the time the update cue was introduced (**Figure 2.6A**). As expected, neural choice representations of the initial choice in prefrontal cortex covaried with view angle at the time of the update cue; if the animal was pointed more towards the initial side, the initial choice coding was higher than trials where the animal was pointed down the center or to the new side (**Figure 2.6B**). Overall, there was a ceiling effect in the amount the initial choice decreased after the update cue, where trials with minimal initial choice commitment had minimal change in their representation of the initial choice. We were surprised to see that in hippocampus, view angle at the time of the new information was also positively correlated with the increase in non-local goal representation of the new arm ($p < 0.0001$, $r_s = 0.1568$, **Figure 2.6C-D**, **Figure 2.15**). In other words, when the animal was more committed to the *initial* side, the introduction of new, pivotal information resulted in an increased representation of the *new, alternative* side compared to trials where the animal was less committed or already heading towards the new side. Interestingly, on stay trials this pattern was observed in reverse; when animals were less committed to the initial side, the introduction of new information indicating that the initial side was the correct arm led to an increased representation of the initial side ($p = 0.0006$, $r_s = -0.1454$, **Figure 2.15**). Overall, these results demonstrate that greater commitment to the initial choice preceding new information leads to a larger increase of hippocampal non-local coding for the new, alternative side in hippocampus. On trials where animals need a larger trajectory adaptation in response to new information, non-local codes for the new goal destination are more prominent.

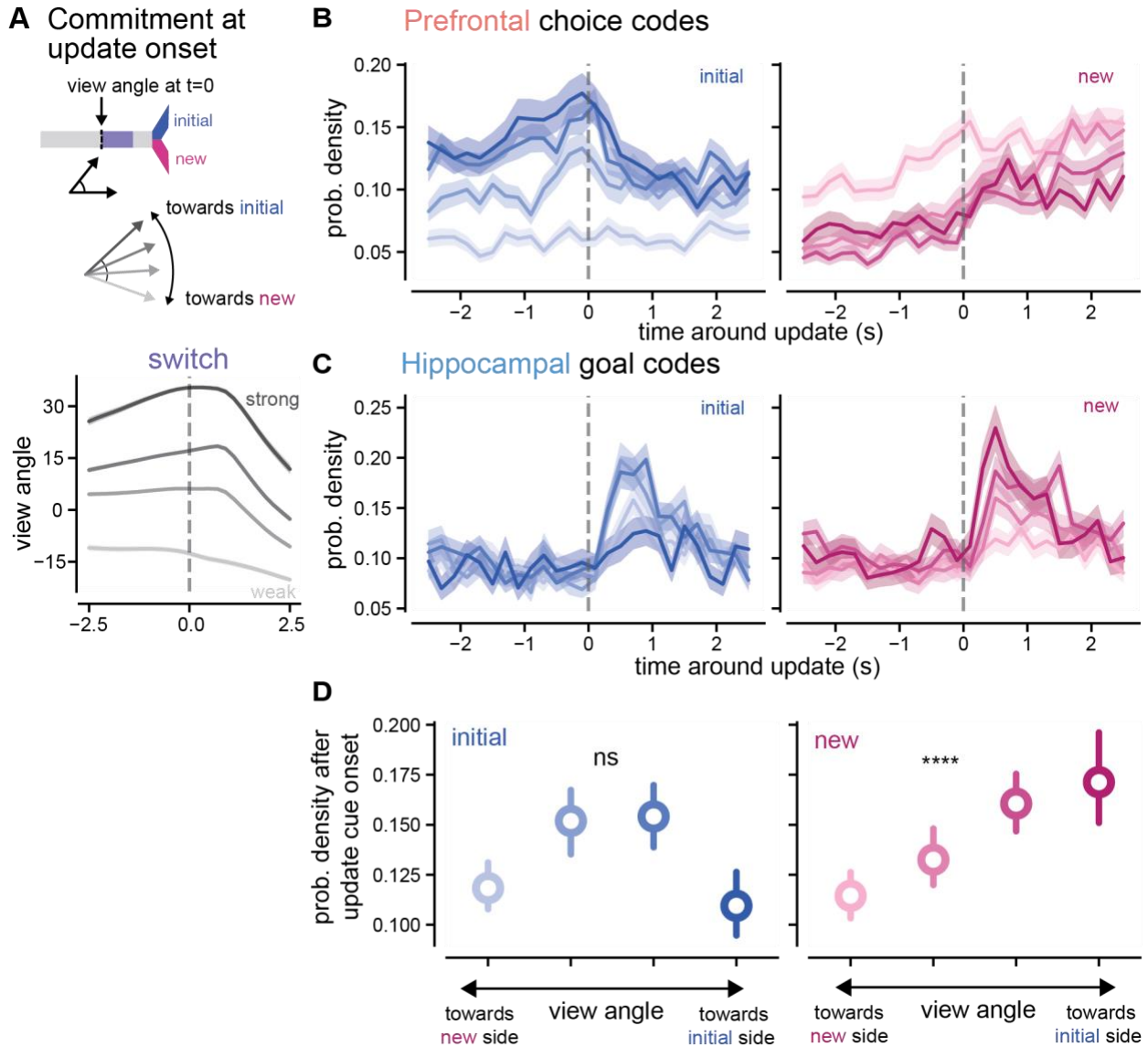


Figure 2.6. Hippocampal codes for *new* goal locations increase more strongly when animals are more committed to the initial goal.

- A. *Top*, schematic of commitment estimate breakdown from behavioral readouts around the update cue. *Bottom*, View angle values were separated out into quartiles from greatest to least at the time of the update cue onset. Darker indicates a greater commitment to the initial side and lighter indicates a greater commitment to the new side.
- B. Prefrontal neural codes for choice representation around the update cue broken down by the animal's view angle at the time of the update cue onset on switch trials. *Left*, initial choice representations, darker blue indicates a view angle towards the initial side and lighter blue indicates a view angle towards to the new side. *Right*, new choice representations, darker indicates a view angle towards the initial side and lighter pink indicates a view angle towards to the new side.
- C. Hippocampal neural codes for goal locations at the time of the update cue onset on switch trials. *Left*, initial goal representations, darker blue indicates a greater view angle towards the initial side at the time of the update cue onset, lighter blue indicates a view

angle towards the new side at the time of the update cue onset. *Right*, as in left for new goal representations

- D.** Average probability density in first 1.5 seconds after the update cue across all view angle quartiles. *Left*, initial goal representations in hippocampus in blue. *Right*, new goal representations in hippocampus in pink.

2.4. Discussion

Using a navigation task with precise timing of environmental changes, simultaneous hippocampal-prefrontal cortex recordings, and decoding of position and choice, we addressed how prospective codes change in response to new information to guide decision making. In our paradigm, animals rapidly update their behavior in dynamic environments in response to new information. In hippocampus, our results show that when new, crucial information is presented that requires animals to update their goal destinations, hippocampus increases non-local coding of *both* potential goal locations. In prefrontal cortex we found new, pivotal information causes choice codes to rapidly switch from representing old to new choices, prior to behavioral responses and prior to choice switching in hippocampus. On incorrect trials, hippocampal non-local goal codes remain relatively intact, but new prefrontal choice coding fails to increase. Furthermore, there was an overall higher initial choice representation *preceding* the update cue on incorrect trials, which may reflect a neural signature of stronger choice commitment or perseveration that results in more difficulty responding to new information. Non-local goal representations in hippocampus increased more when animals needed to produce a larger trajectory change. Together, these results show that non-local codes are generated in response to new, crucial information that requires flexible decision making. New information triggers a rapid adaptation of ongoing plans, with hippocampus providing a swift increase in codes of possible goals and prefrontal cortex suppressing initial choices to select a new action plan. When more behavioral adaptation is needed, these prospective codes are stronger.

Questions about neural correlates of deliberation and planning are often posed within behavioral frameworks in which planning is self-driven and internally modulated. However, one of the scenarios often proposed in which these codes might be used is rapid adaptation in an environment with changing sensory information. Thus, our central question was how prospective codes in hippocampus and prefrontal cortex contribute to flexible decision making in dynamic

environments. We manipulated the sensory information presented and quantified the effects on non-local codes. Our results show that in hippocampus non-local coding for goal locations increases when an environment requires a change in action plans. These non-local codes might be triggered not only by new information about goals, but also by task-relevant information more generally. Recent work found that neural codes in hippocampus of bats navigating down a tunnel shift to code for distance to other bats that might cause collisions or prompt changes in their trajectory (Sarel et al., 2022). This detection of relevant non-local stimuli results in a brief decrease in local position representations, similar to our findings. Interestingly, in our task we observe that representations of *both* goal locations increase similarly in response to new information on correct trials. We did not observe that the planned goal was more strongly decoded than the alternative goal on correct trials until the animals reached the goal arms, tying in with previous work that action plans in rodents are not necessarily predicted by hippocampal prospective codes (Gillespie et al., 2021; Kay et al., 2020; W. Tang et al., 2021; M. Wang et al., 2020). These results suggest that hippocampal prospective coding does not preferentially represent the planned trajectory, but a general increase in prospective coding occurs when new, crucial information is presented in an environment with dynamic stimuli. However, non-local goal coding of the new, upcoming goal increases more when animals need to produce a larger trajectory change in response to the new information. These findings may explain variation in the ability to predict upcoming choices across studies; representation of upcoming choice versus possible paths in hippocampus might be a reflection of the animal's need to consider new information in relationship to its commitment to its current decision. Our data also supports the hypothesis that distinct phases of theta might predominantly code for both potential options as compared to upcoming action plans before the choice point. Previous research analyzing individual neurons with out of field firing in hippocampus of rats also observed non-local events that were isolated to distinct theta phases from local codes and were correlated with increased prefrontal spiking activity (Yu & Frank, 2021). We propose that the non-local spiking events observed by Yu and Frank might reflect moments

of representation of possible outcomes to the animal at a faster timescale scale than other noted behavioral deliberation events such as vicarious trial and error (VTE, Redish, 2016). While animals decrease their velocity slightly after the update cue is presented, the animals do not often pause at the update cue or choice point on the virtual reality track and thus do not exhibit traditional VTE behavioral features during these moments of non-local coding. These results provide further evidence that non-local coding in hippocampus might be important for informing decision-making in other regions, reflecting the need to consider new information and work harder to change behavior.

During flexible decision making, we find that prefrontal cortex rapidly shifts from one choice to the other, suppressing the initial choice for the new choice to take over. Interestingly, prefrontal cortex choice switching occurs faster than that in hippocampus, suggesting that prefrontal cortex reaches a choice consensus more quickly. Prefrontal choice representations also preceded the animal's turning movements on average, though these choice alterations may include some aspects of motor planning. Furthermore, when animals fail to flexibly change their goal destination in response to new information, prefrontal cortex choice representations look very different. In our task, we observe that when the new choice representation fails to overtake the old choice, animals are unable to flexibly respond to changes in the environment. This failure is likely occurring in prefrontal cortex, not hippocampus, given overall similar non-local coding in hippocampus on incorrect and correct trials. However, this study is limited overall in that it does not address how necessary these neural signals from each brain region might be to the animals' behavior. Instead, we manipulated the virtual reality environment to test the how sensory information contributes to non-local coding and its role in decision making. Interestingly, there was also an overall higher initial choice representation *preceding* the update cue on incorrect trials in prefrontal cortex, such that we could predict the behavioral outcome using the choice information preceding the update

cue. These results suggest that during decision making in a dynamic environment, prefrontal cortex activity may reflect a neural correlate of flexibility in the face of new information.

In summary this work shows that prospective codes in hippocampus and prefrontal cortex are triggered in response to new pivotal information in the environment to flexibly integrate new information to adapt navigational plans. We found that new, pivotal information causes rapid increases in prospective coding for non-local positions and switches in coding for upcoming choices and that these codes fail when animals are unable to adapt their previous choices. Furthermore, these prospective codes are more strongly triggered when more navigation adaptation is needed. We propose these non-local codes are neural correlates of planning and consideration of alternative choices that can occur at faster timescales than observable behavioral deliberation and drive neural representations momentarily away from local coding when animals need to adapt their decisions and reconsider potential choices.

2.5. Methods

2.5.1 Animals

All animal work was approved by the National Institute of Health guidelines on animal care and use at Georgia Institute of Technology. Eight-week-old male *WT* mice on a C57Bl/6 background were obtained from the Jackson laboratory. Mice were single-housed on a reverse 12-hour light/12-hour dark cycle. At the start of the behavioral and electrophysiological experiments, mice were food-restricted to 85% percent of their baseline body weight, and water was provided without restriction. Fifteen animals total were trained for electrophysiological recordings, one mouse was excluded for lack of movement and inability to complete trials in the visually guided phase, seven were excluded for never reaching the final phase of the task (usually due to difficulties in performing over longer delays), and one was excluded after electrophysiological recordings were

started due to lack of performance during recording sessions, resulting in seven mice total in the final dataset.

2.5.2 Surgical procedures

Animals were implanted with headplates at approximately 8 weeks of age. Mice were anesthetized with isoflurane before headplate implant surgery. A custom stainless steel headplate was fixed to the skull using dental cement (C&B Metabond, Parkell), and the target craniotomy site for recordings was marked on the skull (in mm, from bregma: -2.0 anterior/ posterior, ± 1.8 medial/lateral for hippocampal CA1 and $+1.0$ anterior/posterior, ± 1.25 medial/lateral for medial prefrontal cortex). Craniotomies were later performed before electrophysiology recording sessions in mice that reached the final phase of the task. These craniotomies (200-500um diameter) were made using a dental drill to thin the skull and then opening a small hole in the skull with a 27-gauge needle. Craniotomies were sealed with a sterile silicone elastomer (Kwik-Sil WPI) and only opened for recording experiments.

2.5.3 Behavioral task and training

The virtual reality environment was designed using ViRME_n (Aronov & Tank, 2014) software in Matlab and displayed on a cylindrical screen using a projector system reflected by two mirrors. Head-fixed animals ran on a spherical treadmill composed of an 8-inch polystyrene foam ball floating on air. The ball movement was recorded with optical mice and converted to velocity signals in LabView. Pitch velocity was used for forward motion through the environment and the roll velocity was used for rotational velocity. Rewards of sweetened condensed milk (1:2 dilution in water) were delivered via a reward spout and licks were detected using a photo-interrupter.

The behavioral task was a virtual y-maze in which animals had to choose to go to the left or right to receive a reward. The full length of the maze was approximately 3 m for the center arm. Trials

were structured as follows: first the screen displayed the central arm of the environment, and the mouse's position was frozen in place for 3 seconds to allow the mouse time to adjust its running patterns before it began to move down the track. After this 3s period, the mouse could begin moving forward, but the view angle and x-position were restricted to 40 degrees and 0 virtual displacement for the first 0.05 fraction of the track. Then, once the mouse passed the initial zone of the track, the mouse could rotate and move freely. The visual cues turned on and off at different locations in the track as the animal passed. On correct trials, a reward was delivered at the end of the track, the VR screen froze for 3 seconds, and then the task shifted into an intertrial interval period of 6 seconds. On incorrect trials, the task immediately shifted into a 12 second intertrial interval, which was longer as a form of punishment.

The animals underwent several phases of behavioral shaping and training to reach the final version of the task. In the first phase, animals ran down a linear track that was used to acclimate the mouse to the head-fixed VR setup. The linear track increased in length until the animal completed a certain number of trials for each track length. The second phase of the task was a short y-maze choice task where visual cues indicating the correct and incorrect locations were visible for the full length of the track. After the animals performed 2 sessions above 75 percent, they advanced to the long y-maze choice task with the same visually guided trials as the previous phase but now with the central arm the same length of the final task. Animals were then advanced through phases with a delay at the end of the track. During the delay the visual cues indicating the correct left or right side were no longer visible and the walls of the track were grey instead. This delay was moved gradually earlier in the track, making it longer in time, through three separate phases. After the animal had reached the learning criteria in the third delay phase, the update cue trials were introduced. In these trials, a second visual cue appeared after the first original visual cue, indicating either the same side as the initial cue or the opposite side. Once the animal showed signs of understanding these second cues, the delay location was moved earlier

once more, so that the final update task trial structure had three different trial types. These trial types consisted of delay only trials (65% of trials), in which the initial cue was shown and there was a long delay until the end of the track, switch trials, in which there was an original cue, brief delay, and second cue on the opposite side of the track as the original cue (25% of trials) and finally stay trials, in which there was an original cue, brief delay, and second cue on the same side of the track as the original cue (10% of trials). Animals were trained approximately 5-7 days per week, 1 hour per day on average. Overall, this training process took 55.43 ± 7.38 days on average (mean \pm SEM, $n = 7$ animals).

2.5.4 Electrophysiology recordings

Recordings occurred during behavioral task performance when animals navigated through the virtual reality environment. Data were acquired using a SpikeGadgets acquisition system with a sampling rate of 30kHz and a ground pellet as reference. Animals were head-fixed on the treadmill for a maximum of one five-hour-long recording session per day (number of sessions ranged from 6-12 per animal). A 64-channel, dual shank NeuroNexus probe was placed in a slightly different location within the craniotomy at the beginning of each recording session and advanced to the target location with the angles of the manipulators adjusted according to the final craniotomy location and target location. In hippocampus, the target location was -1.8-2.0 anterior/posterior, 1.5-1.8 medial/lateral, and 1.4 dorsal/ventral. In medial prefrontal cortex, the target location was 1.7-1.8 anterior/posterior, 0.4 medial/lateral, and 2.0 dorsal/ventral. For hippocampal recordings, the probe was advanced to the CA1 pyramidal layer of hippocampus identified via electrophysiological characteristics: large theta waves, sharp-wave ripples, and 150+ μ V spikes on multiple channels. Recording sites usually spanned the layer. For medial prefrontal cortex recordings, the probe was advanced to the target location using the distance travelled as the primary metric, until a suitable location was found with the maximum number of spikes.

During the final recording session from each hemisphere, a probe was coated with Dil and inserted to the target depth. Brains were then drop-fixed in 4% paraformaldehyde. Brains were sectioned to either 100um thick with a Leica VT1000S vibratome or they were sectioned to 60um thick with a Leica cryostat after freezing at -80 degrees. Sections were then stained with 0.2% 1mMol DAPI and mounted on microscopy slides with Vectashield mounting medium. Images were acquired on a Zeiss confocal microscope. All images with visible Dil were registered to the Allen brain atlas using SHARP-Track (Shamash et al., 2018). Probe regions of interest were added based on Dil location, isolating individual shanks of the electrode when possible, and the software determined a best-fit line as an approximation of the probe path. The deepest identified point of visible Dil was used to calculate an estimated recording location in the Common Coordinate Framework.

2.5.5 Local field potential and single unit preprocessing

The local field potential was obtained by downsampling raw traces to 2kHz and bandpass filtering between 1-300Hz. Outliers were eliminated by interpolating over outliers when the pre-filtered LFP signal was 15 standard deviations above the mean. All LFP analyses used the signal from a single channel that was putatively located in the *stratum pyramidale*. To identify this channel, the LFP was bandpass filtered for the sharp-wave ripple band (150-250 Hz, see details below) and the average of the sharp-wave ripple band envelope over time was calculated from each channel. The channel with the highest average sharp-wave ripple band power was used for all further LFP analyses, and this channel was predominately located in the middle of the depth-wise span of the NeuroNexus probe.

Spike detection and sorting were performed using Kilosort 2.0 spike sorting algorithm (Pachitariu et al., 2016) and then were manually curated using Phy software. Cell types were classified into putative pyramidal cells and narrow interneurons and wide interneurons using the default spike

width and the autocorrelogram criteria from CellExplorer software (Petersen et al., 2021): narrow interneuron if trough to peak value was ≤ 0.425 ms, wide interneuron if trough to peak value was > 0.425 ms and the autocorrelogram tau rise value greater than 6 ms, and the remaining cells were classified as pyramidal cells. The classified distributions of neurons were compared to the ground-truth mouse data provided in the software as a visual confirmation of the accuracy of the classification. Positive spikes were identified with a polarity > 0.5 and were flipped for spike width calculations.

2.5.6 Behavioral analysis

To quantify behavioral performance, we binned behavioral data into 15 trial windows for each trial type to calculate a rolling window of proportion correct throughout the behavioral sessions. We also obtained the spatial trajectories of the animal by calculating an average value for each position bin in the environment across individual trials, and then averaging the left and right trials separately to obtain a final average trajectory for each behavioral readout.

For position representation analyses, the 2D position of the VR environment was converted into a 1D linearized position. Linearized position was calculated by generating a graph of the VR environment with 3 segments and 4 nodes: 1 node was at the start of the track, 1 node was at the choice point at the end of the central arm and between the two choice arms, and then the 2 final nodes were at the end of each choice arm. We used the track-linearization package to project each position in the environment using an HMM (hidden Markov map). Artificial gaps between the segments of the track were added for visualization purposes.

Locomotion periods were defined as times when the animals' movement was above a velocity threshold. To calculate this threshold, we plotted the distribution of optical mouse recorded velocities and observed a bimodal distribution. We selected a threshold that separated these two

distributions and used that for subsequent decoding analyses. Multiple thresholds were tested and the results remained similar.

2.5.7 Choice modelling

To calculate an estimate of choice commitment as animals ran through the environment, we built an LSTM neural network using TensorFlow based on previous choice estimate values obtained in virtual reality two choice maze tasks (Tseng et al., 2022) . The LSTM network contained a 10-unit LSTM layer, followed by a 1-unit dense layer with sigmoid activation to predict the reported choice at every time point in the trial using the velocities, view angle, and position from that trial up until that time point. The network was compiled with an Adam optimizer and a binary cross-entropy loss function. The input data was matrix of the rotational and translational velocity signals, the forward position in the maze, and the view angle of the mouse at each time point. A separate model was trained for each behavioral session using a combination of model-averaging and k-fold cross-validation to train and test the model. We divided the data using stratified k-fold cross-validation with 6 folds, in which a separate model was trained for each group of 5 folds and used to predict/test on the 5th fold, and then redivided. The final prediction for each trial was the average of three repeats of this 6-fold cross validation. The training data was normalized and padded to the length of the longest trial, but all trials with a length greater than twice the average were excluded. The hyperparameters of the neural network were selected using a grid search on a subset of the recording sessions and were as follows: batch size = 32, epochs = 20, learning rate = 0.1. Finally, we took the prediction of the model and calculated the log likelihood with log base 2 to assess the overall performance. The prediction data was then used as a feature input to the Bayesian decoding model to assess how the neural activity represented evolving choice as the animals run through the environment.

2.5.8 Decoding analyses

To identify a neural representation of different features of the task at a population level, we performed a Bayesian decoding analysis to estimate the probability of a feature, position or choice, given the observed spiking activity at that period. For all decoding analyses, we analyzed hippocampal CA1 and medial prefrontal cortex separately. We first excluded any sessions in which there were less than 20 single units for the brain region of interest and there were less than 50 trials for the behavioral session. These thresholds were chosen by visually inspecting and quantifying the overall decoding accuracy of each session and determining a minimum criteria in which high fidelity decoding could be obtained. These criteria were applied separately to each brain region (e.g., data from one brain region might be included for the session if it met the criteria, but the other brain region would be excluded if it did not). Brain region decoding outputs were also calculated separately. To build our encoding model, we used only periods within a behavioral trial (excluding the intertrial interval) and only periods in which the animal's speed was above the movement threshold. We used both correct and incorrect trials but only trials in which there was no update cue. Feature tuning curves were computed by calculating the number of spikes per feature bin ($n = 50$ bins for all features) and normalizing for occupancy time. For decoding, we used 25ms when analyzing decoding by individual theta phase and 200ms windows otherwise. To perform the decoding calculations, we used the Pynapple (Viejo et al., 2022) analysis package using a uniform prior. In a subset of our analyses, we used all trial types (delay only, switch, and stay trials) to build our encoding model as a control. To validate our decoding output, we built the encoding model using 80% of the data and held out a test set of 20% of the data to confirm decoding accuracy across the virtual reality environment.

To calculate representational changes around the update cue, we integrated the posterior probability densities for the initial choice arm and new choice arm based on the boundaries defined by our track graph used for track linearization. We calculated decoding error as the difference between the predicted and actual position. For some analyses, we converted the

decoding output into terms of probability density / chance (Saleem et al., 2018; Sarel et al., 2022), where chance was defined as a uniform representation across all spatial bins. This probability density / chance value was obtained by multiplying the probability density function by a uniform constant of $1 / \text{the number of spatial bins}$. With this output, a value of 1 indicates that the decoding output of that bin is the amount expected if all locations were uniformly represented and no location was represented more than others. A value equal to the number of spatial bins would indicate the maximum likelihood of the bin being represented.

To quantify the changes in prospective goal coding around the update cue, we calculated the average integrated decoding output value in the 0 to 1.5 second window after the update cue was presented to compare relative amounts of prospective coding between trial types. We also quantified the difference in initial and new goal representation on a trial-by-trial basis to compare relative amounts of initial and new goal representations between trial types. For analyses in which we quantified differences in goal coding preceding the update cue onset, we used the -1.5 to 0 second window as our baseline.

To assess how choice commitment affected neural representations around the update cue, we obtained the view angle value at the time of the update cue onset for each trial. We then split this view angle data into quartiles and with these separately grouped trial types, used the same time windows and quantification analysis described above to calculate the average responses.

2.5.9 Theta cycles and phase

For each session, we identified a channel as the putative pyramidal channel in CA1 using sharp-wave ripple power as described above. This channel was used as our LFP recording site. To isolate hippocampal theta oscillations, the LFP was bandpass filtered for theta (4-12 Hz) using an FIR (finite impulse response) equiripple filter. Peaks and troughs of the filtered LFP were detected

and used to define the phase of the LFP. In order to use a common theta reference across recording sessions, we calculated a phase histogram of all putative pyramidal cell spiking activity in CA1 for a recording session using 30-degree bins. We then adjusted the theta phase measurement to be 0 degrees at the location of maximal CA1 firing.

To calculate theta phase modulation of goal decoding, we calculated theta phase histograms by identifying the theta phase at the center time of each decoding window and then calculating the integrated posterior probability densities for each theta phase bin for each trial. To compare values across theta, we divided the theta oscillation into quarters and calculated the average decoding output value for each quarter of the theta oscillation.

2.5.10 Prediction of behavioral choice

For prediction of animal's final choice using neural activity, we performed a trial-by-trial classification analysis using support vector machines (SVMs). For each region and update trial type, we trained independent SVMs. For each trial, we used the quantification of goal representation difference between the initial and new goal as described above as a feature ($n=1$, initial – new) to predict the animal's final choice ($k = 2$, correct or incorrect). Before training the classifier, we balanced the correct and incorrect trial classes using random resampling with replacement until both target classes had the same number of trials. We used a radial basis function (Gaussian) kernel for all SVMs, and we selected the hyperparameters (C and γ) using a random search method with leave one out cross-validation to prevent overfitting. After performing the random search over $n=10$ iterations to optimize classification accuracy, the best hyperparameters were selected. These hyperparameters were then used and a leave-one-out cross validation procedure was used to assess the overall accuracy of the classifier (percentage of trials correctly classified). This randomized hyperparameter search and final accuracy assessment were performed separately for each update trial type. As a control, the randomized

search and cross validation were also performed with randomly shuffled target (choice) labels $n=100$ times. The significance of the classifier was assessed by testing whether the classifier outperformed 95% of the distribution of accuracies from the shuffled classifier (permutation test).

2.5.11 Statistical analyses

We used a linear mixed-effects models approach to assess the significance of differences while controlling for repeated measures from the same animals and sessions. In our model, our variables of interest such as decoding output or single unit firing rates were included as our fixed effects. We set our random effects as session-nested-in-animal random effects with random intercepts at both levels. Statistical significance was first estimated with a Type III ANOVA with Satterthwaite methods to determine whether the predictors had any significant effect. If the F-test was statistically significant, we then performed pairwise comparisons to assess significant differences using estimated marginal means and reported Tukey-adjusted p-values. For one-sample analyses, we used a Wilcoxon signed rank test. For correlation analyses, we calculated the spearman rank-order correlation coefficient. Details on specific statistical parameters and the values of sample size n are described in the figure legends and statistical table (**Table 2.2**).

Analyses were performed using custom pipelines in Matlab, Python, and R with the following libraries: NumPy, SciPy, Matplotlib, Scikit-learn, Pandas, Tensorflow, Pynapple, nwbwidgets, pynwb, seaborn, track-linearization, pingouin, lmer, lmerTest, emmeans, SHARP-Track.

2.6 Supplementary Figures and Tables

Animal	Total sessions	Medial prefrontal cortex approximate* locations	Hippocampal CA1 approximate* locations	Single units**	Behavioral trials***
S17	8	Prelimbic area layer 6a: A/P: 2.02, D/V: 2.94, M/L: -0.75 A/P: 2.0, D/V: 2.89, M/L: 0.8, Anterior cingulate area dorsal part layer 6a: A/P: 2.02, D/V: 2.52, M/L: -0.77 A/P: 1.91, D/V: 2.64, M/L: 0.99	A/P: -1.8, D/V: 1.7, M/L: 1.68 A/P: -2.1, D/V: 1.87, M/L: -1.37 A/P: -2.1, D/V: 1.84, M/L: -1.49	Total: 646 mPFC: 247 CA1: 399	Total: 591 Switch: 114 Stay: 48 Delay: 429
S20	12	Anterior cingulate area ventral part layer 5: A/P: 1.38, D/V: 3.41, M/L: -0.38 A/P: 1.36, D/V: 2.68, M/L: -0.58	A/P: -2.45, D/V: 1.63, M/L: -1.26 A/P: -2.46, D/V: 1.6, M/L: -1.35	Total: 977 mPFC: 272 CA1: 705	Total: 1689 Switch: 303 Stay: 117 Delay: 1269
S25	10	Prelimbic area layer 6a: A/P: 1.63, D/V: 3.05, M/L: -0.74 Prelimbic area layer 2/3: A/P: 1.62, D/V: 2.89, M/L: 0.25 Prelimbic area layer 1: A/P: 1.62, D/V: 2.74, M/L: 0.15	A/P: -2.12, D/V: 1.53, M/L: 1.49 A/P: -2.13, D/V: 1.4, M/L: 1.59	Total: 906 mPFC: 286 CA1: 620	Total: 2244 Switch: 421 Stay: 189 Delay: 1634
S28	12	Slices damaged	Slices damaged	Total: 1262 mPFC: 613 CA1: 649	Total: 2361 Switch: 390 Stay: 133 Delay: 1838
S29	12	Slices damaged	A/P: -1.78, D/V: 1.78, M/L: -1.5 A/P: -1.78, D/V: 1.72, M/L: -1.58 A/P: -1.52, D/V: 1.72, M/L: 1.37 A/P: -1.55, D/V: 1.57, M/L: 1.59	Total: 1530 mPFC: 715 CA1: 815	Total: 2308 Switch: 422 Stay: 161 Delay: 1725
S33	6	Infralimbic area layer 6a: A/P: 1.74, D/V: 3.49, M/L: -0.59 Infralimbic area layer 5: A/P: 1.74, D/V: 3.45, M/L: -0.51	A/P: -2.32, D/V: 1.51, M/L: -1.66	Total: 617 mPFC: 178 CA1: 439	Total: 696 Switch: 97 Stay: 42 Delay: 557
S34	7	Infralimbic area layer 6a: A/P: 1.81, D/V: 3.79, M/L: 0.77 A/P: 1.77, D/V: 3.66, M/L: 0.61 A/P: 1.8, D/V: 3.73, M/L: -0.57 A/P: 1.83, D/V: 3.46, M/L: -0.69	A/P: -1.58, D/V: 1.61, M/L: -1.56 A/P: -1.65, D/V: 1.72, M/L: -1.48 A/P: -1.88, D/V: 1.58, M/L: 1.32 A/P: -1.88, D/V: 1.57, M/L: 1.55	Total: 618 mPFC: 309 CA1: 309	Total: 996 Switch: 139 Stay: 52 Delay: 805

Table 2.1 Experimental metadata for all recording sessions.

*Recording locations are approximate and indicate the Dil-identified locations registered to the Allen Common Coordinate Framework and mouse atlas from the last recording session of each animal for that hemisphere. Exact locations varied slightly between sessions due to day-to-day differences in electrode insertions. Hippocampal CA1 locations were also confirmed with electrophysiological signatures (see **Methods**).

Number of units indicates final unit counts after spike sorting, quality curation, and cell type classification (see **Methods).

***Number of trials indicate all completed trials during recording sessions.

Panel	Data	Group size	Statistical method	Comparison	Test statistic	P-value	Notation
Fig. 1B	Proportion correct	N = 67 sessions N = 7 animals	Wilcoxon signed-rank test	Switch trials vs. 50% correct	W-val = 48.5	<0.0001	****
				Stay trials vs. 50% correct	W-val = 100	<0.0001	****
				Delay only trials vs. 50% correct	W-val = 125.5	<0.0001	****
Fig 2D	Hippocampal position decoding; posterior probability density integrated by goal arm	Switch: n = 1337 trials Stay: n = 572 trials Delay only: n = 945 trials	Linear mixed effects model; ANOVA, Tukey post-hoc	Update type, goal arm	F(5668.63) = 16.28	< 0.0001	****
				Switch vs. stay, initial goal	Z = -5.44	< 0.0001	****
				Switch vs. delay only, initial goal	Z = -5.46	< 0.0001	****
				stay vs. delay only, initial goal	Z = 0.74	0.9769	ns
				Switch vs. stay, new goal	Z = -3.27	0.0139	*
				Switch vs. delay only, new goal	Z = -5.28	<0.0001	****
				stay vs. delay only, new goal	Z = -1.17	0.8524	ns
Fig. 2D	Hippocampal position decoding; difference in initial vs. new goal arm posterior probability density	Switch: n = 1337 trials Stay: n = 572 trials Delay only: n = 945 trials	Linear mixed effects model; ANOVA, Tukey post-hoc	Update type	F(2835.45) = 1.199	0.3014	ns
				Switch vs. stay	t(2830.33) = 1.37	0.3178	ns
				Switch vs. delay only	t(2842.43) = 0.01	1.0	ns
				Stay vs. delay	T(2832.89) = 1.37	0.3563	ns
Fig 2D	Hippocampal position decoding; difference in initial vs. new	Switch: n = 57 sessions, Stay: n = 54 sessions, Delay only: n = 57 sessions	Wilcoxon signed-rank test	Switch vs. zero	W = 689	0.2764	ns
				Stay vs zero	W = 519	0.0548	ns
				Delay only vs zero	W = 744	0.5147	ns
Fig. 3D	Hippocampal position decoding; phase modulation	Switch: n = 1337 trials	Linear mixed effects model; ANOVA Tukey post-hoc	Phase and location	F(7966.89) = 20.08	< 0.0001	****
				First half, initial vs. home	Z = -2.86	0.0480	*
				First half, new vs. home	Z = -3.36	0.0103	*
				Second half, initial vs. home	Z = 6.51	< 0.0001	****
				Second half, new vs. home	Z = 8.72	< 0.0001	****
Fig. 3D	Hippocampal position decoding; phase	Switch: n = 1337 trials	Linear mixed effects model; ANOVA Tukey post-hoc	Pre and post update, location	F(7962.86) = 143.95	< 0.0001	****
				Pre, home vs. post, home	Z = -16.14	< 0.0001	****

	modulation, first half theta			Pre, initial vs. post, initial	Z = 10.19	< 0.0001	****
				Pre, new vs. post, new	Z = 9.94	< 0.0001	****
Fig. 3D	Hippocampal position decoding; phase modulation, second half theta	Switch: n = 1337 trials	Linear mixed effects model; ANOVA Tukey post-hoc	Pre and post update, location	F(7968.02) = 327.23	< 0.0001	****
				Pre, home vs. post, home	Z = -18.18	< 0.0001	****
				Pre, initial vs. post, initial	Z = 10.21	< 0.0001	****
				Pre, new vs. post, new	Z = 8.42	< 0.0001	****
Fig 3.	Hippocampal position decoding; phase modulation	Switch: n = 1337 trials; Stay: n = 571 trials; delay only: n = 946 trials	Linear mixed effects model; ANOVA Tukey post-hoc	Update type, new	F(5667.30) = 15.14	< 0.0001	****
				Switch vs. delay only, first half	Z = -5.47	< 0.0001	****
				Switch vs. delay only, second half	Z = -4.91	< 0.0001	****
				Stay vs. delay only, first half	Z = -1.48	0.6762	ns
				Stay vs. delay only, Second half	Z = -2.64	0.0870	ns
				Switch vs. stay, first half	Z = -3.09	0.0245	*
				Switch vs. stay, second half	Z = -1.38	0.7376	ns
				Fig. 4F	Prefrontal choice decoding; posterior probability density integrated by goal arm	Switch: n = 1151 trials, Stay: n = 504 trials, Delay only: n = 817 trials	Linear mixed effects model; ANOVA, Tukey post-hoc
Switch vs. stay, initial goal	z = 6.80	< 0.0001	****				
Switch vs. delay only, initial goal	z = 12.69	< 0.0001	****				
stay vs. delay only, initial goal	Z = 3.87	0.0015	**				
Switch vs. stay, new goal	Z = -3.49	0.0065	**				
Switch vs. delay only, new goal	Z = -5.85	< 0.0001	****				
stay vs. delay only, new goal	Z = -1.45	0.6968	ns				
Fig. 4F	Prefrontal choice decoding; Difference in initial vs. new goal arm posterior probability density	Switch: n = 1151 trials, Stay: n = 504 trials, Delay only: n = 817 trials	Linear mixed effects model; ANOVA, Tukey post-hoc	Update type	F(2453.08) = 78.97	< 0.0001	****
				Switch vs. stay	T(2447.23) = 6.93	< 0.0001	****
				Switch vs. delay only	T(2460.12) = 12.27	< 0.0001	****
				Stay vs. delay	T(2450.81) = 3.42	0.0018	**

Fig. 5C	Hippocampal position decoding; posterior probability density integrated by goal arm	Switch, correct: n = 1337 trials, Switch, incorrect: n = 411 trials	Linear mixed effects model; ANOVA, Tukey post-hoc	Trial type	F(3468.55) = 6.12	0.0004	***
				Correct vs. incorrect, initial goal	Z = 1.32	0.5475	ns
				Correct vs. incorrect, New goal	Z = 4.12	0.0002	***
Fig. 5C	Hippocampal position decoding; difference in initial vs. new goal arm posterior probability density	Switch, correct: n = 1337 trials, Switch, incorrect: n = 411 trials	Linear mixed effects model; Tukey post-hoc	Correct vs. incorrect, initial vs. new	T(1746.41) = -0.87	0.3831	ns
Fig. 5D	Prefrontal choice decoding; posterior probability density integrated by goal arm	Switch, correct: N = 1151 trials, switch, incorrect: n = 363 trials	Linear mixed effects model; ANOVA, Tukey post-hoc	Trial type	F(3001.87) = 20.03	< 0.0001	****
				Correct vs. incorrect, initial goal	Z = -5.06	< 0.0001	****
				Correct vs. incorrect, New goal	Z = 5.66	< 0.0001	****
Fig. 5D	Prefrontal choice decoding; difference in initial vs. new goal arm posterior probability density	Switch, correct: N = 1151 trials, switch, incorrect: n = 363 trials	Linear mixed effects model; Tukey post-hoc	Correct vs. incorrect, initial vs. new goal	T = 1512.08	< 0.0001	****
Fig. 5	Prefrontal choice decoding; pre update	Switch, correct: N = 1149 trials, switch, incorrect: n = 363 trials	Linear mixed effects model; ANOVA, Tukey post-hoc	Trial type	F(2997.59) = 35.52	< 0.0001	****
				Correct vs. incorrect, initial goal	Z = -5.29	< 0.0001	****
				Correct vs. incorrect, new goal	Z = 1.29	0.5694	
Fig 5E	Hippocampal position prediction accuracy	Switch: n = 1512 trials, n = 100 shuffles	Permutation test	Switch pre update vs. shuffled trials	N/A	< 0.0001	****
				Switch post update vs. shuffled trials	N/A	<0.0001	****
Fig 5E	Prefrontal choice	Switch: n = 1748 trials, n	Permutation test	Switch pre update vs. shuffled trials	N/A	< 0.0001	****

	prediction accuracy	= 100 shuffles		Switch post update vs. shuffled trials	N/A	< 0.0001	****
--	---------------------	----------------	--	--	-----	----------	------

Table 2.2 Statistical analysis details.

Details for all statistical comparisons. Statistical significance abbreviations: ns (not significant) $P > 0.05$, $*P < 0.05$, $**P < 0.01$, $***P < 0.001$, $****P < 0.0001$. Linear mixed effects models were generated using nested random effects for animal and recording session levels.

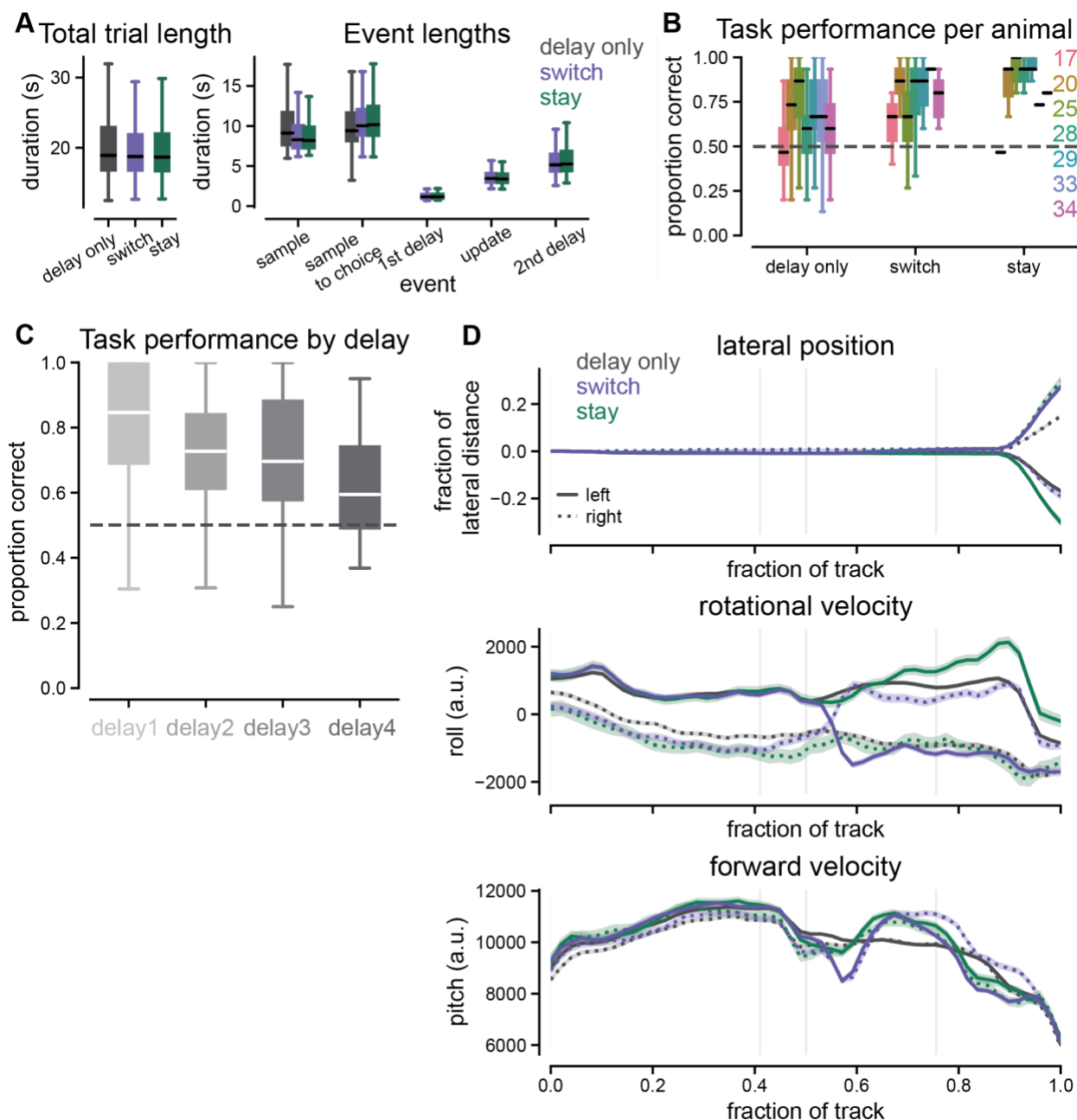


Figure 2.7. Additional update task behavioral metrics and task details.

- A.** Durations of events during behavioral task across trial types. Left, total trial duration from original cue onset to choice being made (Delay only: black, switch: purple, stay: green). (delay only: 20.93 ± 0.09 seconds, $n = 7313$ trials, percentiles = 12.48, 16.83, 18.92, 22.89, 259.97, stay: 20.44 ± 0.23 seconds, $n = 742$ trials, percentiles = 12.70, 16.72, 18.68, 21.98, 98.19, switch: 20.79 ± 0.23 seconds, $n = 1886$ trials, percentiles = 12.66, 16.81, 18.76, 21.86, 240.23). Right, durations for different cue phases of the task across trial types. Original cue to choice indicates period from original cue offset until choice made, equivalent to the duration of the delay phase for delay only trials.
- B.** Performance across trial types by individual animal during recording sessions.

- C.** Performance for delay only trials across different delay duration. Different durations of the delay occurred during the warmup training at the start of each session.
- D.** Trajectories of additional behavioral metrics across trial types (Delay only: black, switch: purple, stay: green). Note that the lateral position is restricted to a very small distance for the stem of the environment.

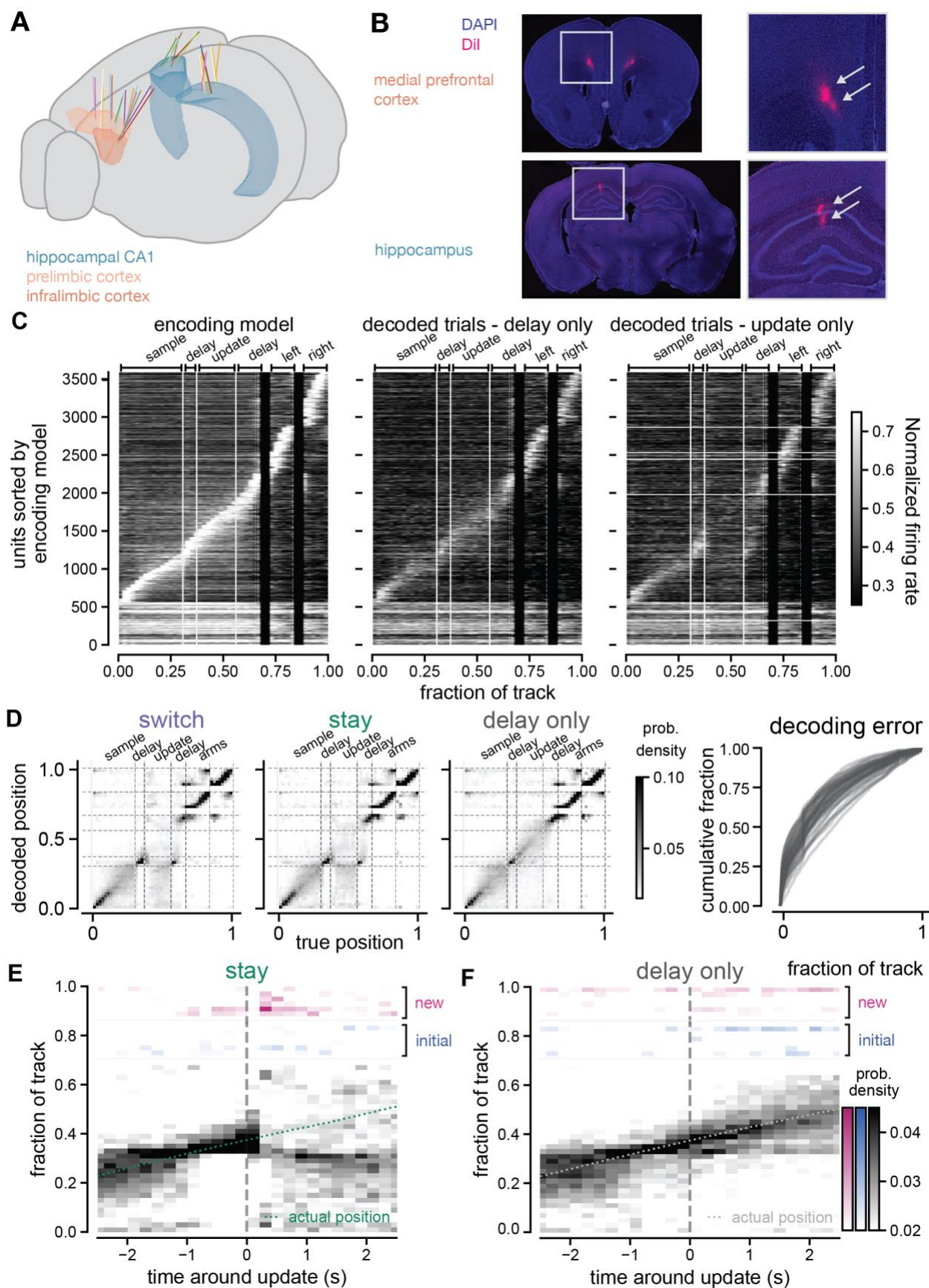


Figure 2.8 Recording location details and Bayesian decoding validation for hippocampal position

- A.** Reconstructed electrode insertion paths from histological data registered to Allen mouse atlas. Each line indicates a separate electrode shank or probe if individual shanks could not be isolated. Hippocampal CA1, prelimbic cortex, and infralimbic cortex regions highlighted.
- B.** Example histological images showing electrode locations (probe dipped in Dil on last recording day) in brain (cells stained with DAPI to visualize structure).
- C.** Tuning curves for position of all units from hippocampal CA1. Left, tuning curves built from encoding model for Bayesian decoder (80% of the delay only trials). Middle, tuning curves from decoded delay only trials (20% of delay only trials). Right, tuning curves from decoded update trials. Units are sorted by place field peak location from the encoding model, bottom units have no significant place fields.
- D.** Confusion matrices (decoded position from hippocampal neural activity compared to actual position from behavioral data) for all decoded trials. *From left to right*, switch, stay, and delay only trials. Dashed lines indicate locations in the environment. *Far right*, Decoding error distributions for each recording session, error calculated as absolute difference between true and peak decoded position.
- E.** Decoding output (probability density) before and after the update cue is presented on stay trials, average for all recording sessions. Heatmap indicates stronger likelihood of those position being decoded by the spiking activity of all hippocampal neurons. Animals actual position (purple dashed line) shown over the same time window.
- F.** Same as **E** for delay only trials

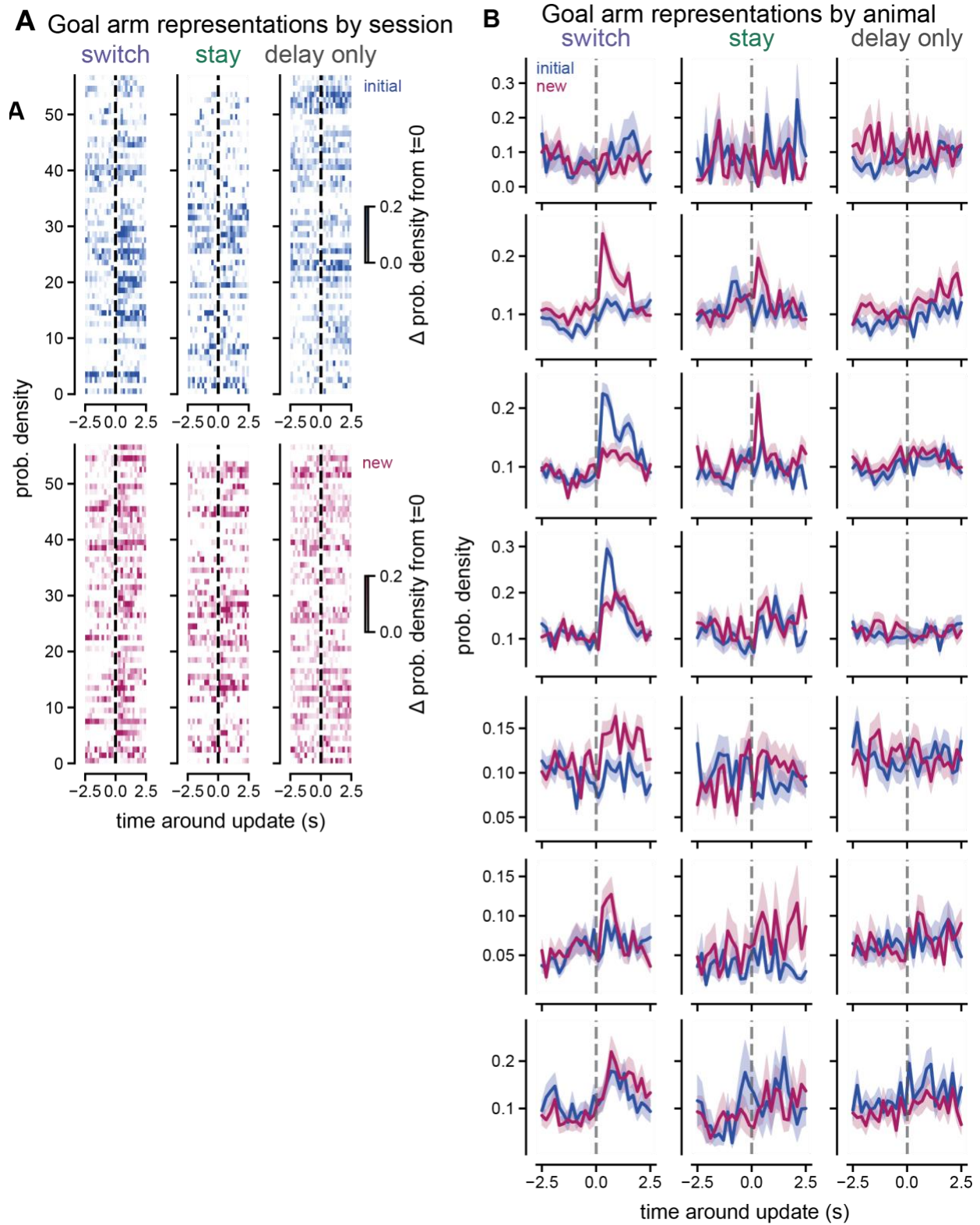


Figure 2.9. Individual session and animal breakdown of hippocampal position codes around the update cue

- A.** Integrated probability densities of the new (pink) and initial (blue) goal arms around the update cue on switch, stay, and delay only trials for individual sessions.
- B.** Same as **B** for individual animals. Each row is the average for an individual animal across switch, stay, and delay only trials.

Figure 2.10. Bayesian decoding validation of position representation for prefrontal cortex

- A.** Tuning curves for position of all units from medial prefrontal cortex. Left, tuning curves built from encoding model for Bayesian decoder (80% of the delay only trials). Middle, tuning curves from decoded trials (20% of delay only trials). Right, tuning curves from decoded update trials.
- B.** *Left*, Confusion matrix (decoded position from prefrontal neural activity compared to actual position from behavioral data) for all decoded trials by switch, stay, and delay only trials. *Right*, cumulative distribution of decoding errors where error is measured as the absolute difference between the actual position and the peak decoding position.
- C.** Decoding output (probability density) before and after the update cue is presented on switch trials, average for all recording sessions. Heatmap indicates stronger likelihood of those position being decoded by the spiking activity of all prefrontal cortex neurons. Animals actual position (purple dashed line) shown over the same time window.
- D.** Integrated probability densities of the new (pink) and initial (blue) goal arms around the update cue on switch, stay, and delay only trials.
- E.** Left, quantification of probability density differences from baseline (value of bin immediately preceding cue onset). Right, quantification of difference between initial and new probability densities after the update cue.

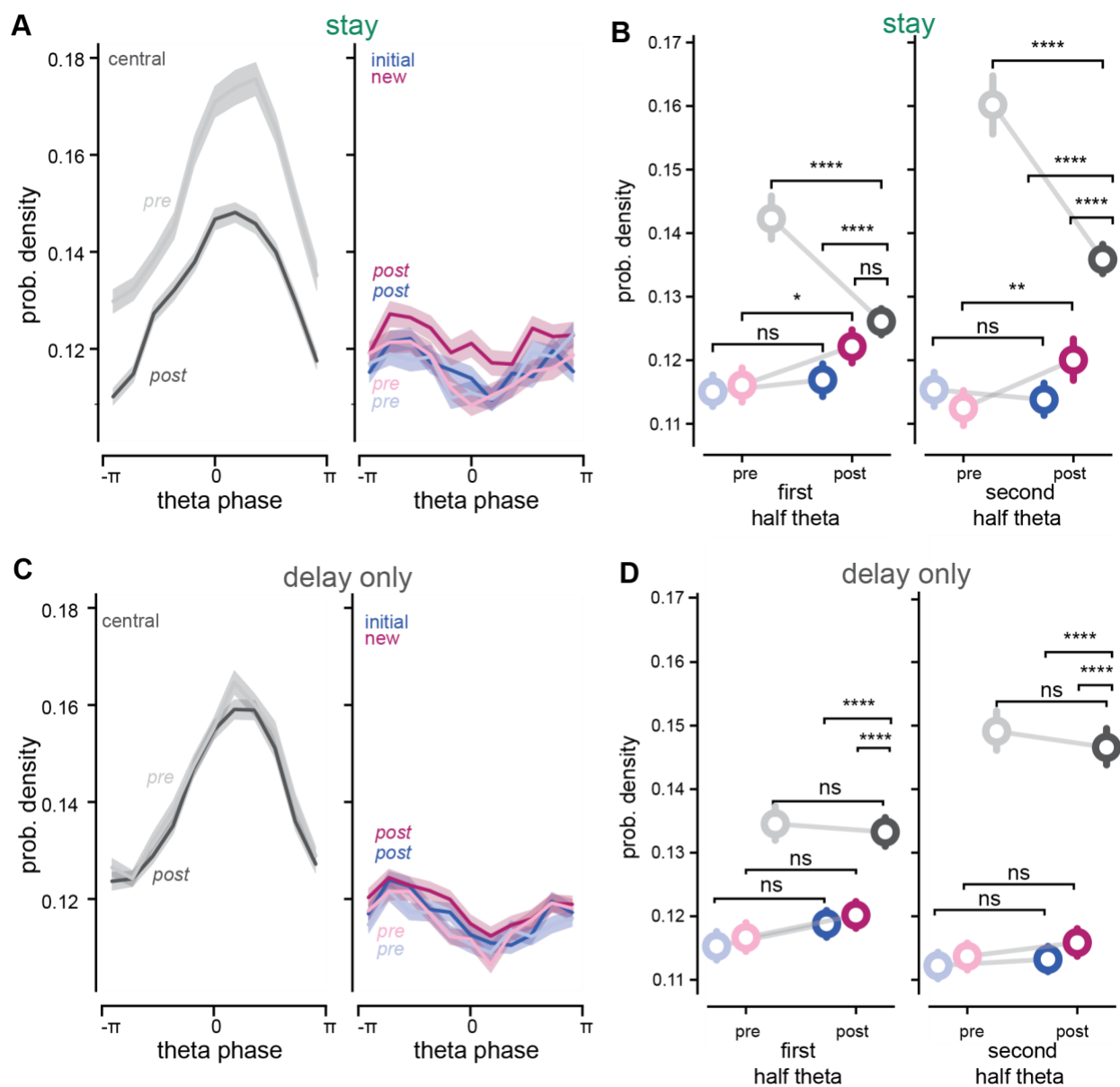


Figure 2.11 Theta phase modulation of position representations for stay and delay only trials

- Average decoded goal arms (pink: new, blue: initial) and central arm (black) posterior probability densities by theta phase pre (-1.5 to 0 seconds) and post (0 to 1.5 seconds) the update cue onset for stay, and delay only trials. Mean \pm SEM across all trials shown. Pre-cue shown in lighter shades, post cue shown in darker shades. *Right*, as in left for initial and new arms.
- Quantification of pre (-1.5 to 0 seconds, on left) and post (0 to 1.5 seconds, on right) probability density around the update cue onset for stay trials. *Left*, first half of theta cycle. *Right*, second half of theta cycle.
- As in **A** for delay only trials
- As in **B** for delay only trials

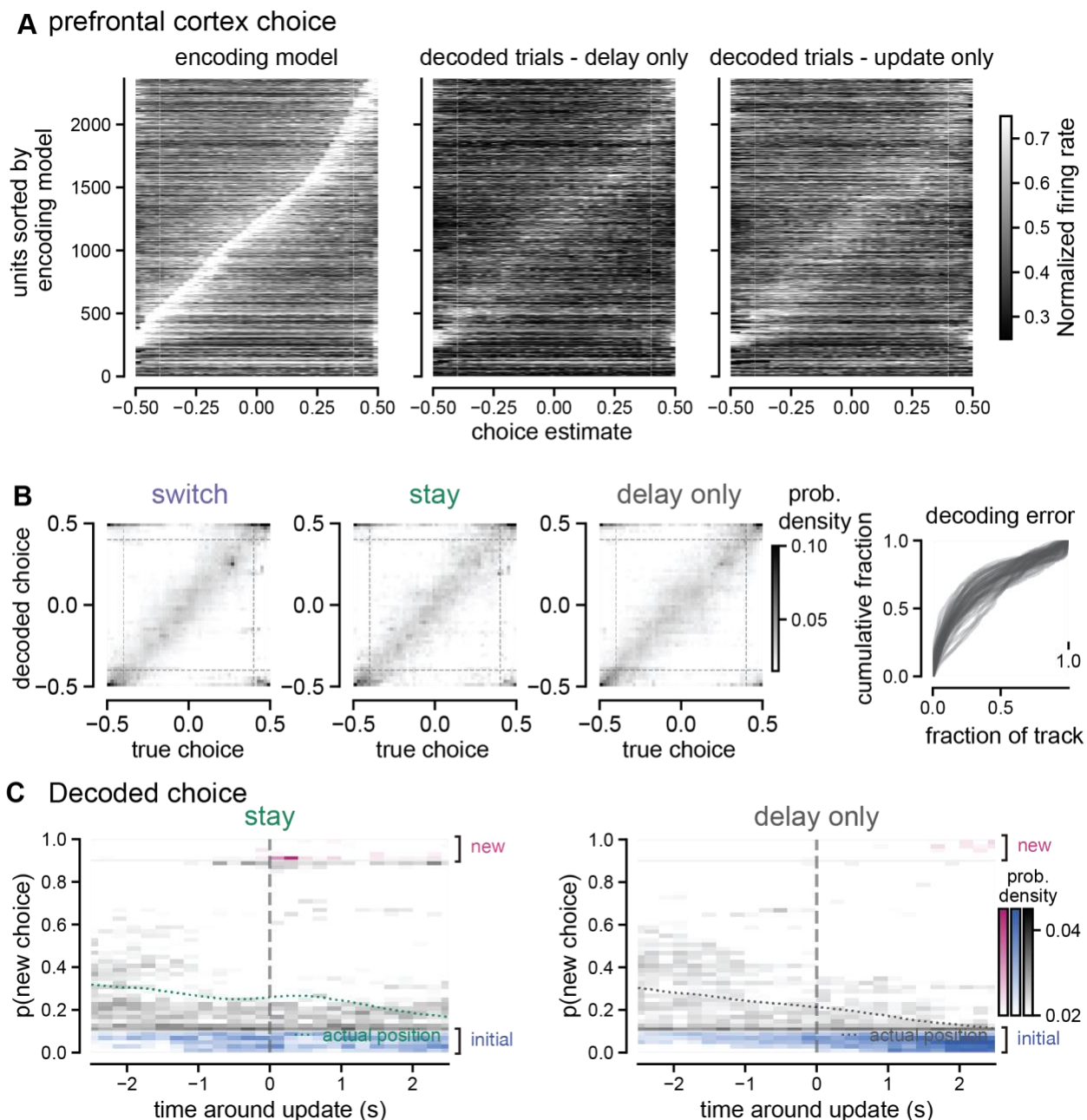


Figure 2.12 Bayesian decoding validation of choice representation and additional controls.

- A.** Tuning curves for choice of all units from medial prefrontal cortex. Left, tuning curves built from encoding model for Bayesian decoder (80% of the delay only trials). Middle, tuning curves from decoded trials (20% of delay only trials). Right, tuning curves from decoded update trials.
- B.** *Left*, Confusion matrix (decoded choice from prefrontal neural activity compared to actual choice estimate from behavioral data) for all decoded trials by switch, stay, and delay only trials. *Right*, cumulative distribution of decoding errors where error is measured as the absolute difference between the actual position and the peak decoding position.

- C. Bayesian decoding output around the update cue for estimated choice commitment representations in prefrontal cortex. Stay trials on left and delay only trials on right.

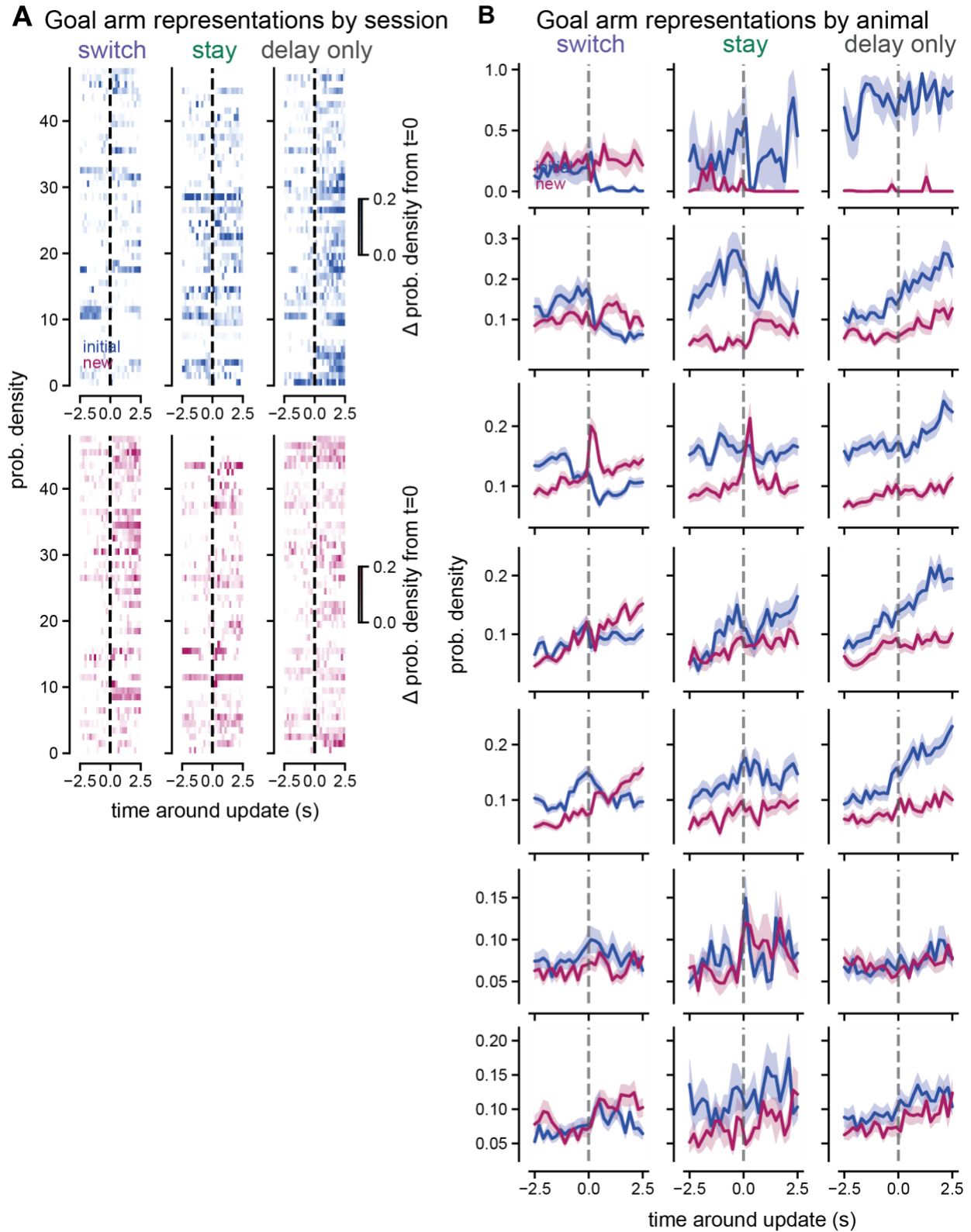


Figure 2.13 Individual session and animal breakdown of prefrontal cortex choice codes around the update cue

- A.** Integrated probability densities of the new (pink) and initial (blue) goal arms around the update cue on switch, stay, and delay only trials for individual sessions.
- B.** Same as **B** for individual animals. Each row is the average for an individual animal across switch, stay, and delay only trials.

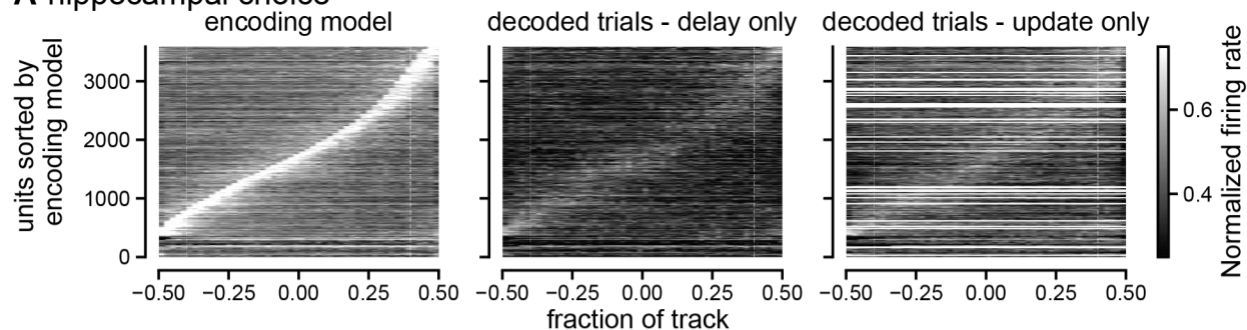
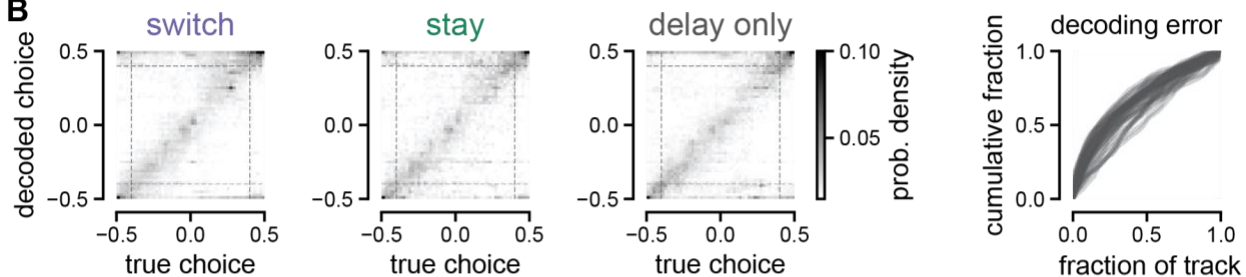
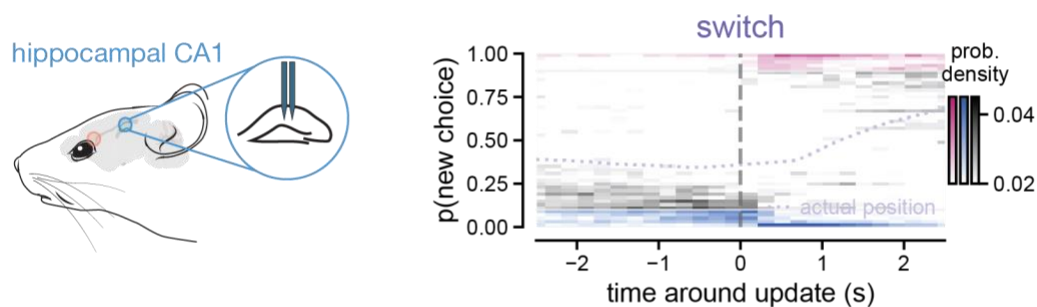
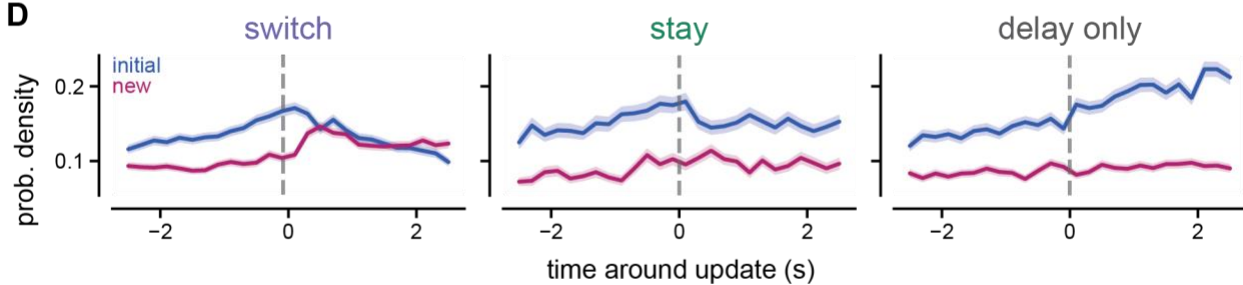
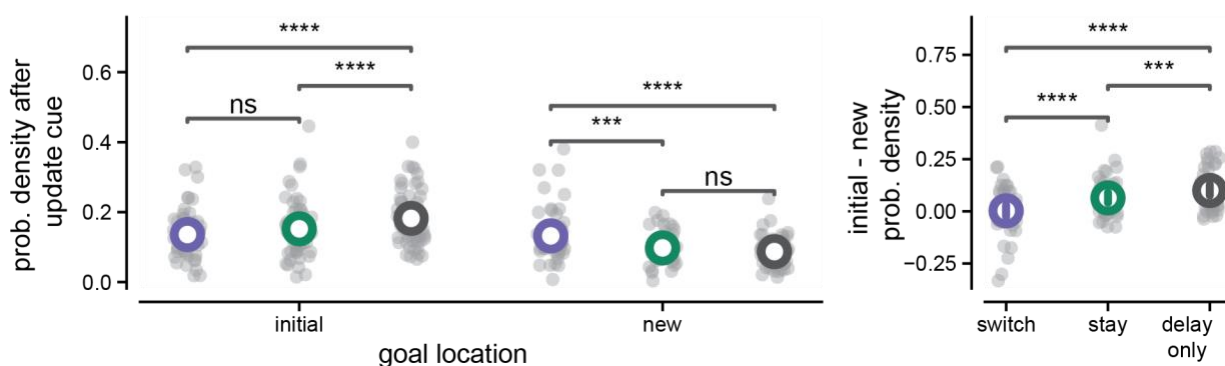
A hippocampal choice**B****C Decoded position****D****E Goal representation quantification**

Figure 2.14. Bayesian decoding of choice representation in hippocampus.

- A. Tuning curves for choice of all units from hippocampus. Left, tuning curves built from encoding model for Bayesian decoder (80% of the delay only trials). Middle, tuning curves from decoded trials (20% of delay only trials). Right, tuning curves from decoded update trials.
- B. *Left*, Confusion matrix (decoded choice from hippocampal neural activity compared to actual choice estimate from behavioral data) for all decoded trials by switch, stay, and delay only trials. *Right*, cumulative distribution of decoding errors where error is measured as the absolute difference between the actual position and the peak decoding position.
- C. Bayesian decoding output around the update cue for estimated choice commitment representations on switch trials in hippocampus.
- D. Integrated probability densities of the new (pink) and initial (blue) choice estimates around the update cue on switch, stay, and delay only trials. Mean \pm SEM shown. Integrations were performed for a subset of “high commitment” decoding outputs, i.e. the highest 10% of all choice commitment values for either choice.
- E. *Left*, quantification of probability density values after the update cue. *Right*, initial vs. new probability density values after the update cue.

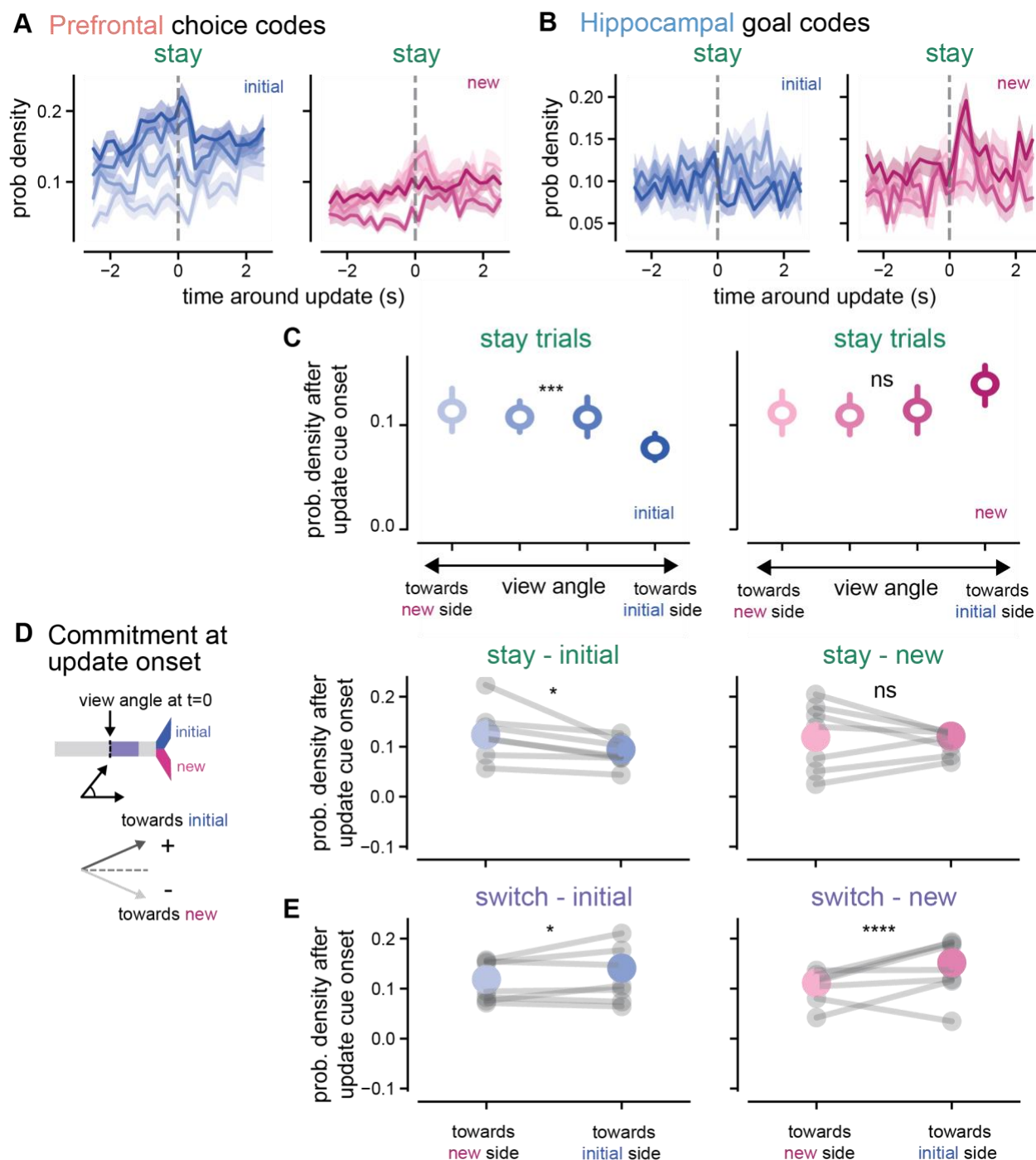


Figure 2.15. Choice commitment breakdown of decoding outputs across trial types

- Prefrontal cortex codes with trials binned by choice commitment quartiles for stay trials. *Left*, initial goal representation, *Right*, new goal representation.
- As in **B** for hippocampal goal location codes on stay trials
- Average probability density after the update across all view angle quartiles and separated by positive view angle values (committed to the new side) and negative view angle values (committed to the initial side). *Left*, initial goal representations in hippocampus in blue. *Right*, new goal representations in hippocampus in pink

- D. Average probability density separated into all trials towards the initial side vs. all trials towards the new side on stay trials. *Left*, initial goal representations, *right*, new goal representations.
- E. As in **D** for switch trials.

**CHAPTER 3 - ALZHEIMER'S PATHOLOGY CAUSES IMPAIRED INHIBITORY
CONNECTIONS AND REACTIVATION OF SPATIAL CODES DURING SPATIAL
NAVIGATION**

This chapter has been reproduced from publication with minor edits:

Prince, S. M., Paulson, A. L., Jeong, N., Zhang, L., Amigues, S., & Singer, A. C. (2021). *Alzheimer's pathology causes impaired inhibitory connections and reactivation of spatial codes during spatial navigation.* *Cell reports*, 35(3), 109008.
<https://doi.org/10.1016/j.celrep.2021.109008>

Abstracts presented from this work:

Prince SM, Paulson AL, Jeong N, Amigues SM, Singer AC. (2019) *Inhibitory connections are disrupted during spatial navigation in the 5XFAD mouse model of Alzheimer's disease.* *Society for Neuroscience. Poster Presentation.*

Prince SM, Paulson AL, Zhang L, Attokaren MK, Amigues S, Tipton JH, Singer AC. (2019) *Disrupted Monosynaptic Connections May Underlie Sharp-Wave Ripple Deficits in the 5XFAD Mouse Model of Alzheimer's Disease.* *Emory University Graduate Division of Biological and Biomedical Sciences Student Research Symposium. Poster Presentation.*

Prince SM, Paulson AL, Zhang L, Attokaren MK, Amigues S, Tipton JH, Singer AC. (2018) *CA1 Neural Activity During Spatial Navigation In The 5XFAD Mouse Model of Alzheimer's Disease.* *Society for Neuroscience. Poster Presentation.*

Prince SM, Paulson AL, Zhang L, Attokaren MK, Amigues S, Tipton JH, Singer AC. (2018) *CA1 Neural Activity During Spatial Navigation In The 5XFAD Mouse Model of Alzheimer's Disease.* *Biomedical Engineering Society Annual Meeting. Poster Presentation.*



Figure 3.1 Cover image illustration of findings on neural activity in Alzheimer's disease

This image is an artistic representation of the neural activity deficits we observe in a mouse model of Alzheimer's disease (AD). On the healthy side of the tree, flowers represent interneurons and pyramidal cells that are connected and strong. On the diseased side of the tree, the flowers have blown away, relating to our finding that interneuron to pyramidal connections are weaker in a mouse model of AD. The branches also represent sharp-wave ripple oscillations, thought to be important to memory, during which we observe these connection strength and other deficits. Art by Annie Stuart.

3.1 Abstract

Synapse loss and altered synaptic strength are thought to underlie cognitive impairment in Alzheimer's disease (AD) by disrupting neural activity essential for memory. While synaptic dysfunction in AD has been well characterized in anesthetized animals and in vitro, it remains unknown how synaptic transmission is altered during behavior. By measuring synaptic efficacy as mice navigate in a virtual reality task, we find deficits in interneuron connection strength onto pyramidal cells in hippocampal CA1 in the *5XFAD* mouse model of AD. These inhibitory synaptic deficits are most pronounced during sharp-wave ripples, network oscillations important for memory that require inhibition. Indeed, *5XFAD* mice exhibit fewer and shorter sharp-wave ripples with impaired place cell reactivation. By showing inhibitory synaptic dysfunction in *5XFAD* mice during spatial navigation behavior and suggesting a synaptic mechanism underlying deficits in network activity essential for memory, this work bridges the gap between synaptic and neural activity deficits in AD.

3.2 Introduction

3.2.1. Synaptic dysfunction in Alzheimer's disease

Alzheimer's disease (AD) is the most common form of dementia and is associated with neural dysfunction from the level of synapses to networks. Synaptic dysfunction is thought to be key to the pathogenesis of AD because synaptic loss is one of the best correlates of cognitive impairment in the disease (DeKosky & Scheff, 1990; Selkoe, 2002; Terry, 2000; Terry et al., 1991). Several studies have shown that amyloid beta, one of the pathogenic proteins that accumulate in AD, affects synaptic transmission (Abramov et al., 2009; Bero et al., 2011; Chapman et al., 1999; Freir et al., 2017; Hsia et al., 1999; Puzzo et al., 2008; Stéphan et al., 2001; Walsh et al., 2002). Together these findings have led to the hypothesis that elevated levels of amyloid beta cause synaptic dysfunction, which disrupts neural activity essential for memory and ultimately leads to cognitive decline (Palop & Mucke, 2010). However, prior work examining synaptic dysfunction in animal models of AD was conducted in vitro or in anesthetized animals; these prior studies have not investigated synaptic changes in awake, behaving animals. Neural activity is much less dynamic in anesthetized animals (Constantinople & Bruno, 2011; Steriade et al., 2001), and anesthesia drastically alters synaptic excitation and inhibition (Haider et al., 2013). Thus, because amyloid beta influences synaptic transmission and is influenced by neural activity, it is important to study synaptic function in AD in awake animals during behavior.

3.2.2. Deficits in neural activity across multiple models of Alzheimer's disease

Synaptic activity alterations caused by AD pathology are thought to disrupt neural activity that is essential for memory. In the *5XFAD* mouse model, a well-established amyloid model of AD with five human familial AD mutations (Oakley et al., 2006), synaptic loss increases with age and synaptic transmission in vitro is correlated with memory deficits (Kimura & Ohno, 2009; Oakley et al., 2006). *5XFAD* and *apoE4* mouse models display a decreased abundance of sharp-wave ripple (SWR) events in hippocampus (Gillespie et al., 2016; Iaccarino et al., 2016; E. A. Jones et

al., 2019). These SWRs, high-frequency oscillations accompanied with bursts of population activity, are of particular interest because they are important for cognitive processes such as learning and memory (Buzsáki, 2015; Carr et al., 2011; Girardeau et al., 2009; Girardeau & Zugaro, 2011; Jadhav et al., 2012; Pfeiffer & Foster, 2013; Singer et al., 2013), and they are generated in the hippocampus, one of the first regions affected in AD (Braak & Braak, 1991). Several studies have shown disrupted synapses in vitro or in post-mortem tissue, as well as deficits in neural activity associated with memory (Leung et al., 2012; Li et al., 2009). It is thought that these synaptic deficits lead to deficits in neural activity because excitatory and inhibitory interactions are important for generating the neural activity that is lacking in AD, such as SWR events. However, it remains unknown how synaptic activity is disrupted in awake, behaving animals, whether excitatory or inhibitory disruptions predominate, and if synaptic deficits occur during patterns of abnormal neural activity, such as SWRs.

Given the hypothesized role of synaptic dysfunction in AD, we asked whether excitatory and inhibitory synaptic connections were disrupted in an awake, behaving mouse model of AD. We hypothesized that *5XFAD* mice would have deficits in excitatory and inhibitory synaptic transmission based on prior work showing spine density loss of pyramidal cells in post-mortem tissue of *5XFAD* mice and interneuron vulnerability in multiple mouse models of AD (Crowe & Ellis-Davies, 2014; De Pins et al., 2019; Leung et al., 2012; Li et al., 2009; Palop et al., 2007; Verret et al., 2012). We aimed to study neural activity in awake, behaving animals at an age when both behavioral and synaptic deficits were clearly present, thus we examined neural and synaptic deficits in older *5XFAD* mice (Buskila et al., 2013; Oakley et al., 2006). We recorded spiking activity from many single neurons in CA1 simultaneously as animals licked for reward in a circular track. We show deficits in the connection strength of interneuron inhibition onto pyramidal cells in *5XFAD* mice during behavior, and these deficits are most pronounced during SWRs. Because interactions between interneurons and pyramidal cells play a key role in SWR generation and

maintenance and SWRs are essential for spatial memory, we thought SWR activity might also be affected (Alger & Nicoll, 1982; Buzsáki, 1986; Buzsáki et al., 1983; Csicsvari et al., 1999; Klausberger et al., 2003; Pouille & Scanziani, 2001; Stark et al., 2014; Ylinen, Bragin, et al., 1995). We find deficits in the abundance, duration, and amplitude of SWR activity in *5XFAD* mice. Lastly, we show that place cells in *5XFAD* mice had impaired reactivation during SWRs compared to *WT* littermates. These results reveal in vivo deficits from the level of synapses to neural codes essential for learning and memory in the *5XFAD* mouse model of AD and that these deficits are most pronounced during SWRs, which are essential for spatial learning and memory. This work bridges gaps between synaptic dysfunction and neural activity essential for memory and thus reveals how AD pathology leads to disruption across multiple scales in memory circuits.

3.3. Results

3.3.1. 5XFAD mice and wild-type littermates lick for reward in a virtual reality spatial task

To investigate altered synaptic efficacy and electrophysiological activity during behavior, we designed a virtual reality (VR) spatial navigation task to record neural activity as older *5XFAD* mice and their wild-type littermates (*WT*) navigated through an environment (**Figure 3.2A**). At this age, *5XFAD* mice have well-established deficits in memory performance (Martorell et al., 2019; Oakley et al., 2006). However, in these behavioral tasks, the impaired animals sample the environment differently than intact animals, thus neural activity during these behaviors is confounded by the animals' differences in sampling. Therefore, we characterized neural activity deficits in a simple task that both *5XFAD* mice and their *WT* littermates sampled similarly, as has been done often in studies comparing neural activity in transgenic and *WT* mice with behavioral differences (Dragoi & Tonegawa, 2013; Gillespie et al., 2016; Suh et al., 2013; Verret et al., 2012). In this task, visual cues were displayed on the walls of a virtual reality annular track. Animals ran in a circle around this environment and were trained to lick at specific locations of the track indicated with the visual cues in order to receive a reward of sweetened condensed milk (**Figure 3.2B, Figure 3.7A**). We quantified behavioral metrics important to hippocampal neural activity, including velocity and licking, and found that animals of both genotypes licked in order to trigger a reward early in the reward zone (see **Methods, Figure 3.2C, Figure 3.7B**). Animals also decreased their speed as they approached the reward zones before they received a reward. Both genotypes received rewards on greater than 90% of trials on average, though the *WT* mice had significantly more trials with no rewards, likely due to the differences in lick rates (**Figure 3.2D, Figure 3.7D, F-G**). To confirm that animals were using visual cues to perform the spatial task, we assessed these same behavioral metrics in a circular track with no visual cues after training in the task with visual cues, and we found that miss rate and lick latency until reward significantly increased in the track without cues (**Figure 3.2E-G, Figure 3.7C, E**). We thus demonstrate that

both *5XFAD* and *WT* mice licked for reward in a specific location using visual cues in a VR spatial task.

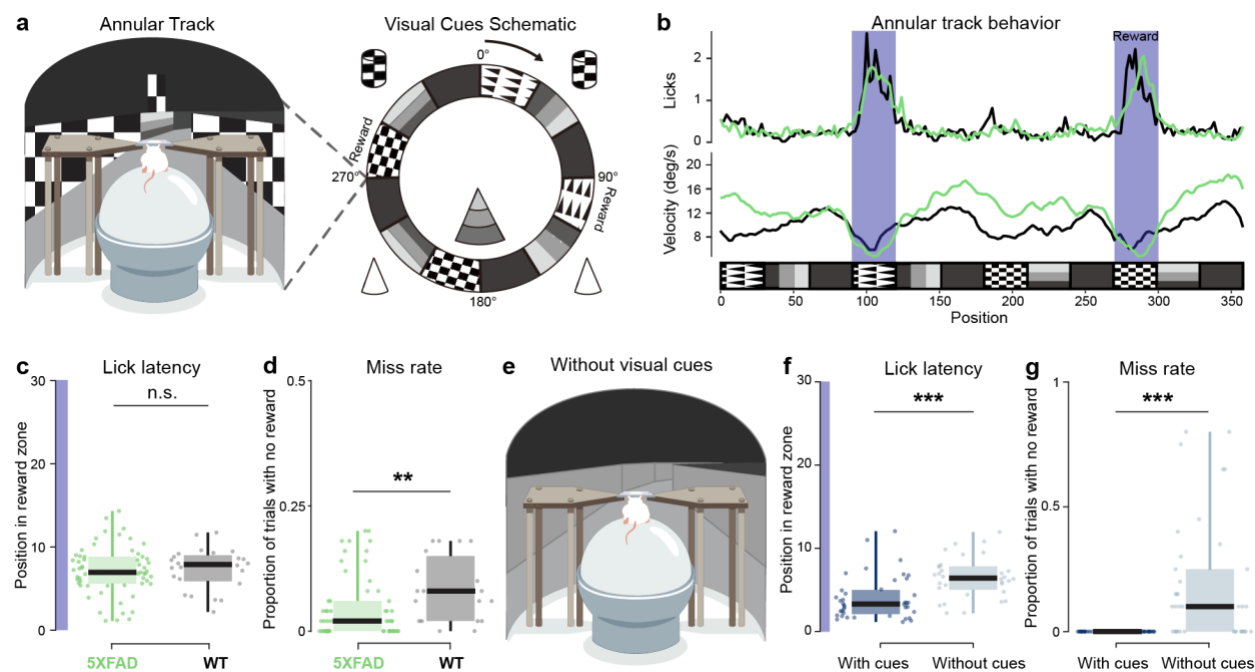


Figure 3.2 *5XFAD* mice and wild-type littermates lick for reward in a virtual reality spatial task.

- A.** Left, schematic of virtual reality experimental set-up. Right, annular track spatial navigation task with local and distal cues.
- B.** Example of lick and velocity rate averaged over 50-trials of *5XFAD* (green) and *WT* (black) mice as a function of position in the annular track. Each trial is considered one lap around the annular track. Reward zones indicated in dark purple.
- C.** Lick latency (position at the first lick after reward zone entry) for 50-trial blocks for all sessions in *5XFAD* (green) and *WT* (black) mice from the start of the reward zone (degree 0) to the end of the reward zone (degree 30) on trials when the animal received a reward. Dot indicates 50-trial block. Purple highlight indicates length of reward zone. *5XFAD*: 7.13 ± 0.72 degrees, $n = 8$ animals, *WT*: 7.38 ± 1.01 degrees, $n = 4$ animals (only including animals with > 50 trials), $\text{prob}(WT \geq 5XFAD) = 0.64$, *5XFAD*: $n = 59$ trial blocks, lick latency percentiles = [1.12, 5.59, 6.95, 8.82, 14.32], *WT*: $n = 24$ trial blocks, lick latency percentiles = [2.19, 6.01, 7.90, 8.91, 11.74].
- D.** Miss rate (number of laps around the annular track with zero rewards received) for 50-trial blocks for all sessions in *5XFAD* (green) and *WT* (black) mice. Each dot indicates a 50-trial-block, *5XFAD*: $4.3\% \pm 1.46\%$ trials with zero rewards, *WT*: $8.4\% \pm 2.72\%$, $\text{prob}(WT \geq 5XFAD) = 0.996$ **, *5XFAD*: $n = 60$ trial blocks, miss rate percentiles = [0 0 0.02 0.060 0.20], *WT*: $n = 19$ trial blocks, miss rate percentiles = [0 0.02 0.08 0.14 0.18].
- E.** Annular track spatial navigation task with visual cues removed.
- F.** As in **C** for track with and without visual cues. Dark blue indicates data from last two sessions in the annular track *with visual cues* and light blue indicates the first two sessions in the

annular track *without visual cues*. Track with cues: *5XFAD*: 5.63 ± 1.37 *WT*: 3.02 ± 0.56 , track without cues: *5XFAD*: 7.65 ± 0.69 , *WT*: 4.99 ± 0.14 , $\text{prob}(\text{with cues} \geq \text{without cues}) < 10^{-4}$ (limit due to resampling 10^4 times) ***, *with visual cues*: *5XFAD*: $n = 3$ animals, lick latency percentiles = [2.46 3.30 4.95 6.94 12.06], *WT*: $n = 3$ animals, lick latency percentiles = [1.14 1.68 2.44 3.50]. *without visual cues*: *5XFAD*: $n = 3$ animals, lick latency percentiles = [6.89 6.97 7.22 7.60 9.56], *WT*: $n = 3$ animals, lick latency percentiles = [3.15 3.58 4.57 6.34 7.48]

- G.** As in **D** for track *with visual cues* (dark blue) versus the track *without visual cues* (light blue) in *5XFAD* and *WT* mice. Track with cues: *5XFAD*: 0 ± 0 , *WT*: 0 ± 0 miss trials, track without cues: *5XFAD*: $34.5\% \pm 0.19\%$ miss trials, *WT*: $40.22\% \pm 0.32\%$ miss trials, $\text{prob}(\text{with cues} \geq \text{without cues}) < 10^{-4}$ (limit due to resampling 10^4 times) ***, *with visual cues*: *5XFAD*: $n = 3$ animals, miss rate percentiles = [0 0 0 0 0], *WT*: $n = 2$ animals, miss rate percentiles = [0 0 0 0 0], *without visual cues*: *5XFAD*: $n = 3$ animals, miss rate percentiles = [6.89 6.97 7.22 7.60 9.56], *WT*: $n = 3$ animals, miss rate percentiles = [3.15 3.58 4.57 6.34 7.47].

Box plot edges indicate quartiles, whiskers indicate range, and black bar indicate median. All percentiles are min, 25th percentile, median, 75th percentile, max. All statistics were performed with a hierarchical bootstrap analysis to determine the direct probability that the resampled mean of *WT* mice is greater than the resampled mean of *5XFAD* mice, in contrast to statistical methods that test whether to reject the null hypothesis. Using this method the probability that *WT* mice have significantly larger resampled means than *5XFAD* mice is indicated by $\text{prob}(WT \geq 5XFAD) > 0.975$, or $\text{prob} > 1 - \alpha/2$ where α is the significance level. The probability that *WT* mice have significantly smaller resampled means than *5XFAD* mice is indicated by $\text{prob}(WT \geq 5XFAD) < 0.025$, or $\text{prob} < \alpha/2$ (see **Methods**). ** indicates $\text{prob} > 0.995$ or $\text{prob} < 0.005$ ($\alpha = 0.01$); *** indicates $\text{prob} > 0.9995$ or $\text{prob} < 0.0005$ ($\alpha = .001$); n.s. indicates not significant throughout

3.3.2. Interneuron-to-pyramidal monosynaptic connections are weaker in *5XFAD* mice

Using this task, we then examined how synapses and neural activity differ between *5XFAD* mice and *WT* littermates. We first focused on whether synaptic efficacy was altered in vivo in *5XFAD* mice. We recorded local field potential (LFP) and single-unit activity of 2,447 neurons (*5XFAD*: 170.38 ± 15.36 single units per animal over multiple sessions, $n = 8$, *WT*: 180.67 ± 17.12 single units per animal, $n = 6$) in hippocampal CA1 of *5XFAD* and *WT* animals (11-14 months) performing the spatial task interleaved with no task periods (see **Methods**, **Figure 3.8**, **Table 3.1**). We assessed neural activity in hippocampal CA1 since it is a major output region of the hippocampal circuit, which is affected early in AD (Braak & Braak, 1991). To assess synaptic connections in awake behaving animals, we used a well-established method of measuring synaptic connectivity and connection strength from extracellular recordings (Alonso et al., 1996; Barthó et al., 2004; Clay Reid & Alonso, 1995; English et al., 2017; Fujisawa et al., 2008; Perkel et al., 1967; Tanaka, 1983; Toyama et al., 2017; Usrey et al., 1999). In this method, putative

monosynaptically connected cell pairs are identified by computing spike train cross-correlations and finding pairs of cells with significant increases or decreases in cross-correlations at time lags consistent with monosynaptic connections: 1-3 ms (see **Methods**). Putative excitatory and inhibitory connections were identified by detecting significant peaks or troughs at a 1-3 ms lag in the cross-correlogram (CCG) compared to the pairs' shuffled CCGs (spike trains jittered on a ± 5 ms timescale, (Diba et al., 2014; Fujisawa et al., 2008), **Figure 3.3A-B, Figure 3.11**). This method preserves the longer timescale temporal dynamics of neural spike trains and thus has the advantage of identifying pairs that have spiking co-occurrences on timescales that cannot be explained by broader firing rate changes. This analysis was performed across all cells recorded in CA1, producing an effectively random sampling of putative monosynaptically connected pairs.

We then determined whether these monosynaptic connections differed between *5XFAD* and *WT* mice by quantifying their connection strength, or functional synaptic efficacy (**Figure 3.3A-B**, see **Methods**). We measured synaptic efficacy during periods with theta oscillations (when animals are running), SWRs, and non-theta periods (when animals are quiescent and SWRs occur) to determine if differences between *5XFAD* and *WT* mice occurred during specific network states. Interestingly, we found that the inhibitory connection strengths of interneurons onto pyramidal cells, that is, the magnitude of the inhibitory troughs, were lower in the *5XFAD* mice compared to their *WT* littermates. This inhibitory connection strength was observed to be 63.16% smaller during SWR periods in *5XFAD* mice (**Figure 3.3C-D, Figure 3.9A**), 43.77% smaller during non-theta periods (**Figure 3.3E-F, Figure 3.9B**), and 38.38% smaller in *5XFAD* mice during theta periods (**Figure 3.3G-H, Figure 3.9C**). Importantly, these changes in connection strength could not be explained by differences in firing rate between genotypes (**Figure 3.3I**). For INT-to-PYR cell pairs, there were no significant differences in firing rate (**Figure 3.3I**). Furthermore, our cross-correlation normalization method controlled for firing rate differences for the specific time periods used in the connection strength analysis (see **Methods**). We controlled for differences in SWR

duration and spike numbers between *5XFAD* and *WT* groups and found the *WT* mice still had larger inhibitory trough magnitudes than the *5XFAD* mice using multiple subsampling approaches (see **Methods**, **Figure 3.9E-F**).

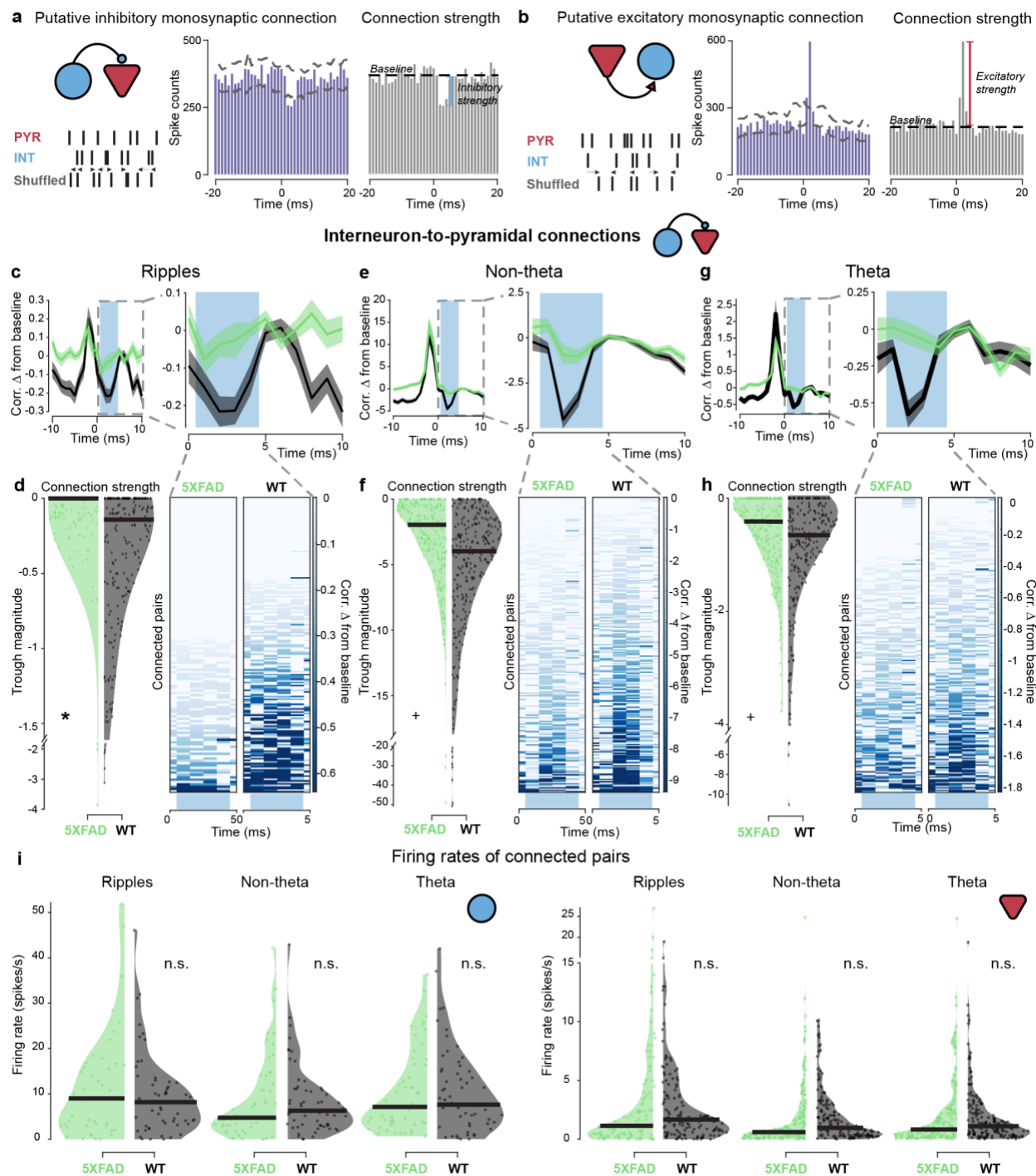


Figure 3.3 Interneuron-to-pyramidal monosynaptic connections are weaker in 5XFAD mice.

- A.** Schematic of monosynaptic connection identification analysis and quantification of inhibitory connection strength. *Left*, connection type and illustration of shuffled spike train controls. *Center*, example of putative interneuron-to-pyramidal (INT-to-PYR) connection with cross-correlation values from -20 to 20 ms lags, and the dashed lines indicating the maximum and minimum values of the cross-correlation of shuffle controls. Connections were identified by a significant trough below the shuffle controls in the 1-3 ms range. *Right*, schematic of inhibitory connection strength: baseline (an average taken outside the 1-4 ms window) minus the trough (minimum value in the 1-4ms window) of the cross-correlogram (CCG).
- B.** As in **A** for excitatory connection strength of a PYR-to-INT connection.
- C.** *Left*, Average CCG of monosynaptically connected INT-to-PYR cell pairs between 5XFAD (green) and WT (black) mice during sharp-wave ripple (SWR) periods from -10 to +10 ms lags normalized by geometric mean firing rate and displayed as difference from baseline, mean \pm SEM. *Right*, zoomed in view of average CCG on *left* from 0 to 10s lag. Light blue box indicates region where connection strength was measured. Inhibitory connection strength was measured as the minimum value in the 1-4ms window. These CCGs that were rectified for the strength measurement are not included in the visualization of the average and individual CCGs. Statistics described in **D**.
- D.** Connection strength as measured by trough magnitude in 5XFAD and WT mice during SWR periods. Each dot indicates the connection strength measured from a single INT-to-PYR cell pair across all SWR periods. *Right*, individual CCGs of putative INT-to-PYR cell connected pairs during SWR periods that make up the average shown above in **C**. Heat map indicates change in correlation from baseline measurement. Note CCGs during SWRs look more variable because there are fewer spikes during-sharp wave ripples than during non-theta and theta periods. The number of spikes included in this figure was 49,649 in 5XFAD mice and 167,402 in WT mice. 5XFAD: -0.14 ± 0.13 trough magnitude, WT: -0.38 ± 0.19 trough magnitude, $\text{prob}(5XFAD \geq WT) = 0.981^*$, here $5XFAD \geq WT$ indicates a deficit in inhibition because inhibitory troughs are negative, 5XFAD: $n = 146$ INT-to-PYR cell pairs, connection strength percentiles = $[-3.86 -0.13 0.00 0.00 0.00]$, WT: $n = 213$ INT-to-PYR cell pairs, connection strength percentiles = $[-3.12 -0.59 -0.14 0.00 0.00]$,
- E.** As in **C** for INT-to-PYR connections during non-theta periods. Statistics described in **F**.
- F.** As in **D** for INT-to-PYR connections during non-theta periods. The number of spikes included in this figure was 12,201,118 in 5XFAD mice and 15,240,501 in WT mice. 5XFAD: -3.25 ± 1.04 trough magnitude, WT: -5.78 ± 2.61 trough magnitude, $\text{prob}(5XFAD \geq WT) = 0.954^+$, 5XFAD: $n = 250$ INT-to-PYR cell pairs, connection strength percentiles = $[-49.17 -4.35 -1.96 -0.59 0.00]$, WT: $n = 249$ INT-to-PYR cell pairs, connection strength percentiles = $[-50.78 -7.46 -3.98 -1.88 0.00]$.
- G.** As in **C** for INT-to-PYR connections during theta periods. Statistics described in **H**.
- H.** As in **D** for INT-to-PYR connections during theta periods. The number of spikes included in this figure was 1,122,202 in 5XFAD mice and 1,451,377 in WT mice. 5XFAD: -0.61 ± 0.22 trough magnitude, WT: -0.99 ± 0.44 trough magnitude, $\text{prob}(5XFAD \geq WT) = 0.952^+$, 5XFAD: $n = 257$ INT-to-PYR cell pairs, connection strength percentiles = $[-3.77 -0.93 -0.41 0.00 0.00]$, WT: $n = 244$ INT-to-PYR cell pairs, connection strength percentiles = $[-11.06 -1.29 -0.65 -0.25 0.00]$.
- I.** Firing rates for putative INT-to-PYR cell connected pairs during the time periods of interest in 5XFAD (green) versus WT (black) mice. *Left*, firing rates of pre-synaptic interneurons during time periods of interest, single dot represents one single unit even if it is part of multiple cell pairs. During ripples: 5XFAD: 11.66 ± 4.50 Hz, WT: 9.67 ± 2.91 , $\text{prob}(WT \geq 5XFAD) = 0.24$, 5XFAD: 43 interneurons, firing rate percentiles = $[0 3.00 9.00 16.48, 51.95]$, WT: $n = 56$

interneurons, firing rate percentiles = [0 3.52 8.20 12.53, 46.12], non-theta: *5XFAD*: 8.59 ± 3.14 , *WT*: 8.43 ± 2.53 $\text{prob}(WT \geq 5XFAD) = 0.46$, *5XFAD*: $n = 54$ interneurons, firing rate percentiles = [0 2.71 4.78 11.87 42.16], *WT*: $n = 59$ interneurons, firing rate percentiles = [0 3.05 6.32 11.00 42.92], theta: *5XFAD* 10.27 ± 2.74 , *WT*: 10.53 ± 2.95 , $\text{prob}(WT \geq 5XFAD) = 0.54$, *5XFAD*: $n = 54$ interneurons, firing rate percentiles = [0.62 3.72 7.11 15.62 36.32], *WT*: $n = 59$ interneurons, firing rate percentiles = [0 3.61 7.65 14.96 42.01]. *Right*, firing rates of post-synaptic pyramidal cells during time periods of interest. During ripples: *5XFAD*: 3.17 ± 1.78 , *WT*: 2.80 ± 0.65 , $\text{prob}(WT \geq 5XFAD) = 0.38$, *5XFAD*: $n = 108$ pyramidal cells, firing rate percentiles = [0 0.36 1.14 3.94 26.97], *WT*: $n = 131$ pyramidal cells, firing rate percentiles = [0 0.60 1.67 3.75 18.98], non-theta: *5XFAD*: 1.78 ± 0.64 , *WT*: 1.96 ± 0.43 , $\text{prob}(WT \geq 5XFAD) = 0.72$, *5XFAD*: $n = 175$ pyramidal cells, firing rate percentiles = [0 0.27 0.61 2.01 24.79], *WT*: $n = 161$ pyramidal cells, firing rate percentiles = [0 0.34 0.98 2.68 10.16], theta: *5XFAD*: 2.01 ± 0.68 , *WT*: 1.95 ± 0.56 , $\text{prob}(WT \geq 5XFAD) = 0.47$, *5XFAD*: $n = 171$ pyramidal cells, firing rate percentiles = [0 0.24 0.82 2.39 24.53], *WT*: $n = 160$ pyramidal cells, firing rate percentiles = [0 0.41 1.09 2.41 18.80].

Black bar indicates median for violin plots. All percentiles are min, 25th percentile, median, 75th percentile, max. + indicates $\text{prob} > 0.95$ or $\text{prob} < 0.05$ ($\alpha = 0.10$); * indicates $p > 0.975$ or $\text{prob} < 0.025$ ($\alpha = 0.05$); n.s. indicates not significant throughout as tested by the hierarchical bootstrap analysis, which directly tests the hypothesis that the resampled means differ instead of the likelihood that the null hypothesis should be rejected.

In contrast to the INT-to-PYR connections, the connection strength of pyramidal-to-interneuron (PYR-to-INT) connections did not differ significantly between *5XFAD* and *WT* mice. PYR-to-INT connections were weaker in the *5XFAD* mice compared to *WT*, most noticeably 48.57% weaker during SWR events and 34.91% weaker during theta periods (**Figure 3.4A-B, E-F, Figure 3.10A, C**). These trends were less clear during non-theta periods (**Figure 3.4C-D, Figure 3.10B**). For PYR-to-INT cell pairs, there were also no significant differences in firing rate (**Figure 3.4G**). We also found similar results using multiple subsampling approaches to control for differences in spike numbers between *5XFAD* and *WT* groups during SWRs (see **Methods, Figure 3.10E-F**). In summary, these results demonstrate that *5XFAD* mice exhibit significantly weaker INT-to-PYR connection strengths that were dependent on the network state during awake behavior, with the most prominent synaptic deficits occurred during SWRs.

We then asked whether the proportions of monosynaptically connected cells were altered in these mice compared to *WT* littermates. We found that the proportion of INT-to-PYR connections were

greater in *WT* mice, while the proportion of detectable PYR-to-INT connections were not significantly different between *5XFAD* and *WT* mice (**Figure 3.9D**, **Figure 3.10D**). Overall, the proportions of cells with detected connections between pyramidal cells and interneurons were similar to previous monosynaptic connection analyses in *WT* rats (Fujisawa et al., 2008). These differences in the proportion of connected cells were not due to the location of those cells within the pyramidal layer (**Figure 3.11**). These results show that *5XFAD* mice have a smaller proportion of detectable INT-to-PYR connections.

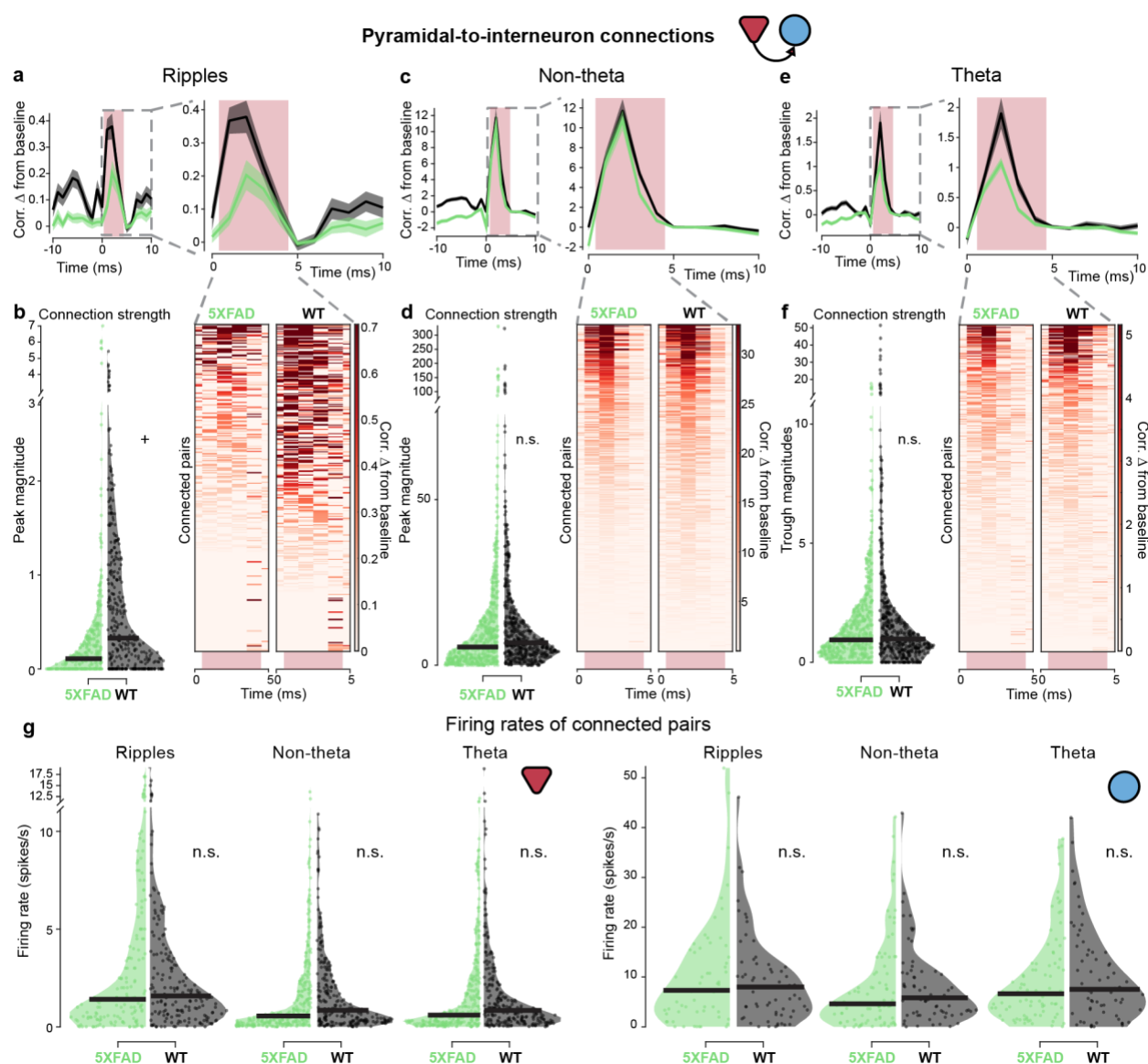


Figure 3.4 Pyramidal-to-interneuron monosynaptic connections in *5XFAD* mice.

- A.** *Left*, Average cross-correlogram (CCG) of monosynaptically connected pyramidal-to-interneuron (PYR-to-INT) cell pairs between *5XFAD* (green) and *WT* (black) mice during sharp-wave ripple (SWR) periods from -10 to +10 ms lags. Normalized by geometric mean firing rate and displayed as difference from baseline, mean \pm SEM. *Right*, view of average CCG on *left* from 0 to 10 ms lag. Light pink box indicates region where connection strength was measured. Excitatory connection strength was measured as the maximum value in the 1-4ms window. Statistics described in **B**.
- B.** *Left*, Connection strength as measured by peak magnitude in *5XFAD* and *WT* mice during SWR periods. Dot indicates the connection strength measured from a single PYR-to-INT cell pair across all SWR periods. *Right*, individual CCGs of putative PYR-to-INT cell connected pairs during SWR periods. The individual CCGs make up the average shown above. Heat map indicates change in correlation from baseline measurement. Note CCGs during SWRs look more variable because there are significantly fewer spikes during sharp wave ripples than during non-theta and theta periods. The number of spikes included in this figure was 116,444 in *5XFAD* mice and 243,457 in *WT* mice. *5XFAD*: 0.36 ± 0.28 peak magnitude, *WT*: 0.70 ± 0.24 peak magnitude, $\text{prob}(WT \geq 5XFAD) = 0.96$, *5XFAD*: $n = 306$ PYR-to-INT cell pairs, connection strength percentiles = [0 0 0.12 0.35 7.01], *WT*: $n = 349$ PYR-to-INT cell pairs, connection strength percentiles = [0 0 0.32 1.11 5.40], min, 25th percentile, median, 75th percentile, max, respectively.
- C.** As in **A** for PYR-to-INT connections during non-theta periods. Statistics described in **D**.
- D.** As in **B** for PYR-to-INT connections during non-theta periods. The number of spikes included in this figure was 12,201,118 in *5XFAD* mice and 21,369,627 in *WT* mice. *5XFAD*: 12.70 ± 5.35 peak magnitude, *WT*: 13.81 ± 6.08 peak magnitude, $\text{prob}(WT \geq 5XFAD) = 0.62$, *5XFAD*: $n = 527$ PYR-to-INT cell pairs, connection strength percentiles = [0 1.91 5.55 13.61 330.81], *WT*: $n = 447$ PYR-to-INT cell pairs, connection strength percentiles = [0 3.51 6.78 13.89 323.36].
- E.** As in **A** for PYR-to-INT connections during theta periods. Statistics described in **F**.
- F.** As in **B** for PYR-to-INT connections during theta periods. The number of spikes included in this figure was 2,362,729 in *5XFAD* mice and 2,258,135 in *WT* mice. *5XFAD*: 1.51 ± 0.54 peak magnitude, *WT*: 2.32 ± 1.32 peak magnitude, $\text{prob}(WT \geq 5XFAD) = 0.89$, *5XFAD*: $n = 539$ PYR-to-INT cell pairs, connection strength percentiles = [0 0.36 0.95 1.93 17.53], *WT*: $n = 442$ PYR-to-INT cell pairs, connection strength percentiles = [0 0.52 1.00 1.99 51.43].
- G.** Firing rates for putative PYR-to-INT cell connected pairs during the time periods of interest in *5XFAD* (green) versus *WT* (black) mice. *Left*, firing rates of pre-synaptic pyramidal cells during time periods of interest, each single unit is represented once even if it is part of multiple cell pairs. During ripples: *5XFAD*: 3.35 ± 1.42 , *WT*: 2.72 ± 0.65 , $\text{prob}(WT \geq 5XFAD) = 0.22$, *5XFAD*: $n = 153$ pyramidal cells, firing rate percentiles = [0 0.47 1.40 4.50 26.97], *WT*: $n = 168$ pyramidal cells, firing rate percentiles = [0 0.64 1.58 3.63 18.98], non-theta: *5XFAD*: 1.57 ± 0.42 , *WT*: 1.72 ± 0.38 , $\text{prob}(WT \geq 5XFAD) = 0.73$, *5XFAD*: $n = 293$ pyramidal cells, firing rate percentiles = [0 0.19 0.55 1.91 24.79], *WT*: $n = 238$ pyramidal cells, firing rate percentiles = [0 0.30 0.85 2.33 10.88], theta: *5XFAD*: 1.73 ± 0.47 , *WT*: 1.73 ± 0.47 , $\text{prob}(WT \geq 5XFAD) = 0.51$, *5XFAD*: $n = 284$ pyramidal cells, firing rate percentiles = [0 0.20 0.59 2.20 24.53], *WT*: $n = 234$ pyramidal cells, firing rate percentiles = [0 0.30 0.85 2.16 18.80]. *Right*, Firing rates of post-synaptic interneurons during time periods of interest. During ripples: *5XFAD*: 10.31 ± 3.54 , *WT*: 9.30 ± 2.66 , $\text{prob}(WT \geq 5XFAD) = 0.36$, *5XFAD*: $n = 57$ interneurons, firing rate percentiles = [0 3.00 7.31 15.45 51.95], *WT*: $n = 63$ interneurons, firing rate percentiles = [0 3.02 7.99 12.24 46.12], non-theta: *5XFAD*: 8.00 ± 2.32 , *WT*: 8.08 ± 2.49 , $\text{prob}(WT \geq 5XFAD) = 0.53$, *5XFAD*: $n = 83$ interneurons, firing rate percentiles = [0 1.35 4.60 10.82 42.16], *WT*: $n = 67$ interneurons, firing rate percentiles = [0 2.77 5.83 10.80, 42.92], theta: *5XFAD*: 9.43 ± 2.14 , *WT*: 10.29 ± 2.80 , $\text{prob}(WT \geq 5XFAD) = 0.71$, *5XFAD*: $n = 88$ interneurons, firing rate

percentiles = [0.029 2.96 6.63 12.68 37.76], *WT*: n = 68 interneurons, firing rate percentiles = [0 3.46 7.51, 14.95, 42.01].

Black bar indicates median for violin plots. All percentiles are min, 25th percentile, median, 75th percentile, max. + indicates prob > 0.95 or prob < 0.05 ($\alpha = 0.10$), n.s. indicates not significant throughout.

3.3.3. *5XFAD* mice have shorter and fewer sharp-wave ripples compared to *WT* mice

Interactions between interneurons and pyramidal cells are essential to SWR generation and maintenance (Alger & Nicoll, 1982; Buzsáki, 1986; Buzsáki et al., 1983; Csicsvari et al., 1999; Klausberger et al., 2003; Pouille & Scanziani, 2001; Stark et al., 2014; Ylinen, Bragin, et al., 1995), and previous work has shown decreased abundance of SWR events in *5XFAD* mice at a younger age (three to four months old, (Iaccarino et al., 2016)). Since we observed deficits in interneuron and pyramidal cell monosynaptic connections, we wondered whether SWRs were also disrupted in these older *5XFAD* mice. We found that there was an 82.43% decrease in SWR abundance on average in *5XFAD* versus *WT* mice (**Figure 3.5A-B, Figure 3.12A**). The *5XFAD* mice also had 27.27% more periods with no SWR events (**Figure 3.5C**). These differences in SWR abundance were not an effect of variations in non-theta periods (see **Methods, Figure 2.11B,E**). We then examined the characteristics of the remaining SWRs in the *5XFAD* mice. While the average local field potential traces looked relatively typical in *5XFAD* and *WT* mice, showing that the hallmark features of ripples are intact (**Figure 3.5D**), when we quantified duration and power of the remaining ripples, we found significant but small decreases in the *5XFAD* mice. The SWRs that remained in the *5XFAD* mice were 18.18% shorter in duration on average and had 10.88% decreased amplitude on average (**Figure 3.5E-F, Figure 3.12C, Figure 3.12D**). These results indicate a large deficit in the generation and maintenance of SWR events in *5XFAD* mice.

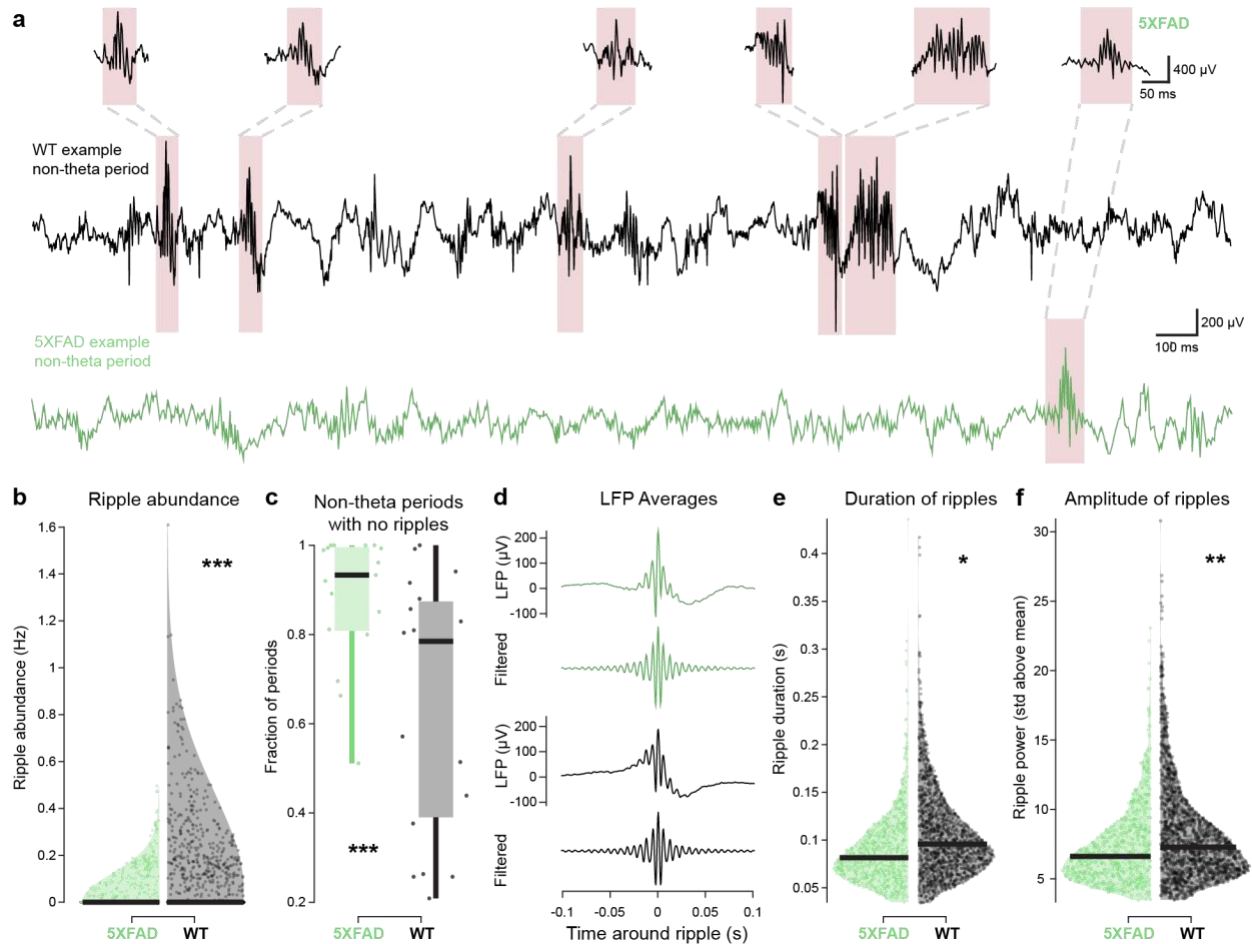


Figure 3.5 5XFAD mice have shorter and fewer sharp-wave ripples compared to WT mice.

- A.** Example non-theta periods with representative sharp-wave ripples (SWRs) in 5XFAD (green) and WT (black) mice.
- B.** Violin plot of SWR abundance during non-theta periods longer than five seconds in 5XFAD (green) versus WT (black) mice. Each dot indicates a non-theta period. Black bar at bottom indicates median. 5XFAD: 0.013 ± 0.0082 SWR abundance (Hz), WT: 0.074 ± 0.043 SWR abundance (Hz), $\text{prob}(WT \geq 5XFAD) = 0.9999$ (limit due to resampling 10^4 times) ***, 5XFAD: $n = 1969$ non-theta periods five seconds or longer, ripple abundance percentiles = [0, 0, 0, 0, 0.50], WT: $n = 1389$ non-theta periods five seconds or longer, ripple abundance percentiles = [0, 0, 0, 0.08, 1.61], min, 25th percentile, median, 75th percentile, max, respectively.
- C.** Fraction of non-theta periods five seconds or longer with no SWRs in 5XFAD (green) and WT (black) mice. Each data point indicates a single recording session. Box plot edges indicate quartiles, whiskers indicate range, and black bar indicates median, 5XFAD: 0.88 ± 0.053 proportion of periods, WT: 0.64 ± 0.098 proportion of periods, $\text{prob}(WT \geq 5XFAD) < 10^{-4}$ (limit due to resampling 10^4 times) *** 5XFAD: $n = 17$ sessions, fraction of periods with no ripples percentiles = [0.51, 0.81, 0.93, 0.99, 1], WT: $n = 19$ sessions, fraction of periods with no ripples percentiles = [0.21, 0.40, 0.78, 0.87, 1].
- D.** Averages of all SWR events in 5XFAD (green) and WT (black) mice aligned by peak of filtered signal. For green and black traces, *top* indicates LFP signal (1-300 Hz) from the peak ripple power channel, *bottom* indicates filtered LFP signal (150-250 Hz) from the peak ripple power channel.

- E.** Distribution of SWR durations in *5XFAD* (green) versus *WT* (black) mice. Each dot indicates a SWR event. Black bar indicates median. SWRs had to be a minimum of 0.015 seconds above a threshold, so no SWRs are shorter than 0.015 seconds, *5XFAD*: 0.090 ± 0.0098 s, *WT*: 0.11 ± 0.0074 s, $\text{prob}(WT \geq 5XFAD) = 0.9787$ *, *5XFAD*: $n = 776$ SWRs, ripple duration percentiles = [0.035, 0.065, 0.082, 0.11, 0.44], *WT*: $n = 1542$ SWRs, ripple duration percentiles = [-0.034, 0.074, 0.096, 0.13, 0.42].
- F.** As in **E** for SWR power as measured in standard deviations above the SWR power mean. SWRs had to be a minimum of 3 standard deviations above the mean, so no SWRs have less power than 3 std. *5XFAD*: 7.29 ± 1.01 std above the mean, *WT*: 8.18 ± 0.49 std above the mean, $\text{prob}(WT \geq 5XFAD) = 0.9977$ **, *5XFAD*: $n = 776$ SWRs, ripple power percentiles = [3.45, 5.35, 6.61, 8.48, 23.08], *WT*: $n = 1542$ SWRs, ripple duration percentiles = [3.48, 5.71, 7.28, 9.53, 30.79].

All percentiles are min, 25th percentile, median, 75th percentile, max. * indicates $\text{prob} > 0.975$ or $\text{prob} < 0.025$ ($\alpha = 0.05$); ** indicates $\text{prob} > 0.995$ or $\text{prob} < 0.005$ ($\alpha = 0.01$); *** indicates $\text{prob} > 0.9995$ or $\text{prob} < 0.0005$ ($\alpha = .001$) throughout.

3.3.4. Place cells of *5XFAD* mice have decreased reactivation during sharp-wave ripples

In light of altered synaptic connections and SWRs in CA1, we asked if *5XFAD* mice have altered hippocampal neural codes, such as the encoding of spatial information via place cells or the activation and reactivation of place cells during SWRs, both of which are important for cognitive processes such as spatial memory (Davidson et al., 2009; Diba & Buzsáki, 2007; Foster & Wilson, 2006; Karlsson & Frank, 2009; J. O'Neill et al., 2008; Stella et al., 2019; Wilson & McNaughton, 1994). Both *5XFAD* and *WT* animals had pyramidal cells with spatially tuned firing, e.g. place cells (**Figure 3.6A**, see **Methods**). Interestingly, several place cells had multiple peaks that seemed to follow the repetitive visual cues and reward zones present on the virtual reality track (Geiller et al., 2017, **Figure 3.6A**). We found that place cells in the *5XFAD* mice had 12.5% less spatial information content on average (**Figure 3.6B**, **Figure 3.13A**), and 13.88% lower peak firing rates, but neither were significantly different (**Figure 3.6C**, **Figure 3.13B**).

We then determined if *5XFAD* mice had lower place cell reactivation during SWRs. Because there were far fewer SWR events in *5XFAD* mice and the remaining SWRs were shorter in duration, we measured reactivation of place cell pairs during SWRs to include as many SWRs as possible. If coherent sequences of neural activity are reactivated during SWRs, two cells that fire closely

together during theta will also fire closely together during SWRs. Thus, to assess reactivation among cell pairs, we first identified place cell pairs that fire closely together during theta (within \pm 35ms) and then asked how closely those same cells fired together during SWRs. In *WT* mice place cell pairs firing near in time during theta fired on average 27.46% more closely together during SWRs than *5XFAD* mice (**Figure 3.6D-E, Figure 3.13C**). We still found weaker reactivation in *5XFAD* than *WT* mice when we controlled for differences in spike numbers between *5XFAD* and *WT* groups (see **Methods, Figure 3.13G-H**). We also analyzed SWR activation in terms of co-activation probability of cell pairs and found that the co-activation probability of place cells during SWRs was 78.18% lower in *5XFAD* mice than in *WT* mice on average (**Figure 3.6F, Figure 3.13D**). Activation probability of place cells was also lower in *5XFAD* mice (**Figure 3.6G, Figure 3.13E**). We found that pyramidal cell and interneuron z-scored peak firing activity did not significantly differ during SWRs in the *5XFAD* mice (**Figure 3.13F**). There were small differences in the location of recorded cells in the layer between genotypes, but the differences were on average 12 μ m for pyramidal cells and 33 μ m for interneurons, which is close to our resolution for measuring distance between channels (27.5 μ m, **Figure 3.8**). These results demonstrate that *5XFAD* mice have relatively intact spatial information content while they have much lower coactivation and coordinated reactivation of those place cells during SWR events. Thus, *5XFAD* mice have compounding deficits; they have drastically fewer and shorter SWRs, as well as less place cell activation and reactivation during the few remaining SWR events.

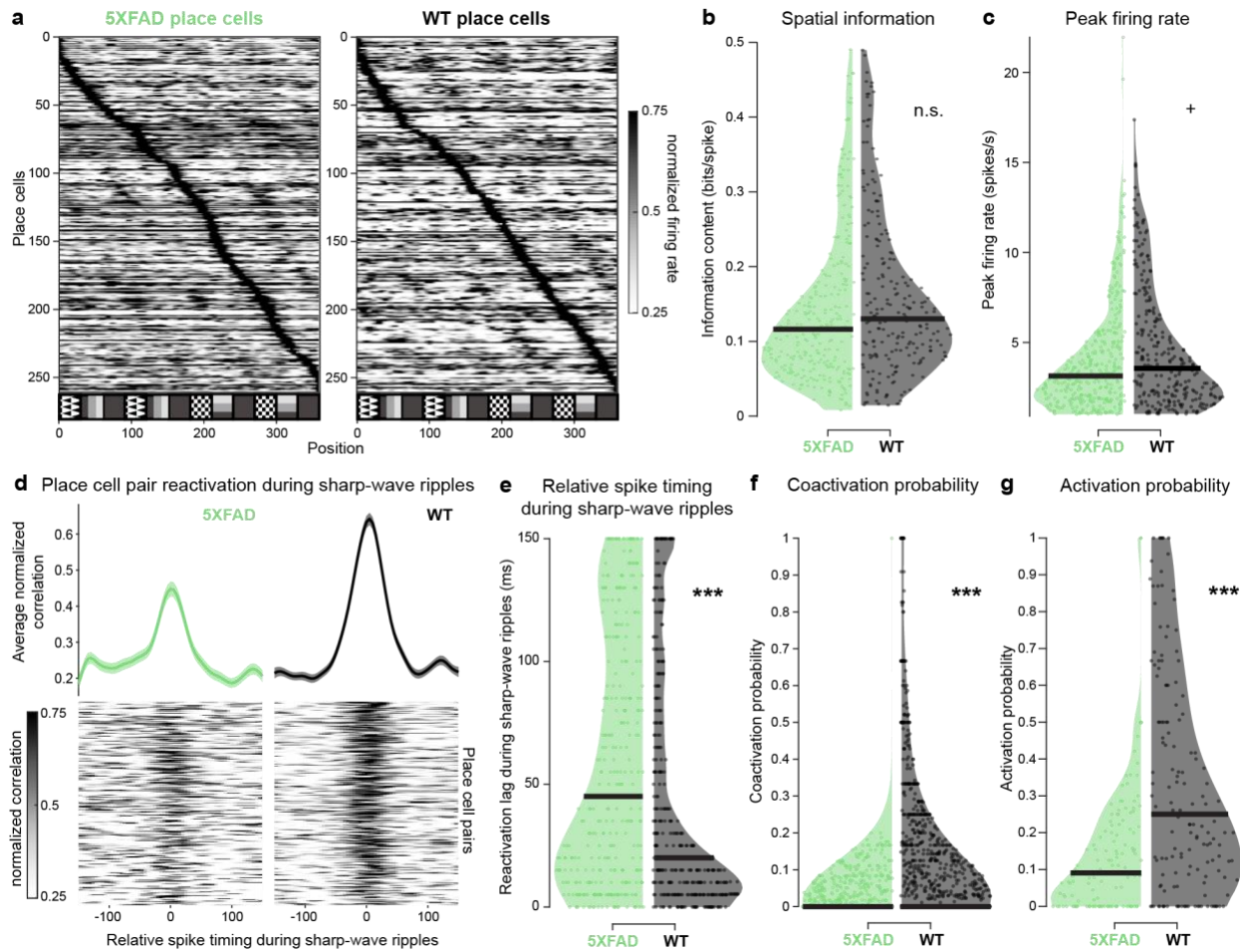


Figure 3.6 Place cells of 5XFAD mice have lower probability of activation and coactivation during sharp-wave ripples.

- A.** All place cells in 5XFAD and WT mice, sorted by normalized peak firing rate.
- B.** Distribution of spatial information of place cells with spatially tuned firing in this task in 5XFAD (green) versus WT (black) mice. Each dot indicates a single place cell. 5XFAD: 0.14 ± 0.016 bits/spike, WT: 0.16 ± 0.018 bits/spike, $\text{prob}(WT \geq 5XFAD) = 0.94$, 5XFAD: $n = 271$ place cells, spatial information percentiles = [0.0081, 0.068, 0.12, 0.18, 0.49], WT: $n = 215$, spatial information percentiles = [0.015, 0.082, 0.13, 0.21, 0.49], min, 25th percentile, median, 75th percentile, max, respectively. We observed some outliers and so we removed them as described in the Methods.
- C.** As in B for peak firing rate of place cells. 5XFAD: 3.97 ± 0.52 Hz, WT: 4.61 ± 0.53 Hz, $\text{prob}(WT \geq 5XFAD) = 0.96$ +, 5XFAD: $n = 336$ place cells, firing rate percentiles = [1.01, 1.89, 3.14, 5.03, 21.95], WT: $n = 265$, firing rate percentiles = [1.03, 2.02, 3.56, 6.29, 17.37].
- D.** Reactivation during sharp-wave ripple (SWR) events of place cell pairs with spiking near in time during theta in 5XFAD and WT mice. *Bottom*, heat maps of normalized CCGs of place cell pairs during SWR with spiking near in time during theta (lower half of the activity index of all place cell pairs). *Top*, average of all place cell pair reactivation during SWR events with spiking near in time during theta. Activity index distributions: 5XFAD: 0.37 ± 0.035 $n = 335$ place cell pairs WT: 0.28 ± 0.065 $n = 387$ place cell pairs, $\text{prob}(WT \geq 5XFAD) = 0.030$, bootstrap test.

- E.** Relative spike timing during SWRs in place cells that spike near in time during theta in *5XFAD* (green) and *WT* (black) mice. Each dot indicates the peak reactivation lag of a single place cell pair across all SWR events. The number of spikes included in this figure was 107,276 in *5XFAD* mice and 131,910 in *WT* mice. *5XFAD*: 59.84 ± 7.37 ms, *WT*: 43.41 ± 5.77 ms, $\text{prob}(WT \geq 5XFAD) = 0.0003$, $\text{prob}(WT \geq 5XFAD) = 0.0003$ ***, *5XFAD*: $n = 335$ place cell pairs, spike timing lags during ripples percentiles = [0 10 45 110 150], *WT*: $n = 387$, spike timing lags during ripples percentiles = [0 5 20 70 150].
- F.** SWR coactivation probabilities of place cells with spatially tuned firing in this task in *5XFAD* (green) versus *WT* (black) mice. Only animals with at least 10 SWRs during non-theta periods per recording were included. Each dot indicates the coactivation probability of a place cell pair across all SWR events. *5XFAD*: 0.024 ± 0.0049 probability, *WT*: 0.11 ± 0.025 probability, $\text{prob}(WT \geq 5XFAD) > 0.9999$ (limit due to resampling 10^4 times) ***, *5XFAD*: $n = 845$ place cell pairs, coactivation probability percentiles = [0, 0, 0, 0.026, 1], *WT*: $n = 1061$ place cell pairs, coactivation probability percentiles = [0, 0, 0, 0.15, 1].
- G.** As in **F** for SWR activation probabilities of place cells. *5XFAD*: 0.14 ± 0.035 probability, *WT*: 0.32 ± 0.049 probability, $\text{prob}(WT \geq 5XFAD) > 0.9999$ (limit due to resampling 10^4 times) ***, *5XFAD*: $n = 125$ place cells, activation probability percentiles = [0, 0, 0.091, 0.22, 1], *WT*: $n = 157$, activation probability percentiles = [0, 0.081, 0.25, 0.50, 1].

Black bars indicate median of distribution for violin plots. All percentiles are min, 25th percentile, median, 75th percentile, max. ** indicates $\text{prob} > 0.995$ or $\text{prob} < 0.005$ ($\alpha = .01$); *** indicates $\text{prob} > 0.9995$ or $\text{prob} < 0.0005$ ($\alpha = .001$); n.s. indicates not significant throughout.

3.4. Discussion

In this study, we used in vivo electrophysiological recordings of many single neurons in hippocampal CA1 to identify synaptic connection and neural coding deficits in the *5XFAD* mouse model of AD. We discovered *5XFAD* mice had significantly weaker inhibitory synaptic efficacy onto pyramidal cells in awake animals during SWRs compared to *WT* mice. Because interneuron and pyramidal cell activity is critical for SWR oscillations, we then examined SWR activity. We found that *5XFAD* mice had 82% fewer SWRs on average, as well as 18% shorter SWRs on average. Finally, while spatial information of place cells was relatively intact in *5XFAD* mice, we found significant impairments in activation, coactivation, and coordinated reactivation of these cells during SWRs. These results demonstrate synaptic dysfunction, shorter SWRs, and weaker place cell reactivation during SWRs in an awake, behaving mouse model of AD.

3.4.1. Linking synaptic dysfunction and interneuron deficit hypotheses in Alzheimer's disease

Synaptic dysfunction in AD has been of special interest because synaptic loss is one of the best correlates of cognitive impairment in AD (DeKosky & Scheff, 1990; Terry et al., 1991). Prior work has found that spatial memory impairment in *5XFAD* mice is correlated with molecular markers of synaptic degeneration, measured via decreased levels of pre-synaptic (syntaxin, synaptophysin) and post-synaptic (PSD-95) markers (Oakley et al., 2006; Schneider et al., 2014; Xiao et al., 2015). Furthermore, synaptic function has important implications outside of learning and memory deficits; synaptic dysfunction plays a key role in a wide variety of neurodevelopmental and neurodegenerative diseases and inhibitory synapses are critical to maintain synchronized network oscillations such as SWRs (Bartos et al., 2002, 2007; Coghlan et al., 2012; Gonzalez-Burgos & Lewis, 2008; Isaacson & Scanziani, 2011; Stephan et al., 2006; Van Spronsen & Hoogenraad, 2010). Prior research examining spine density of pyramidal cells in *5XFAD* mice found significant spine loss in somatosensory, prefrontal cortex, and hippocampus (Crowe & Ellis-Davies, 2014; De Pins et al., 2019). Another study investigating synaptic activity

in *5XFAD* mice in vitro found an increase in the ratio of excitatory to inhibitory charge in pyramidal cells and a decrease in this ratio in PV+ interneurons, however they observed increased SWR frequency and amplitude, contrary to our findings in awake, behaving animals (Caccavano et al., 2020). While there has been extensive previous work on the role of amyloid beta on synaptic activity in vitro (Abramov et al., 2009; Petrache et al., 2019; Puzzo et al., 2008) or in anesthetized animals in vivo (Chapman et al., 1999; Freir et al., 2017; Stéphan et al., 2001), no prior studies have investigated these synaptic changes in awake, behaving animals. Thus it was not clear exactly how previously characterized synaptic changes would affect synaptic efficacy in awake animals.

Recent studies have also revealed inhibitory interneuron dysfunction in AD mice. Several studies have shown the loss of parvalbumin-positive (PV+) inhibitory interneurons in *5XFAD* mice (Ali et al., 2019; Flanigan et al., 2014; Giesers & Wirths, 2020). Both *hAPP* mice and human patients with AD have lower levels of sodium channel Nav1.1 specifically in inhibitory interneurons. In *hAPP* mice, which overexpress amyloid precursor protein (APP) due to two human familial AD mutations (Games et al., 1995), implanting interneurons that overexpressed Nav1.1 sodium channels rescued gamma activity deficits and epileptic-like network hypersynchrony previously observed in these mice, as well as improved cognitive function (Martinez-Losa et al., 2018; Palop et al., 2007; Verret et al., 2012). In *apoE4* mice, which express the major genetic risk factor for late-onset sporadic AD, GABAergic dysfunction and interneuron loss in the dentate gyrus is correlated with deficits in learning and memory (Leung et al., 2012; Li et al., 2009). In *APP23xPS45* mice, a model that overexpresses both amyloid precursor protein and mutant presenilin, hyperactivity was reduced by increasing inhibition with a GABA-a receptor channel agonist (Busche et al., 2008). Thus, there is evidence for deficits in inhibitory activity in multiple brain regions and mouse models of AD. Of course, no mouse model recapitulates AD faithfully (Scarce-Levie et al., 2020). For example, the *5XFAD* mouse model used in this study does not

mimic all the symptoms of human AD, most notably they lack neurofibrillary tangles, a major hallmark of AD (Oakley et al., 2006). Furthermore, the *5XFAD* mouse model is a relatively aggressive model with a rapid progression. However, converging evidence from multiple mouse models with different genetic pathogenesis suggests that inhibitory interneurons are especially vulnerable.

Our findings connect these two lines of research by showing a deficit in inhibition on the synaptic level. We found deficits in interneuron inhibition onto pyramidal cells in a mouse model of AD. While spine loss and inhibitory deficits have been previously characterized in AD models in vitro or in post-mortem tissue, our work reveals how these deficits manifest in awake behaving animals. It is important to note that measuring synaptic connectivity in vivo is a complicated task, and the main limitation of our results is that cross-correlation measures only indirectly infer monosynaptic connectivity and connection strength. Additionally, the overall number of detected connections is lower than is thought to be physiologically present. This approach is limited in that it does not detect all synaptic connections, for instance it cannot accurately detect connections in cells with low firing rates, and it quantifies spike transmission but not postsynaptic potentials. Even considering these limitations, this method of detecting monosynaptic connections and measuring synaptic strength is well established, has been used in many other studies, and has been validated with optogenetic and juxtacellular stimulation (Alonso et al., 1996; Barthó et al., 2004; Clay Reid and Alonso, 1995; English et al., 2017; Fujisawa et al., 2008; Perkel et al., 1967; Tanaka, 1983; Toyama et al., 2017; Usrey et al., 1999; Vizuete et al., 2012). In short, our findings reveal deficits in inhibitory synaptic strength during behavior, linking prior work on synaptic dysfunction and interneuron deficits.

3.4.2. Synaptic changes and sharp-wave ripple deficits could underlie memory impairment

The observed deficits in interneuron connection strength onto pyramidal cells could explain the decreased abundance, power, and duration of SWRs in *5XFAD* mice. Importantly, SWRs are present and associated with memory in both rodents and humans (Axmacher et al., 2008; Buzsáki, 2015; Carr et al., 2011; Girardeau et al., 2009; Girardeau & Zugaro, 2011; Jadhav et al., 2012; Pfeiffer & Foster, 2013; Singer et al., 2013; Staresina et al., 2015; Vaz et al., 2019). Prior work shows that both interneuron and pyramidal cell activity is critical for SWR oscillations (Buzsáki, 2015; Schlingloff et al., 2014; Stark et al., 2014). Furthermore, inhibition is thought to prolong the recruitment of excitatory pyramidal cells during SWRs (Csicsvari et al., 1999; Klausberger et al., 2003), and optogenetic stimulation of inhibitory cells can initiate SWR events (Schlingloff et al., 2014). Pharmacologically disrupting GABA receptor activity results in fewer and shorter ripples, similar to our findings in *5XFAD* mice (Ponomarenko et al., 2004). Intriguingly, we observed more pronounced inhibitory deficits during SWRs. Fewer and shorter SWRs could underlie cognitive deficits in these mice because SWRs are essential for intact memory consolidation. Indeed, longer SWRs are associated with improved memory performance and SWR abundance predicts spatial memory impairments (Fernández-Ruiz et al., 2019; E. A. Jones et al., 2019). SWR deficits have also been observed in multiple mouse models of AD (Gillespie et al., 2016; Iaccarino et al., 2016). This converging evidence from multiple animal models of AD suggests the intriguing possibility that multiple molecular pathologies underlying AD could produce similar deficits in SWRs.

During SWRs, ensembles of hippocampal place cells that were previously active during exploration are reactivated in an experience-dependent manner (Davidson et al., 2009; Diba & Buzsáki, 2007; Foster & Wilson, 2006; Karlsson & Frank, 2009; J. O'Neill et al., 2008; Stella et al., 2019; Wilson & McNaughton, 1994). Disruption of SWR events is thought to impair memory and results in worse behavioral performance on a spatial navigation memory task (Girardeau et al., 2009; Jadhav et al., 2012). Furthermore, higher reactivation, as measured by coactivation of

place cells during SWRs, predicted a higher likelihood of the animal performing correctly on the next trial in a spatial memory task (Singer et al., 2013). Interestingly, we found decreased coactivation of place cell pairs and weaker reactivation during SWRs. Though we did not observe task performance impairments due to the simplicity of our task, several prior studies of *5XFAD* mice have found spatial and memory impairments (novel object location, novel object recognition, Morris water maze) at or before this age (Flanigan et al., 2014; Martorell et al., 2019; Oakley et al., 2006; O'Leary et al., 2018; Xiao et al., 2015). Together these findings of disrupted place cell activation and reactivation during SWRs could be a mechanism of spatial memory impairment observed in mouse models and humans with AD.

Our findings reveal inhibitory synaptic changes, shorter SWRs, and disrupted place cell reactivation during SWRs in an awake mouse model of AD during behavior. In line with previous work, these results point to an important role for both synaptic dysfunction and inhibition deficits in AD (Palop & Mucke, 2016; Selkoe, 2002). Based on the role of inhibition in SWR generation and maintenance and the fact that SWRs are essential for spatial memory in healthy mice, these findings suggest a mechanism by which synaptic deficits in AD lead to dysfunction of neural activity and neural codes essential for memory.

3.5. Methods

3.5.1. Animals

All animal work was approved by the National Institute of Health guidelines on animal care and use at Georgia Institute of Technology. Male (11-14 month-old) *5XFAD* and *WT* mice on a C57Bl/6 background were either obtained from the Jackson laboratory (F1, F7, F8) or bred in the animal facilities at Georgia Institute of Technology. All mice were littermates (**Table 2.1**). Mice were single-housed on a reverse 12-hour light/12-hour dark cycle, and all electrophysiology and behavioral experiments were performed during the dark cycle. At the start of the behavioral and electrophysiological experiments, mice were food-restricted between 85-90% percent of their baseline body weight, and water was provided without restriction. Animals were excluded from further behavioral training and electrophysiological recording if they developed any health problems (2 animals) or if they never licked in response to reward during behavioral training (1 animal). The experimenter was blind to genotype during behavior, recording, and preprocessing analysis of data.

3.5.2. Surgical procedures

Mice were anesthetized with isoflurane before headplate implant surgery. A custom stainless steel headplate was fixed to the skull using dental cement (C&B Metabond, Parkell), and the target craniotomy site for LFP recordings was marked on the skull (in mm, from bregma: -2.0 anterior/posterior, +/-1.8 medial/lateral for CA1). Craniotomies were later performed in 11-14 month-old mice before electrophysiology recording sessions. These craniotomies (200-500um diameter) were made by using a dental drill to thin the skull and then opening up a small hole in the skull with a 27-gauge needle. Craniotomies were sealed with a sterile silicone elastomer (Kwik-Sil WPI) and only opened for recording experiments.

3.5.3. Behavioral training and analysis

The virtual reality annular track environment was designed using ViRMEN (Aronov & Tank, 2014) open-source software and displayed on a cylindrical screen using an HD projector system reflected by several mirrors. To begin the behavioral task, head-fixed animals ran on a spherical treadmill composed of an 8-inch polystyrene foam ball floating on air. Animals either immediately began behavioral training in the virtual reality environment the first time they were head-fixed on the treadmill ($n = 11$), while others were given 1-3 days of habituation to the treadmill without the virtual reality projector system turned on ($n = 3$). The transition to habituation without VR occurred because we observed animals became more comfortable more quickly with the VR turned on. Animals ran on the ball and their translational and rotational velocities were tracked via an optical mouse and converted into movement through the virtual reality environment. In the first phase of behavioral training, animals navigated around the annular track environment and received a sweetened condensed milk reward (1:2 water dilution) when they entered either of the two patterned reward zones. These locations were indicated with visual cues, and the reward location was the second instance of a patterned visual cue on each lap around the circular track. Thus the reward location was not indicated only by the visual cues, but also by its order in the sequence of visual cues. An average trial was approximately 9 m around the entire annulus, however the exact distance traveled varied from trial to trial. Once animals began demonstrating anticipatory licking before the reward zone, the animals were transitioned to the second phase of the behavioral task. In the second phase of behavioral training, animals navigated around the annular track and licked in the reward zone in order to receive a reward (**Figure 2.6**). The second phase of behavioral training was the same environment and used the same visual cues as the first phase of training. However, in this phase animals did not automatically receive a reward for entering the reward zone, but they had to trigger the reward with their licking activity. Licks were detected using a photo-interrupter placed in front of the animal's mouth around the reward spout. In one group of animals ($n = 5$), electrophysiology recordings began when the animal successfully transitioned

from the automatic reward delivery phase to the second phase of the task. In another group of animals ($n = 5$), electrophysiology recordings began after the animals demonstrated more than 2 days of licking for reward behavior (see **Behavioral Analysis** below). All of the behavioral analysis was performed on data from the second phase of the behavioral tasks during which the animals had to lick to receive the reward.

Raw behavioral data tracking translational and rotational velocity, licks, position, and time were analyzed using Matlab®. Position and velocity data were smoothed using a moving average and all data was segmented into trials in which each trial was one full lap (360 degrees) around the annular track in which the animal passed through two reward zones. Data were then combined across behavioral sessions into trial blocks of 50 trials each. We quantified lick latency as the number of degrees from entering the reward zone until the animal received its first reward. We quantified miss rate, with a miss consisting of a trial where the animal received no reward in either of the two reward zones. We also quantified lick and velocity rate as licks per second and degrees traveled in the track per second respectively. Finally, for comparisons between the track with and without visual cues, we analyzed data from the last two sessions in the track with cues and the first two sessions of the track without visual cues.

3.5.4. Electrophysiology recordings

All recordings were performed using the same virtual reality and treadmill set-up as described above. Animals were head-fixed on the treadmill for a maximum five-hour-long recording session, with one recording session per day (number of sessions ranged from 1-4 per animal, **Table 2.1**, **Figure 2.6**). A 32-channel, single shank probe (NeuroNexus) was placed in a slightly different location within the craniotomy at the beginning of each recording session and advanced vertically to the CA1 pyramidal layer of hippocampus identified via electrophysiological characteristics: large theta waves, sharp-wave ripples, and 150+ μV spikes on multiple channels. Recording sites

(250 μ m from farthest sites) spanned the layer (**Figure 2.8**). Recordings consisted of interleaved periods of behavioral task performance when animals navigated through the virtual reality environment, and no-task periods, during which no virtual reality environment was displayed on the screen (**Figure 2.6**). Though we did not explicitly quantify sleep during the task, we observed that animals head-fixed on the spherical treadmill were either moving or maintaining their balance on the ball and thus were very unlikely to be sleeping during these recordings. We also observed that most non-theta periods (when the animals are still) were less than 30 seconds long on average, and therefore unlikely to include sleep. Data were acquired with a sampling rate of 20 kHz using an Intan RHD2000 Evaluation System using a ground pellet as reference.

3.5.5. Local Field Potential Analyses

LFP was obtained by downsampling raw traces to 2kHz and bandpass filtering between 1-300Hz. Outliers were eliminated by interpolating over outliers when the pre-filtered LFP signal were 7 standard deviations above the mean. All LFP analyses used the signal from a single channel that was putatively located in the stratum pyramidale. To identify this channel, the LFP was bandpass filtered for the sharp-wave ripple band (150-250 Hz, see details below) and the average of the sharp-wave ripple band envelope over time was calculated from each channel. The channel with the highest average sharp-wave ripple band power was used for all further analyses, and this channel was predominately located in the middle of the depth-wise span of the NeuroNexus probe. In order to ensure that probe depth placements were similar across genotypes, we analyzed the distribution of ripple power across all channels for all recording sessions, centered by the LFP channel.

LFP was used to detect theta, non-theta, and sharp-wave ripple periods. To detect theta periods, the LFP was bandpass filtered for theta (4-12 Hz), delta (1-4 Hz), and beta (12-30 Hz) using an FIR (finite impulse response) equiripple filter. The envelope amplitude of the filtered theta signal

was divided by the sum of the envelope amplitudes of the delta and beta signals. A theta period was defined as a period during which this theta to delta and beta ratio was 2 standard deviations above the mean for at least 2 seconds (Csicsvari et al., 1999; Iaccharino et al., 2016; Jackson et al., 2006). Theta periods were visually inspected to ensure that the criteria used accurately included theta periods. To detect non-theta period, the same theta to delta and beta ratio as described above was used. A non-theta period was defined as a period during which this ratio threshold was less than 1.1 for at least 2 seconds. Non-theta periods were visually inspected to ensure that the criteria used accurately included non-theta periods. To detect sharp-wave ripple events, the LFP was bandpass filtered for the sharp-wave ripple band (150-250 Hz) using an FIR equiripple filter. Sharp-wave ripples were detected when the envelope amplitude of the filtered sharp-wave ripple trace was greater than 3 standard deviations above the mean for at least 20 ms (Karlsson & Frank, 2009; Singer et al., 2013; Singer & Frank, 2009). We excluded any events that had an LFP amplitude greater than 1500 μV or less than -1500 μV to eliminate artifacts. We also applied a power ratio threshold (power from 100 to 250 Hz / power from 250 to 400 Hz) based on the typically observed frequency range of sharp-wave ripples (Ylinen, Bragin, et al., 1995). We excluded any detected events that had a power ratio less than 4. Sharp-wave ripples were visually inspected to ensure that the criteria used accurately detected sharp-wave ripple events.

Duration of sharp-wave ripples was defined as the length of time the sharp-wave ripple envelope was greater than the threshold of 3 standard deviations above the mean. Gamma power before, during, and after SWRs was computed by filtering the LFP for low gamma and z-scoring the amplitude of the envelope of the Hilbert transform. Sharp-wave ripple power was quantified as standard deviations above the mean ripple power for the entire recording session.

3.5.6. Classification of cell types

Spike detection and sorting were performed using MountainSort automated spike sorting and automated curation, followed by manual curation guided by visual inspection of waveforms and cross-correlograms (Chung et al., 2017). Prior to manual curation, automatic curation was performed by applying quality thresholds to include units with a peak signal to noise ratio (SNR) greater than or equal to 1, less than 10% overlap with noise, and greater than 95% isolation against other units. To account for periods of instability in the recordings during which single units were lost, stability criteria were applied such that only stable periods (no sudden loss of a single unit's firing rate) would be considered in analysis. Firing rate (FR) for each unit was computed throughout the recording session. Firing rate was clustered into two distributions, low FR and high FR, using k-means clustering. A stable period was defined as the longest length of time that the FR was 2 standard deviations above the low FR mean. If the firing rate of the unit never dropped below 10% of the high FR mean, the stable period was defined as the whole recording session.

Cell types were classified into putative pyramidal cells and putative interneurons based on the spike width and the first moment of the autocorrelogram. These measurements are well-established metrics used for cell-type classification (Barthó et al., 2004; Csicsvari et al., 1998, 1999; Niell & Stryker, 2008; Senzai et al., 2019). Spike width was calculated as the length in milliseconds from the negative peak of the spike to the positive trough, where the trough was defined as the first instance when the differential of the waveform was equal to 0. The first moment of the autocorrelogram was calculated as the center of mass along the time-axis of an autocorrelogram calculated with lags of 0 to 50 ms. Single units were excluded if the autocorrelograms had a peak spike count less than 10. Mean firing rate was computed for each single unit and only stable periods for each unit contributed to the mean FR calculation (described above). The three parameters (spike width, firing rate, autocorrelogram moment) were then plotted for all single units, and these plots revealed two clear clusters that could be isolated using the spike width and autocorrelogram moment parameters. Putative pyramidal cells were defined

as units that had a spike width greater than 0.5 ms and a first moment of the autocorrelogram less than 5 ms. Putative interneurons were defined as units that had a spike width less than 0.5 ms and a first moment of the autocorrelogram greater than 4 ms. Overall these thresholds for spike width and first moment of the autocorrelogram are similar to previously reported classification criteria, although the autocorrelogram function is dependent on the window it is measured within (Csicsvari et al., 1998, 1999; Senzai et al., 2019). This classification was further validated by the identification of putative monosynaptic connections (described below). Only units localized in the two predominant clusters were included in further analyses, and as a result, several neurons were unclassified and excluded. In order to ensure we were not sampling from different populations of interneurons and pyramidal cells across genotypes (i.e. superficial or deep neurons relative to CA1), we inspected the population of classified interneurons and pyramidal cells for all recording sessions, centered by the LFP channel (the channel with the highest ripple power).

3.5.7. Identification of monosynaptic connections

Analysis for the identification of putative monosynaptic connections was drawn from previous studies (Amarasingham et al., 2011; Fujisawa et al., 2008; Hatsopoulos et al., 2003). To identify connections, cross-correlations were calculated between spike trains of all cell pairs with lags from 0 to 50 ms. Out of all detected cells, there were 110,132 possible connections in *5XFAD* mice and 87,320 in *WT* mice (counting each actual pair of cells twice for both directions of connectivity). If the spike train cross-correlation pair had no bins with a spike count of less than 2.5, then a jittered cross-correlation was calculated 200 times for all cell pairs. Spike trains of the second neuron were jittered such that each spike time was shifted by a random integer value between -5 and +5 ms. This approach preserved the longer timescale temporal dynamics of the spike trains while removing any spiking correlations not due to monosynaptic connections. The maximum and minimum of the 200 shuffled cross-correlations were then taken and defined as

the significance bands. If the original cross-correlation between the cell pair was greater than the significance band maximum at lags of 1-3 ms, then the pair was classified as an excitatory monosynaptic connection. If the cross-correlation between the cell pair was less than the significance band minimum at lags of 1-3 ms, then the pair was classified as an inhibitory monosynaptic connection. We were careful to only include single unit pairs with good isolation, so all pairs that shared the same principal channel, or recording channel on which the amplitude of the spike was largest, were discarded from further analyses. We also separated cell types based on spike width and firing properties. Furthermore, all cross-correlograms were manually curated by inspecting the cross-correlograms and waveforms across all recording channels (**Figure 2.10**). Pairs were excluded if the waveforms looked similar and the cross-correlograms appeared to be autocorrelograms (a very large peak or trough at 0 ms). Furthermore, the excitatory (peak) or inhibitory (trough) properties of the connected units were further confirmation of their cell type classification. In order to ensure there were no differences in the sampling of monosynaptically-connected cell pairs across the depth of the probe, we also inspected the distribution of putatively connected cell pairs across the recording probe, centered using the channel with the peak ripple power (**Figures S8-9**). We also observed that several of the detected interneuron-to-pyramidal (INT-to-PYR) connections were likely reciprocally driven by pyramidal cells, as evidenced by the large excitatory peak in the -3 to -1 ms range (**Figures 2C, 2E, 2G**). Notably, we detected interneuron to pyramidal connections solely based on the presence of a significant inhibitory trough in the 1-3 ms range

3.5.8. Quantification of connection strength

To quantify connection strength of excitatory and inhibitory pairs, cross-correlograms were calculated for all putative monosynaptically connected pairs (see **Identification of putative monosynaptic connections**) during different periods, such as when theta was detected (see **LFP analyses**). These cross-correlograms were then normalized by the geometric mean firing

rate to control for any possible firing rate differences between pairs. These firing rates were calculated for the subset of time windows during which connection strength were analyzed. To control for differences in sharp-wave ripple duration between genotypes, we also used the same time window around the midpoint of the sharp-wave ripple for all analyses of connection strength during sharp-wave ripples. To calculate the connection strength, we took the peak or trough of the normalized cross-correlograms over 1-4 ms time lags, and subtracted the average of the normalized baseline cross-correlogram, specifically the baseline at lags from 5 to 6 ms or 1 ms beyond the monosynaptic connection latency windows. Thus, this peak magnitude value was a metric of the increase or decrease in spiking activity due to the monosynaptic connection, while controlling for baseline firing activity. Since these cell pairs had previously been identified as putative excitatory or inhibitory connections based on the cross-correlations over all time, we rectified any opposite-signed values (e.g., an excitatory connection with a negative peak value, less than 7% of all cases) to zero to correct for pairs that likely did not fire enough spikes or were too noisy during the periods we analyzed. We also performed the same analysis but removed all opposite-signed values from the analysis entirely and found similar results. For plotting purposes, all cross-correlogram averages are displayed as a difference from baseline.

To control for the potential that differences in spike numbers between *5XFAD* and *WT* groups during sharp-wave ripples contributed to the observed differences in trough and peak magnitudes, we subsampled spikes in the *WT* group so that both *5XFAD* and *WT* groups had a similar number of spikes total. We matched total spike counts during sharp-wave ripples between *5XFAD* and *WT* groups using two approaches. In both approaches, both groups had approximately the same number of spikes total after subsampling, erring on the side of the *5XFAD* group having more spikes if the numbers were not exactly the same. In one approach, spikes were removed from spike trains of the *WT* cells before calculating the cross-correlograms and the monosynaptic connection strengths. First, we matched each *5XFAD* recording session with a *WT* session with

the smallest difference in spike counts between them without replacement. Spikes were then randomly selected for removal from the *WT* cell pairs so that the corresponding *WT* session had the same or fewer spikes as the matched *5XFAD* session. Connection strengths were then computed. This spike removal subsampling process and connection strength calculation was repeated 50 times and then averaged across the 50 subsampling events so that each *WT* pair had one metric of connection strength. To ensure a reasonable number of spikes were included in the measurement of connection strength, we also only included pairs with at least 200 spikes across all sharp-wave ripple periods. We found similar results using another approach in which we used the original spike trains but then removed cell pairs from the *WT* group in order to match the spike count total of the *5XFAD* group. Across both of these subsampling analyses, we found similar trends as the full dataset. Furthermore, we found no evidence that differences in synaptic strength were due to differences in firing rates of the neurons or in the cells' spatial position in the CA1 layer.

3.5.9. Place cell identification

To quantify place cells, we calculated an occupancy-normalized firing rate map of putative pyramidal cells as a function of position on the annular track, using spike counts and time spent in 2-degree bins each smoothed with a Gaussian curve. Two degrees is equivalent to 1/180th of the track, which is approximately equivalent to 5 cm physical distance on the ball. These firing rate maps were calculated only using the cell's stable times (as described above). Spatial information for pyramidal cells was then calculated using the firing rate maps by applying the following equation:

$$\text{Spatial information} = \sum_i p_i \frac{\lambda_i}{\lambda} \log_2 \frac{\lambda_i}{\lambda}$$

Where p_i was the probability the animal was in the i th bin, λ was the mean firing rate of the cell, and λ_i was the firing rate of the cell in the i th bin (Langston et al., 2010; Skaggs et al., 1996). We then defined a place cell as any pyramidal cell with a peak firing rate greater than 1 Hz, an average firing rate of less than 10 Hz (to exclude potential interneurons), and a spatial information content in the 95th percentile or above compared to the shuffled spike train data. Because these place cells were recorded in mice and in virtual reality, which tend to have lower spatial information, spatial information is expected to be lower than rats and than recordings made in the real world (Ravassard et al., 2013).

3.5.10. Reactivation during sharp-wave ripples

We examined place cell pair reactivation, activation probability, and pairwise coactivation probability during sharp-wave ripples to assess sharp-wave ripple reactivation while including as many sharp-wave ripple events as possible since *5XFAD* mice had significantly fewer sharp-wave ripples. Standard replay analyses criteria, such as a minimum number of cells active per sharp-wave ripple event, would have biased our analyses against the typical sharp-wave ripples found in the *5XFAD* mice (ripples with shorter duration and altered pyramidal cell firing activity). Instead, we used measures of coactivation and reactivation that assess coordinated spike timing of pairs of cells. Coactivation probability during SWRs in particular is predictive of behavioral performance (Singer et al., 2013). Coactivation probability was calculated by first identifying how many sharp-wave ripples occurred in which a pair of place cells was both stable and active, and then dividing this number by how many total sharp-wave ripples occurred in which the same pair of cells was stable (see **Spike sorting and single unit stability**). Activation probability was calculated similarly, but for single cells instead of pairs of cells. Notably, this analysis is different from analyzing firing activity during sharp-wave ripple events, because we specifically test the activation of place cells and place cell pairs (not all cells), and this metric tests the proportion of sharp-wave ripple events in which place cells are active, not the average firing rate of all cells

during sharp-wave ripple events. To assess place field similarity and reactivation during sharp-wave ripples, we examined relative spike timing of place cell pairs during theta and compared it to relative spike timing during sharp-wave ripples. We quantified spiking near in time versus far in time by taking the sum of the place cell pair cross-correlogram during theta at short time lags (-35ms to +35ms) versus the sum of the cross correlogram during theta at longer time lags (-70 to -35ms, and +35 to +70ms). We converted this to an activity index (short time lag activity – long time lag activity / short time lag activity + long time lag activity), in which a place cell pair with the majority of its spiking within a 70ms window would have a value of 1. We used this activity during theta index to sort these place cell pairs, and examined the cross-correlograms of the same place cell pairs during sharp-wave ripples. We then quantified relative spike timing during sharp-wave ripples as the absolute value of the lag of the maximum correlation value. For these analyses, we excluded sessions with less than 10 sharp-wave ripples because reactivation measures are less accurate over fewer ripples. We found similar results if we included all sessions. To control for the potential that differences in spike numbers between *5XFAD* and *WT* groups during sharp-wave ripples contributed to the observed differences in relative spike timing during sharp-wave ripples, we subsampled spikes in the *WT* group so that both *5XFAD* and *WT* groups had a similar number of spikes total. We matched total spike counts between *5XFAD* and *WT* groups using multiple approaches. In one approach, spikes were removed from spike trains of the *5XFAD* and *WT* cells before calculating the relative spike timing during sharp-wave ripples. First, we matched each *5XFAD* recording session with a *WT* session with the smallest difference in spike counts between them without replacement. Spikes were randomly selected for removal from the *WT* cell pairs if the *WT* session had more spikes than the corresponding *5XFAD* session. Relative spike timing during sharp-wave ripples was then computed. This subsampling process was repeated 50 times and then averaged across the 50 subsampling events so that each pair had one metric of connection strength. We found similar results using another approach in which we used the original spike trains but then removed cell pairs from the *WT* group in order to match the spike

count total of the *5XFAD* group. Across both of these subsampling analyses, we found similar trends as the full dataset.

3.5.11. Quantification and statistical analysis

For each of our genotype groups, we had 6-8 animals, 1-4 recording sessions per animal, and many experimental measurements from each animal (e.g., neurons, ripples, time-periods). As a result, we had a hierarchical data structure with many data points that were not independent of each other. To accurately assess the significance of differences between these genotypes without falsely inflating our sample size via pseudoreplication, we used a hierarchical bootstrapping approach (Carpenter et al., 2003; Efron, 1992; Efron & Tibshirani, 1993; Field & Welsh, 2007; Harden, 2011; Saravanan et al., 2020; Thai et al., 2013). In bootstrapping, N subsamples of the dataset are resampled with replacement from the original data and then the metric of interest is calculated for each subsample. This results in a distribution ($n = N$) of values of the metric of interest. To address the non-independence of the hierarchical data, we applied this bootstrapping separately across all of the levels of the hierarchical data. Thus, to calculate a single subsample, we resampled across the following levels: genotype, animal, recording sessions, data point of interest. For each genotype population (*5XFAD* and *WT*), we resampled with replacement from the second level (animals), then for each resampled animal, we resampled with replacement from the next level (sessions), and finally for each session we resampled with replacement from the lowest level (our data point of interest).

To apply this hierarchical bootstrap approach to our statistical analyses, we calculated the direct posterior probabilities for the hypotheses we tested, and thus we reported our results in terms of direct probabilities of the *WT* population being greater than or equal to the *5XFAD* population. This is in contrast to statistical tests such as t-tests or ANOVAs, which test whether to reject the null hypothesis and their p-values indicate the probability that the null hypothesis is true. We

performed the hierarchical bootstrapping as described above, then calculated the mean of this resampled population of values, and then repeated the bootstrapping 10^4 times. We thus produced a distribution of resampled means for each genotype. These resampled distributions were used to compute whether the metric of interest was significantly different between genotypes. To do so, we calculated a joint probability distribution between the bootstrapped means of the *WT* and *5XFAD* groups. The null hypothesis of no difference between the populations would correspond to a circle centered about the unity line. To test the difference between the *WT* and *5XFAD* groups, we compute the volume of the joint probability distribution on one side of the unity line, thus we quantified the probability of the *WT* population of bootstrapped means being greater than or equal to the *5XFAD* population of bootstrapped means. To quantify error accurately given our hierarchical data, we also used the *WT* and *5XFAD* populations of bootstrapped means to quantify standard error of the mean as the 95% confidence interval of the sample of means. Note that for all reports of mean \pm SEM, the mean was calculated from the actual, not-resampled data, and the SEM was generated from the resampled population. These analyses were performed with custom MATLAB and Python scripts. For a few metrics with noticeable outliers, we excluded outliers detected to be greater than 3 scaled median absolute deviations from the median taken from the distribution of all data from both genotypes. The probability is significant if the direct probability supporting the hypothesis, $p < \alpha/2$ or if $p > (1-\alpha/2)$. Throughout the paper, $\text{prob}(WT \geq 5XFAD)$ is used as shorthand to indicate the probability of the resampled mean metric of *WT* mice being greater than or equal to that of the resampled mean of *5XFAD* mice. Significance values are reported as follows: $\text{prob} > 0.95$ or $\text{prob} < 0.05$ ($\alpha = 0.10$, +), $p > 0.975$ or $\text{prob} < 0.025$ ($\alpha = 0.05$, *), $\text{prob} > 0.995$ or $\text{prob} < 0.005$ ($\alpha = 0.01$, **), $\text{prob} > 0.9995$ or $\text{prob} < 0.0005$ ($\alpha = .001$, ***). Details on specific statistical parameters are described in the figure legends.

3.6. Supplementary Figures and Tables

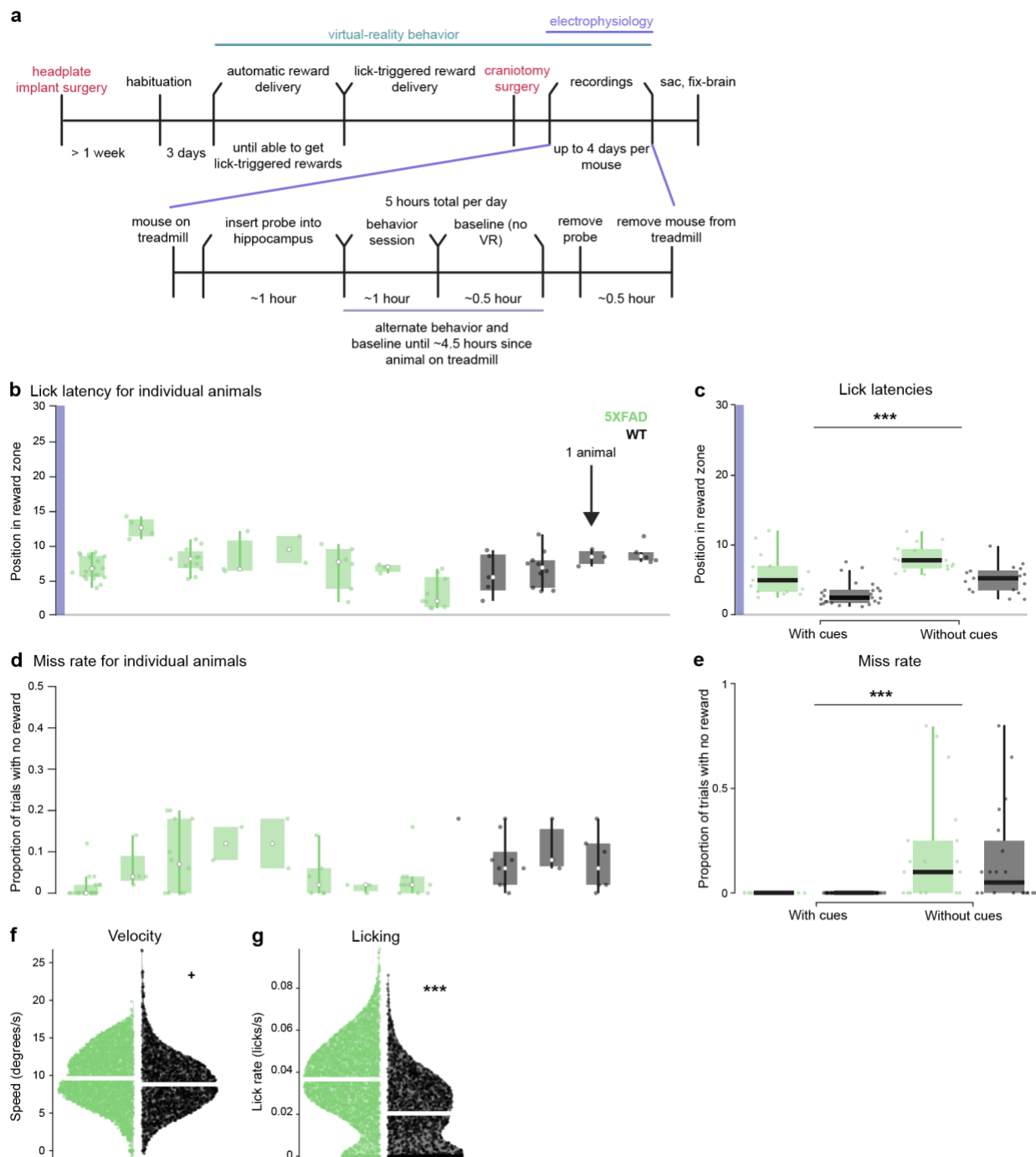


Figure 3.7 Experimental timeline and behavioral metrics for individual animals.

- A.** Timeline of surgeries, behavioral training, and electrophysiological recording sessions.
- B.** Lick latency for 50-trial blocks for individual animals in *5XFAD* (green) and *WT* (black) mice. Purple highlight indicates length of reward zone. Lick latency was only calculated if the animal licked in the reward zone. White dots indicate median value for each animal's distribution, black and green dots indicate 50-trial blocks.
- C.** Lick latency for 50-trial blocks in *5XFAD* (green) and *WT* (black) mice in the track *with visual cues* and the track *without visual cues*. For the comparison between tracks with and without visual cues, six mice not included in the electrophysiological analysis were trained on the annular track. The last two days of the track with cues and the first two days of the track without cues were used for comparison. Black bar indicates median of distribution. Prob(with cues \geq without cues) $< 10^{-4}$ (limit due to resampling 10^4 times) ***. *With cues*: *5XFAD* lick latency percentiles: [2.46 3.30 4.95 6.94 12.06], *WT* lick latency percentiles: [1.15 1.68 2.44 3.49 7.58], *without cues*: *5XFAD* lick latency percentiles: [5.75 6.75 7.82 9.37 11.96], *WT* lick latency percentiles: [2.21 3.57 5.23 6.28 9.86].
- D.** Miss rate (number of laps around the annular track with zero rewards received) for 50-trial blocks for individual animals in *5XFAD* (green) and *WT* (black) mice. We observed some outlier trial blocks, and we removed these outliers as described in the **Methods**.
- E.** Miss rate for 50-trial-blocks in the annular track *with visual cues* versus the track *without visual cues* in both *5XFAD* (green) and *WT* (black) mice. Black bar indicates median of distribution. Prob(with cues \geq without cues) $< 10^{-4}$ (limit due to resampling 10^4 times) ***. *With cues*: *5XFAD* miss rate percentiles: [0 0 0 0 0], *WT* miss rate percentiles: [0 0 0 0 0], *without cues*: *5XFAD* miss rate percentiles: [0 0 0.10 0.25 0.80], *WT* miss rate percentiles: [0 0 0.05 0.23 0.80].
- F.** Distribution of velocities (degrees per second) in *5XFAD* (green) and *WT* (black) mice. Each data point is the average for a trial, not an entire session. White bar indicates median of distribution. *5XFAD*: 9.77 ± 0.58 , *WT*: 8.98 ± 0.57 . Prob(*WT* \geq *5XFAD*) = 0.036 +, *5XFAD*: degrees per second percentiles = [-0.75 7.18 9.62 12.46 19.85], *WT*: degrees per second percentiles = [-0.39 6.41 8.83 11.32 26.68].
- G.** Distribution of licking rates in *5XFAD* (green) and *WT* (black) mice. Each data point is the average for a trial, not an entire session. White bar indicates median of distribution. *5XFAD*: 0.036 ± 0.0028 Hz, *WT*: 0.021 ± 0.0027 . Prob(*WT* \geq *5XFAD*) $< 10^{-4}$ (limit due to resampling 10^4 times) ***, *5XFAD*: lick rate percentiles = [0 0.024 0.037 0.049 0.098], *WT*: lick rate percentiles = [0 0.0045 0.020 0.033 0.086].

All percentiles are min, 25th percentile, median, 75th percentile, max.

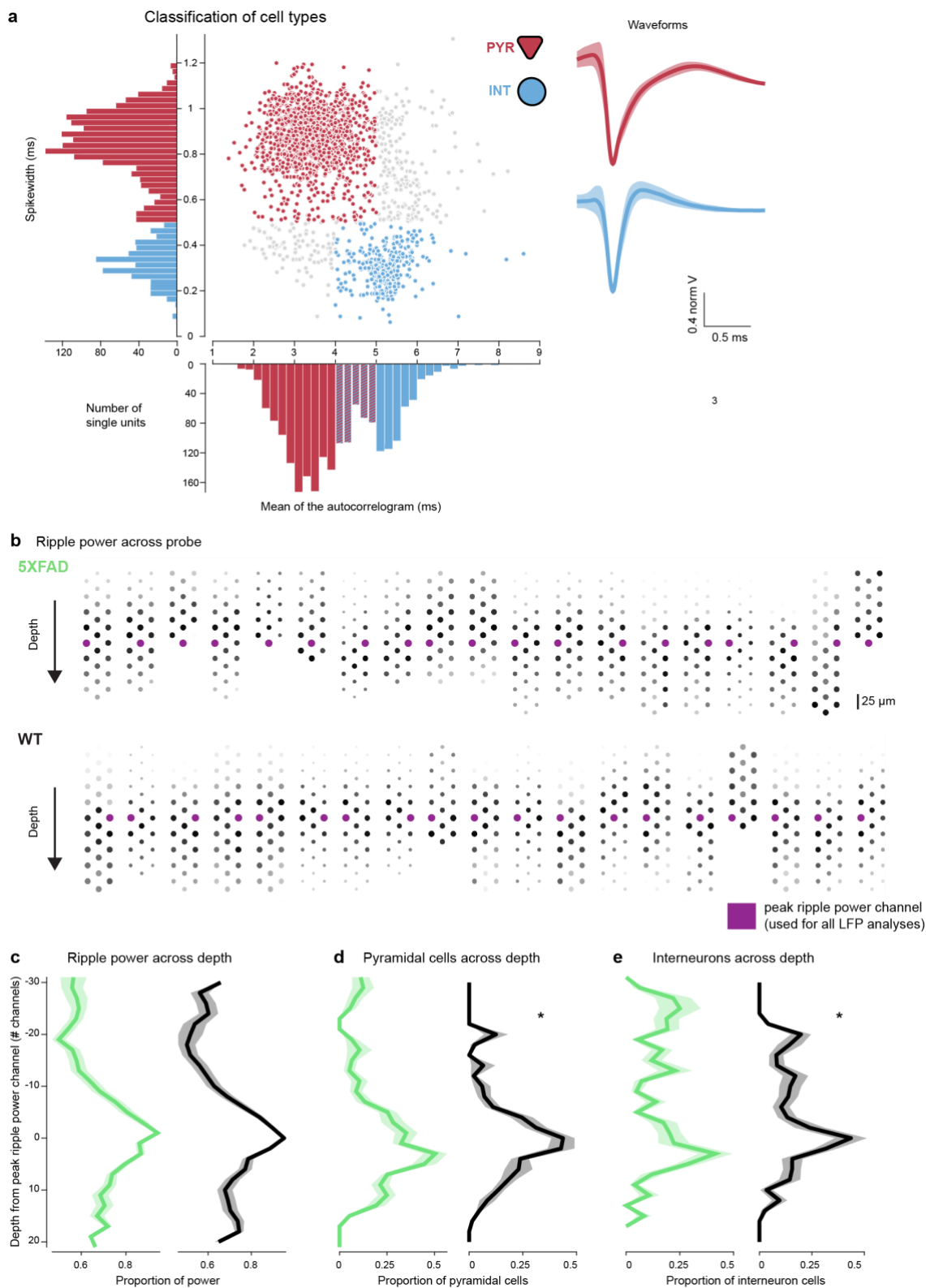


Figure 3.8 Recording locations and classification of putative pyramidal cells and interneurons.

- A.** Spike width and mean of the autocorrelogram distributions for all recorded single units with putative pyramidal cells in red and putative interneurons in blue. Each point is a single unit. For histograms, color indicates how cells in this part of the distribution were classified. Inset, *right*, shows average waveforms with standard deviation (shaded) of the classified pyramidal cells and interneurons.
- B.** *Top*, Sharp-wave ripple power across 32-channel NeuroNexus recording electrodes in *5XFAD* mice. Darker color and larger circles indicate higher sharp-wave ripple power (150-250 Hz), purple channel indicates the channel with the highest sharp-wave ripple power and is the channel used in all LFP analyses. *Bottom*, same as top in *WT* mice.
- C.** Average proportion of sharp-wave ripple power across recording depth (linearized probe channels), centered by channel with peak sharp-wave ripple power in *5XFAD* (green) and *WT* (black) mice, mean \pm SEM..
- D.** Average proportion of pyramidal cells across recording depth, centered by peak ripple power channel in *5XFAD* (green) and *WT* (black) mice. *5XFAD*: $-3.62 \pm 7.64 \mu\text{m}$, $n = 708$ *WT*: $-15.75 \pm 6.53 \mu\text{m}$, $n = 580$ cells. $\text{Prob}(WT \geq 5XFAD) = 0.016 *$, *5XFAD*: distance from center (μm) percentiles = [-125 -25 50 112.5 250], *WT*: distance from center (μm) percentiles =[-125 -25 0 75 175].
- E.** As in **D** for interneurons. *5XFAD*: $54.95 \pm 20.89 \mu\text{m}$, $n = 187$ cells, *WT*: $21.66 \pm 23.05 \mu\text{m}$, $n = 146$ cells. $\text{Prob}(WT \geq 5XFAD) = 0.0058 *$, *5XFAD*: distance from center (μm) percentiles = [-125 -37.5 -12.5 25 275], *WT*: distance from center (μm) percentiles =[-137.5 -50 -12.5 12.5 150].

All percentiles are min, 25th percentile, median, 75th percentile, max

Figure 3.9 Interneuron-to-pyramidal cell connection strength for individual animals and percent connections.

- A.** Interneuron-to-pyramidal (INT-to-PYR) cell connection strength during sharp-wave ripples for individual recording sessions in *5XFAD* (green) and *WT* (black) mice. Each data point is the connection strength of an INT-to-PYR cell pair across all sharp-wave ripple periods. Each violin plot represents a single recording session, white dots indicate median, and the bars along the x-axis indicate all recording sessions belonging to a single animal. Sessions with no putatively connected INT-to-PYR cell pairs with spiking during sharp-wave ripple periods were excluded from the plot.
- B.** As in **A** during non-theta periods.
- C.** As in **A** during theta periods.
- D.** Proportion of INT-to-PYR monosynaptic connections out of all cell pairs in *5XFAD* (green) and *WT* (black) mice. Boxplot indicates quartiles, whiskers indicate range, and black line indicates median of distribution. Each individual data point represents a single recording session. Of pairs of cells that had enough spikes to detect potential monosynaptic connections, INT-to-PYR connections accounted for $2.21\% \pm 0.46\%$ and $4.44\% \pm 2.34\%$ of pairs in *5XFAD* and *WT* mice, respectively. $\text{Prob}(WT \geq 5XFAD) = 0.98^*$, *5XFAD*: $n = 19$ sessions, proportion of connections percentiles = [0, 0.49, 1.71, 3.10, 7.70], *WT*: $n = 20$ sessions, proportion of connections percentiles = [0, 0.94, 2.05, 5.21, 25.00].
- E.** Example of subsampled results from monosynaptic connection strength analysis that controlled for total spike count numbers between *5XFAD* and *WT* mice by subsampling spikes from connected pair spike trains. A randomly selected subsampled iteration is shown; subsampling was repeated 50 times. The results for the other subsampling approach removing INT-to-PYR connected pairs were as follows: *5XFAD*: -0.14 ± 0.13 trough magnitude, $n = 146$ cell pairs, *WT*: -0.34 ± 0.20 trough magnitude, $n = 65$ cell pairs, $\text{prob}(5XFAD \geq WT) = 0.9534$, bootstrap test. *Left*, Average cross-correlogram of monosynaptically connected INT-to-PYR cell pairs between *5XFAD* (green) and *WT* (black) mice during sharp-wave ripple periods from -10 to +10 ms lags normalized by geometric mean firing rate and displayed as difference from baseline, mean \pm SEM. *Right*, zoomed in view of average cross-correlogram on *left* from 0 to 10s lag. Light blue box indicates region where connection strength was measured. Inhibitory connection strength was measured as the minimum value in the 1-4ms window. We rectified any positive peak values to zero to correct for pairs that likely did not fire enough spikes or were too noisy during the periods we analyzed. We found similar results when we excluded these pairs entirely. These cross-correlograms that were rectified for the strength measurement are not included in the visualization of the average and individual cross-correlograms. Statistics described in **F**.
- F.** *Left*, Example of subsampled results to control for spike counts as in **E**. Connection strengths as measured by trough magnitude in *5XFAD* and *WT* mice during sharp-wave ripple periods were averaged across 50 random subsampling iterations. Each dot indicates the connection strength measured from a single INT-to-PYR cell pair across all non-theta periods. *Right*, individual cross-correlograms of putative INT-to-PYR cell connected pairs during sharp-wave ripple periods that make up the average shown above in **E**. Heat map indicates change in correlation from baseline measurement. Note cross-correlograms during sharp-wave ripples look more variable because there are fewer spikes during sharp wave ripples than during non-theta and theta periods. The number of spikes included in this figure was 42,065 in *5XFAD* mice and 41,227 in *WT* mice. *5XFAD*: -0.22 ± 0.078 trough magnitude, *WT*: -0.35 ± 0.13 trough magnitude. $\text{Prob}(5XFAD \geq WT) = 0.988^*$; here $5XFAD \geq WT$ indicates a deficit in inhibition because inhibitory troughs are negative, *5XFAD*: $n = 79$ INT-to-PYR cell pairs,

connection strength percentiles = [-3.86 -0.24 -0.09 0 0], WT: n = 87 INT-to-PYR cell pairs,
connection strength percentiles = [-1.65 -0.48 -0.30 -0.14 0].
All percentiles are min, 25th percentile, median, 75th percentile, max

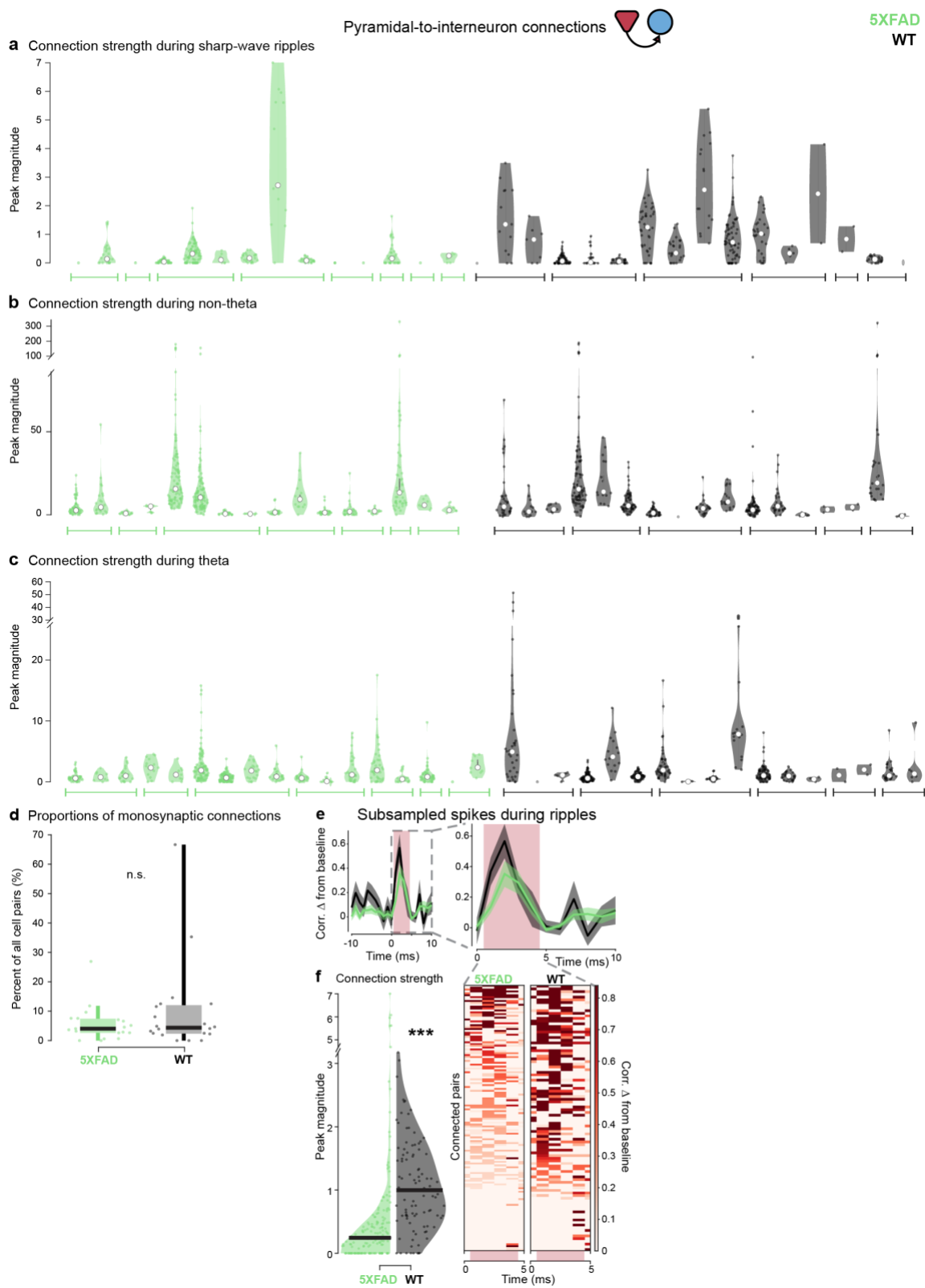


Figure 3.10 Pyramidal-to-interneuron connection strength for individual animals and percent connections.

- A.** Pyramidal-to-interneuron (PYR-to-INT) cell connection strength during sharp-wave ripples for individual recording sessions in *5XFAD* (green) and *WT* (black) mice. Each data point is the connection strength of a PYR-to-INT pair across all sharp-wave ripple periods. Each violin plot represents a single recording session, and the bars along the x-axis indicate all recording sessions belonging to a single animal.
- B.** As in **A** for during non-theta periods.
- C.** As in **A** during theta periods.
- D.** Proportion of PYR-to-INT monosynaptic connections out of all cell pairs in *5XFAD* (green) and *WT* (black) mice. Boxplot indicates quartiles, whiskers indicate range, and black line indicates median of distribution. Each individual data point represents a single recording session. Of pairs of cells that had enough spikes to detect potential monosynaptic connections, we found that on average $5.64\% \pm 0.78\%$ were putative PYR-to-INT connections in *5XFAD* mice, and $9.84\% \pm 6.04\%$ of cell pairs were PYR-to-INT connections in *WT* mice. $\text{Prob}(WT \geq 5XFAD) = 0.93$, *5XFAD*: $n = 19$ sessions, proportion of connections percentiles = [0, 2.64, 4.05, 7.33, 26.92], *WT*: $n = 20$ sessions, proportion of connections percentiles = [0, 2.41, 4.37, 11.81, 66.67].
- E.** Example of subsampled results from monosynaptic connection strength analysis that controlled for total spike count numbers between *5XFAD* and *WT* mice by subsampling spikes from connected pair spike trains. A randomly selected subsampled iteration is shown; subsampling was repeated 50 times. The results for the other subsampling removing PYR-to-INT connected pairs were as follows: *5XFAD*: 0.36 ± 0.28 peak magnitude, $n = 306$ cell pairs, *WT*: 0.62 ± 0.23 peak magnitude, $n = 166$ cell pairs, $\text{prob}(WT \geq 5XFAD) = 0.9221$, *Left*, Average cross-correlogram of monosynaptically connected PYR-to-INT cell pairs between *5XFAD* (green) and *WT* (black) mice during sharp-wave ripple periods from -10 to +10 ms lags. Normalized by geometric mean firing rate and displayed as difference from baseline, mean \pm SEM. *Right*, view of average cross-correlogram on *left* from 0 to 10 ms lag. Light pink box indicates region where connection strength was measured. Excitatory connection strength was measured as the maximum value in the 1-4ms window. Statistics described in **F**.
- F.** *Left*, Example of subsampled results to control for spike counts as in **E**. Connection strengths as measured by peak magnitude in *5XFAD* and *WT* mice during sharp-wave ripple periods were averaged across 50 random subsampling iterations. Each dot indicates the connection strength measured from a single PYR-to-INT cell pair across all sharp-wave ripple periods. *Right*, individual cross-correlograms of putative PYR-to-INT cell connected pairs during sharp-wave ripple periods. The individual cross-correlograms make up the average shown above in **E**. Heat map indicates change in correlation from baseline measurement. Note cross-correlograms during sharp-wave ripples look more variable because there are significantly fewer spikes during sharp wave ripples than during non-theta and theta periods. The number of spikes included in this figure was 96,736 in *5XFAD* mice and 95,871 in *WT* mice. *5XFAD*: 0.57 ± 0.36 peak magnitude, *WT*: 1.08 ± 0.17 peak magnitude. $\text{Prob}(WT \geq 5XFAD) = 0.9988^{***}$, *5XFAD*: $n = 162$ PYR-to-INT cell pairs, connection strength percentiles = [0 0 0.25 0.52 7.0], *WT*: $n = 98$ INT-to-PYR cell pairs, connection strength percentiles = [0 0.59 1.0 1.57 3.18].

All percentiles are min, 25th percentile, median, 75th percentile, max

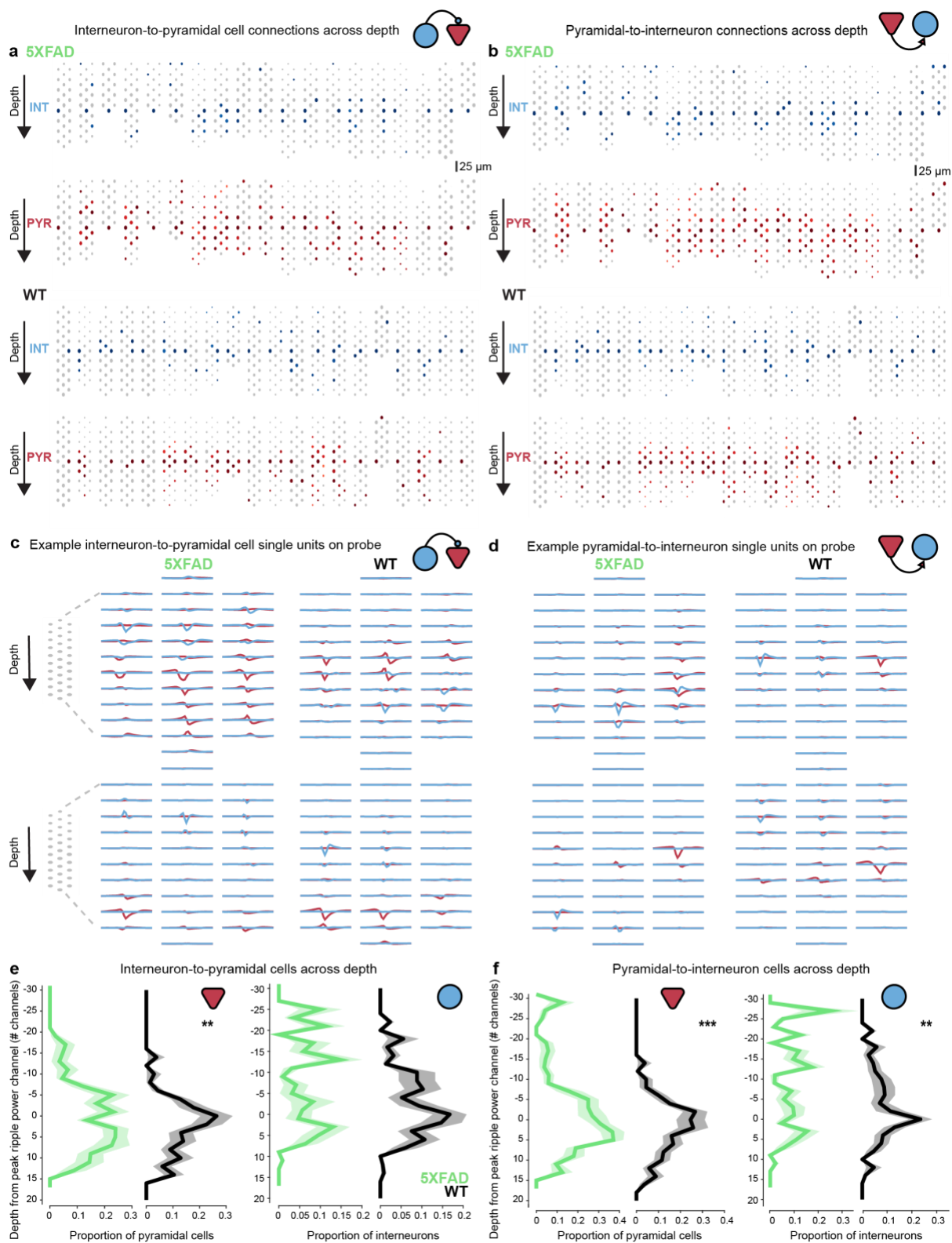


Figure 3.11 Distribution of monosynaptically connected cell pairs across the electrode.

- A.** Distribution across 32-channel NeuroNexus probe of putative pyramidal cells and interneurons that are part of monosynaptically connected interneuron-to-pyramidal cell pairs in *5XFAD* mice, centered by the peak sharp-wave ripple power channel. Dot size indicates ripple power relative to the peak ripple channel. Darker color indicates larger proportion of single units, blue indicates interneurons, red indicates pyramidal cells. We examined the distribution of pyramidal cells and interneurons that were part of monosynaptically connected pairs relative to the center of the pyramidal layer as measured by the peak ripple power channel of the recording probe.
- B.** As in **A** for pyramidal-to-interneuron cell pairs.
- C.** Examples of average waveforms across 32-channel NeuroNexus probe of putative pyramidal cells and interneurons that are part of monosynaptically connected interneuron-to-pyramidal cell pairs in *5XFAD* (left) and *WT* (right) mice. Blue indicates interneurons, red indicates pyramidal cells.
- D.** As in **C** for pyramidal-to-interneuron cell pairs.
- E.** Distributions of putative pyramidal cells and interneurons that are part of monosynaptically connected interneuron-to-pyramidal cell pairs across recording depth. *Left*, Average proportion of putative pyramidal cells out of all pyramidal cells across recording depth, centered by peak sharp-wave ripple power channel in *5XFAD* (green) and *WT* (black) mice. *5XFAD*: $-3.98 \pm 6.90 \mu\text{m}$, $n = 176$ cells, *WT*: $-19.49 \pm 8.15 \mu\text{m}$, $n = 161$. $\text{Prob}(WT \geq 5XFAD) = 0.0017$ **, *5XFAD*: distance from center (μm) percentiles = [-112.5 -37.5 -6.25 25 150], *WT*: distance from center (μm) percentiles = [-125 -50 -12.5 12.5 112.5]. We controlled for these differences and found similar results for deficits in inhibitory connection strengths (see **Methods**). *Right*, As in **C** for interneurons. *5XFAD*: $46.30 \pm 22.94 \mu\text{m}$ from peak ripple channel, $n = 54$ cells, *WT*: $14.62 \pm 22.32 \mu\text{m}$, $n = 59$ cells. $\text{Prob}(WT \geq 5XFAD) = 0.028$ +, *5XFAD*: distance from center (μm) percentiles = [-100 -25 25 112.5 200], *WT*: distance from center (μm) percentiles = [-125 -25 0 56.25 175].
- F.** As in **E** for pyramidal-to-interneuron cell pairs. *Left*, Average proportion of putative pyramidal cells out all pyramidal cells across recording depth, centered by peak sharp-wave ripple power channel in *5XFAD* (green) and *WT* (black) mice. *5XFAD*: $1.91 \pm 9.72 \mu\text{m}$, $n = 308$ cells, *WT*: $-18.25 \pm 7.56 \mu\text{m}$, $n = 252$ cells. $\text{Prob}(WT \geq 5XFAD) = 0.0001$ ***, *5XFAD*: distance from center (μm) percentiles = [-112.5 -37.5 0 25 237.5], *WT*: distance from center (μm) percentiles = [-137.5 -50 -12.5 12.5 112.5]. *Right*, As in **C** for interneurons. *5XFAD*: $56.11 \pm 22.11 \mu\text{m}$, $n = 88$ cells, *WT*: $13.97 \pm 20.44 \mu\text{m}$, $n = 68$ cells $\text{Prob}(WT \geq 5XFAD) = 0.0025$ **, *5XFAD*: distance from center (μm) percentiles = [-100 -25 43.75 112.5 225], *WT*: distance from center (μm) percentiles = [-125 -25 0 53.13 175].

All percentiles are min, 25th percentile, median, 75th percentile, max

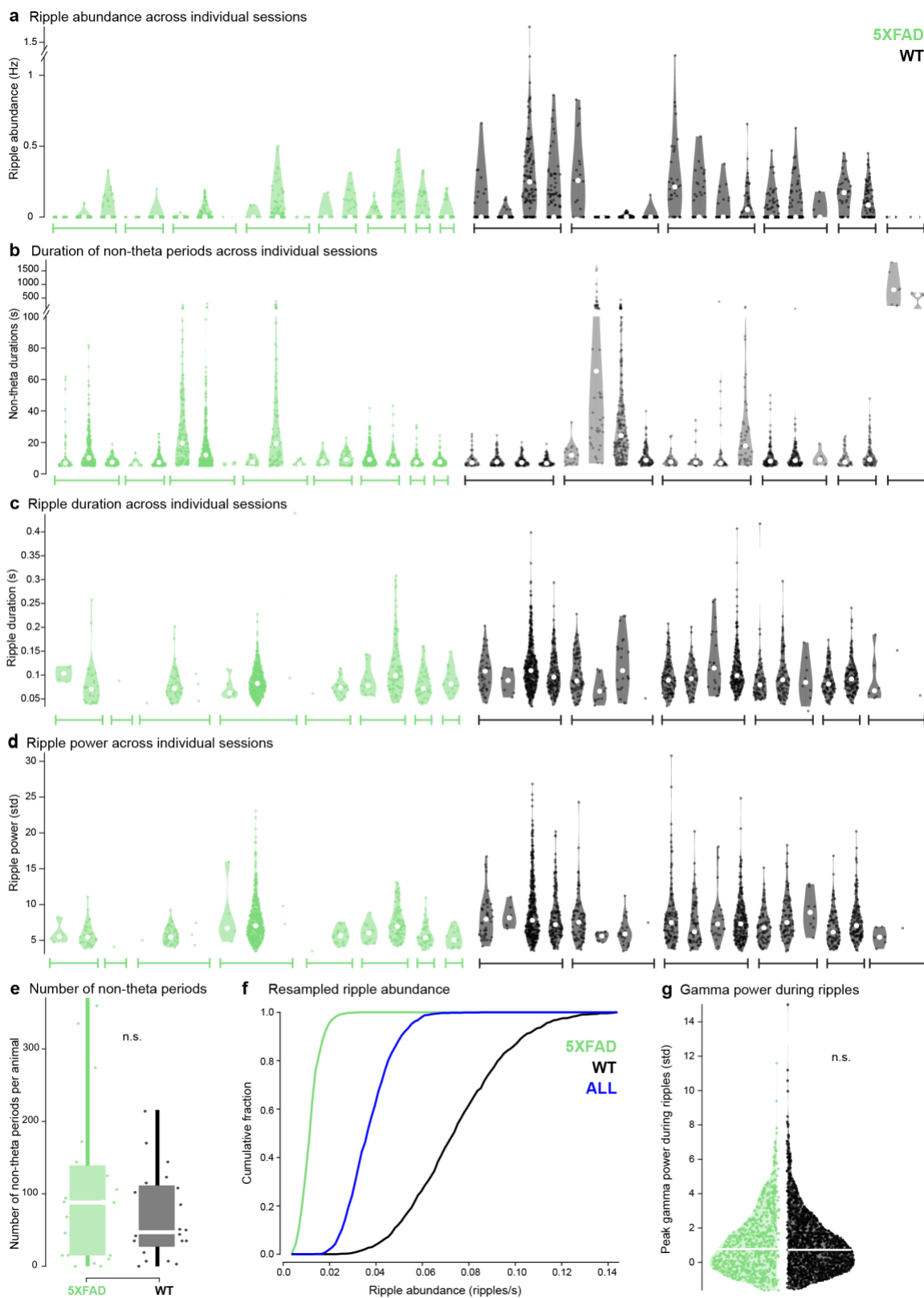


Figure 3.12 Ripple abundance, duration, and power per recording and resampled distributions.

- A.** Abundance of sharp-wave ripple events during non-theta periods longer than five seconds in *5XFAD* (green) and *WT* (black) mice by individual recording sessions. Each data point represents a non-theta period. White dots indicate median of distribution. Each violin plot represents a single recording session, and the bars along the x-axis indicate all recording sessions belonging to a single animal. We also controlled for the potential of poor ripple detection by excluding sessions with fewer than 10 SWR events, and we found that *5XFAD* mice still had significantly lower SWR abundance (*5XFAD*: 0.020 ± 0.011 SWR abundance, $n = 1252$ non-theta periods five seconds or longer, *WT*: 0.093 ± 0.047 SWR abundance $n = 1097$ non-theta periods five seconds or longer, $\text{prob}(WT \geq 5XFAD) > 0.9999$ (limit due to resampling 10^4 times), bootstrap test).
- B.** Duration of non-theta periods five seconds or longer for individual recording sessions in *5XFAD* (green) and *WT* (black) mice. Each data point represents a non-theta period. $\text{Prob}(WT \geq 5XFAD) = 0.9811$, *5XFAD*: $n = 1969$ non-theta periods, duration of non-theta periods percentiles = [5.00, 6.47, 9.06, 14.93, 375.47], *WT*: $n = 20$ sessions, duration of non-theta periods percentiles = [5, 6.50, 8.95, 16.16, 1815.09].
- C.** Duration of sharp-wave ripple events in *5XFAD* (green) and *WT* (black) mice by individual recording sessions. Each data point represents a sharp-wave ripple event. Each violin plot represents a single recording session, and the bars along the x-axis indicate all recording sessions belonging to a single animal. White dots indicate median of distribution. Violin plot outlines (but not the individual data points) were removed for sessions with 3 or fewer data points.
- D.** Standardized power of sharp-wave ripple events in *5XFAD* (green) and *WT* (black) mice by individual recording sessions. Each data point represents a sharp-wave ripple event. White dots indicate median of distribution.
- E.** Number of non-theta periods greater than five seconds long for individual recording sessions in *5XFAD* (green) vs *WT* (black) mice. Each data point represents a single recording session. White line indicates median of distribution. *5XFAD*: 103.63 ± 43.39 periods per session, *WT*: 69.45 ± 20.27 periods per session. $\text{Prob} = 0.078$, *5XFAD*: $n = 19$ sessions, number of non-theta periods percentiles = [0, 15, 88, 134.5, 369], *WT*: $n = 20$ sessions, number of non-theta periods percentiles = [0, 31, 47, 109.75, 214].
- F.** Resampled distributions of abundance of sharp-wave ripple events during non-theta periods longer than five seconds from hierarchical bootstrapping within *5XFAD* (green) and *WT* (black) groups versus across *all* (blue) groups. These results show that resampling from within each group is very different than resampling across groups, which would not be the case if there was no difference between the *5XFAD* and *WT* groups.
- G.** When analyzing z-scored gamma power during SWRs, we found the strength of gamma was not different in the remaining SWRs of the *5XFAD* animals compared to the *WT* littermates. Z-scored peak slow gamma power (20-50 Hz) of sharp-wave ripple events in *5XFAD* (green) and *WT* (black) for all sessions. White line indicates median of distribution. *5XFAD*: 1.15 ± 0.80 z-scored power, $n = 776$ sharp-wave ripples, *WT*: 1.11 ± 0.34 z-scored power, $n = 1542$ sharp-wave ripples, $\text{prob}(WT \geq 5XFAD) = 0.53$.
- All percentiles are min, 25th percentile, median, 75th percentile, max

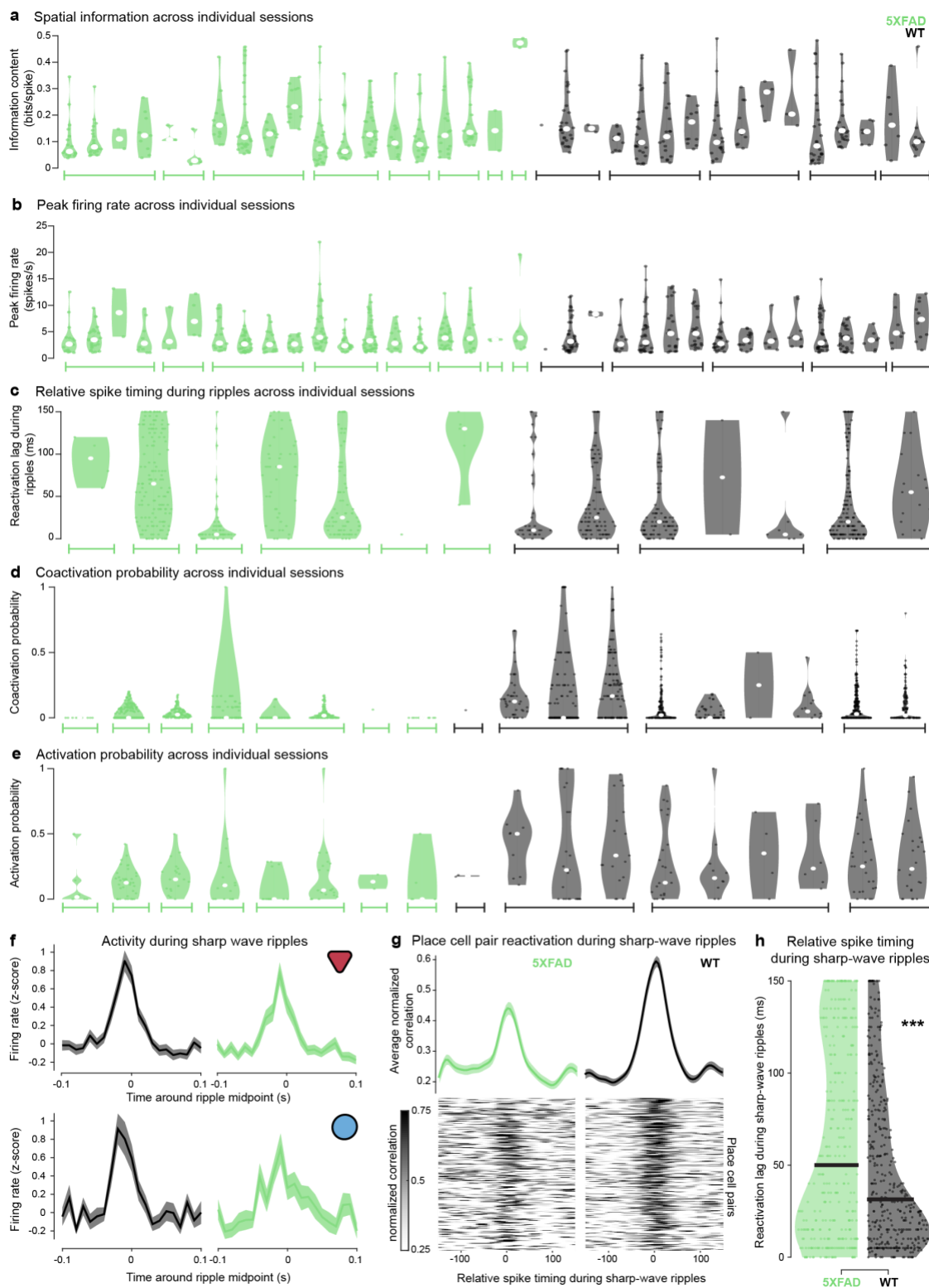


Figure 3.13 Place cell properties and place cell pair reactivation during sharp-wave ripples for individual sessions.

- A.** Individual recording session distributions of spatial information of place cells with spatially tuned firing in the task in *5XFAD* (green) and *WT* (black) mice. Each data point represents a place cell. Each violin plot represents a single recording session, and the bars along the x-axis indicate all recording sessions belonging to a single animal. White dots indicate median of distribution. Sessions with no place cells are not shown.
- B.** Individual recording session distributions of peak firing rate of place cells with spatially tuned firing in the task in *5XFAD* and *WT* mice. Each data point represents a place cell.
- C.** Reactivation lag (or relative spike timing) of place cell pairs during sharp-wave ripples in *5XFAD* (green) and *WT* (black) mice for individual recording sessions. Reactivation lag was measured as the peak relative spike timing during sharp-wave ripples. Each data point represents the reactivation lag of a place cell pair during all sharp-wave ripple events. Each violin plot represents a single recording session, and the bars along the x-axis indicate all recording sessions belonging to a single animal. Sessions with fewer than 10 sharp-wave ripple events were excluded from the analysis. When we included all sessions we saw similar results.
- D.** Coactivation probabilities of place cell pairs during sharp-wave ripples in *5XFAD* (green) versus *WT* (black) mice for individual recording sessions. Each data point represents the coactivation probability of a place cell pair during all sharp-wave ripple events. Sessions with fewer than 10 sharp-wave ripple events were excluded from the analysis. Sessions with no co-active place cell pairs are also not shown here.
- E.** Activation probabilities of place cell pairs during sharp-wave ripples in *5XFAD* (green) versus *WT* (black) mice for individual recording sessions. Each data point represents the activation probability of a place cell during all sharp-wave ripple events. Sessions with fewer than 10 sharp-wave ripple events were excluded from the analysis.
- F.** *Top left*, putative pyramidal cell firing activity during sharp-wave ripples in *5XFAD* (green) vs *WT* (black) mice, centered around ripple midpoint, mean \pm SEM. *Top right*, peak z-scored firing rate of pyramidal cells during sharp-wave ripples. Each data point represents the z-scored firing rate of a single pyramidal cell across all sharp-wave ripple events. *5XFAD*: 2.11 ± 0.44 probability, *WT*: 2.35 ± 0.49 probability, $\text{Prob}(WT \geq 5XFAD) = 0.75$, *5XFAD*: $n = 237$ pyramidal cells, z-scored firing rate percentiles = [-0.59 -0.18 1.95 3.85 7.68], *WT*: $n = 266$ pyramidal cells, z-scored firing rate percentiles = [-0.74 -0.13 2.32 3.93 7.68]. *Bottom left*, interneuron cell firing activity during sharp-wave ripples in *5XFAD* (green) vs *WT* (black) mice, centered around ripple midpoint, mean \pm SEM. *Bottom right*, peak z-scored firing rate of interneurons during sharp-wave ripples. Each data point represents the z-scored firing rate of a single pyramidal cell across all sharp-wave ripple events. *5XFAD*: 1.89 ± 0.32 probability, *WT*: 1.96 ± 0.57 probability $\text{Prob}(WT \geq 5XFAD) = 0.62$, *5XFAD*: $n = 81$ interneurons, z-scored firing rate percentiles = [-0.33 0.74 1.93 2.93 5.39], *WT*: $n = 94$ interneurons, z-scored firing rate percentiles = [-0.46 -0.13 1.78 3.49 7.68]. We also found the firing rates of putative pyramidal cells and interneurons did not differ during non-theta and theta periods (non-theta periods *5XFAD*: 1.85 ± 0.89 Hz, $n = 627$ pyramidal cells, *WT*: 2.14 ± 0.36 Hz, $n = 519$ pyramidal cells, $\text{prob}(WT \geq 5XFAD) = 0.90$ *5XFAD*: 7.90 ± 1.45 Hz, $n = 163$ interneurons, *WT*: 7.96 ± 2.22 Hz, $n = 135$ interneurons, $\text{prob}(WT \geq 5XFAD) = 0.54$ bootstrap test; theta periods *5XFAD*: 1.85 ± 0.33 Hz, $n = 593$ pyramidal cells, *WT*: 2.11 ± 0.33 Hz, $n = 460$ pyramidal cells, $\text{prob}(WT \geq 5XFAD) = 0.89$ *5XFAD*: 8.52 ± 1.70 Hz, $n = 169$ interneurons, *WT*: 9.99 ± 2.59 Hz, $n = 126$ interneurons, $\text{prob}(WT \geq 5XFAD) = 0.87$ data not shown).
- G.** Example output of place cell reactivation analysis controlling for spike numbers between *5XFAD* and *WT* mice by subsampling spikes from place cell pair spike trains so that the final spike counts are more similar. The averages and heatmaps demonstrate one random subsampling, which was repeated 50 times to get an average relative spike timing during sharp-wave ripples for each cell pair. Reactivation during sharp-wave ripple events of place

cell pairs with spiking near in time during theta in *5XFAD* and *WT* mice. For the other subsampling approach of removing place cell pairs, the results were as follows: *5XFAD*: 59.99 ± 7.36 ms, $n = 334$ place cell pairs, *WT*: 43.42 ± 6.47 ms, $317 =$ place cell pairs, $\text{prob}(WT \geq 5XFAD) = 0.0003$. *Bottom*, heat maps of normalized cross-correlograms of place cell pairs during sharp-wave ripples with spiking near in time during theta (lower half of the activity index of all place cell pairs). *Top*, average of all place cell pair reactivation during sharp-wave ripple events with spiking near in time during theta.

- H.** Relative spike timing during sharp-wave ripples in place cells were averaged across 50 random subsampling iterations. Since the *5XFAD* group was not subsampled, these reactivation lag values follow discrete time bins versus the *WT* group which were averages of 50 discrete time bin values for each place cell pair from the subsampling analysis. Relative spike timing during sharp-wave ripples in place cells that spike near in time during theta in *5XFAD* (green) and *WT* (black) mice. Each dot indicates the peak reactivation lag of a single place cell pair across all sharp-wave ripple events. The number of spikes included in this figure was 107,412 in *5XFAD* mice and 107,232 in *WT* mice. Black bar indicates median of distribution. *5XFAD*: 64.15 ± 7.03 ms, *WT*: 47.96 ± 4.89 ms. $\text{Prob}(WT \geq 5XFAD) = 0.0001$ (limit due to resampling 10^4 times) ^{***}, *5XFAD*: $n = 335$ place cell pairs, spike timing lags during ripples percentiles = [0 15 50 120 150], *WT*: $n = 385$, spike timing lags during ripples percentiles = [0 10 31.40 79.2 150].

All percentiles are min, 25th percentile, median, 75th percentile, max

Animal	Genotype	Breeding pair	Recording session	Total duration of recording sessions (min)	Single units	Sharp-wave ripples	Total duration of non-theta periods (min)	Monosynaptic connections (PYR-INT, INT-PYR)
F1	5XFAD	A	1	185.21	83	0	21.61	0,0
F1	5XFAD	A	2	181.62	85	4	83.08	63,21
F1	5XFAD	A	3	86.76	24	0	0	10,0
F1	5XFAD	A	4	129.60	85	32	22.63	25,18
F7	5XFAD	A	1	105.59	71	0	7.41	15,4
F7	5XFAD	A	2	136.22	61	1	39.16	9,9
F8	WT	A	1	104.99	7	45	15.40	0,0
F8	WT	A	2	112.81	119	7	26.41	34,18
F8	WT	A	3	124.14	20	392	24.08	13,4
F8	WT	A	4	125.57	12	157	24.58	7,3
F9	WT	B	1	123.23	33	83	5.30	0,0
F9	WT	B	2	170.61	58	11	169.21	86,59
F9	WT	B	3	164.45	43	23	154.14	16,11
F9	WT	B	4	50.27	92	1	28.95	62,21
F10	5XFAD	B	1	78.43	99	1	71.64	100,57
F10	5XFAD	B	2	170.93	89	45	122.23	103,45
F10	5XFAD	B	3	150.86	53	3	3.46	22,15
F10	5XFAD	B	4	50.30	122	0	0.19	21,6
F11	5XFAD	B	1	157.87	92	6	6.70	27,6
F11	5XFAD	B	2	142.93	81	501	73.13	14,6
F11	5XFAD	B	3	152.93	86	2	3.88	32,13
F12	WT	B	1	146.18	110	113	8.25	43,26
F12	WT	B	2	141.64	87	67	9.56	23,3
F12	WT	B	3	98.61	30	24	17.45	25,11
F12	WT	B	4	46.77	60	216	23.00	16,6
F13	5XFAD	B	1	207.25	57	1	4.37	40,26
F13	5XFAD	B	2	186.25	58	22	11.43	21,10
F14	WT	B	1	153.42	141	74	38.65	71,56
F14	WT	B	2	155.48	84	87	43.90	29,11
F14	WT	B	3	50.20	53	8	2.33	6,2
F15	WT	C	1	135.00	14	91	9.01	2,2
F15	WT	C	2	126.71	10	135	21.38	2,2
F16	5XFAD	C	1	161.75	90	15	80.00	51,26
F16	5XFAD	C	2	75.71	85	87	24.43	0,0

F18	<i>5XFAD</i>	C	1	94.89	12	40	25.93	7,2
F19	<i>5XFAD</i>	D	1	96.52	30	16	28.39	10,1
F20	<i>WT</i>	D	1	133.97	56	6	93.62	26,14
F20	<i>WT</i>	D	2	95.88	24	1	1.08	6,2
F20	<i>WT</i>	D	3	23.45	31	1	23.41	0,0

Table 3.1 Genotypes, recording sessions, single units, sharp-wave ripples, and putative monosynaptic connections per animal.

CHAPTER 4 - DISCUSSION

4.1 Results summary

In this work we asked how our brains integrate past, present, and future information to make decisions and adapt plans in our changing environments, and how neural codes for these processes are disrupted in Alzheimer's disease. In *Chapter 2*, we focused on how neural representations for future locations or choices in hippocampus and prefrontal cortex contribute to the ability to flexibly adapt behavior with new information. To address this question, we developed a novel behavioral task in which we precisely controlled the timing of new information and we recorded simultaneously from many single units in hippocampus and prefrontal cortex. We found that codes for future locations in hippocampus are overrepresented in response to new information while codes for choices in prefrontal cortex rapidly switch from the old choice to the new choice in response to new information. Furthermore, failure to successfully update behavior is reflected in prefrontal neural activity despite similar goal overrepresentation in hippocampus on correct and incorrect trials. This work shows how prospective codes change when new, pivotal information is presented for flexible planning and decision making in dynamic environments. In *Chapter 3*, we asked how neural codes for memory and navigation were disrupted in Alzheimer's disease and how these codes might be related to synaptic activity in vivo. To address this question, we leveraged in vivo, large-scale recordings in an awake, behaving mouse to ask how putative monosynaptic connections and sharp-wave ripple activity were altered in a mouse model of Alzheimer's disease. We found that inhibitory-to-excitatory connections were disrupted, and this disruption was most pronounced during sharp-wave ripple oscillations. Furthermore, these animals had fewer and shorter sharp-wave ripples and impaired place cell reactivation during ripples. These results connected inhibitory and synaptic dysfunction literature and suggested a possible mechanism underlying deficits in network activity important for memory processes.

Since our *Chapter 3* work was published, we have also asked how goal codes in the hippocampus contribute to navigation in health and Alzheimer's disease (Zhang et al., 2022). For this study, the dissertation author collected and preprocessed the electrophysiological and behavioral data, and Lu Zhang and Abigail Paulson performed the analyses. In this work, we used the same data from *Chapter 3*, in which our virtual reality task had the same cues used in multiple locations in the track, so animals had to discriminate between true and false reward zone locations. This work leveraged the ambiguity of the spatial information from visual cues to examine how non-spatially selective cells contribute to navigation when visual information is ambiguous. In this work, we found that cells without significant spatial information (nonplace cells) contributed to this discrimination between ambiguous spatial locations better than cells with significant spatial information in wild-type mice. By contrast, in the *5XFAD* mice, these same cells without significant spatial information failed to discriminate between true and false goal locations. While goal-coding in this study was examined locally, unlike non-local goal codes in *Chapter 2*, this work provides additional evidence of the importance of hippocampal representations for goal-directed navigation in complex environments. Furthermore, by taking a population level approach, this work reveals important information is encoded in cells without significant spatial modulation. In wild-type mice, these non-spatially selective cells were also differentially modulated by gamma band activity on correct and incorrect trials specifically in the false goal location. Unlike the wild-type mice, the *5XFAD* mice did not exhibit distinct slow and medium gamma-modulation of nonplace cells in the false goal location on correct and incorrect trials. Inhibitory-excitatory connections are also thought to underlie gamma band oscillations in the hippocampus, suggesting a potential shared mechanism underlying sharp-wave ripple and gamma oscillation deficits in the mouse model of Alzheimer's disease. However, there were no significant differences in the overall gamma power between genotypes, suggesting that sharp-wave ripple activity may degrade before gamma activity in this mouse model. Overall, this work points to a spatial deficit in *5XFAD* mice for goal coding, connecting our work in *Chapter 2* and

Chapter 3, and suggesting a potential mechanism by which hippocampal representations of key environment variables might be impaired in Alzheimer's disease to cause navigation deficits.

4.2 Caveats and limitations

4.2.1 Ethological validity of virtual reality experiments

One of the main limitations of head-fixed, virtual reality tasks in rodents is the generalizability of the findings to more naturalistic navigation in the real world. In our virtual reality task, animal must acquire the motor capabilities to successfully turn the treadmill, which is rapidly acquired but not completely natural. Furthermore, the virtual reality environment lacks the rich sensory inputs of the real world. Direct comparisons between hippocampal function in the real world and virtual world have been studied, though some these studies have used freely moving rats held by a harness in virtual reality, not head-fixed animals. In head-fixed studies, vestibular inputs and head-direction cells, observed in the parasubiculum, presubiculum, and medial entorhinal cortex of the hippocampus, are likely impaired (Sargolini et al., 2006; Q. Tang et al., 2016; Taube et al., 1990). Research comparing neural codes in the real world versus virtual world in rodents has found that place cells are more likely to code distances than spatial locations in virtual reality, and fewer neurons have significant spatial coding in virtual reality compared to the real world. However, theta phase precession of these spatially selective cells is largely intact (Aghajan et al., 2015; Chen et al., 2013; Ravassard et al., 2013). Furthermore, spatially selective cells recorded from CA1 in head-fixed virtual reality have been shown to accurately represent position at a population level as well (Fournier et al., 2020; Saleem et al., 2018). The advantages of this approach are highly stable recordings as well as easily manipulable environments that take advantage of the capabilities of virtual reality, as in our tasks. Further advances to virtual reality in terms of realistic rendering or designing similar tasks in the real world would better determine the generalizability of our findings.

4.2.2 Clinical relevance of mouse models of Alzheimer's disease

No mouse model of Alzheimer's disease currently recapitulates the full spectrum of effects of Alzheimer's disease observed in humans (Jankowsky & Zheng, 2017; Scearce-Levie et al., 2020). Thus, one of the central limitations of *Chapter 3* in terms of clinical relevance is that we use a single mouse model of Alzheimer's disease that exhibits amyloidosis. *5XFAD* mice are recommended by the Model Organism Development and Evaluation for Late-Onset Alzheimer's Disease consortium specifically for studies on the impacts of amyloid-beta deposition, immune regulation, and sex-based differences, but the *5XFAD* model is not recommended for studies evaluating potential therapeutics to rescue cognitive impairments (Oblak et al., 2021). Our work was suited for this model in that it was based on previous research on the impacts of amyloid beta on synaptic function. Furthermore, we did find electrophysiological characteristics that were similar across other mouse models of Alzheimer's, suggesting a potential shared mechanism. However, the *5XFAD* mice do not exhibit tauopathy and so it remains unclear how those pathological changes might also contribute to synaptic function and neural codes in Alzheimer's disease. Further work along this line of research, especially those identifying potential therapeutics, would be made even more robust if it employed multiple mouse models addressing different aspects of Alzheimer's pathogenesis.

4.3 Future directions

4.3.1 Causally manipulating prospective codes to impact behavior

One exciting future direction of our research on prospective codes would be a targeted causal manipulation to explicitly test if non-local goal coding and choice commitment representations are necessary and sufficient to planning and flexible decision making. However, determining exactly how to perform these manipulations may be challenging. One approach could be to leverage a transgenic mouse line of PV-Cre animals and perform brief pulses of optogenetic stimulation to increase firing of inhibitory neurons and thus temporarily silence neural activity at

specific timepoints in the task. Given our findings on the theta phase specificity of non-local codes in hippocampus even after the update cue is presented, we could perform this optogenetic stimulation at theta frequency or with theta phase specificity (as in Siegle & Wilson, 2014). Separation of inhibition trials by theta phase could provide evidence of the necessity of these cues to flexible adaptation to new information. We would hypothesize that inhibition on phases of theta with more non-local coding might diminish the animals' ability to update choices, while inhibition on phases of theta with more local coding would have no impact or would even enhance the ability to flexibly update decisions. In prefrontal cortex, optogenetic inhibition of activity after the update cue is presented on switch trials could be used to prevent the flip from one choice to another. On stay trials, the same stimulation may have no effect on animals' performance if the network resets back to the original choice after the stimulation is completed. With all of these proposed studies, the groundwork in establishing whether the optogenetic stimulation has the intended effects would be critical before performing the manipulations during behavior.

One experiment to test the sufficiency of prospective codes in guiding behavior would be to optogenetically induce prospective coding at various locations in the environment without any sensory cueing. Preliminary observations from individual trials show that non-local events in hippocampus outside of the update cue presentation may be *followed* by small changes in speed in the virtual reality environment. Furthermore, other researchers have observed that prefrontal cortex activity predicts non-local activity in hippocampus, but the connection of these events to behavioral performance is unclear (Hasz & Redish, 2020; Yu & Frank, 2021). It would thus be interesting to explore whether non-local activity triggers behavioral switches in trajectory even when no new sensory information is presented. Specifically triggering goal-selective cells with an extracellular electrophysiological approach may prove particularly challenging. Further work could examine the cell-type specificity of these goal-selective cells using extracellular

electrophysiology cell-type classification techniques to determine whether interneuron disinhibition or pyramidal cell activity from specific locations in the pyramidal layer of CA1 contributes more to this neural activity. If a specific population was identified, we could target those cells with optogenetics. An alternative method could employ calcium or voltage imaging during virtual reality behavior. We could then identify goal-selective cells and use holographic optogenetics to selectively increase the activity of those cells at randomized location in the track, to test whether brief stimulation either in hippocampus or in prefrontal cortex is enough to induce behavioral modulation. Demonstrating whether non-local coding and choice switching is sufficient to induce updates in behavior would also suggest that these non-local coding events might precede 'changes of mind' and deliberation more generally, not only with cued sensory information.

4.3.2 Integrating environmental changes and neural activity

Integrating environmental manipulations and neural activity more closely could also yield interesting insights. Given the impact of choice commitment *preceding* the update cue on the ability to respond accurately, one manipulation would be to perform online decoding of choice commitment from the neural activity data (or simply the behavioral data-based choice estimate value). An update cue could then be selectively triggered in the environment at different choice commitment levels to enhance or disrupt behavior. We would expect that introducing new information when the animal is in a less committed state would result in increased flexibility in adapting to the new information. We could then use this approach to further explore how neural responses to the new information vary with choice commitment. This approach could also be applied while measuring hippocampal-prefrontal coherence, which has been shown to be elevated during spatial navigation decision-making in rodents (Benchenane et al., 2010). We could trigger environmental changes at timepoints with higher coherence levels to improve

behavioral performance. This would allow us to explicitly test the role of behavioral and neural state on flexibility in response to new information.

4.3.3 Rescuing neural activity deficits and memory in Alzheimer's disease

The central motivator of research on Alzheimer's pathology and its effects on neural activity is so that we might better identify early biomarkers or develop treatments and preventative measures for this devastating disease. Our work provides additional insight on the connection between synaptic dysfunction and cognitive deficits and contributes to evidence from multiple mouse models to point towards the manipulation of neural oscillations as a potential approach to rescue neural activity. However, manipulating oscillation deficits in mouse models via optogenetics or electrical stimulation is an invasive procedure, and thus it would be difficult to directly translate these approaches to humans. Motivated by these oscillatory deficits and the need for a non-invasive manipulation approach, previous work from our lab has shown 40 Hz visual and auditory stimulation modulates neural activity at this frequency and rescues cognitive deficits that occur in a mouse model of Alzheimer's disease (Martorell et al., 2019). Ongoing work is now testing how this stimulation might impact neural circuits and the synaptic deficits we observed. Our work also fits in with a large body of research suggesting that interneurons in the brain might be especially vulnerable to Alzheimer's pathology. Therapeutic and pharmacological measures that target these populations might prove to be more effective in slowing the progression of Alzheimer's in the hippocampus and across the brain. Potential therapeutic approaches to Alzheimer's disease could involve combination therapy such as drugs targeting amyloid-beta accumulation, synaptic degeneration, and neuroimmune responses in combination with non-invasive stimulation techniques to alter neural oscillations.

4.3.4 Leveraging unique virtual reality tasks to test cognitive function

One of the more tool-focused insights from the research described in this dissertation is the advantages of virtual reality to create behavioral tasks that are more challenging to implement in the real world but can be used to test hypotheses in interesting ways. As virtual reality and augmented reality developments continue in the commercial space, the capabilities of rodent and human virtual reality task designs could be dramatically improved. We describe here some potential ways to manipulate environments that we have considered or others have shown that could be applied in the future in the lab. One group was able to test neural responses to familiarity and novelty by building two distinct virtual reality environments that slowly morphed between each other over an extensive gradient to test when neural codes switch between distinct maps (Plitt & Giocomo, 2021). Others have generated virtual spaces that are not visually driven, but generated from other sensory inputs such as auditory, olfactory, and tactile information, to test the generalizability of hippocampal codes to nonspatial features (Aronov et al., 2017; Radvansky & Dombeck, 2018; Sofroniew et al., 2014). Employing combinations of these sensory signals in unique ways to generate richer environments could allow for interesting studies on multi-sensory integration in hippocampal circuits. Environmental changes such rapid cue shifts, artificial obstacles, and teleportation allow for highly controlled experimental manipulations and stimulus sets that would be difficult to implement in real world spatial navigation (Pinto et al., 2018). Furthermore, environment manipulations could be triggered by neural activity to explore the relationship between new information and ongoing neural processes. Augmented reality could also be incorporated into research to improve the ethological validity of studies while giving the experimenter freedom to manipulate the environment in specific ways. One approach uses real world environments with augmented reality visual cues that can be used to rapidly switch between stimuli. Recent work has used augmented reality to disentangle the spatial coding contributions of internal and external information by creating conflicts between internal self-motion cues and external sensory information in an augmented space of virtual cues displayed in a real-world annular track

(Jayakumar et al., 2019; Madhav et al., 2022). Finally, virtual reality environments could be used to conserve experimental parameters and environments for cross-species studies of spatial navigation, combining resources across virtual reality studies conducted in species such as insects, rodents, and humans (Doucet et al., 2016).

4.4 Conclusions

In this work, we ask how our brains integrate pivotal, new information to make decisions and adapt plans, and how these neural codes are related to memory deficits in Alzheimer's disease. First, we show how prospective codes play a role in planning and deliberation behaviors and are modulated specifically when new information is presented that requires an adaptation or reconsideration of choices to occur. Second, we bridge the gap between synaptic dysfunction and cognitive deficits in a mouse model of Alzheimer's disease and suggest a possible mechanism that might underlie neural coding deficits in vivo. Overall, this dissertation provides insights into the role of neural codes for past, present, and future during flexible decision-making and how these codes might be disrupted in neurodegenerative disease.

CHAPTER 5 – APPENDIX: A SPATIAL NAVIGATION PARADIGM TO TEST FLEXIBLE DECISION MAKING IN MICE USING VIRTUAL REALITY

5.1 Introduction

Open science and sharing of data, software, tools, and resources has made great strides in the neuroscience community in recent years. Efforts from groups such as the International Neuroinformatics Coordinating Facility have worked to advocate for FAIR (Findable, Accessible, Interoperable, and Re-usable) and open neuroscience resources and practices (Wilkinson et al., 2016). In systems neuroscience, open-source data standards and ecosystems such as NeuroData Without Borders (NWB) and Brain Imaging Data Structures (BIDS) have begun to unify neuroscience data collection, analysis, visualization, and sharing (Gorgolewski et al., 2016; Rübél et al., 2022). With this new abundance of available tools, databases such as Open Neuroscience, Open Behavior, have been established to disseminate these resources more easily and facilitate the adoption of these new tools. However, one area that remains lacking is the distribution of specific behavioral task code and training paradigms for behavioral neuroscience researchers.

Much of the time spent in labs employing complex navigation and decision-making tasks is in the training of animals or debugging training approaches and parameters. Recent strides have been made to relieve these bottlenecks with automated behavioral boxes and shared software suites for task design. In the subfield of virtual reality behavioral assays, resources such as Stytra, PiVR, FreemoVR, ViRMEn, BonVision, ratCAVE, and Unity have facilitated researchers in virtual reality task design (Aronov & Tank, 2014; Brookes et al., 2020; del Grosso & Sirota, 2019; Lopes et al., 2021; Štih et al., 2019; Stowers et al., 2017). However, these advances have largely focused on sharing the apparatus or software systems. Some virtual reality decision-making tasks and training protocols have been shared as part of larger studies or independent

behavioral papers (Cushman et al., 2013; Kira et al., 2022; Pinto et al., 2018; Ravassard et al., 2013; Tseng et al., 2022). However, they are not accompanied by easily accessible training or environment code, and they address a variety of distinct behavioral questions. In these virtual reality tasks, especially for ones that involve more complex behaviors, there are several components that require finetuning such as overall training paradigms, habituation approaches, movement translation from the treadmill to the virtual world, and environment design.

In this work, we provide a detailed training paradigm protocol and behavioral assessment of a novel virtual reality behavioral task to test flexible navigation in response to new information in rodents. We give an overview of the behavioral task with the accompanying software, a detailed description of behavioral interventions and commonly observed behavioral pitfalls, and an automation pipeline to improve training efficiency and reproducibility across researchers and labs. This work provides a novel task that can be more quickly implemented in other labs, as well as resources for other tasks in virtual reality navigation involving multiple choices and memory-guided decision making.

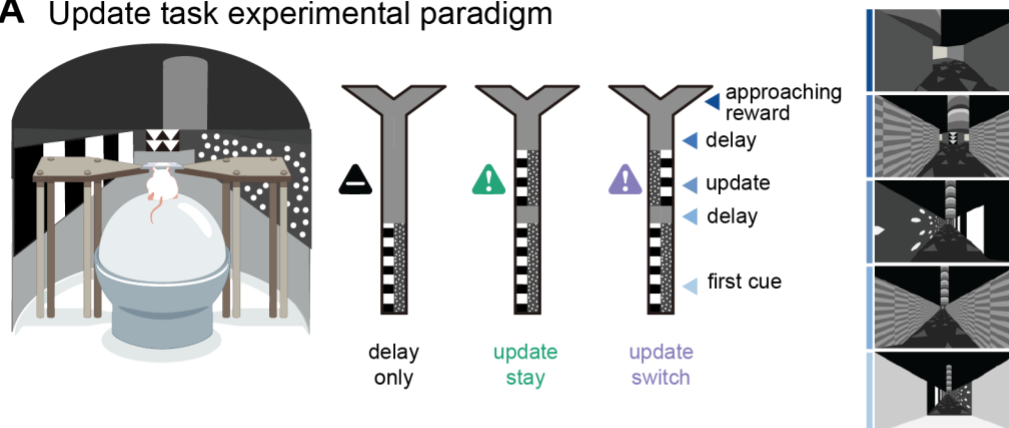
5.2 Behavioral task development and validation

5.2.1 A virtual reality paradigm to test flexible decision making in response to new information

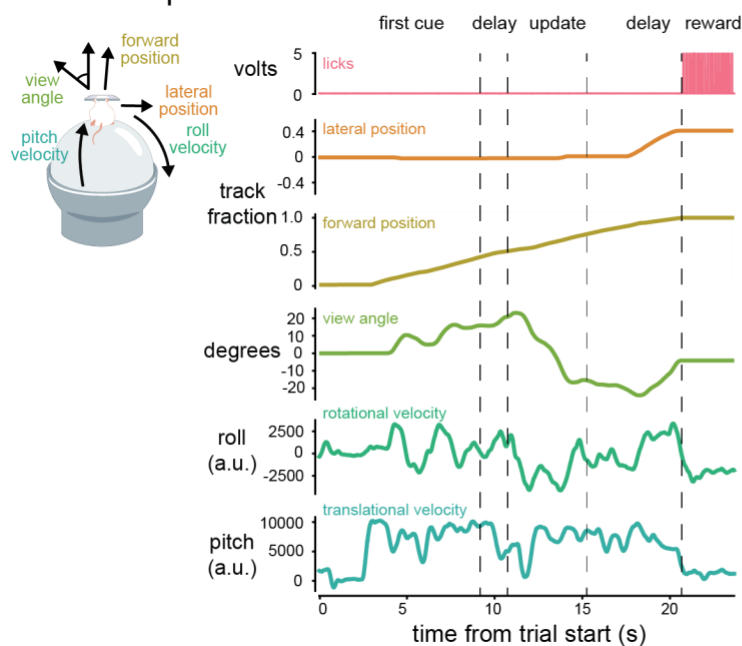
To test flexible decision-making in rodents in response to new information, we designed a virtual reality ‘update task’ that requires memory-guided decision-making (**Figure 5.1A**). On most trials, we present animals with an initial visual cue that indicates the correct goal location in the environment, and animals must then run down the track and remember the correct arm to turn towards to receive a reward. However, on a subset of trials, a second visual cue appears which indicates that the reward location has either changed (switch trials) or stayed the same (stay trials). On these trials, animals must choose to keep their original goal destination or switch to the other goal destination. During this behavioral task, we measured several aspects of the

animals ongoing behavior and decision making. We recorded the licking activity, position, heading direction, and velocity of the animal throughout the trial (**Figure 5.1B**). Over the course of a session, animals successfully performed the behavior across all trial types (**Figure 5.1C**).

A Update task experimental paradigm



B example trial



C example session

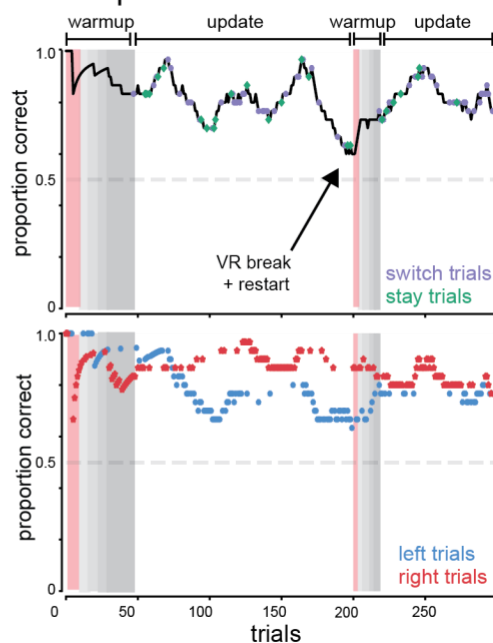


Figure 5.1. A novel behavioral task to test flexible responses to new information during spatial navigation

- A.** Overview of virtual reality experimental paradigm and update task trials. *Left*, schematic of mouse head-fixed on spherical treadmill with virtual reality environment. *Middle*, example visual cues and trials, black and white stripes indicate correct side of the track. *Right*, example screenshots of mouse's view in virtual reality environment as animal runs down the track.

- B. Example trial and behavioral readouts of licking, velocity, position, and heading direction over the course of a trial. Lateral position is restricted down the center until the mice are able to choose a side. Forward position and view angle are frozen for 3 seconds at the start of the trial and at the end of the trial if a reward is being delivered. View angle indicates the heading direction in the environment. The velocities shown indicate treadmill movement along the pitch and roll axes.
- C. Example session of behavioral performance over time. *Top*, proportion of correct trials over the course of a session calculated via a rolling average with a sliding window bin size of 30 trials. Behavioral performance fluctuates but remains above 50% correct performance across the session. Sessions often began with a warmup stage progressing from visually guided trials (pink) to progressively longer delay lengths (darker shades indicate longer delay length). Update phase with no highlight indicates combination of delay only trials, switch trials indicated with purple stars, and stay trials indicated with green stars. Virtual reality breaks were used to improve performance if it began to decline over the course of the session. *Bottom*, performance separated into left (blue) and right (red) trial types indicates fluctuations in bias (the animals preference for one side or another). Left and right trials were analyzed separately, and proportion correct was calculated as a rolling average with a sliding window bin size of 30 trials of the respective side type. Gaps in stars mean there was a consecutive sequence of trials of the other side type.

5.2.2 Virtual reality environments across stages of behavior training

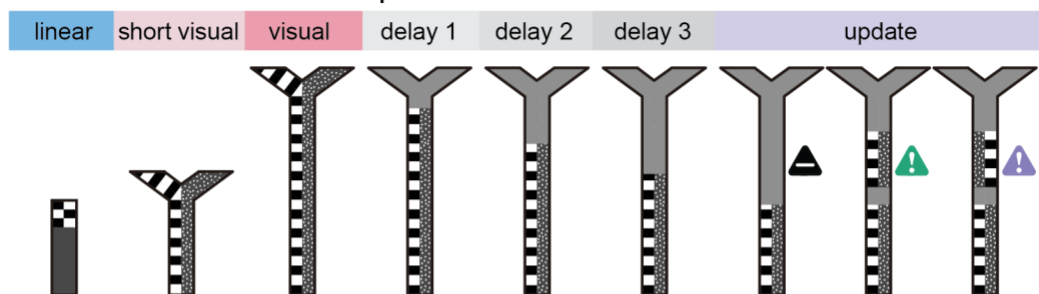
We used several shaping environments to reach the final stage of the task in which animals successfully performed all trial types (**Figure 5.2A**). The first environment was a linear track with black and white stripes that were visible at the very end of the track. Animals were teleported to the beginning of the track at the start of each trial, and the length of the track increased from 0.5 to 1 m over the course of two to four days. In the second track, the environment was y-shaped with a central arm and two choice arms. The correct arm where the reward was delivered was indicated by black and white stripes, and the non-rewarding side was indicated with grey cues and polka dots. In the third track, we increased the length of the central arm to approximately 3 m from the starting point to the reward. In the next phases of the task, we introduced a delay period during which the visual cues indicating the correct and incorrect side of the environment disappeared when the mouse reached different locations in the track. The delay period gradually increased in duration so that the cues would ‘turn off’ and be replaced with grey cues progressively earlier in the environment. Finally, the last phase introduced the update cue component of the task where a second cue appeared after the original cue. On 25% of the trials,

the visual cues flipped sides at the location where the delay occurred, indicating that the reward location had changed. On 10% of trials a second set of visual cues appeared but the cues were the same as the original visual cues and the rewarded location remained on the same side. In the final version of the task, 65% of the trials remained 'delay only' trials without an update cue, so there was no second cue presented and the animal was not aware that there would be no second cue until after it has passed that location in the environment. Overall, animals successfully learned and perform all phases of the update task training paradigm, though some animals were excluded from further training if they failed to meet the advancement criteria (**Figure 5.2B**). In the dataset shown here, fifteen animals total began training, one mouse was excluded for lack of movement and inability to complete trials in the visually guided phase, seven were excluded for never reaching the final phase of the task (usually due to difficulties in performing over longer delays), and one was excluded due to lack of consistent performance after training, resulting in seven mice total in the final dataset.

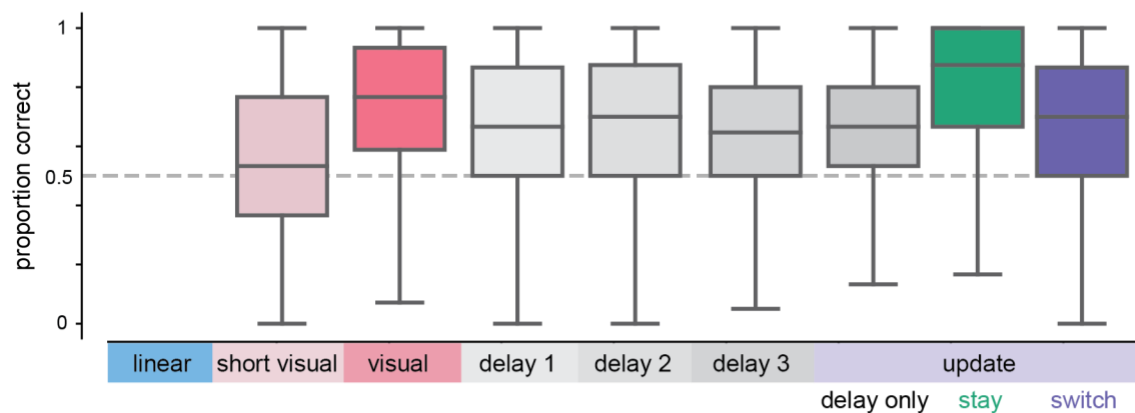
There were several minor virtual reality parameters that contributed greatly to the animals' ability to acquire the task. At the beginning of each trial, the view angle (i.e., heading direction) was reset to zero degrees and restricted for the first 0.05 fraction of the track to allow the animal time to adjust its running trajectory. We also restricted the view angle to a 40-degree maximum magnitude on the central arm of the track to prevent the animal from turning around and running backwards in the environment. In other virtual reality tasks, the view angle has been restricted to zero degrees to prevent animals from turning before reaching the end of the track, though running patterns often reflect this turning even when the heading direction is restricted (Kira et al., 2022). We also froze the screen and position of the animal for three seconds at the trial onset to allow the animal time to reorient itself to the start of the trial. When the animal entered the correct arm and received a reward, the screen was again frozen for three seconds to allow

the mouse time to consume the reward and recognize the rewarding cues before beginning the intertrial interval.

A Environment cues across task phases



B Behavioral performance across task phases



C Sessions spent on each task phase

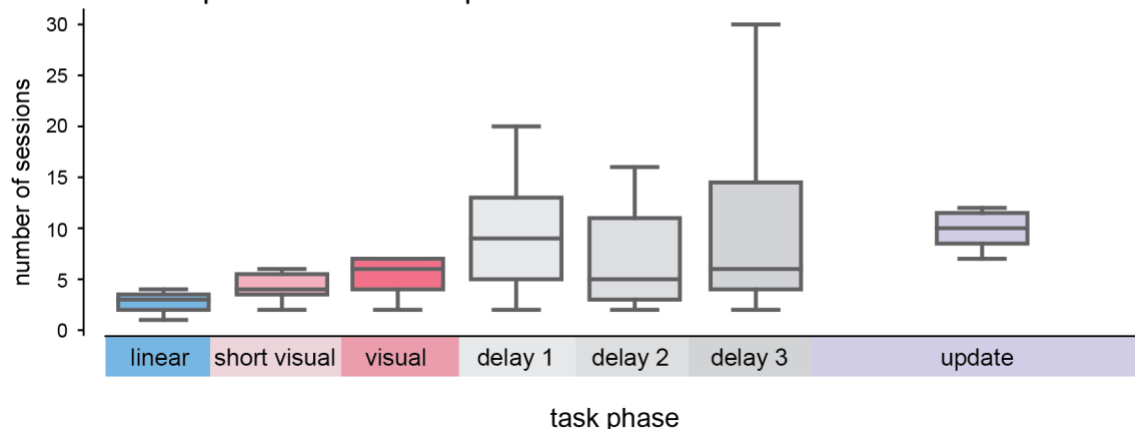


Figure 5.2. Animals progress across training phases and learn to successfully perform task across all trial types.

- A. Schematic of training phases and visual cues for all virtual reality environments
- B. Overall performance (proportion correct) for each training phase. For all animals, the average percent correct by trail type is shown. Linear is not included due to the lack of a

correct vs. incorrect choice option. Percent correct is calculated with a rolling average with a sliding window bin size of 30 trials ($n = 7$ animals, short visually guided: $54.81 \pm 25.17\%$ correct $n = 5227$ trials; visually guided: $71.88 \pm 25.97\%$ correct $n = 10007$ trials; delay 1: $66.07 \pm 25.58\%$ correct $n = 7327$ trials; delay 2: $66.15 \pm 27.16\%$ correct $n = 5854$ trials; delay 3: $64.31 \pm 22.59\%$ correct $n = 9466$ trials; delay 4: $65.92 \pm 19.55\%$ correct $n = 10107$ trials; update stay: $78.30 \pm 26.40\%$ correct $n = 1586$ trials; update switch: $66.49 \pm 24.78\%$ correct $n = 4054$ trials).

- C. Average number of trials all animals spent on each session type. Update includes combination of delay only, switch, and stay trials. Sessions were categorized based on the percentage of each trial type. One session excluded for not enough trials of any trial type. All numbers reported as mean \pm std ($n = 7$ animals, linear: 2.71 ± 1.11 sessions, short visually guided: 4.71 ± 2.29 sessions; visually guided: 6.57 ± 4.54 sessions; delay 1: 9.57 ± 6.85 sessions; delay 2: 7.29 ± 5.53 sessions; delay 3: 10.71 ± 10.11 sessions; delay 4: 1.75 ± 1.5 sessions; update: 13.71 ± 11.28 sessions).

5.2.3 Behavioral training procedure

Animals were trained approximately five to seven days per week, one hour per day. We performed headplate implant surgery on these animals at approximately eight weeks old. After a three-day post-procedure recovery period, animals were food deprived to 85% of their free-feeding body weight. Animal's weights were as close to 85% of their original weight as possible throughout training to achieve optimal performance in the task. We trained animals at approximately the same time each day to keep performance most consistent and to ensure the animals were motivated. Rewards of sweetened condensed milk (1:2 dilution in water) were delivered via a reward spout and licks were detected using a photo-interrupter.

Each phase of behavioral training had a distinct goal and advancement criteria that the animals were expected to meet before they could move on to the next phase of the task (**Table 5.1**). In the first habituation and acclimation period of training, the goal was to habituate animals to the virtual reality apparatus and head-fixed setup, as well as teach the animal how to advance down the track to a rewarded location. The first day of training was 30 minutes long, and the second day of training was 45 minutes long to allow mice to acclimate to head-fixation and the treadmill. After this acclimation period, each training session lasted approximately 60 minutes. The duration of a training session in this case indicates the time point from when the virtual reality

environment was turned on to when it was shut off. During the initial acclimation period, we extended the reward delivery needle out in front of the photointerrupter beam. This approach ensured the mouse received reward but was not distracted by the photointerrupter apparatus close to its face. Over approximately two to three sessions, we moved the need backward to position between the lick detector beam so licks could be detected. To ensure the mouse was comfortable controlling the spherical treadmill and licking, the linear track phase lasted for two days at minimum. The mice completed 50 trials on each length of the linear track before advancing to the short visual cue guided phase of the task.

Once the mouse acclimated to the set-up of the experiment and completed trials in the linear track, the y-maze phase was started. The next phases all included a y-shaped track with one correct side determined for each trial and indicated with black and white striped cues. The goal of this phase was to have the mouse turn in both directions to follow the cues for a reward. To advance from a shortened y-maze to the long y-maze phase, the mouse needed to complete 2 sessions with at least 75 trials completed and with 75% accuracy. Similar criteria were used to advance the mouse from the long visually guided y-maze to the introduction of a delay phase. After the delay phase began, the visual cues indicating the distinction between the correct and incorrect arms of the environment disappeared after the animals passed a specific point in the track. The delay component was often the most challenging aspect of the task for the mouse to learn and acquire and this is where most animals spent most of their training sessions (**Figure 5.2C**). The advancement criteria for these phases were the same as the short to long y-maze transition, though 70% accuracy was sufficient for advancement from the longest delay phase due to the level of difficulty. Finally, once the animals learned to complete the longest delay duration, we introduced the update component during which a second visual cue appeared on some trials and in these cases the correct arm stayed or switched from the arm the original cue indicated. After the animal learned to respond to the new information, we added an additional

delay between the original cue and the update cue. Once the mouse completed this phase, they were considered successfully trained. Performance remained largely stable after the update cues were introduced. However, we performed an additional habituation period for neural activity recordings with the trained animals to ensure successful behavior during recordings.

Phase	Linear	Short visual	Long visual	Delay 1	Delay 2	Delay 3	Update
Goal	Habituate to virtual reality setup, lick detector, and moving on treadmill	Learn to follow cues and to turn on treadmill	Learn to follow cues on full length track	Remember goal destination over the short delay	Maintain memory over medium delays	Maintain memory over long delays	Flexibly respond to new information about goal location
Advancement criteria to next phase	50 trials on each length of linear track (short, medium, long)	75% correct over two sessions (at least 50 trials each)	75% correct over two sessions (at least 50 trials each)	75% correct over two sessions (at least 50 trials each)	75% correct over two sessions (at least 50 trials each)	70% correct over three sessions (at least 50 trials each)	Not applicable
Warmup	10 trials on a shorter length	10 linear track trials at longest length	10 trials on short visual y-maze	10 trials on long visual y-maze with at least 70% correct with <30% bias	Delay 1 warmup + 10 trials on delay 1 with at least 70% correct with <30% bias	Delay 2 warmup + 10 trials on delay 1 with at least 70% correct with <30% bias	Delay 3 warmup with 5 trials on each delay
Virtual reality environment	Linear	Short y-maze	Long y-maze	Long y-maze	Long y-maze	Long y-maze	Long y-maze
Delay location	Not applicable	Not applicable	Not applicable	Delay 1	Delay 2	Delay 3	Delay 3 + Delay 4
Update location	Not applicable	Not applicable	Not applicable	Not applicable	Not applicable	Not applicable	Delay 3 location
Notes	First day of training for 30 min, second day for 45 min, remaining sessions for 60 min						Introduce update with delay 3, once learned advance to delay 4

Table 5.1 Advancement criteria and goals of each training phase for update task paradigm.

To reach the final version of the update task, animals must progress through several training phases to learn different components of the virtual reality task. Advancement criteria, phase details, and training goals are detailed here.

5.2.4 Behavioral interventions for successful task acquisition and performance

During behavioral training there are many factors that impact the ability of mice to learn and perform complex behavioral tasks. This time-intensive and sensitive process can be a major bottleneck to data collection, and lack of well-trained animals can set back experiment progress. We found that there were several experimental interventions throughout the training process that facilitated task learning. Here we describe these interventions as well as scenarios for when to apply them to standardize training practices and improve training success rates (**Figure 5.3**). We will later describe and share code for a training pipeline that will automate some of these behavioral interventions for easier implementation and standardization across researchers.

During the habituation phase, the animal's comfort and motivation are key factors to successful task acquisition. One behavior observed early in training is when the animals push the lick detector away or hold onto it while running. In this scenario, the experimenter should check the placement of the lick detector to ensure it is not touching the animal's nose or face and consider moving the needle slightly forward to make the mouse more comfortable. Unsteady movement on the ball or holding the lick detector will usually self-resolve, provided that the spherical treadmill and headplate holder height has been calibrated (for a description of optimized heights and mouse positioning on the treadmill, see github.com/HarveyLab/mouseVR). Another common habituation behavior is pausing on the spherical treadmill for extended periods of time. This can indicate the mice are unmotivated for reward. Experimenters should make note of the percent weight of the animal, as the lowest approved weight (in our studies, 85% of the initial free-feeding weight) for food deprived mice is the optimal amount for good performance. This

behavior can resolve with improved food deprivation, additional habituation, or with additional manual reward delivery at the end of the reward zone to provide extra motivation.

During the main task acquisition phase, the most commonly observed behavior that requires intervention is side bias. Mice prefer to continue running in the same direction on the spherical treadmill, and they will often fall into side biases during which they run to the same arm regardless of whether it is correct or not. One way to address this is via the implementation of a bias correction trial selection algorithm. With this algorithm, we change the underlying probability that the next trial will be a left or right trial using the animal's history of side bias. In short, the probability that the next trial will be on the left side is dependent on the history of left trial errors and right trial errors. If the animal prefers the right side of the track and has missed mainly left trials, then there will be a higher likelihood of the next trial being on the left, or non-preferred, side (Hu et al., 2009; Pinto et al., 2018). The researcher can manually queue trials at specific moments throughout the task to attempt to address side biases and repetition. These manual interventions are useful when animals are trying to turn towards their non-preferred side but are having difficulties with motor control on the ball and are not able to successfully turn every time. An additional reward can also be manually delivered when animals have a successful trial on their non-preferred side to shift their bias, though these should be applied short-term so as not to introduce the alternative side bias. This intervention is useful when the animals can turn towards the non-preferred side easily without motor difficulties but are unmotivated to do so. Other groups have also implemented a maximum number of consecutive trials for each side to correct these biases, though we have not implemented this in our own task (Zhao et al., 2022).

Another commonly observed behavior that may also underlie side biases and poor performance is lack of motivation. Experimenters may find that animals become less motivated as the

session progresses and they have received more rewards. Animals may begin to run in the same direction over and over which still leads to some diminished level of rewards, and thus they may become unmotivated to ever perform the task. In this case, a virtual reality break can be applied during which the session is temporarily paused and the screen is turned off. With this intervention, the animal is still required to be head-fixed on the treadmill for the duration of the session, but the animal no longer has the ability to obtain additional rewards. When applied no more than once a session, this intervention can be very successful and the animal will restart the session after the break with improved performance (see example session in **Figure 5.1C**). Another approach is to introduce an easy trial break during the session. This intervention is applied during the delay training phases, when the extended delay durations make the task more challenging. Easy breaks should be used when the animals do not have good performance from the start of the session, while virtual reality breaks are more useful when the animal was performing well but became demotivated over time. A short break of approximately 10-20 visually guided trials with no delay can remind the animal of the rules of the task. These easy breaks should also be applied no more than once per session so that the animal does not give up performing the more difficult phases. A similar principle is employed with a warmup phase at the start of the session, during which animals are provided with visually guided trials to start the session and remind them of the task, and then they are progressively and quickly advanced through the delay phases until the current training phase is reached. This warmup reminds the animal of the task rules but should be no longer than 20 trials so that animals do not consume too many rewards and give up for the rest of the behavioral session.

The progression of animals through the task is not always linear. The experimenter should continue to monitor the animal closely so that potential pitfalls and animals' performance in the task can be addressed quickly. Behaviors such as licking for incorrect rewards, difficulty progressing through the training phases, or motivation drop-out over a certain time course are

important indicators of the need to implement interventions or change training approaches (see **Figure 5.3** for an overview). Factors outside of the training session such as food given, home cage environment, noise, vibrations, and other disturbances affect animals' performance and should be noted in behavioral logs throughout the training process. Overall, these behavioral interventions standardize the scenarios and interventions to be applied across experimenters.

Behavioral interventions

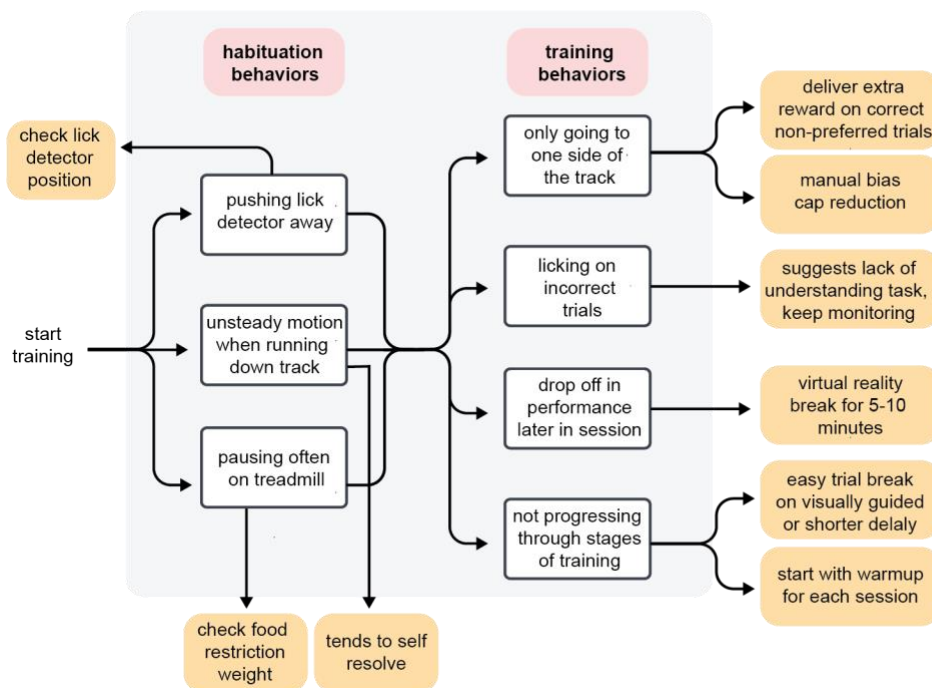


Figure 5.3. Implementing behavioral interventions can produce quicker and better training outcomes.

During training, animals exhibit several behaviors that can be improved or addressed with behavioral interventions from the experimenter. Behaviors are divided into those that occur during habituation to the virtual reality setup (primarily on the linear phase of the task) and those that occur during training. Interventions are highlighted in orange.

5.3 Software and analysis features

5.3.1 Automation approaches to task software use and behavioral training

To standardize these approaches across researchers, we are currently building an automation pipeline to apply behavioral interventions and advancement criteria during training (**Figure 5.4**).

This behavioral setup requires the installation of ViRMEn and MATLAB 2015b and additional training code which will be shared via the Singer lab GitHub page. In this pipeline, training data is saved to a database for each session, and when an experimenter is about to begin a training session, they input the animal ID to pull the specific training history. The advancement criteria (**Table 5.1**) are then applied to determine what environment and training parameters will be used for this session. The experimenter then checks this information and begins training. Throughout the training session, behavioral interventions described in **Figure 5.3** that can be applied via the computer will be prompted to the experimenter and approved as needed. Finally, session data is saved and key information about the session is stored in the training database for later use. The data from ViRMEn software can be customized according to the experimenter preferences. We provide a module to export the data to the standardized NWB format for improved incorporation into other analysis pipelines.

5.3.2 Synchronization to other acquisition systems

Experimenters often need to incorporate and synchronize behavioral data with other data streams such as electrophysiological and imaging data acquisition. We provide code to send randomized TTL pulses to other acquisition systems and to later synchronize those signals. In cases where experimenters record videos of animal behavior for visualization and educational purposes, we describe here a video recording setup to synchronize behavioral data with videos. We acquired video recordings using a color USB camera (a2A1920-160ucPRO, Basler) with an 8mm lens (C125-0818-5M, Basler). We mount the camera behind the mouse during behavior and use Basler Pylon software to initialize and save the video recordings. A Basler USB cable connects the camera to a separate data storage computer and a Basler I/O cable connects the camera to the NIDAQ for triggering camera frame acquisition from ViRMEn. A 20 Hz trigger signal is sent to the camera through the I/O cable to allow for data synchronization while

experimenters take recordings of mouse behavior during training sessions. We provide a module to analyze these behavioral videos and the accompanying behavioral data in order to generate visualizations of concurrent behavioral data with video recordings.

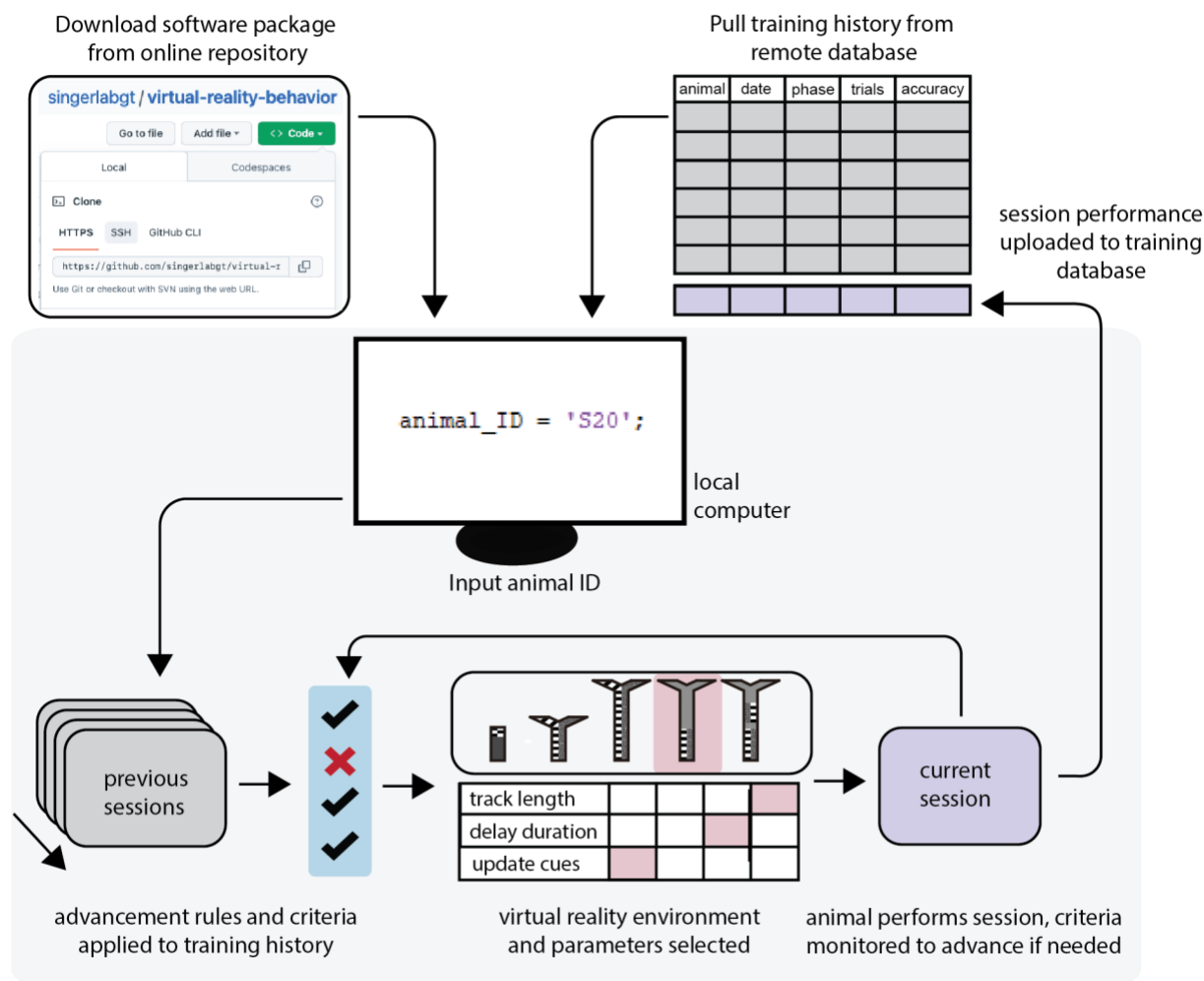


Figure 5.4. Software and automation pipeline to facilitate efficient and consistent training practices.

Virtual reality code repository will be made available on GitHub to use custom task code. During each behavioral session, experimenters input the animal information to pull any existing training history, apply a function to assess advancement rules and criteria, and thus select the appropriate environment and parameters. During the session, behavioral performance is continuously assessed to determine if environment or task parameters should be updated. If the algorithm detects advancement criteria are met or behavioral interventions should be applied, the computer will prompt the user who can approve these changes. After the session is finished, performance information is saved to the training history database.

5.4 Discussion

Well-designed behavioral tasks are an essential part of systems neuroscience research, but there are several challenges and particular details that are critical to successful behavior but not always described in full in papers. Here, we describe several components of a novel virtual reality behavioral paradigm for testing flexible decision making. We also provide a comprehensive training paradigm with several behaviors and interventions to consider throughout the training process. We will also share the code and automation software that implements these training criteria for improved reproducibility and efficiency of training across researchers and institutions.

Our aim is to make this flexible decision-making task freely available and more easily implementable, so that researchers can apply this task in their own labs as well as iterate more quickly on similar task designs. One of the main limitations preventing a common database of behavioral tasks is the lack of a standardized behavioral task software ecosystem. Recent work has promoted behavioral task design suites that have improved capabilities, performance, and flexibility in applying tasks across species. However, a uniform software ecosystem for virtual reality tasks that is standardized across systems neuroscience subfields of perceptual decision-making, visually guided behavior, and memory-based navigation remains to be established. Until then, distribution of task designs and parameters is helpful to researchers regardless of specific software. This information sharing codifies best practices and various approaches to training animals in virtual navigation and decision-making. Behavioral training can often be treated more as an art than a systematic procedure, and thus automating these aspects of training and working towards shared procedures enhances reproducibility of scientific research. These small details are especially critical for open access to science across institutions and helps researchers setting up behavioral tasks for the first time that may be unfamiliar with common pitfalls or lack expert resources.

REFERENCES

- Abramov, E., Dolev, I., Fogel, H., Ciccotosto, G. D., Ruff, E., & Slutsky, I. (2009). Amyloid-B as a positive endogenous regulator of release probability at hippocampal synapses. *Nature Neuroscience*. <https://doi.org/10.1038/nn.2433>
- Aghajan, Z. M., Acharya, L., Moore, J. J., Cushman, J. D., Vuong, C., & Mehta, M. R. (2015). Impaired spatial selectivity and intact phase precession in two-dimensional virtual reality. *Nature Neuroscience*, *18*(1). <https://doi.org/10.1038/nn.3884>
- Agster, K. L., & Burwell, R. D. (2009). Cortical efferents of the perirhinal, postrhinal, and entorhinal cortices of the rat. *Hippocampus*, *19*(12), 1159–1186. <https://doi.org/10.1002/hipo.20578>
- Alger, B. E., & Nicoll, R. A. (1982). Feed-forward dendritic inhibition in rat hippocampal pyramidal cells studied in vitro. *The Journal of Physiology*. <https://doi.org/10.1113/jphysiol.1982.sp014255>
- Ali, F., Baringer, S. L., Neal, A., Choi, E. Y., Kwan, A. C., & Wirths, O. (2019). Parvalbumin-Positive Neuron Loss and Amyloid- β Deposits in the Frontal Cortex of Alzheimer's Disease-Related Mice. *Journal of Alzheimer's Disease*. <https://doi.org/10.3233/JAD-181190>
- Allison, S. L., Fagan, A. M., Morris, J. C., & Head, D. (2016). Spatial Navigation in Preclinical Alzheimer's Disease. *Journal of Alzheimer's Disease*, *52*(1). <https://doi.org/10.3233/JAD-150855>
- Alonso, J. M., Usrey, W. M., & Reid, R. C. (1996). Precisely correlated firing in cells of the lateral geniculate nucleus. *Nature*. <https://doi.org/10.1038/383815a0>
- Amarasingham, A., Harrison, M. T., Hatsopoulos, N. G., & Geman, S. (2011). Conditional modeling and the jitter method of spike resampling. *Journal of Neurophysiology*. <https://doi.org/10.1152/jn.00633.2011>
- Andrianova, L., Yanakieva, S., Margetts-Smith, G., Kohli, S., Brady, E. S., Aggleton, J. P., & Craig, M. T. (2022). No evidence from complementary data sources of a direct projection from the mouse anterior cingulate area to the hippocampal formation. *BioRxiv*.
- Aronov, D., Nevers, R., & Tank, D. W. (2017). Mapping of a non-spatial dimension by the hippocampal–entorhinal circuit. *Nature*, *543*(7647), 719–722. <https://doi.org/10.1038/nature21692>
- Aronov, D., & Tank, D. W. (2014). Engagement of Neural Circuits Underlying 2D Spatial Navigation in a Rodent Virtual Reality System. *Neuron*, *84*(2), 442–456. <https://doi.org/10.1016/j.neuron.2014.08.042>
- Axmacher, N., Elger, C. E., & Fell, J. (2008). Ripples in the medial temporal lobe are relevant for human memory consolidation. *Brain*. <https://doi.org/10.1093/brain/awn103>
- Barthó, P., Hirase, H., Monconduit, L., Zugaro, M., Harris, K. D., & Buzsáki, G. (2004). Characterization of neocortical principal cells and interneurons by network interactions and extracellular features. *Journal of Neurophysiology*. <https://doi.org/10.1152/jn.01170.2003>
- Bartos, M., Vida, I., Frotscher, M., Meyer, A., Monyer, H., Geiger, J. R. P., Jonas, P., & Heidelberg. (2002). Fast synaptic inhibition promotes synchronized gamma oscillations in hippocampal interneuron networks. *Proceedings of the National Academy of Sciences of the United States of America*. <https://doi.org/10.1073/pnas.192233099>
- Bartos, M., Vida, I., & Jonas, P. (2007). Synaptic mechanisms of synchronized gamma oscillations in inhibitory interneuron networks. In *Nature Reviews Neuroscience*. <https://doi.org/10.1038/nrn2044>
- Behrens, T. E. J., Muller, T. H., Whittington, J. C. R., Mark, S., Baram, A. B., Stachenfeld, K. L., & Kurth-Nelson, Z. (2018). What Is a Cognitive Map? Organizing Knowledge for Flexible Behavior. In *Neuron* (Vol. 100, Issue 2). <https://doi.org/10.1016/j.neuron.2018.10.002>

- Benchenane, K., Peyrache, A., Khamassi, M., Tierney, P. L., Gioanni, Y., Battaglia, F. P., & Wiener, S. I. (2010). Coherent theta oscillations and reorganization of spike timing in the hippocampal- prefrontal network upon learning. *Neuron*, *66*(6), 921–936. <https://doi.org/10.1016/j.neuron.2010.05.013>
- Berners-Lee, A., Wu, X., & Foster, D. J. (2021). Prefrontal cortical neurons are selective for non-local hippocampal representations during replay and behavior. *Journal of Neuroscience*, *41*(27). <https://doi.org/10.1523/JNEUROSCI.1158-20.2021>
- Bero, A. W., Yan, P., Roh, J. H., Cirrito, J. R., Stewart, F. R., Raichle, M. E., Lee, J.-M., & Holtzman, D. M. (2011). Neuronal activity regulates the regional vulnerability to amyloid- β deposition. *Nature Neuroscience*, *14*(6), 750–756. <https://doi.org/10.1038/nn.2801>
- Bohm, C., & Lee, A. K. (2020). Canonical goal-selective representations are absent from prefrontal cortex in a spatial working memory task requiring behavioral flexibility. *eLife*, *9*. <https://doi.org/10.7554/eLife.63035>
- Booth, C. A., Witton, J., Nowacki, J., Tsaneva-Atanasova, K., Jones, M. W., Randall, A. D., & Brown, J. T. (2016). Altered Intrinsic Pyramidal Neuron Properties and Pathway-Specific Synaptic Dysfunction Underlie Aberrant Hippocampal Network Function in a Mouse Model of Tauopathy. *Journal of Neuroscience*, *36*(2), 350–363. <https://doi.org/10.1523/JNEUROSCI.2151-15.2016>
- Braak, H., & Braak, E. (1991). Neuropathological staging of Alzheimer-related changes. In *Acta Neuropathologica* (Vol. 82, Issue 4). <https://doi.org/10.1007/BF00308809>
- Bradshaw, J., Saling, M., Hopwood, M., Anderson, V., & Brodtmann, A. (2004). Fluctuating cognition in dementia with Lewy bodies and Alzheimer's disease is qualitatively distinct. *Journal of Neurology, Neurosurgery and Psychiatry*, *75*(3). <https://doi.org/10.1136/jnnp.2002.002576>
- Brookes, J., Warburton, M., Alghadier, M., Mon-Williams, M., & Mushtaq, F. (2020). Studying human behavior with virtual reality: The Unity Experiment Framework. *Behavior Research Methods*, *52*(2). <https://doi.org/10.3758/s13428-019-01242-0>
- Buckner, R. L. (2010). The role of the hippocampus in prediction and imagination. *Annual Review of Psychology*, *61*. <https://doi.org/10.1146/annurev.psych.60.110707.163508>
- Burwell, R. D., & Amaral, D. G. (1998). Cortical afferents of the perirhinal, postrhinal, and entorhinal cortices of the rat. *The Journal of Comparative Neurology*, *398*(2), 179–205. [https://doi.org/10.1002/\(SICI\)1096-9861\(19980824\)398:2<179::AID-CNE3>3.3.CO;2-E](https://doi.org/10.1002/(SICI)1096-9861(19980824)398:2<179::AID-CNE3>3.3.CO;2-E)
- Busche, M. A., Eichhoff, G., Adelsberger, H., Abramowski, D., Wiederhold, K. H., Haass, C., Staufenbiel, M., Konnerth, A., & Garaschuk, O. (2008). Clusters of hyperactive neurons near amyloid plaques in a mouse model of Alzheimer's disease. *Science*. <https://doi.org/10.1126/science.1162844>
- Buskila, Y., Crowe, S. E., & Ellis-Davies, G. C. R. (2013). Synaptic deficits in layer 5 neurons precede overt structural decay in 5xFAD mice. *Neuroscience*, *254*, 152–159. <https://doi.org/10.1016/j.neuroscience.2013.09.016>
- Buzsáki, G. (1986). Hippocampal sharp waves: Their origin and significance. *Brain Research*, *398*(2). [https://doi.org/10.1016/0006-8993\(86\)91483-6](https://doi.org/10.1016/0006-8993(86)91483-6)
- Buzsáki, G. (2015). Hippocampal sharp wave-ripple: A cognitive biomarker for episodic memory and planning. *Hippocampus*, *25*(10). <https://doi.org/10.1002/hipo.22488>
- Buzsáki, G., Lai-Wo S., L., & Vanderwolf, C. H. (1983). Cellular bases of hippocampal EEG in the behaving rat. In *Brain Research Reviews*. [https://doi.org/10.1016/0165-0173\(83\)90037-1](https://doi.org/10.1016/0165-0173(83)90037-1)
- Caccavano, A., Bozzelli, P. L., Forcelli, P. A., Pak, D. T. S., Wu, J.-Y., Conant, K., & Vicini, S. (2020). Inhibitory parvalbumin basket cell activity is selectively reduced during hippocampal sharp wave ripples in a mouse model of familial Alzheimer's disease. *Journal of Neuroscience*. <https://doi.org/10.1523/JNEUROSCI.0425-20.2020>

- Carpenter, J. R., Goldstein, H., & Rasbash, J. (2003). A novel bootstrap procedure for assessing the relationship between class size and achievement. In *Journal of the Royal Statistical Society. Series C: Applied Statistics*. <https://doi.org/10.1111/1467-9876.00415>
- Carr, M. F., Jadhav, S. P., & Frank, L. M. (2011). Hippocampal replay in the awake state: a potential substrate for memory consolidation and retrieval. *Nat Neurosci*, *14*(2), 147–153. <https://doi.org/10.1038/nn.2732>
- Cenquizca, L. A., & Swanson, L. W. (2007). Spatial organization of direct hippocampal field CA1 axonal projections to the rest of the cerebral cortex. In *Brain Research Reviews* (Vol. 56, Issue 1). <https://doi.org/10.1016/j.brainresrev.2007.05.002>
- Chao, L. L., & Knight, R. T. (1997). Prefrontal deficits in attention and inhibitory control with aging. *Cerebral Cortex*, *7*(1). <https://doi.org/10.1093/cercor/7.1.63>
- Chapman, P. F., White, G. L., Jones, M. W., Cooper-Blacketer, D., Marshall, V. J., Irizarry, M., Younkin, L., Good, M. A., Bliss, T. V. P., Hyman, B. T., Younkin, S. G., & Hsiao, K. K. (1999). Impaired synaptic plasticity and learning in aged amyloid precursor protein transgenic mice. *Nature Neuroscience*. <https://doi.org/10.1038/6374>
- Chen, G., King, J. A., Burgess, N., & O'Keefe, J. (2013). How vision and movement combine in the hippocampal place code. *Proceedings of the National Academy of Sciences of the United States of America*, *110*(1). <https://doi.org/10.1073/pnas.1215834110>
- Chung, J. E., Magland, J. F., Barnett, A. H., Tolosa, V. M., Tooker, A. C., Lee, K. Y., Shah, K. G., Felix, S. H., Frank, L. M., & Greengard, L. F. (2017). A Fully Automated Approach to Spike Sorting. *Neuron*. <https://doi.org/10.1016/j.neuron.2017.08.030>
- Ciaramelli, E. (2008). The role of ventromedial prefrontal cortex in navigation: A case of impaired wayfinding and rehabilitation. *Neuropsychologia*, *46*(7). <https://doi.org/10.1016/j.neuropsychologia.2007.11.029>
- Clay Reid, R., & Alonso, J. M. (1995). Specificity of monosynaptic connections from thalamus to visual cortex. *Nature*. <https://doi.org/10.1038/378281a0>
- Coghlan, S., Horder, J., Inkster, B., Mendez, M. A., Murphy, D. G., & Nutt, D. J. (2012). GABA system dysfunction in autism and related disorders: From synapse to symptoms. In *Neuroscience and Biobehavioral Reviews*. <https://doi.org/10.1016/j.neubiorev.2012.07.005>
- Comrie, A. E., Frank, L. M., & Kay, K. (2022). Imagination as a fundamental function of the hippocampus. *Philosophical Transactions of the Royal Society B: Biological Sciences*, *377*(1866). <https://doi.org/10.1098/rstb.2021.0336>
- Constantinople, C. M., & Bruno, R. M. (2011). Neuron Report Effects and Mechanisms of Wakefulness on Local Cortical Networks. *Neuron*, *69*, 1061–1068. <https://doi.org/10.1016/j.neuron.2011.02.040>
- Coutureau, E., & Killcross, S. (2003). Inactivation of the infralimbic prefrontal cortex reinstates goal-directed responding in overtrained rats. *Behavioural Brain Research*, *146*(1–2). <https://doi.org/10.1016/j.bbr.2003.09.025>
- Crowe, S. E., & Ellis-Davies, G. C. R. (2014). Spine pruning in 5xFAD mice starts on basal dendrites of layer 5 pyramidal neurons. *Brain Structure and Function*. <https://doi.org/10.1007/s00429-013-0518-6>
- Csicsvari, J., Hirase, H., Czurko, A., & Buzsáki, G. (1998). Reliability and State Dependence of Pyramidal Cell–Interneuron Synapses in the Hippocampus: an Ensemble Approach in the Behaving Rat. *Neuron*, *21*(1), 179–189. [https://doi.org/10.1016/S0896-6273\(00\)80525-5](https://doi.org/10.1016/S0896-6273(00)80525-5)
- Csicsvari, J., Hirase, H., Czurkó, A., Mamiya, A., & Buzsáki, G. (1999). Oscillatory coupling of hippocampal pyramidal cells and interneurons in the behaving Rat. *The Journal of Neuroscience : The Official Journal of the Society for Neuroscience*.
- Csicsvari, J., Hirase, H., Mamiya, A., & Buzsáki, G. (2000). Ensemble patterns of hippocampal CA3-CA1 neurons during sharp wave-associated population events. *Neuron*, *28*(2). [https://doi.org/10.1016/S0896-6273\(00\)00135-5](https://doi.org/10.1016/S0896-6273(00)00135-5)

- Cushman, J. D., Aharoni, D. B., Willers, B., Ravassard, P., Kees, A., Vuong, C., Popeney, B., Arisaka, K., & Mehta, M. R. (2013). Multisensory Control of Multimodal Behavior: Do the Legs Know What the Tongue Is Doing? *PLoS ONE*, *8*(11), e80465. <https://doi.org/10.1371/journal.pone.0080465>
- Davidson, T. J., Kloosterman, F., & Wilson, M. A. (2009). Hippocampal Replay of Extended Experience. *Neuron*. <https://doi.org/10.1016/j.neuron.2009.07.027>
- De Pins, B., Cifuentes-Díaz, C., Thamila Farah, A., López-Molina, L., Montalban, E., Sancho-Balsells, A., López, A., Ginés, S., Delgado-García, J. M., Alberch, J., Gruart, A., Girault, J. A., & Giralt, A. (2019). Conditional BDNF delivery from astrocytes rescues memory deficits, spine density, and synaptic properties in the 5xFAD mouse model of alzheimer disease. *Journal of Neuroscience*. <https://doi.org/10.1523/JNEUROSCI.2121-18.2019>
- de Vito, S., & della Sala, S. (2011). Predicting the future. *Cortex*, *47*(8). <https://doi.org/10.1016/j.cortex.2011.02.020>
- delpolyi, A. R., Rankin, K. P., Mucke, L., Miller, B. L., & Gorno-Tempini, M. L. (2007). Spatial cognition and the human navigation network in AD and MCI. *Neurology*, *69*(10), 986–997. <https://doi.org/10.1212/01.wnl.0000271376.19515.c6>
- DeKosky, S. T., & Scheff, S. W. (1990). Synapse loss in frontal cortex biopsies in Alzheimer's disease: Correlation with cognitive severity. *Annals of Neurology*, *27*(5). <https://doi.org/10.1002/ana.410270502>
- del Grosso, N. A., & Sirota, A. (2019). Ratcave: A 3D graphics python package for cognitive psychology experiments. *Behavior Research Methods*, *51*(5). <https://doi.org/10.3758/s13428-019-01245-x>
- Diba, K., Amarasingham, A., Mizuseki, K., & Buzsáki, G. (2014). Millisecond timescale synchrony among hippocampal neurons. *The Journal of Neuroscience : The Official Journal of the Society for Neuroscience*, *34*(45), 14984–14994. <https://doi.org/10.1523/JNEUROSCI.1091-14.2014>
- Diba, K., & Buzsáki, G. (2007). Forward and reverse hippocampal place-cell sequences during ripples. *Nature Neuroscience*. <https://doi.org/10.1038/nn1961>
- Diehl, G. W., & Redish, A. David. (2022). Differential processing of decision information in subregions of rodent medial prefrontal cortex. *BioRxiv*.
- Doucet, G., Gulli, R. A., & Martinez-Trujillo, J. C. (2016). Cross-species 3D virtual reality toolbox for visual and cognitive experiments. *Journal of Neuroscience Methods*, *266*. <https://doi.org/10.1016/j.jneumeth.2016.03.009>
- Dragoi, G., & Tonegawa, S. (2013). Development of schemas revealed by prior experience and NMDA receptor knock-out. *ELife*. <https://doi.org/10.7554/elife.01326>
- Dubois, B., Feldman, H. H., Jacova, C., Hampel, H., Molinuevo, J. L., Blennow, K., Dekosky, S. T., Gauthier, S., Selkoe, D., Bateman, R., Cappa, S., Crutch, S., Engelborghs, S., Frisoni, G. B., Fox, N. C., Galasko, D., Habert, M. O., Jicha, G. A., Nordberg, A., ... Cummings, J. L. (2014). Advancing research diagnostic criteria for Alzheimer's disease: The IWG-2 criteria. In *The Lancet Neurology* (Vol. 13, Issue 6). [https://doi.org/10.1016/S1474-4422\(14\)70090-0](https://doi.org/10.1016/S1474-4422(14)70090-0)
- Duncan, K., Ketz, N., Inati, S. J., & Davachi, L. (2012). Evidence for area CA1 as a match/mismatch detector: A high-resolution fMRI study of the human hippocampus. *Hippocampus*, *22*(3). <https://doi.org/10.1002/hipo.20933>
- Efron, B. (1992). *Bootstrap Methods: Another Look at the Jackknife*. https://doi.org/10.1007/978-1-4612-4380-9_41
- Efron, B., & Tibshirani, R. J. (1993). An Introduction to the Bootstrap. In *An Introduction to the Bootstrap*. <https://doi.org/10.1007/978-1-4899-4541-9>
- Ego-Stengel, V., & Wilson, M. A. (2007). Spatial selectivity and theta phase precession in CA1 interneurons. *Hippocampus*, *17*(2), 161–174. <https://doi.org/10.1002/hipo.20253>

- English, D. F., McKenzie, S., Evans, T., Kim, K., Yoon, E., & Buzsáki, G. (2017). Pyramidal Cell-Interneuron Circuit Architecture and Dynamics in Hippocampal Networks. *Neuron*, *96*(2), 505-520.e7. <https://doi.org/10.1016/j.neuron.2017.09.033>
- Euston, D. R., Tatsuno, M., & McNaughton, B. L. (2007). Fast-forward playback of recent memory sequences in prefrontal cortex during sleep. *Science*, *318*(5853). <https://doi.org/10.1126/science.1148979>
- Feng, T., Silva, D., & Foster, D. J. (2015). Dissociation between the Experience-Dependent Development of Hippocampal Theta Sequences and Single-Trial Phase Precession. *Journal of Neuroscience*, *35*(12), 4890–4902. <https://doi.org/10.1523/JNEUROSCI.2614-14.2015>
- Fernández-Ruiz, A., Oliva, A., Fermino de Oliveira, E., Rocha-Almeida, F., Tingley, D., & Buzsáki, G. (2019). Long-duration hippocampal sharp wave ripples improve memory. *Science*, *364*(6445), 1082–1086. <https://doi.org/10.1126/science.aax0758>
- Field, C. A., & Welsh, A. H. (2007). Bootstrapping clustered data. *Journal of the Royal Statistical Society. Series B: Statistical Methodology*. <https://doi.org/10.1111/j.1467-9868.2007.00593.x>
- Flanigan, T. J., Xue, Y., Rao, S. K., Dhanushkodi, A., & McDonald, M. P. (2014). Abnormal vibrissa-related behavior and loss of barrel field inhibitory neurons in 5xFAD transgenics. *Genes, Brain and Behavior*. <https://doi.org/10.1111/gbb.12133>
- Foster, D. J., & Wilson, M. A. (2006). Reverse replay of behavioural sequences in hippocampal place cells during the awake state. *Nature*, *440*(7084). <https://doi.org/10.1038/nature04587>
- Foster, D. J., & Wilson, M. A. (2007). Hippocampal theta sequences. *Hippocampus*, *17*(11), 1093–1099. <https://doi.org/10.1002/hipo.20345>
- Fournier, J., Saleem, A. B., Diamanti, E. M., Wells, M. J., Harris, K. D., & Carandini, M. (2020). Mouse Visual Cortex Is Modulated by Distance Traveled and by Theta Oscillations. *Current Biology*, *30*(19). <https://doi.org/10.1016/j.cub.2020.07.006>
- Freir, D. B., Holscher, C., & Herron, C. E. (2017). Blockade of Long-Term Potentiation by β -Amyloid Peptides in the CA1 Region of the Rat Hippocampus In Vivo. *Journal of Neurophysiology*. <https://doi.org/10.1152/jn.2001.85.2.708>
- Fujisawa, S., Amarasingham, A., Harrison, M. T., & Buzsáki, G. (2008). Behavior-dependent short-term assembly dynamics in the medial prefrontal cortex. *Nature Neuroscience*, *11*(7), 823–833. <https://doi.org/10.1038/nn.2134>
- Fujisawa, S., & Buzsáki, G. (2011). A 4 Hz Oscillation Adaptively Synchronizes Prefrontal, VTA, and Hippocampal Activities. *Neuron*, *72*(1). <https://doi.org/10.1016/j.neuron.2011.08.018>
- Fuster, J. M. (2015). *The Prefrontal Cortex*. Academic Press. <https://doi.org/10.1016/C2012-0-06164-9>
- Fuster, J. M., & Alexander, G. E. (1971). Neuron activity related to short-term memory. *Science*, *173*(3997). <https://doi.org/10.1126/science.173.3997.652>
- Games, D., Adams, D., Alessandrini, R., Barbour, R., Borthelette, P., Blackwell, C., Carr, T., Clemens, J., Donaldson, T., Gillespie, F., Guido, T., Hagopian, S., Johnson-Wood, K., Khan, K., Lee, M., Leibowitz, P., Lieberburg, I., Little, S., Masliah, E., ... Zhao, J. (1995). Alzheimer-type neuropathology in transgenic mice overexpressing V717F β -amyloid precursor protein. *Nature*. <https://doi.org/10.1038/373523a0>
- Geiller, T., Fattahi, M., Choi, J. S., & Royer, S. (2017). Place cells are more strongly tied to landmarks in deep than in superficial CA1. *Nature Communications*. <https://doi.org/10.1038/ncomms14531>
- Giesers, N. K., & Wirths, O. (2020). Loss of Hippocampal Calretinin and Parvalbumin Interneurons in the 5XFAD Mouse Model of Alzheimer's Disease. *ASN Neuro*. <https://doi.org/10.1177/1759091420925356>
- Gillespie, A. K., Astudillo Maya, D. A., Denovellis, E. L., Liu, D. F., Kastner, D. B., Coulter, M. E., Roumis, D. K., Eden, U. T., & Frank, L. M. (2021). Hippocampal replay reflects specific

- past experiences rather than a plan for subsequent choice. *Neuron*, 109(19).
<https://doi.org/10.1016/j.neuron.2021.07.029>
- Gillespie, A. K., Jones, E. A., Lin, Y. H., Karlsson, M. P., Kay, K., Yoon, S. Y., Tong, L. M., Nova, P., Carr, J. S., Frank, L. M., & Huang, Y. (2016). Apolipoprotein E4 Causes Age-Dependent Disruption of Slow Gamma Oscillations during Hippocampal Sharp-Wave Ripples. *Neuron*, 90(4), 740–751. <https://doi.org/10.1016/j.neuron.2016.04.009>
- Girardeau, G., Benchenane, K., Wiener, S. I., Buzsáki, G., & Zugaro, M. B. (2009). Selective suppression of hippocampal ripples impairs spatial memory. *Nature Neuroscience*, 12(10), 1222–1223. <https://doi.org/10.1038/nn.2384>
- Girardeau, G., & Zugaro, M. (2011). Hippocampal ripples and memory consolidation. *Current Opinion in Neurobiology*. <https://doi.org/10.1016/j.conb.2011.02.005>
- Goldman-Rakic, P. S. (1995). Cellular basis of working memory. *Neuron*, 14(3), 477–485. [https://doi.org/10.1016/0896-6273\(95\)90304-6](https://doi.org/10.1016/0896-6273(95)90304-6)
- Gonzalez-Burgos, G., & Lewis, D. A. (2008). GABA neurons and the mechanisms of network oscillations: Implications for understanding cortical dysfunction in schizophrenia. In *Schizophrenia Bulletin*. <https://doi.org/10.1093/schbul/sbn070>
- Gorgolewski, K. J., Auer, T., Calhoun, V. D., Craddock, R. C., Das, S., Duff, E. P., Flandin, G., Ghosh, S. S., Glatard, T., Halchenko, Y. O., Handwerker, D. A., Hanke, M., Keator, D., Li, X., Michael, Z., Maumet, C., Nichols, B. N., Nichols, T. E., Pellman, J., ... Poldrack, R. A. (2016). The brain imaging data structure, a format for organizing and describing outputs of neuroimaging experiments. *Scientific Data*, 3. <https://doi.org/10.1038/sdata.2016.44>
- Goutagny, R., & Krantic, S. (2013). Hippocampal oscillatory activity in Alzheimer's disease: Toward the identification of early biomarkers? In *Aging and Disease* (Vol. 4, Issue 3).
- Guise, K. G., & Shapiro, M. L. (2017). Medial Prefrontal Cortex Reduces Memory Interference by Modifying Hippocampal Encoding. *Neuron*, 94(1), 183-192.e8. <https://doi.org/10.1016/j.neuron.2017.03.011>
- Gupta, A. S., van der Meer, M. A. A., Touretzky, D. S., & Redish, A. D. (2010). Hippocampal Replay Is Not a Simple Function of Experience. *Neuron*, 65(5). <https://doi.org/10.1016/j.neuron.2010.01.034>
- Gupta, A. S., van der Meer, M. A. A., Touretzky, D. S., & Redish, A. D. (2012). Segmentation of spatial experience by hippocampal theta sequences. *Nature Neuroscience*, 15(7). <https://doi.org/10.1038/nn.3138>
- Haider, B., Hausser, M., & Carandini, M. (2013). Inhibition dominates sensory responses in the awake cortex. *Nature*, 493(7430), 97–100. <https://doi.org/10.1038/nature11665>
- Harden, J. J. (2011). A bootstrap method for conducting statistical inference with clustered data. *State Politics and Policy Quarterly*. <https://doi.org/10.1177/1532440011406233>
- Hartley, T., Lever, C., Burgess, N., & O'Keefe, J. (2014). Space in the brain: How the hippocampal formation supports spatial cognition. In *Philosophical Transactions of the Royal Society B: Biological Sciences* (Vol. 369, Issue 1635). <https://doi.org/10.1098/rstb.2012.0510>
- Hassabis, D., Kumaran, D., Vann, S. D., & Maguire, E. A. (2007). Patients with hippocampal amnesia cannot imagine new experiences. *Proceedings of the National Academy of Sciences of the United States of America*, 104(5). <https://doi.org/10.1073/pnas.0610561104>
- Hasselmo, M. E., Bodelón, C., & Wyble, B. P. (2002). A proposed function for hippocampal theta rhythm: Separate phases of encoding and retrieval enhance reversal of prior learning. *Neural Computation*, 14(4). <https://doi.org/10.1162/089976602317318965>
- Hasz, B. M., & Redish, A. D. (2018). Deliberation and procedural automation on a two-step task for rats. *Frontiers in Integrative Neuroscience*, 12. <https://doi.org/10.3389/fnint.2018.00030>

- Hasz, B. M., & Redish, A. D. (2020). Spatial encoding in dorsomedial prefrontal cortex and hippocampus is related during deliberation. *Hippocampus*, *30*(11). <https://doi.org/10.1002/hipo.23250>
- Hatsopoulos, N., Geman, S., Amarasingham, A., & Bienenstock, E. (2003). At what time scale does the nervous system operate? *Neurocomputing*. [https://doi.org/10.1016/s0925-2312\(02\)00773-7](https://doi.org/10.1016/s0925-2312(02)00773-7)
- Heidbreder, C. A., & Groenewegen, H. J. (2003). The medial prefrontal cortex in the rat: Evidence for a dorso-ventral distinction based upon functional and anatomical characteristics. In *Neuroscience and Biobehavioral Reviews* (Vol. 27, Issue 6). <https://doi.org/10.1016/j.neubiorev.2003.09.003>
- Hok, V., Save, E., & Poucet, B. (2005). Coding for Spatial Goals in the Prelimbic-Infralimbic. *Proceedings of the National Academy of Sciences (PNAS)*, *102*(12).
- Holczer, A., Németh, V. L., Vékony, T., Vécsei, L., Klivényi, P., & Must, A. (2020). Non-invasive brain stimulation in alzheimer's disease and mild cognitive impairment—a state-of-the-art review on methodological characteristics and stimulation parameters. In *Frontiers in Human Neuroscience* (Vol. 14). <https://doi.org/10.3389/fnhum.2020.00179>
- Hoover, W. B., & Vertes, R. P. (2007). Anatomical analysis of afferent projections to the medial prefrontal cortex in the rat. *Brain Structure & Function*, *212*(2), 149–179. <https://doi.org/10.1007/s00429-007-0150-4>
- Hsia, A. Y., Masliah, E., McConlogue, L., Yu, G. Q., Tatsuno, G., Hu, K., Kholodenko, D., Malenka, R. C., Nicoll, R. A., & Mucke, L. (1999). Plaque-independent disruption of neural circuits in Alzheimer's disease mouse models. *Proceedings of the National Academy of Sciences of the United States of America*.
- Hu, F., Zhang, L.-X., & He, X. (2009). Efficient randomized-adaptive designs. *The Annals of Statistics*, *37*(5A). <https://doi.org/10.1214/08-AOS655>
- Hunt, L. T., Daw, N. D., Kaanders, P., MacIver, M. A., Mugan, U., Procyk, E., Redish, A. D., Russo, E., Scholl, J., Stachenfeld, K., Wilson, C. R. E., & Kolling, N. (2021). Formalizing planning and information search in naturalistic decision-making. In *Nature Neuroscience* (Vol. 24, Issue 8). <https://doi.org/10.1038/s41593-021-00866-w>
- Hyman, J. M., Whitman, J., Emberly, E., Woodward, T. S., & Seamans, J. K. (2013). Action and outcome activity state patterns in the anterior cingulate cortex. *Cerebral Cortex*, *23*(6). <https://doi.org/10.1093/cercor/bhs104>
- Hyman, J. M., Zilli, E. A., Paley, A. M., & Hasselmo, M. E. (2005). Medial prefrontal cortex cells show dynamic modulation with the hippocampal theta rhythm dependent on behavior. *Hippocampus*, *15*(6), 739–749. <https://doi.org/10.1002/hipo.20106>
- Iaccarino, H. F., Singer, A. C., Martorell, A. J., Rudenko, A., Gao, F., Gillingham, T. Z., Mathys, H., Seo, J., Kritskiy, O., Abdurrob, F., Adaikkan, C., Canter, R. G., Rueda, R., Brown, E. N., Boyden, E. S., & Tsai, L. H. (2016). Gamma frequency entrainment attenuates amyloid load and modifies microglia. *Nature*, *540*(7632), 230–235. <https://doi.org/10.1038/nature20587>
- Isaacson, J. S., & Scanziani, M. (2011). How inhibition shapes cortical activity. In *Neuron*. <https://doi.org/10.1016/j.neuron.2011.09.027>
- Ito, H. T. (2018). Prefrontal–hippocampal interactions for spatial navigation. In *Neuroscience Research* (Vol. 129). <https://doi.org/10.1016/j.neures.2017.04.016>
- Jackson, J. C., Johnson, A., & Redish, A. D. (2006). Hippocampal Sharp Waves and Reactivation during Awake States Depend on Repeated Sequential Experience. *Journal of Neuroscience*. <https://doi.org/10.1523/jneurosci.4118-06.2006>
- Jadhav, S. P., Kemere, C., German, P. W., & Frank, L. M. (2012). Awake Hippocampal Sharp-Wave Ripples Support Spatial Memory. *Science*, *336*(6087), 1454–1458. <https://doi.org/10.1126/science.1217230>

- Jadhav, S. P., Rothschild, G., Roumis, D. K., & Frank, L. M. (2016). *Coordinated Excitation and Inhibition of Prefrontal Ensembles during Awake Hippocampal Sharp-Wave Ripple Events*. <https://doi.org/10.1016/j.neuron.2016.02.010>
- Jankowsky, J. L., & Zheng, H. (2017). Practical considerations for choosing a mouse model of Alzheimer's disease. In *Molecular Neurodegeneration* (Vol. 12, Issue 1). <https://doi.org/10.1186/s13024-017-0231-7>
- Javadi, A. H., Patai, E. Z., Marin-Garcia, E., Margois, A., Tan, H. R. M., Kumaran, D., Nardini, M., Penny, W., Duzel, E., Dayan, P., & Spiers, H. J. (2019). Backtracking during navigation is correlated with enhanced anterior cingulate activity and suppression of alpha oscillations and the "default-mode" network. *Proceedings of the Royal Society B: Biological Sciences*, 286(1908). <https://doi.org/10.1098/rspb.2019.1016>
- Jay, T. M., & Witter, M. P. (1991). Distribution of hippocampal CA1 and subicular efferents in the prefrontal cortex of the rat studied by means of anterograde transport of Phaseolus vulgaris-leucoagglutinin. *The Journal of Comparative Neurology*, 313(4), 574–586. <https://doi.org/10.1002/cne.903130404>
- Jayakumar, R. P., Madhav, M. S., Savelli, F., Blair, H. T., Cowan, N. J., & Knierim, J. J. (2019). Recalibration of path integration in hippocampal place cells. *Nature*, 566(7745). <https://doi.org/10.1038/s41586-019-0939-3>
- Jezeq, K., Henriksen, E. J., Treves, A., Moser, E. I., & Moser, M. B. (2011). Theta-paced flickering between place-cell maps in the hippocampus. *Nature*, 478(7368). <https://doi.org/10.1038/nature10439>
- Johnson, A., & Redish, A. D. (2007). Neural ensembles in CA3 transiently encode paths forward of the animal at a decision point. *Journal of Neuroscience*, 27(45). <https://doi.org/10.1523/JNEUROSCI.3761-07.2007>
- Jones, E. A., Gillespie, A. K., Yoon, S. Y., Frank, L. M., & Huang, Y. (2019). Early Hippocampal Sharp-Wave Ripple Deficits Predict Later Learning and Memory Impairments in an Alzheimer's Disease Mouse Model. *Cell Reports*, 29(8). <https://doi.org/10.1016/j.celrep.2019.10.056>
- Jones, M. W., & Wilson, M. A. (2005). Theta rhythms coordinate hippocampal-prefrontal interactions in a spatial memory task. *PLoS Biology*, 3(12), e402. <https://doi.org/10.1371/journal.pbio.0030402>
- Jura, B., Macrez, N., Meyrand, P., & Bem, T. (2019). Deficit in hippocampal ripples does not preclude spatial memory formation in APP/PS1 mice. *Scientific Reports*, 9(1). <https://doi.org/10.1038/s41598-019-56582-w>
- Kaefer, K., Nardin, M., Blahna, K., & Csicsvari, J. (2020). Replay of Behavioral Sequences in the Medial Prefrontal Cortex during Rule Switching. *Neuron*, 106(1). <https://doi.org/10.1016/j.neuron.2020.01.015>
- Kapl, S., Tichanek, F., Zitricky, F., & Jezeq, K. (2022). Context-independent expression of spatial code in hippocampus. *Scientific Reports*, 12(1), 20711. <https://doi.org/10.1038/s41598-022-25006-7>
- Kaplan, R., Bush, D., Bisby, J. A., Horner, A. J., Meyer, S. S., & Burgess, N. (2017). Medial prefrontal–medial temporal theta phase coupling in dynamic spatial imagery. *Journal of Cognitive Neuroscience*, 29(3). https://doi.org/10.1162/jocn_a_01064
- Karlsson, M. P., & Frank, L. M. (2009). Awake replay of remote experiences in the hippocampus. *Nature Neuroscience*. <https://doi.org/10.1038/nn.2344>
- Kay, K., Chung, J. E., Sosa, M., Schor, J. S., Karlsson, M. P., Larkin, M. C., Liu, D. F., & Frank, L. M. (2020). Constant Sub-second Cycling between Representations of Possible Futures in the Hippocampus. *Cell*, 180(3). <https://doi.org/10.1016/j.cell.2020.01.014>
- Kimura, R., & Ohno, M. (2009). Impairments in remote memory stabilization precede hippocampal synaptic and cognitive failures in 5XFAD Alzheimer mouse model. *Neurobiology of Disease*, 33(2), 229–235. <https://doi.org/10.1016/j.nbd.2008.10.006>

- Kira, S., Safaai, H., Morcos, A. S., Panzeri, S., & Harvey, C. D. (2022). A distributed and efficient population code of mixed selectivity neurons for flexible navigation decisions. *BioRxiv*, 2022.04.10.487349. <https://doi.org/10.1101/2022.04.10.487349>
- Klausberger, T., Magill, P. J., Márton, L. F., Roberts, J. D. B., Cobden, P. M., Buzsáki, G., & Somogyi, P. (2003). Brain-state- and cell-type-specific firing of hippocampal interneurons in vivo. *Nature*. <https://doi.org/10.1038/nature01374>
- Klein, S. B., Loftus, J., & Kihlstrom, J. F. (2002). Memory and temporal experience: The effects of episodic memory loss on an amnesic patient's ability to remember the past and imagine the future. *Social Cognition*, 20(5). <https://doi.org/10.1521/soco.20.5.353.21125>
- Kubota, K., & Niki, H. (1971). Prefrontal cortical unit activity and delayed alternation performance in monkeys. *Journal of Neurophysiology*, 34(3). <https://doi.org/10.1152/jn.1971.34.3.337>
- Langston, R. F., Ainge, J. A., Couey, J. J., Canto, C. B., Bjerknes, T. L., Witter, M. P., Moser, E. I., & Moser, M. B. (2010). Development of the spatial representation system in the rat. *Science*. <https://doi.org/10.1126/science.1188210>
- Laubach, M., Amarante, L. M., Swanson, K., & White, S. R. (2018). What, if anything, is rodent prefrontal cortex? In *eNeuro* (Vol. 5, Issue 5). <https://doi.org/10.1523/ENEURO.0315-18.2018>
- Leung, L., Andrews-Zwilling, Y., Yoon, S. Y., Jain, S., Ring, K., Dai, J., Wang, M. M., Tong, L., Walker, D., & Huang, Y. (2012). Apolipoprotein E4 Causes Age- and Sex-Dependent Impairments of Hilar GABAergic Interneurons and Learning and Memory Deficits in Mice. *PLoS ONE*. <https://doi.org/10.1371/journal.pone.0053569>
- Li, G., Bien-Ly, N., Andrews-Zwilling, Y., Xu, Q., Bernardo, A., Ring, K., Halabisky, B., Deng, C., Mahley, R. W., & Huang, Y. (2009). GABAergic Interneuron Dysfunction Impairs Hippocampal Neurogenesis in Adult Apolipoprotein E4 Knockin Mice. *Cell Stem Cell*. <https://doi.org/10.1016/j.stem.2009.10.015>
- Lisman, J. E., & Grace, A. A. (2005). The hippocampal-VTA loop: Controlling the entry of information into long-term memory. In *Neuron* (Vol. 46, Issue 5). <https://doi.org/10.1016/j.neuron.2005.05.002>
- Lisman, J., & Redish, A. D. (2009). Prediction, sequences and the hippocampus. *Philosophical Transactions of the Royal Society B: Biological Sciences*, 364(1521), 1193–1201. <https://doi.org/10.1098/rstb.2008.0316>
- Lopes, G., Farrell, K., Horrocks, E. A. B., Lee, C. Y., Morimoto, M. M., Muzzu, T., Papanikolaou, A., Rodrigues, F. R., Wheatcroft, T., Zucca, S., Solomon, S. G., & Saleem, A. B. (2021). Creating and controlling visual environments using bonvision. *ELife*, 10. <https://doi.org/10.7554/ELIFE.65541>
- Madhav, M. S., Jayakumar, R. P., Lashkari, S. G., Savelli, F., Blair, H. T., Knierim, J. J., & Cowan, N. J. (2022). The Dome: A virtual reality apparatus for freely locomoting rodents. *Journal of Neuroscience Methods*, 368. <https://doi.org/10.1016/j.jneumeth.2021.109336>
- Malik, R., Li, Y., Schamiloglu, S., & Sohal, V. S. (2022). Top-down control of hippocampal signal-to-noise by prefrontal long-range inhibition. *Cell*, 185(9). <https://doi.org/10.1016/j.cell.2022.04.001>
- Manns, J. R., Zilli, E. A., Ong, K. C., Hasselmo, M. E., & Eichenbaum, H. (2007). Hippocampal CA1 spiking during encoding and retrieval: Relation to theta phase. *Neurobiology of Learning and Memory*, 87(1). <https://doi.org/10.1016/j.nlm.2006.05.007>
- Martinez-Losa, M., Tracy, T. E., Ma, K., Verret, L., Clemente-Perez, A., Khan, A. S., Cobos, I., Ho, K., Gan, L., Mucke, L., Alvarez-Dolado, M., & Palop, J. J. (2018). Nav1.1-Overexpressing Interneuron Transplants Restore Brain Rhythms and Cognition in a Mouse Model of Alzheimer's Disease. *Neuron*, 98(1). <https://doi.org/10.1016/j.neuron.2018.02.029>
- Martorell, A. J., Paulson, A. L., Suk, H.-J., Abdurrob, F., Drummond, G. T., Guan, W., Young, J. Z., Kim, D. N.-W., Kritskiy, O., Barker, S. J., Mangena, V., Prince, S. M., Brown, E. N.,

- Chung, K., Boyden, E. S., Singer, A. C., & Tsai, L.-H. (2019). Multi-sensory Gamma Stimulation Ameliorates Alzheimer's-Associated Pathology and Improves Cognition. *Cell*, 177(2), 256-271.e22. <https://doi.org/10.1016/j.cell.2019.02.014>
- Mashhoori, A., Hashemnia, S., McNaughton, B. L., Euston, D. R., & Gruber, A. J. (2018). Rat anterior cingulate cortex recalls features of remote reward locations after disfavoured reinforcements. *ELife*, 7. <https://doi.org/10.7554/eLife.29793>
- Miller, E. K., & Cohen, J. D. (2001). An integrative theory of prefrontal cortex function. *Annual Review of Neuroscience*, 24(1), 167–202. <https://doi.org/10.1146/annurev.neuro.24.1.167>
- Miller, K. J., Botvinick, M. M., & Brody, C. D. (2017). Dorsal hippocampus contributes to model-based planning. *Nature Neuroscience*, 20(9), 1269–1276. <https://doi.org/10.1038/nn.4613>
- Mishkin, M. (1964). Perseveration of central sets after frontal lesions in monkeys. In J. M. Warren & K. Abert (Eds.), *The Frontal Granular Cortex and Behavior* (pp. 219–241). McGraw-Hill.
- Mullally, S. L., & Maguire, E. A. (2014). Memory, Imagination, and Predicting the Future. *The Neuroscientist*, 20(3). <https://doi.org/10.1177/1073858413495091>
- Nicole, O., Hadzibegovic, S., Gajda, J., Bontempi, B., Bem, T., & Meyrand, P. (2016). Soluble amyloid beta oligomers block the learning-induced increase in hippocampal sharp wave-ripple rate and impair spatial memory formation. *Scientific Reports*, 6. <https://doi.org/10.1038/srep22728>
- Niell, C. M., & Stryker, M. P. (2008). Highly Selective Receptive Fields in Mouse Visual Cortex. *Journal of Neuroscience*. <https://doi.org/10.1523/jneurosci.0623-08.2008>
- Nyberg, N., Duvelle, É., Barry, C., & Spiers, H. J. (2022). Spatial goal coding in the hippocampal formation. *Neuron*, 110(3), 394–422. <https://doi.org/10.1016/j.neuron.2021.12.012>
- Oakley, H., Cole, S. L., Logan, S., Maus, E., Shao, P., Craft, J., Guillozet-Bongaarts, A., Ohno, M., Disterhoft, J., van Eldik, L., Berry, R., & Vassar, R. (2006). Intraneuronal β -Amyloid Aggregates, Neurodegeneration, and Neuron Loss in Transgenic Mice with Five Familial Alzheimer's Disease Mutations: Potential Factors in Amyloid Plaque Formation. *The Journal of Neuroscience*, 26(40), 10129. <https://doi.org/10.1523/JNEUROSCI.1202-06.2006>
- Oblak, A. L., Lin, P. B., Kotredes, K. P., Pandey, R. S., Garceau, D., Williams, H. M., Uyar, A., O'Rourke, R., O'Rourke, S., Ingraham, C., Bednarczyk, D., Belanger, M., Cope, Z. A., Little, G. J., Williams, S. P. G., Ash, C., Bleckert, A., Ragan, T., Logsdon, B. A., ... Lamb, B. T. (2021). Comprehensive Evaluation of the 5XFAD Mouse Model for Preclinical Testing Applications: A MODEL-AD Study. *Frontiers in Aging Neuroscience*, 13. <https://doi.org/10.3389/fnagi.2021.713726>
- O'Keefe, J., & Dostrovsky, J. (1971). The hippocampus as a spatial map. Preliminary evidence from unit activity in the freely-moving rat. *Brain Res*, 34(1), 171–175. <https://www.ncbi.nlm.nih.gov/pubmed/5124915>
- O'Keefe, J., & Nadel, L. (1978). *The hippocampus as a cognitive map*. Clarendon Press ; Oxford University Press.
- O'Keefe, J., & Recce, M. L. (1993). Phase relationship between hippocampal place units and the EEG theta rhythm. *Hippocampus*, 3(3). <https://doi.org/10.1002/hipo.450030307>
- O'Leary, T. P., Robertson, A., Chipman, P. H., Rafuse, V. F., & Brown, R. E. (2018). Motor function deficits in the 12 month-old female 5xFAD mouse model of Alzheimer's disease. *Behavioural Brain Research*. <https://doi.org/10.1016/j.bbr.2017.09.009>
- O'Neill, J., Senior, T. J., Allen, K., Huxter, J. R., & Csicsvari, J. (2008). Reactivation of experience-dependent cell assembly patterns in the hippocampus. *Nature Neuroscience*, 11(2), 209–215. <https://doi.org/10.1038/nn2037>
- O'Neill, P.-K., Gordon, J. A., & Sigurdsson, T. (2013). Theta oscillations in the medial prefrontal cortex are modulated by spatial working memory and synchronize with the hippocampus through its ventral subregion. *The Journal of Neuroscience : The Official Journal of the*

- Society for Neuroscience*, 33(35), 14211–14224.
<https://doi.org/10.1523/JNEUROSCI.2378-13.2013>
- Pachitariu, M., Steinmetz, N., Kadir, S., Carandini, M., & Harris, K. D. (2016). Kilosort: realtime spike-sorting for extracellular electrophysiology with hundreds of channels. In *bioRxiv*.
- Palop, J. J., Chin, J., & Mucke, L. (2006). A network dysfunction perspective on neurodegenerative diseases. In *Nature* (Vol. 443, Issue 7113).
<https://doi.org/10.1038/nature05289>
- Palop, J. J., Chin, J., Roberson, E. D., Wang, J., Thwin, M. T., Bien-Ly, N., Yoo, J., Ho, K. O., Yu, G. Q., Kreitzer, A., Finkbeiner, S., Noebels, J. L., & Mucke, L. (2007). Aberrant Excitatory Neuronal Activity and Compensatory Remodeling of Inhibitory Hippocampal Circuits in Mouse Models of Alzheimer's Disease. *Neuron*.
<https://doi.org/10.1016/j.neuron.2007.07.025>
- Palop, J. J., & Mucke, L. (2010). Amyloid-beta-induced neuronal dysfunction in Alzheimer's disease: from synapses toward neural networks. *Nature Neuroscience*, 13(7), 812–818.
<https://doi.org/10.1038/nn.2583>
- Palop, J. J., & Mucke, L. (2016). Network abnormalities and interneuron dysfunction in Alzheimer disease. *Nature Reviews Neuroscience*, 17(12), 777–792.
<https://doi.org/10.1038/nrn.2016.141>
- Patai, E. Z., & Spiers, H. J. (2021). The Versatile Wayfinder: Prefrontal Contributions to Spatial Navigation. In *Trends in Cognitive Sciences* (Vol. 25, Issue 6).
<https://doi.org/10.1016/j.tics.2021.02.010>
- Perkel, D. H., Gerstein, G. L., & Moore, G. P. (1967). Neuronal Spike Trains and Stochastic Point Processes: II. Simultaneous Spike Trains. *Biophysical Journal*.
[https://doi.org/10.1016/S0006-3495\(67\)86597-4](https://doi.org/10.1016/S0006-3495(67)86597-4)
- Petersen, P. C., Siegle, J. H., Steinmetz, N. A., Mahallati, S., & Buzsáki, G. (2021). CellExplorer: A framework for visualizing and characterizing single neurons. *Neuron*, 109(22). <https://doi.org/10.1016/j.neuron.2021.09.002>
- Petrache, A. L., Rajulawalla, A., Shi, A., Wetzels, A., Saito, T., Saido, T. C., Harvey, K., & Ali, A. B. (2019). Aberrant Excitatory–Inhibitory Synaptic Mechanisms in Entorhinal Cortex Microcircuits During the Pathogenesis of Alzheimer's Disease. *Cerebral Cortex*.
<https://doi.org/10.1093/cercor/bhz016>
- Peyrache, A., Battaglia, F. P., & Destexhe, A. (2011). Inhibition recruitment in prefrontal cortex during sleep spindles and gating of hippocampal inputs. *Proceedings of the National Academy of Sciences of the United States of America*, 108(41).
<https://doi.org/10.1073/pnas.1103612108>
- Peyrache, A., Khamassi, M., Benchenane, K., Wiener, S. I., & Battaglia, F. P. (2009). Replay of rule-learning related neural patterns in the prefrontal cortex during sleep. *Nat Neurosci*, 12(7), 919–926. <https://doi.org/10.1038/nn.2337>
- Pezzulo, G., Donnarumma, F., Maisto, D., & Stoianov, I. (2019). Planning at decision time and in the background during spatial navigation. In *Current Opinion in Behavioral Sciences* (Vol. 29). <https://doi.org/10.1016/j.cobeha.2019.04.009>
- Pezzulo, G., Kemere, C., & van der Meer, M. A. A. (2017). Internally generated hippocampal sequences as a vantage point to probe future-oriented cognition. In *Annals of the New York Academy of Sciences* (Vol. 1396, Issue 1). <https://doi.org/10.1111/nyas.13329>
- Pfeiffer, B. E., & Foster, D. J. (2013). Hippocampal place-cell sequences depict future paths to remembered goals. *Nature*. <https://doi.org/10.1038/nature12112>
- Pinto, L., Koay, S. A., Engelhard, B., Yoon, A. M., Deverett, B., Thiberge, S. Y., Witten, I. B., Tank, D. W., & Brody, C. D. (2018). An accumulation-of-evidence task using visual pulses for mice navigating in virtual reality. *Frontiers in Behavioral Neuroscience*, 12.
<https://doi.org/10.3389/fnbeh.2018.00036>

- Place, R., Farovik, A., Brockmann, M., & Eichenbaum, H. (2016). Bidirectional prefrontal-hippocampal interactions support context-guided memory. *Nature Neuroscience*, *19*(8), 992–994. <https://doi.org/10.1038/nn.4327>
- Plitt, M. H., & Giocomo, L. M. (2021). Experience-dependent contextual codes in the hippocampus. *Nature Neuroscience*, *24*(5). <https://doi.org/10.1038/s41593-021-00816-6>
- Ponomarenko, A. A., Korotkova, T. M., Sergeeva, O. A., & Haas, H. L. (2004). Multiple GABAA receptor subtypes regulate hippocampal ripple oscillations. *European Journal of Neuroscience*. <https://doi.org/10.1111/j.1460-9568.2004.03685.x>
- Pouille, F., & Scanziani, M. (2001). Enforcement of temporal fidelity in pyramidal cells by somatic feed-forward inhibition. *Science*. <https://doi.org/10.1126/science.1060342>
- Preuss, T. M. (1995). Do rats have prefrontal cortex? The Rose-Woolsey-Akert program reconsidered. In *Journal of Cognitive Neuroscience* (Vol. 7, Issue 1). <https://doi.org/10.1162/jocn.1995.7.1.1>
- Puzzo, D., Privitera, L., Leznik, E., Fa, M., Staniszewski, A., Palmeri, A., & Arancio, O. (2008). Picomolar Amyloid- Positively Modulates Synaptic Plasticity and Memory in Hippocampus. *Journal of Neuroscience*. <https://doi.org/10.1523/JNEUROSCI.2692-08.2008>
- Radvansky, B. A., & Dombeck, D. A. (2018). An olfactory virtual reality system for mice. *Nature Communications*, *9*(1). <https://doi.org/10.1038/s41467-018-03262-4>
- Ragozzino, M. E., Adams, S., & Kesner, R. P. (1998). Differential involvement of the dorsal anterior cingulate and prelimbic- infralimbic areas of the rodent prefrontal cortex in spatial working memory. *Behavioral Neuroscience*, *112*(2). <https://doi.org/10.1037/0735-7044.112.2.293>
- Rajasethupathy, P., Sankaran, S., Marshel, J. H., Kim, C. K., Ferenczi, E., Lee, S. Y., Berndt, A., Ramakrishnan, C., Jaffe, A., Lo, M., Liston, C., & Deisseroth, K. (2015). Projections from neocortex mediate top-down control of memory retrieval. *Nature*, *526*(7575), 653–659. <https://doi.org/10.1038/nature15389>
- Ravassard, P., Kees, A., Willers, B., Ho, D., Aharoni, D., Cushman, J., Aghajan, Z. M., & Mehta, M. R. (2013). Multisensory control of hippocampal spatiotemporal selectivity. *Science*, *340*(6138). <https://doi.org/10.1126/science.1232655>
- Redish, A. D. (2016). Vicarious trial and error. *Nature Reviews Neuroscience*, *17*(3), 147–159. <https://doi.org/10.1038/nrn.2015.30>
- Robinson, J. C., & Brandon, M. P. (2021). Skipping ahead: A circuit for representing the past, present, and future. In *eLife* (Vol. 10). <https://doi.org/10.7554/eLife.68795>
- Rübel, O., Tritt, A., Ly, R., Dichter, B. K., Ghosh, S., Niu, L., Baker, P., Soltesz, I., Ng, L., Svoboda, K., Frank, L., & Bouchard, K. E. (2022). The Neurodata Without Borders ecosystem for neurophysiological data science. *ELife*, *11*. <https://doi.org/10.7554/eLife.78362>
- Saleem, A. B., Diamanti, E. M., Fournier, J., Harris, K. D., & Carandini, M. (2018). Coherent encoding of subjective spatial position in visual cortex and hippocampus. *Nature*. <https://doi.org/10.1038/s41586-018-0516-1>
- Salloway, S., Chalkias, S., Barkhof, F., Burkett, P., Barakos, J., Purcell, D., Suhy, J., Forrestal, F., Tian, Y., Umans, K., Wang, G., Singhal, P., Budd Haeberlein, S., & Smirnakis, K. (2022). Amyloid-Related Imaging Abnormalities in 2 Phase 3 Studies Evaluating Aducanumab in Patients with Early Alzheimer Disease. *JAMA Neurology*, *79*(1). <https://doi.org/10.1001/jamaneurol.2021.4161>
- Saravanan, V., Berman, G. J., & Sober, S. J. (2020). Application of the hierarchical bootstrap to multi-level data in neuroscience. *Neurons, Behavior, Data Analysis and Theory*, *3*(5).
- Sarel, A., Palgi, S., Blum, D., Aljadeff, J., Las, L., & Ulanovsky, N. (2022). Natural switches in behaviour rapidly modulate hippocampal coding. *Nature*, *609*(7925), 119–127. <https://doi.org/10.1038/s41586-022-05112-2>

- Sargolini, F., Fyhn, M., Hafting, T., McNaughton, B. L., Witter, M. P., Moser, M. B., & Moser, E. I. (2006). Conjunctive representation of position, direction, and velocity in entorhinal cortex. *Science*, *312*(5774). <https://doi.org/10.1126/science.1125572>
- Satler, C., Guimarães, L., & Tomaz, C. (2017). Planning ability impairments in probable Alzheimer's disease patients: Evidence from the tower of London test. *Dementia e Neuropsychologia*, *11*(2). <https://doi.org/10.1590/1980-57642016dn11-020006>
- Scearce-Levie, K., Sanchez, P. E., & Lewcock, J. W. (2020). Leveraging preclinical models for the development of Alzheimer disease therapeutics. In *Nature Reviews Drug Discovery*. <https://doi.org/10.1038/s41573-020-0065-9>
- Schlingloff, D., Kali, S., Freund, T. F., Hajos, N., & Gulyas, A. I. (2014). Mechanisms of Sharp Wave Initiation and Ripple Generation. *Journal of Neuroscience*. <https://doi.org/10.1523/jneurosci.0867-14.2014>
- Schmidt, B., Duin, A. A., & Redish, A. D. (2019). Disrupting the medial prefrontal cortex alters hippocampal sequences during deliberative decision making. *Journal of Neurophysiology*, *121*(6). <https://doi.org/10.1152/jn.00793.2018>
- Schneider, F., Baldauf, K., Wetzel, W., & Reymann, K. G. G. (2014). Behavioral and EEG changes in male 5xFAD mice. *Physiology and Behavior*, *135*, 25–33. <https://doi.org/10.1016/j.physbeh.2014.05.041>
- Scoville, W. B., & Milner, B. (1957). LOSS OF RECENT MEMORY AFTER BILATERAL HIPPOCAMPAL LESIONS. *Journal of Neurology, Neurosurgery & Psychiatry*, *20*(1), 11–21. <https://doi.org/10.1136/jnnp.20.1.11>
- Seamans, J. K., Floresco, S. B., & Phillips, A. G. (1995). Functional differences between the prelimbic and anterior cingulate regions of the rat prefrontal cortex. *Behavioral Neuroscience*, *109*(6). <https://doi.org/10.1037//0735-7044.109.6.1063>
- Selkoe, D. J. (2002). Alzheimer's Disease Is a Synaptic Failure. *Science*, *298*(5594), 789–791. <https://doi.org/10.1126/science.1074069>
- Senzai, Y., Fernandez-Ruiz, A., & Buzsáki, G. (2019). Layer-Specific Physiological Features and Interlaminar Interactions in the Primary Visual Cortex of the Mouse. *Neuron*. <https://doi.org/10.1016/j.neuron.2018.12.009>
- Sevigny, J., Chiao, P., Bussière, T., Weinreb, P. H., Williams, L., Maier, M., Dunstan, R., Salloway, S., Chen, T., Ling, Y., O'Gorman, J., Qian, F., Arastu, M., Li, M., Chollate, S., Brennan, M. S., Quintero-Monzon, O., Scannevin, R. H., Arnold, H. M., ... Sandrock, A. (2016). The antibody aducanumab reduces A β plaques in Alzheimer's disease. *Nature*, *537*(7618). <https://doi.org/10.1038/nature19323>
- Shamash, P., Carandini, M., Harris, K., & Steinmetz, N. (2018). A tool for analyzing electrode tracks from slice histology. *BioRxiv*.
- Shin, J. D., & Jadhav, S. P. (2016). Multiple modes of hippocampal–prefrontal interactions in memory-guided behavior. In *Current Opinion in Neurobiology* (Vol. 40). <https://doi.org/10.1016/j.conb.2016.07.015>
- Shin, J. D., Tang, W., & Jadhav, S. P. (2019). Dynamics of Awake Hippocampal-Prefrontal Replay for Spatial Learning and Memory-Guided Decision Making. *Neuron*, *104*(6). <https://doi.org/10.1016/j.neuron.2019.09.012>
- Siapas, A. G., Lubenov, E. v., & Wilson, M. A. (2005). Prefrontal phase locking to hippocampal theta oscillations. *Neuron*, *46*(1), 141–151. <https://doi.org/10.1016/j.neuron.2005.02.028>
- Siegle, J. H., & Wilson, M. A. (2014). Enhancement of encoding and retrieval functions through theta phase-specific manipulation of hippocampus. *ELife*, *3*. <https://doi.org/10.7554/elife.03061>
- Singer, A. C., Carr, M. F., Karlsson, M. P., & Frank, L. M. (2013). Hippocampal SWR Activity Predicts Correct Decisions during the Initial Learning of an Alternation Task. *Neuron*, *77*(6), 1163–1173. <https://doi.org/10.1016/j.neuron.2013.01.027>

- Singer, A. C., & Frank, L. M. (2009). Rewarded Outcomes Enhance Reactivation of Experience in the Hippocampus. *Neuron*, 64(6). <https://doi.org/10.1016/j.neuron.2009.11.016>
- Skaggs, W. E., & McNaughton, B. L. (1996). Replay of neuronal firing sequences in rat hippocampus during sleep following spatial experience. *Science*, 271(5257). <https://doi.org/10.1126/science.271.5257.1870>
- Skaggs, W. E., McNaughton, B. L., Wilson, M. A., & Barnes, C. A. (1996). Theta phase precession in hippocampal neuronal populations and the compression of temporal sequences. *Hippocampus*. [https://doi.org/10.1002/\(SICI\)1098-1063\(1996\)6:2<149::AID-HIPO6>3.0.CO;2-K](https://doi.org/10.1002/(SICI)1098-1063(1996)6:2<149::AID-HIPO6>3.0.CO;2-K)
- Smith, K. S., Virkud, A., Deisseroth, K., & Graybiel, A. M. (2012). Reversible online control of habitual behavior by optogenetic perturbation of medial prefrontal cortex. *Proceedings of the National Academy of Sciences of the United States of America*, 109(46). <https://doi.org/10.1073/pnas.1216264109>
- Sofroniew, N. J., Cohen, J. D., Lee, A. K., & Svoboda, K. (2014). Natural whisker-guided behavior by head-fixed mice in tactile virtual reality. *Journal of Neuroscience*, 34(29). <https://doi.org/10.1523/JNEUROSCI.0712-14.2014>
- Spellman, T., Rigotti, M., Ahmari, S. E., Fusi, S., Gogos, J. A., & Gordon, J. A. (2015). Hippocampal–prefrontal input supports spatial encoding in working memory. *Nature*, 522(7556), 309–314. <https://doi.org/10.1038/nature14445>
- Spiers, H. J. (2008). Keeping the goal in mind: Prefrontal contributions to spatial navigation. *Neuropsychologia*, 46(7). <https://doi.org/10.1016/j.neuropsychologia.2008.01.028>
- Staresina, B. P., Bergmann, T. O., Bonnefond, M., Van Der Meij, R., Jensen, O., Deuker, L., Elger, C. E., Axmacher, N., & Fell, J. (2015). Hierarchical nesting of slow oscillations, spindles and ripples in the human hippocampus during sleep. *Nature Neuroscience*. <https://doi.org/10.1038/nn.4119>
- Stark, E., Roux, L., Eichler, R., Senzai, Y., Royer, S., & Buzsáki, G. (2014). Pyramidal cell-interneuron interactions underlie hippocampal ripple oscillations. *Neuron*. <https://doi.org/10.1016/j.neuron.2014.06.023>
- Stella, F., Baracska, P., O'Neill, J., & Csicsvari, J. (2019). Hippocampal Reactivation of Random Trajectories Resembling Brownian Diffusion. *Neuron*, 102(2). <https://doi.org/10.1016/j.neuron.2019.01.052>
- Stéphan, A., Laroche, S., & Davis, S. (2001). Generation of aggregated beta-amyloid in the rat hippocampus impairs synaptic transmission and plasticity and causes memory deficits. *The Journal of Neuroscience : The Official Journal of the Society for Neuroscience*.
- Stephan, K. E., Baldeweg, T., & Friston, K. J. (2006). Synaptic Plasticity and Dysconnection in Schizophrenia. In *Biological Psychiatry*. <https://doi.org/10.1016/j.biopsych.2005.10.005>
- Steriade, M., Timofeev, I., & Grenier, F. (2001). Natural Waking and Sleep States. *Journal of Neurophysiology*.
- Štih, V., Petrucco, L., Kist, A. M., & Portugues, R. (2019). Stytra: An open-source, integrated system for stimulation, tracking and closed-loop behavioral experiments. *PLoS Computational Biology*, 15(4). <https://doi.org/10.1371/journal.pcbi.1006699>
- Stowers, J. R., Hofbauer, M., Bastien, R., Griessner, J., Higgins, P., Farooqui, S., Fischer, R. M., Nowikovsky, K., Haubensak, W., Couzin, I. D., Tessmar-Raible, K., & Straw, A. D. (2017). Virtual reality for freely moving animals. *Nature Methods*, 14(10). <https://doi.org/10.1038/nmeth.4399>
- Suh, J., Foster, D. J., Davoudi, H., Wilson, M. A., & Tonegawa, S. (2013). Impaired Hippocampal Ripple-Associated Replay in a Mouse Model of Schizophrenia. *Neuron*. <https://doi.org/10.1016/j.neuron.2013.09.014>
- Tamura, M., Spellman, T. J., Rosen, A. M., Gogos, J. A., & Gordon, J. A. (2017). Hippocampal-prefrontal theta-gamma coupling during performance of a spatial working memory task. *Nature Communications*, 8(1). <https://doi.org/10.1038/s41467-017-02108-9>

- Tanaka, K. (1983). Cross-correlation analysis of geniculostriate neuronal relationships in cats. *Journal of Neurophysiology*, *49*(6), 1303–1318. <https://doi.org/10.1152/jn.1983.49.6.1303>
- Tang, Q., Burgalossi, A., Ebbesen, C. L., Sanguinetti-Scheck, J. I., Schmidt, H., Tukker, J. J., Naumann, R., Ray, S., Preston-Ferrer, P., Schmitz, D., & Brecht, M. (2016). Functional architecture of the rat parasubiculum. *Journal of Neuroscience*, *36*(7). <https://doi.org/10.1523/JNEUROSCI.3749-15.2016>
- Tang, W., Shin, J. D., Frank, L. M., & Jadhav, S. P. (2017). Hippocampal-prefrontal reactivation during learning is stronger in awake compared with sleep states. *Journal of Neuroscience*, *37*(49). <https://doi.org/10.1523/JNEUROSCI.2291-17.2017>
- Tang, W., Shin, J. D., & Jadhav, S. P. (2021). Multiple time-scales of decision-making in the hippocampus and prefrontal cortex. *ELife*, *10*. <https://doi.org/10.7554/eLife.66227>
- Taube, J. S., Muller, R. U., & Ranck, J. B. (1990). Head-direction cells recorded from the postsubiculum in freely moving rats. I. Description and quantitative analysis. *Journal of Neuroscience*, *10*(2). <https://doi.org/10.1523/jneurosci.10-02-00420.1990>
- Terry, R. D. (2000). Cell death or synaptic loss in Alzheimer disease. In *Journal of Neuropathology and Experimental Neurology* (Vol. 59, Issue 12). <https://doi.org/10.1093/jnen/59.12.1118>
- Terry, R. D., Masliah, E., Salmon, D. P., Butters, N., DeTeresa, R., Hill, R., Hansen, L. A., & Katzman, R. (1991). Physical basis of cognitive alterations in alzheimer's disease: Synapse loss is the major correlate of cognitive impairment. *Annals of Neurology*, *30*(4). <https://doi.org/10.1002/ana.410300410>
- Thai, H. T., Mentré, F., Holford, N. H. G., Veyrat-Follet, C., & Comets, E. (2013). A comparison of bootstrap approaches for estimating uncertainty of parameters in linear mixed-effects models. *Pharmaceutical Statistics*. <https://doi.org/10.1002/pst.1561>
- Tolman, E. C. (1948). Cognitive maps in rats and men. *Psychological Review*, *55*(4). <https://doi.org/10.1037/h0061626>
- Toyama, K., Kimura, M., & Tanaka, K. (2017). Organization of cat visual cortex as investigated by cross-correlation technique. *Journal of Neurophysiology*. <https://doi.org/10.1152/jn.1981.46.2.202>
- Tran-Tu-Yen, D. A. S., Marchand, A. R., Pape, J. R., di Scala, G., & Coutureau, E. (2009). Transient role of the rat prelimbic cortex in goal-directed behaviour. *European Journal of Neuroscience*, *30*(3). <https://doi.org/10.1111/j.1460-9568.2009.06834.x>
- Tseng, S.-Y., Chettih, S. N., Arlt, C., Barroso-Luque, R., & Harvey, C. D. (2022). Shared and specialized coding across posterior cortical areas for dynamic navigation decisions. *Neuron*, *110*(15), 2484-2502.e16. <https://doi.org/10.1016/j.neuron.2022.05.012>
- Usrey, W. M., Reppas, J. B., & Reid, R. C. (1999). Specificity and strength of retinogeniculate connections. *Journal of Neurophysiology*. <https://doi.org/10.1152/jn.1999.82.6.3527>
- van Dyck, C. H., Swanson, C. J., Aisen, P., Bateman, R. J., Chen, C., Gee, M., Kanekiyo, M., Li, D., Reyderman, L., Cohen, S., Froelich, L., Katayama, S., Sabbagh, M., Vellas, B., Watson, D., Dhadda, S., Irizarry, M., Kramer, L. D., & Iwatsubo, T. (2023). Lecanemab in Early Alzheimer's Disease. *New England Journal of Medicine*, *388*(1), 9–21. <https://doi.org/10.1056/NEJMoa2212948>
- van Groen, T., & Wyss, J. M. (1990). Extrinsic projections from area CA1 of the rat hippocampus: Olfactory, cortical, subcortical, and bilateral hippocampal formation projections. *Journal of Comparative Neurology*, *302*(3). <https://doi.org/10.1002/cne.903020308>
- Van Spronsen, M., & Hoogenraad, C. C. (2010). Synapse pathology in psychiatric and neurologic disease. In *Current Neurology and Neuroscience Reports*. <https://doi.org/10.1007/s11910-010-0104-8>

- van Strien, N. M., Cappaert, N. L. M., & Witter, M. P. (2009). The anatomy of memory: An interactive overview of the parahippocampal- hippocampal network. In *Nature Reviews Neuroscience* (Vol. 10, Issue 4). <https://doi.org/10.1038/nrn2614>
- Vaz, A. P., Inati, S. K., Brunel, N., & Zaghloul, K. A. (2019). Coupled ripple oscillations between the medial temporal lobe and neocortex retrieve human memory. *Science*. <https://doi.org/10.1126/science.aau8956>
- Verret, L., Mann, E. O., Hang, G. B., Barth, A. M., Cobos, I., Ho, K., Devidze, N., Masliah, E., Kreitzer, A. C., Mody, I., Mucke, L., & Palop, J. J. (2012). Inhibitory interneuron deficit links altered network activity and cognitive dysfunction in Alzheimer model. *Cell*, *149*(3), 708–721. <https://doi.org/10.1016/j.cell.2012.02.046>
- Vertes, R. P. (2004). Differential Projections of the Infralimbic and Prelimbic Cortex in the Rat. *Synapse*, *51*(1). <https://doi.org/10.1002/syn.10279>
- Vertes, R. P. (2006). Interactions among the medial prefrontal cortex, hippocampus and midline thalamus in emotional and cognitive processing in the rat. *Neuroscience*, *142*(1), 1–20. <https://doi.org/10.1016/j.neuroscience.2006.06.027>
- Vertes, R. P., Hoover, W. B., Szigeti-Buck, K., & Leranth, C. (2007). Nucleus reuniens of the midline thalamus: link between the medial prefrontal cortex and the hippocampus. *Brain Research Bulletin*, *71*(6), 601–609. <https://doi.org/10.1016/j.brainresbull.2006.12.002>
- Vertes, R. P., & Kocsis, B. (1997). Brainstem-diencephalo-septohippocampal systems controlling the theta rhythm of the hippocampus. In *Neuroscience* (Vol. 81, Issue 4). [https://doi.org/10.1016/S0306-4522\(97\)00239-X](https://doi.org/10.1016/S0306-4522(97)00239-X)
- Viejo, G., Levenstein, D., Carrasco, S. S., Mehrotra, D., Mahallati, S., Vite, G. R., Denny, H., Sjulson, L., Battaglia, F. P., & Peyrache, A. (2022). Pynapple: a toolbox for data analysis in neuroscience. *BioRxiv*, 2022.12.06.519376. <https://doi.org/10.1101/2022.12.06.519376>
- Vizuete, J. A., Pillay, S., Diba, K., Ropella, K. M., & Hudetz, A. G. (2012). Monosynaptic functional connectivity in cerebral cortex during wakefulness and under graded levels of anesthesia. In *Frontiers in Integrative Neuroscience*. <https://doi.org/10.3389/fnint.2012.00090>
- Vogt, B., & Gabriel, M. (1993). *Neurobiology of cingulate cortex and limbic thalamus: a comprehensive handbook: Vol. No. 577.25 NEU*. Birkhäuser.
- Vossel, K. A., Beagle, A. J., Rabinovici, G. D., Shu, H., Lee, S. E., Naasan, G., Hegde, M., Cornes, S. B., Henry, M. L., Nelson, A. B., Seeley, W. W., Geschwind, M. D., Gorno-Tempini, M. L., Shih, T., Kirsch, H. E., Garcia, P. A., Miller, B. L., & Mucke, L. (2013). Seizures and epileptiform activity in the early stages of Alzheimer disease. *JAMA Neurology*, *70*(9). <https://doi.org/10.1001/jamaneurol.2013.136>
- Walsh, D. M., Klyubin, I., Fadeeva, J. V., Cullen, W. K., Anwyl, R., Wolfe, M. S., Rowan, M. J., & Selkoe, D. J. (2002). Naturally secreted oligomers of amyloid β protein potently inhibit hippocampal long-term potentiation in vivo. *Nature*. <https://doi.org/10.1038/416535a>
- Wang, M., Foster, D. J., & Pfeiffer, B. E. (2020). Alternating sequences of future and past behavior encoded within hippocampal theta oscillations. *Science*, *370*(6513). <https://doi.org/10.1126/science.abb4151>
- Wang, D. v., & Ikemoto, S. (2016). Coordinated interaction between hippocampal sharp-wave ripples and anterior cingulate unit activity. *Journal of Neuroscience*, *36*(41). <https://doi.org/10.1523/JNEUROSCI.1042-16.2016>
- Wang, Y., Romani, S., Lustig, B., Leonardo, A., & Pastalkova, E. (2014). Theta sequences are essential for internally generated hippocampal firing fields. *Nature Neuroscience*, *18*(2), 282–288. <https://doi.org/10.1038/nn.3904>
- Wierzynski, C. M., Lubenov, E. v, Gu, M., & Siapas, A. G. (2009). State-dependent spike-timing relationships between hippocampal and prefrontal circuits during sleep. *Neuron*, *61*(4), 587–596. <https://doi.org/10.1016/j.neuron.2009.01.011>

- Wikenheiser, A. M., & Redish, A. D. (2012). Hippocampal sequences link past, present, and future. In *Trends in Cognitive Sciences* (Vol. 16, Issue 7).
<https://doi.org/10.1016/j.tics.2012.05.005>
- Wikenheiser, A. M., & Redish, A. D. (2014). Decoding the cognitive map: Ensemble hippocampal sequences and decision making. In *Current Opinion in Neurobiology* (Vol. 32). <https://doi.org/10.1016/j.conb.2014.10.002>
- Wikenheiser, A. M., & Redish, A. D. (2015). Hippocampal theta sequences reflect current goals. *Nature Neuroscience*, 18(2). <https://doi.org/10.1038/nn.3909>
- Wilkinson, M. D., Dumontier, M., Aalbersberg, I. J., Appleton, G., Axton, M., Baak, A., Blomberg, N., Boiten, J. W., da Silva Santos, L. B., Bourne, P. E., Bouwman, J., Brookes, A. J., Clark, T., Crosas, M., Dillo, I., Dumon, O., Edmunds, S., Evelo, C. T., Finkers, R., ... Mons, B. (2016). Comment: The FAIR Guiding Principles for scientific data management and stewardship. *Scientific Data*, 3. <https://doi.org/10.1038/sdata.2016.18>
- Wilson, M. A., & McNaughton, B. L. (1994). Reactivation of hippocampal ensemble memories during sleep. *Science*, 265(5172). <https://doi.org/10.1126/science.8036517>
- Winson, J. (1974). Patterns of hippocampal theta rhythm in the freely moving rat. *Electroencephalography and Clinical Neurophysiology*, 36(C). [https://doi.org/10.1016/0013-4694\(74\)90171-0](https://doi.org/10.1016/0013-4694(74)90171-0)
- Wirt, R. A., Crew, L. A., Ortiz, A. A., McNeela, A. M., Flores, E., Kinney, J. W., & Hyman, J. M. (2021). Altered theta rhythm and hippocampal-cortical interactions underlie working memory deficits in a hyperglycemia risk factor model of Alzheimer's disease. *Communications Biology*, 4(1). <https://doi.org/10.1038/s42003-021-02558-4>
- Witton, J., Staniaszek, L. E., Bartsch, U., Randall, A. D., Jones, M. W., & Brown, J. T. (2016). Disrupted hippocampal sharp-wave ripple-associated spike dynamics in a transgenic mouse model of dementia. *Journal of Physiology*, 594(16). <https://doi.org/10.1113/jphysiol.2014.282889>
- Xiao, N. A., Zhang, J., Zhou, M., Wei, Z., Wu, X. L., Dai, X. M., Zhu, Y. G., & Chen, X. C. (2015). Reduction of glucose metabolism in olfactory bulb is an earlier Alzheimer's disease-related biomarker in 5XFAD mice. *Chinese Medical Journal*. <https://doi.org/10.4103/0366-6999.162507>
- Ye, X., Kapeller-Libermann, D., Travaglia, A., Inda, M. C., & Alberini, C. M. (2017). Direct dorsal hippocampal-prelimbic cortex connections strengthen fear memories. *Nature Neuroscience*, 20(1), 52–61. <https://doi.org/10.1038/nn.4443>
- Ylinen, A., Bragin, A., Nadasdy, Z., Jando, G., Szabo, I., Sik, A., & Buzsáki, G. (1995). Sharp wave-associated high-frequency oscillation (200 Hz) in the intact hippocampus: Network and intracellular mechanisms. *Journal of Neuroscience*. <https://doi.org/10.1523/jneurosci.15-01-00030.1995>
- Ylinen, A., Soltész, I., Bragin, A., Penttonen, M., Sik, A., & Buzsáki, G. (1995). Intracellular correlates of hippocampal theta rhythm in identified pyramidal cells, granule cells, and basket cells. *Hippocampus*, 5(1). <https://doi.org/10.1002/hipo.450050110>
- Yu, J. Y., & Frank, L. M. (2021). Prefrontal cortical activity predicts the occurrence of nonlocal hippocampal representations during spatial navigation. *PLoS Biology*, 19(9). <https://doi.org/10.1371/journal.pbio.3001393>
- Zhang, L., Prince, S. M., Paulson, A. L., & Singer, A. C. (2022). Goal discrimination in hippocampal nonplace cells when place information is ambiguous. *Proceedings of the National Academy of Sciences of the United States of America*, 119(11). <https://doi.org/10.1073/pnas.2107337119>
- Zhao, X., Hsu, C. L., & Spruston, N. (2022). Rapid synaptic plasticity contributes to a learned conjunctive code of position and choice-related information in the hippocampus. *Neuron*, 110(1). <https://doi.org/10.1016/j.neuron.2021.10.003>

Zielinski, M. C., Shin, J. D., & Jadhav, S. P. (2019). Coherent coding of spatial position mediated by theta oscillations in the hippocampus and prefrontal cortex. *Journal of Neuroscience*, 39(23). <https://doi.org/10.1523/JNEUROSCI.0106-19.2019>